Adam Mickiewicz University

Faculty of Chemistry

Influence of thermodynamic conditions on the structure and optical properties of organic semiconductors

Wpływ warunków termodynamicznych na strukturę i właściwości optyczne półprzewodników organicznych

Paulina Ratajczyk

Supervision: Prof. dr hab. Andrzej Katrusiak

Co-supervision: Dr Szymon Sobczak

Poznań, 2025

Doktorat dedykuję moim
Rodzicom oraz Dziadkom

Dziękuję

mojemu Promotorowi, Profesorowi Andrzejowi Katrusiakowi oraz Promotorowi pomocniczemu, dr. Szymonowi Sobczakowi za poświęcony czas, przekazaną wiedzę, oraz stworzenie mi możliwości rozwoju

wszystkim Członkom Zakładu Chemii Materiałów

mojej Rodzinie oraz Przyjaciołom

The research presented in this thesis was carried out at
the Department of Materials Chemistry, Adam Mickiewicz University in Poznań

This work was financially supported by the Polish Ministry of Education and Science
(Diamentowy Grant DI2019/0160/49)

Diamentowy
Grant

Table of Contents

List of abbreviations

CSD	Cambridge Structural Database
d_{π}	π-π stacking distance
DAC	diamond anvil cell
DSC	differential scanning calorimetry
E_{g}	bandgap energy
HOMO	highest occupied molecular orbital
HSM	hot-stage microscopy
LUMO	lowest unoccupied molecular orbital
NLC	negative linear compressibility
NTE	negative thermal expansion
OSCs	organic solar cells
PCE	power conversion efficiency
PDI	perylene diimide
PL	photoluminescence
PTB7	poly[[4,8-bis[(2-ethylhexyl)oxy]benzo[1,2-b:4,5-b′]dithiophene-2,6-diyl][3-fluoro-2-(2-ethylhexyl)carbonyl]thieno[3,4-b]thiophenediyl]]
PXRD	powder X-ray diffraction
SEM	scanning electron microscopy
SCXRD	single-crystal X-ray diffraction
SOFs	site occupancy factors
UV-Vis-NIR	ultraviolet-visible-near infrared
V_{m}	molecular volume

Summary in Polish

(Streszczenie po polsku)

Celem mojej rozprawy doktorskiej było zbadanie wpływu wysokiego ciśnienia oraz zmian temperatury na strukturę i właściwości fotofizyczne wybranych półprzewodników organicznych, aby pogłębić wiedzę o zależności struktura–właściwości w tej grupie związków. Inspiracją do podjęcia badań były liczne doniesienia literaturowe dotyczące materiałów perowskitowych, w których wykazano, że ekstremalne warunki stanowią skuteczne narzędzie do analizy mechanizmów przemian fazowych oraz zależności między strukturą a właściwościami. W przypadku półprzewodników organicznych takie podejście wciąż pozostaje stosunkowo rzadko wykorzystywane, mimo że materiały te odgrywają coraz większą rolę w rozwoju nowoczesnych technologii fotowoltaicznych i optoelektronicznych.

Rozprawa obejmuje cykl czterech artykułów przedstawiających wyniki badań sześciu wybranych półprzewodników organicznych: polimeru PTB7 oraz małocząsteczkowych pochodnych diimidu perylenowego (PDI) różniących się podstawnikami w pozycji imidowej. Analizy strukturalne, przeprowadzone metodą dyfrakcji rentgenowskiej, skorelowałam z pomiarami spektroskopowymi UV-Vis-NIR i fotoluminescencji, co umożliwiło identyfikację i szczegółową charakterystykę szeregu nowych polimorfów. Wyniki badań wykazały, że wzrost ciśnienia lub temperatury prowadzi do istotnych zmian w odległościach π–π pomiędzy rdzeniami aromatycznymi, konformacji cząsteczek oraz sposobie ich agregacji. Modyfikacje te wpływają na przerwę energetyczną pasm i właściwości luminescencyjne analizowanych materiałów.

W artykule **A1** przedstawiłam wyniki badań dotyczących PTCDI-Ph, pochodnej PDI z podstawnikami fenylowymi, dla której zidentyfikowałam trzy polimorfy: stabilny w warunkach atmosferycznych, wysokotemperaturowy występujący powyżej 493 K oraz wysokociśnieniowy stabilny powyżej 3 GPa. Zaobserwowałam odwracalne przesunięcia batochromowe oraz zmiany intensywności fotoluminescencji zależne od ciśnienia i temperatury, wskazujące na możliwość zastosowania PTCDI-Ph jako materiału aktywnego w czujnikach multimodalnych. Artykuł **A2** poświęcony został badaniom pochodnej PDI-C_6 z *N*-podstawionymi *n*-heksylami, dla której zidentyfikowałam pięć

polimorfów, w tym dwa wysokociśnieniowe i dwa wysokotemperaturowe. Wykazałam, że ciśnienie prowadzi do stopniowych zmian konformacji łańcuchów alkilowych, natomiast wysoka temperatura powoduje dodatkowo rotacje rdzeni perylenowych. Artykuł **A3** obejmuje analizę serii PDI-C_n (gdzie n = 5–8) z podstawnikami alkilowymi (C_nH_{2n+1}) o różnej długości. Zastosowanie dyfrakcji rentgenowskiej monokryształów w warunkach wysokiego ciśnienia pozwoliło mi zidentyfikować nowe fazy, a uzyskane dane strukturalne skorelowałam z obserwowanymi przesunięciami w widmach absorpcji UV-Vis-NIR i emisji. W artykule **A4** opisałam wyniki badań dotyczących polimeru PTB7, ze szczególnym uwzględnieniem wpływu wysokiego ciśnienia oraz sposobu przygotowania warstwy pomiarowej na jego właściwości optyczne. Wykazałam, że wzrost ciśnienia powoduje batochromowe przesunięcie krawędzi absorpcji oraz zwężenie przerwy energetycznej (E_g).

Przeprowadzone badania wykazały, że wykorzystanie warunków ekstremalnych stanowi efektywne narzędzie do modelowania zmian strukturalnych, które bezpośrednio wpływają na podstawowe właściwości materiałów organicznych, takie jak przerwa energetyczna i luminescencja. Wyniki te nie tylko dostarczają nowych informacji na temat zachowania półprzewodników organicznych pod wpływem wysokiego ciśnienia i zmian temperatury, lecz także wskazują na możliwość świadomego dostosowywania ich właściwości optycznych poprzez kontrolowane modyfikacje strukturalne.

Summary in English

The aim of my doctoral dissertation was to investigate the influence of high pressure and temperature changes on the structure and photophysical properties of selected organic semiconductors, in order to deepen the understanding of the structure–property relationships in this group of compounds. The research was inspired by numerous literature reports on perovskite materials, which have shown that extreme conditions provide an effective tool for analyzing phase transition mechanisms and the relationship between structure and properties. However, in the case of organic semiconductors, this approach is still rarely applied, even though these materials play an increasingly important role in the development of modern photovoltaic and optoelectronic technologies.

The dissertation comprises a series of four articles presenting the results of studies on six selected organic semiconductors: the polymer PTB7 and small-molecule perylene diimide (PDI) derivatives with different substituents at the imide position. I correlated the structural analyses, conducted using X-ray diffraction, with UV-Vis-NIR and photoluminescence spectroscopy measurements, which enabled the identification and detailed characterization of several new polymorphs. The results revealed that variations in pressure or temperature induce significant changes in π–π stacking distances between aromatic cores, the conformation of the molecules, and their aggregation behavior. These structural modifications directly influence the band gap energy and the luminescent properties of the investigated materials.

In article **A1**, I presented the results of studies on PTCDI-Ph, a PDI derivative with phenyl substituents, for which I identified three polymorphs: one stable at ambient conditions, a high-temperature phase occurring above 493 K, and a high-pressure phase above 3 GPa. I observed reversible bathochromic shifts and changes in photoluminescence intensity that were dependent on pressure and temperature, indicating the potential of PTCDI-Ph as an active material in multimodal sensors. Article **A2** focuses on PDI-C_6, a derivative with N-substituted *n*-hexyl groups, for which I identified five polymorphs, including two high-pressure and two high-temperature phases. I demonstrated that pressure induces gradual conformational changes in the alkyl

chains, while high temperature additionally causes rotations of the perylene cores. Article **A3** analyzes the PDI-C_n series (where n = 5–8) with alkyl substituents (C_nH_{2n+1}) of varying length. Using high-pressure single-crystal X-ray diffraction, I identified new phases and correlated the obtained structural data with the observed shifts in the UV-Vis-NIR absorption and emission spectra. Article **A4** presents results on the polymer PTB7, with particular emphasis on the effects of high pressure and film preparation methods on its optical properties. I demonstrated that increasing pressure causes a bathochromic shift of the absorption edge and a narrowing of the band gap (E_g).

The conducted studies demonstrated that the use of extreme conditions provides an effective tool for modeling structural changes that directly influence fundamental properties of organic materials, such as band gap and luminescence. These results not only provide new insights into the behavior of organic semiconductors under high pressure and variable temperature but also highlight the possibility of tuning their optical properties through controlled structural modifications.

1. Introduction

The advent of semiconductor technology has revolutionized modern life, profoundly changing our work, how we communicate, and access information. Semiconductors are versatile materials, characterized by electrical conductivity intermediate between those of conductors and insulators. They owe their unique properties to their distinct energy band structures. Semiconductors possess a relatively small energy gap, typically less than 3.0 eV, separating the valence and conduction bands.[1] As fundamental building blocks of nearly all modern electronic devices, including transistors,[2] solar cells,[3] light-emitting diodes (LEDs),[4,5] and sensors,[6] they have become indispensable in everyday life. Semiconductors exhibit exceptional diversity in chemical composition and solid-state structures. This group includes elemental semiconductors, such as the most widely used silicon (Si), binary compounds like gallium arsenide (GaAs), and a large and rapidly growing family of organic semiconductors.[7] Among the latter, perylene diimides (PDIs) exhibit promising semiconducting properties and are the primary focus of my research.

1.1. Organic Semiconductors

Organic semiconductors are materials composed primarily of carbon and hydrogen atoms, often containing heteroatoms such as oxygen, sulfur, and nitrogen. Their semiconducting behavior arises from a delocalized π-electron system, which enables the absorption and emission of visible light as well as electrical conductivity. These properties make organic semiconductors highly suitable for a wide range of optoelectronic applications, including organic light-emitting diodes (OLEDs),[8,9] organic field-effect transistors (OFETs),[10] and organic photovoltaic cells (OPVs).[11,12]

The history of organic semiconductors dates back to the early 20th century. One of the first significant developments was Pochettino's discovery of photoconductivity in anthracene crystals.[13] Today, organic semiconductors are broadly classified into two main categories: low molecular weight compounds and polymers (Figure 1). A common feature of both classes is their conjugated π-electron system, formed by the overlap of p_z-orbitals in sp^2-hybridized carbon atoms, which enables delocalization and charge transport.[14] The

performance of organic electronic devices critically depends on the charge carrier mobility (electrons and/or holes) within these π-conjugated materials.[15] Based on their dominant charge carrier, both polymeric and molecular organic semiconductors are classified as p-type (where the majority carriers are holes), n-type (where the majority carriers are electrons), or ambipolar (capable of transporting both electrons and holes).[16] However, the development of high-performance n-type semiconductors has significantly lagged behind that of p-type materials, primarily due to their lower electron mobility and instability in air.[17,18]

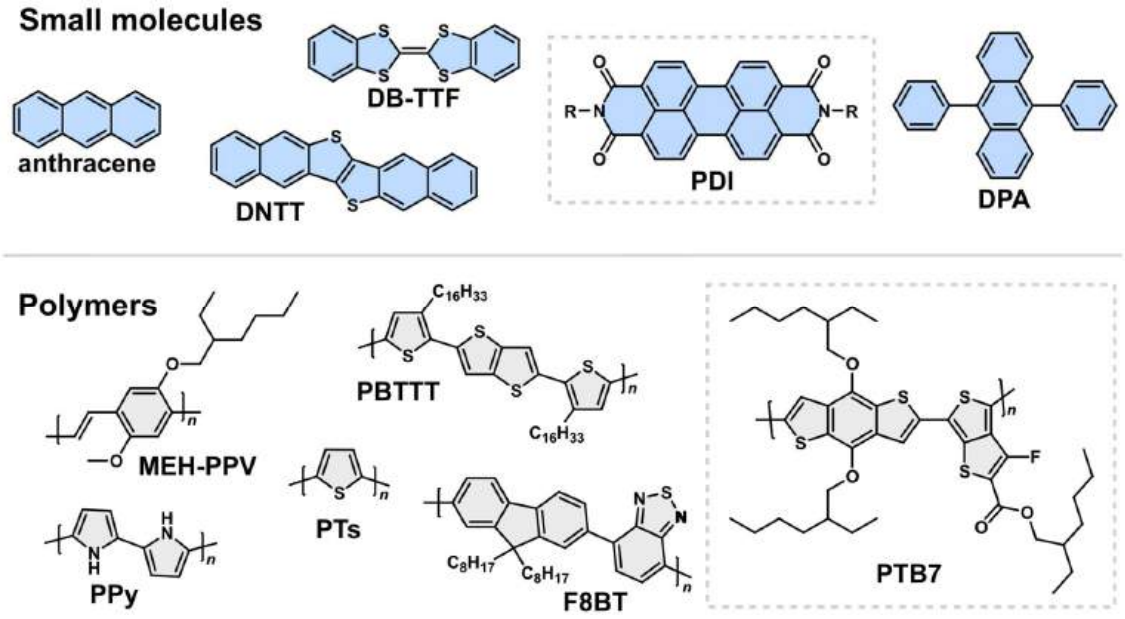

Figure 1. Chemical structures of several popular small-molecule and polymer semiconductors. The materials studied in this PhD research are highlighted with frames.

In contrast to inorganic semiconductors, which are typically stabilized by strong covalent or ionic bonds, organic semiconductors are molecular solids held together by weak noncovalent interactions such as van der Waals forces. This fundamental difference in the dominant aggregation force leads to distinct mechanical, optical, and electrical properties.[19] Another key distinction is their processing. Inorganic semiconductors typically require expensive, high-purity crystalline substrates, high-temperature and low-throughput fabrication techniques. In contrast, organic semiconductors can be deposited on inexpensive substrates, like glass or plastic, using solution-based techniques, thus

eliminating the need for high-quality crystalline substrates.[20] This provides advantages in terms of cost, ease of processing, and thin-film formation.[21–23] Moreover, a significant advantage of organic semiconductors is the ease of tailoring their properties through chemical synthesis. The introduction of substituents into conjugated organic molecules provides an effective approach to tuning molecular orbital energy levels. For instance, electron-donating substituents (e.g., amino or alkyl groups) typically raise the energy of the highest occupied molecular orbital (HOMO). In contrast, electron-withdrawing groups, such as cyano substituents, lower the energies of both the HOMO and the lowest unoccupied molecular orbital (LUMO).[24] The importance of organic electronic materials was recognized in 2000, when Hideki Shirakawa, Alan J. Heeger, and Alan G. MacDiarmid were awarded the Nobel Prize in Chemistry for their discovery and development of conductive polymers.[25] Despite recent progress and the promising potential of organic materials, Si continues to dominate the semiconductor market due to its superior performance.[26,27] Advancing the technological applications of organic semiconductors requires overcoming key challenges, primarily their lower charge carrier mobility and an incomplete understanding of fundamental structure–property relationships.[28–30]

1.2. Perylene diimides

In recent years, significant research efforts have focused on a wide range of organic semiconductors, including fullerenes,[15,31,32] thiazole derivatives,[33] oligoacenes,[15,31,34] oligothiophenes,[15,31,32] and perylenes.[15,31,32,34,35] Among these, perylene-3,4,9,10-tetracarboxylic acid diimides, also known as perylene diimides or PDIs, stand out as a prominent class that has attracted considerable scientific interest due to their exceptional combination of properties (Figure 2). These include strong absorption in the visible region, relatively high electron mobility, and excellent photo, thermal, and chemical stability.[36] These characteristics make PDIs highly promising n-type semiconductors for organic electronic devices and a compelling alternative to fullerene-based materials.[37–42] Consequently, PDIs are actively investigated for a diverse range of applications, including optoelectronic and photovoltaic devices, as well as light-emitting diodes.[42–44]

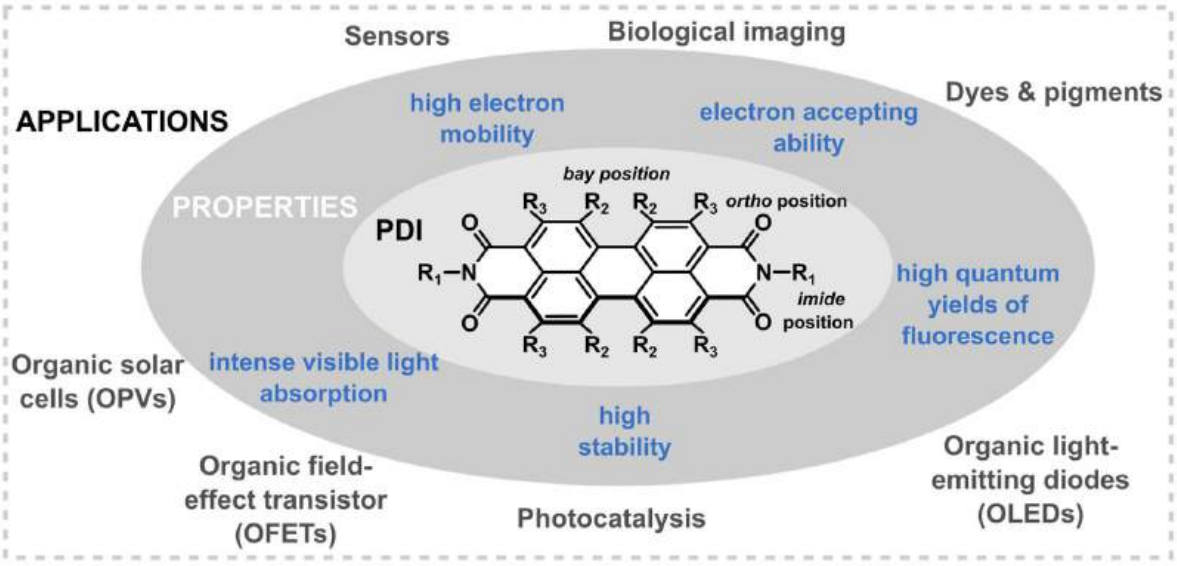

Figure 2. Chemical structure of a PDI highlighting the possible substitution sites: *imide*, *ortho*, and *bay* positions with examples of PDI properties and applications.

First synthesized in 1913,[45] perylene dyes were initially employed exclusively as industrial pigments, providing a broad color range from orange, red, and brown, to black.[46] These color variations are highly sensitive to subtle changes in their chemical structure and solid-state molecular packing.[47,48] Beyond their original applications, PDIs possess a range of properties that make them suitable for numerous emerging technologies. Their potential in organic solar cells (OSCs) was first demonstrated by Tang in 1986,[49] initiating a rapid growth of research and subsequent performance improvements.[37] The scientific interest in PDIs has grown dramatically in recent years: of the more than 2870 publications identified in Scopus, over 84% have been published since 2010, highlighting rapidly growing interest in these compounds (Figure 3a). Continued development has raised the power conversion efficiency (PCE) of OSCs with PDI-based active layers to above 11%.[50] One of the most prominent applications of PDIs lies in their use as cathode interlayers (CILs). A variety of PDI derivatives have been successfully implemented as CILs in OSCs, enabling PCEs exceeding 19%.[51–54] Furthermore, PDIs have also proven effective as CILs in perovskite solar cells.[55,56]

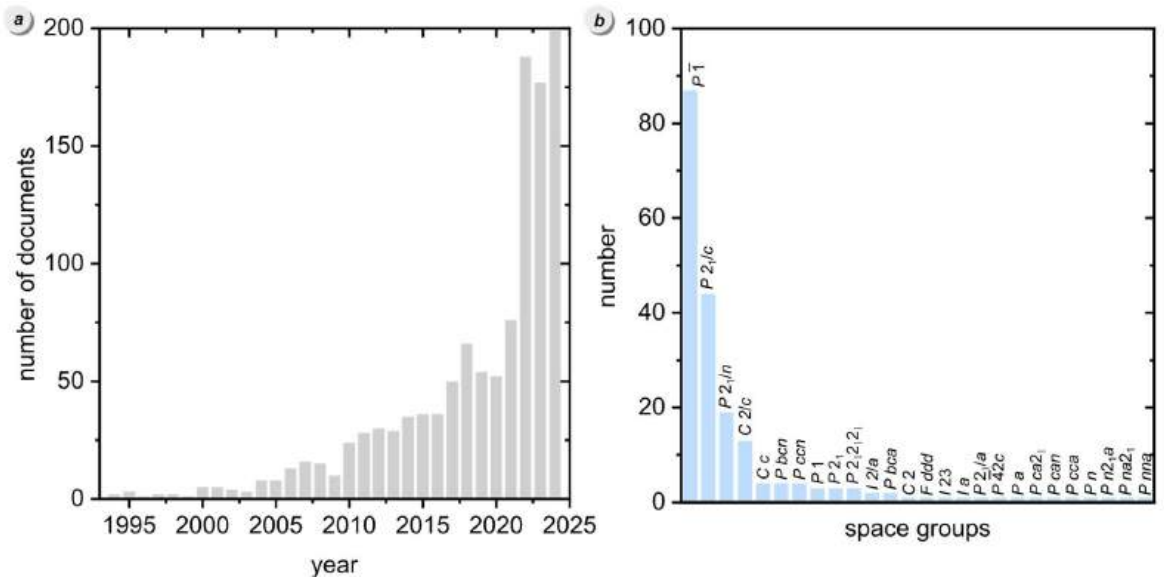

Figure 3. Number of scientific articles related to perylene diimides published per year, based on a Scopus search using the keyword '*perylene diimide*' (a), and the distribution of crystallographic space groups for PDIs deposited in the CSD database version 2025.2 (b), illustrating preferred crystal symmetries for these compounds.

The synthesis of PDIs typically involves a condensation reaction between 3,4,9,10-perylenetetracarboxylic dianhydride (PTCDA) and alkylamines or anilines under inert atmosphere, using solvents such as *N*,*N*-dimethylformamide (DMF), imidazole (ImH), or quinoline.[57,58] This synthetic route enables high yields in a few steps, which is crucial for meeting the requirements of large-scale manufacturing and commercialization.[59] The remarkable versatility of PDIs is significantly enhanced by their facile chemical modification. Substituents can be introduced at ten distinct positions, specifically the two *imide*, four *bay*, and four *ortho* sites of the perylene core, allowing precise tailoring of their physicochemical properties (Figure 2). Substitution at the *imide* position primarily influences solubility and aggregation behavior while preserving the planarity of the perylene core and having a relatively minor impact on absorption and emission properties.[60] My PhD research is focused on PDIs substituted at this position. In contrast, substitution at the *bay* and *ortho* positions affects the electronic and optical properties more significantly.[48] *Bay* substitutions can induce twisting of the perylene core due to steric effects.[61] Such geometric distortions may weaken intermolecular π-π overlap, potentially reducing charge carrier mobility.[48] On the other hand, *ortho* functionalization

can modify the optoelectronic properties, while maintaining the planarity of the perylene core.[48] These functionalization strategies enable the rational design of PDIs with tailored physical, chemical, and optoelectronic properties for targeted applications.[40]

PDIs are known for their rich polymorphism,[62–65] and the strong correlation between their molecular packing and electrical as well as optical properties.[66–68] Polymorphism is the ability of a substance to crystallize in more than one phase, characterized by different molecular arrangements or conformations within the crystal lattice.[69] My analysis of over 200 distinct crystal structures of PDI derivatives (excluding solvates, polymers, and duplicate entries recorded under different conditions) deposited in the Cambridge Structural Database (CSD)[70] version 2025.2 reveals a dominant occurrence of triclinic (44%) and monoclinic (44%) crystal systems (Figure 3b). However, most of these PDI structures were determined at a single measurement point, either at ambient conditions or at low temperature. Consequently, the polymorphic behavior of PDIs under variable thermodynamic conditions remains largely unexplored. To date, only solid–solid phase transitions upon heating have been documented,[62] while their behavior at high pressure has not yet been investigated. Systematic structural studies beyond ambient temperature have been reported for PDI-C_5 (Figure 4a) and PDIF-CN_2 (Figure 4b).[62,71] For PDI-C_5, high temperature studies up to 553 K revealed three distinct phases, while for PDIF-CN_2, investigations at low temperature, between 100 and 300 K, showed no evidence of a phase transition. Further details on these compounds are provided in the *Results* and *Discussion* sections. This knowledge gap is critical because even small differences in molecular packing can significantly influence the optoelectronic and charge-transport properties.[72,73] For example, minor shifts in the aggregation of 6,13-bis(triisopropylsilylethynyl)pentacene (TIPS-PEN) molecules have been shown to alter hole mobility by three orders of magnitude.[74]

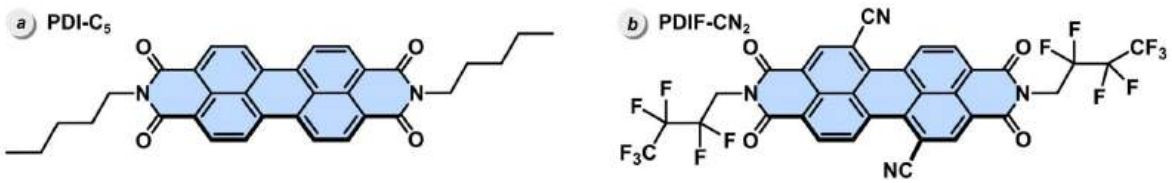

Figure 4. Chemical structure of PDI derivatives: (a) PDI-C_5,[62] and (b) PDIF-CN_2.[71]

1.3. PTB7

As a part of my dissertation, I investigated poly[[4,8-bis[(2-ethylhexyl)oxy]benzo[1,2-b:4,5-b′]dithiophene-2,6-diyl][3-fluoro-2-(2-ethylhexyl)carbonyl]thieno[3,4-b]thiophenediyl]] (PTB7), Figure 5. The donor material PTB7 is a widely studied and well-established polymer semiconductor. It is recognized for its favorable optoelectronic properties and high performance in organic photovoltaic applications, specifically as one of the most efficient narrow-bandgap conjugated polymers for bulk heterojunction (BHJ) polymer solar cells (PSCs).[75] PTB7 exhibits some of the highest reported efficiencies for polymer–fullerene solar cells due to its extended absorption into the near-infrared and lower HOMO level. A notable PCE of approximately 7.4% achieved with PTB7/$PC_{71}BM$ ($PC_{71}BM$ – phenyl-C_{71}-butyric acid methyl ester) solar cell devices was the first reported efficiency exceeding 7% for polymer solar cells.[76] The presence of small branched side chains in PTB7 enhances its solubility in organic solvents, which is important for device fabrication.

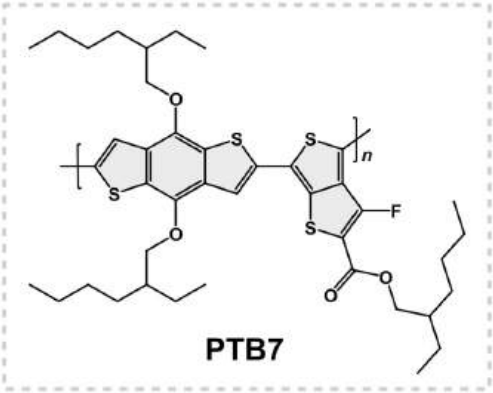

Figure 5. Chemical structure of PTB7.

1.4. Extreme conditions

Initial structural investigations of chemical compounds were traditionally performed at ambient conditions, typically defined as 15–25℃ and 0.1 MPa, due to experimental constraints. Presently, owing to significant advances in instrumentation, it is possible to access extreme pressures and temperatures,[77,78] in which materials can exhibit unexpected and often fundamentally different behavior compared to that observed under ambient conditions. In this thesis, I report experiments conducted at pressures up to 6.5 GPa and within a temperature range of 100–650 K.

Variable-temperature experiments significantly enhanced understanding of solid-state behavior, including phase transitions, chemical reactions, changes in atomic positions, crystal packing, and molecular conformations.[79–82] Since the heating and

cooling of crystalline samples is relatively easy, single-crystal structure determinations under variable-temperature conditions quickly became a standard practice. The field of high-pressure research was later revolutionized by the pioneering and Nobel Prize-winning work of P.W. Bridgman, who established the fundamental basis for investigating material properties under high pressure.[83] Nevertheless, the application of *in situ* X-ray diffraction techniques at high pressure remained challenging until the development of the diamond anvil cell (DAC) in the 1950s, which made such studies more accessible.[84,85] Today, high-pressure techniques are widely employed to explore material compressibility, pressure-induced phase transitions,[86,87] and the effects of pressure on chemical bonding, molecular conformations, intermolecular interactions,[88] and amorphization.[66,89,90] Pressure can also induce a variety of other phenomena, such as energy bandgap narrowing, prolonged carrier-lifetime,[91,92] and enhanced photoluminescence (PL) intensity.[93] Thus, extreme temperatures and pressures offer a powerful means to synthesize novel compounds and to observe and understand fundamental phenomena more comprehensively.[94]

1.5. Structure–property relationship

Understanding the relation between a structure and properties is fundamental to design novel materials with tailored functionalities. In crystalline materials, physical and chemical properties are linked to molecular packing within the crystal lattice.[95] This connection enables systematic studies of the correlation between structure and a wide range of physical and chemical properties, including magnetism, electrical conductivity, and optical behavior. Thermodynamic conditions, such as temperature and pressure, can significantly influence these properties, and their impact can be directly correlated with structural changes in the material, making them invaluable for studying structure–property relations.

Crystal structure analysis is a powerful, nondestructive, and indispensable technique in materials science. It offers detailed insights into the geometry of molecules and the nature of their interactions with neighboring molecules and ions. This structural information is essential across a broad range of scientific disciplines. In particular, it plays

a critical role in crystal engineering,[96] crystal growth,[97,98] crystal structure prediction,[99] and the study of polymorphism,[100] all key elements in the rational design of materials.[101]

Likewise, single crystals of organic semiconductors offer advantages for studying intrinsic material properties, structure–property correlations, identification of structural features that enhance device performance, and exploration of fundamental aspects of charge transport in organic systems.[102] In such materials, efficient charge transport strongly depends on the molecular arrangement. Achieving optimal molecular packing motifs that facilitate strong and long-range intermolecular interactions, such as hydrogen bonds, C–H···π and π–π stacking, is most important for efficient charge transport and, consequently, improved device performance. The hydrogen bonds and π–π stacking interactions usually define the resulting molecular packing architectures. The typical packing motifs observed in organic semiconductor crystals can be divided into four types (Figure 6): (a) lamellar one-dimensional (1D) π–π stacking (e.g., 1,2,3,4-tetrafluoroanthracene);[103] (b) lamellar two-dimensional (2D) π–π stacking, also referred to as brick layer stacking (e.g., TIPS-PEN);[104] (c) herringbone pattern with π–π overlap between adjacent molecules (e.g., rubrene);[105] and (d) herringbone pattern without π–π overlap between molecules (e.g., pentacene).[102,106] High charge-carrier mobility is expected when conjugated molecules pack with minimal displacement from an ideal π-stack and strong intermolecular interactions, thereby maximizing π-orbital overlap.[107,108] Among these four motifs, the lamellar 2D π–stacking (Figure 6b) is considered the most efficient for charge transport, while a herringbone packing motif without efficient π–π overlap (Figure 6d) is unfavorable for charge transport.[109–111]

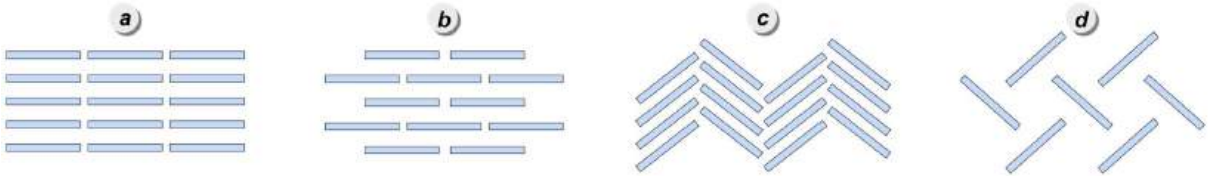

Figure 6. Typical crystal packing motifs in organic semiconductor crystals: (a) lamellar π–π stacking with 1D charge-carrier channels, (b) lamellar 2D π–π stacking; (c) herringbone π–π stacking; (d) herringbone packing without π–π stacking.

The position and nature of substituents play a crucial role in governing π–π interactions and packing motifs. For instance, studies on anthradithiophenes have demonstrated that molecular packing is highly sensitive to the type of chemical substitution.[112] Among the three derivatives examined by Jackson *et al.*,[112] the triethylsilyl-substituted compound crystallizes in a 2D π-stacking arrangement and displays the highest charge-carrier mobility. In the case of PDI derivatives, substitution restricted to the *imide* positions typically allows them to form strong π–π interactions.[113] When the *imide* substituents are alkyl chains or related groups, dispersion forces between them can increase packing efficiency, leading to short interplanar distances, typically around 3.4 Å. In contrast, aromatic substituents at the *imide* positions may introduce electrostatic repulsion, which either increases the stacking distance above 3.45 Å or induces molecular twisting that alters the stacking arrangement. For example, PDI-C_3 (Figure 7a) exhibits a π-π stacking distance (d_π) of 3.416(4) Å at 295 K, whereas PDI-3,5-Xy (Figure 7b) of 3.458(2) Å at 296 K (CSD deposition numbers: 1140265 and 186059, respectively).[114,115] Throughout this thesis, d_π is defined as the distance between the centroid of one perylene core and the plane of the perylene core of a neigbouring molecule in a column. Substitution at the *bay* positions disrupts the planarity of the PDI core, thereby weakening π–π interactions.[113] The d_π for PDI-1(Pr) (Figure 7c) at 100 K is 3.5128(11) Å (CSD deposition number: 2002333).[116] In contrast, substitution at the *ortho* positions is expected to maintain molecular planarity, promoting favorable π–π contacts and directional intermolecular interactions, and thus supporting well-defined stacking motifs.[113] Although no PDI derivative with only *ortho* substitution is available in the CSD database, my analysis of the compound obPDI-1 (Figure 7d), which contains both *imide* and *ortho* substituents, revealed a d_π of 3.4505(13) Å at 100 K (CSD deposition number: 1949530).[117] Interestingly, the corresponding bPDI-1 (Figure 7e) with the same *imide* substituents but lacking *ortho* substitution, exhibits a slightly shorter d_π of 3.3470(6) Å at the same temperature (CSD deposition number: 1949528).[117] Notably, the molecular arrangements differ: in obPDI-1 the perylene cores are aligned in parallel, whereas in bPDI-1 adjacent perylene cores are rotated. Even minor modifications in the substitution can significantly influence molecular packing,[113] as demonstrated by PDIs with halogenated aromatic groups at the *imide* position. In this case, replacing Cl with an F atom at the *meta* position of the phenyl ring (Figure 7f, g) induces a rotation of the

molecules around the stacking axis, which decreases the d_π by 0.15 Å, and transforms the crystal color from black-blue to dark red.[118]

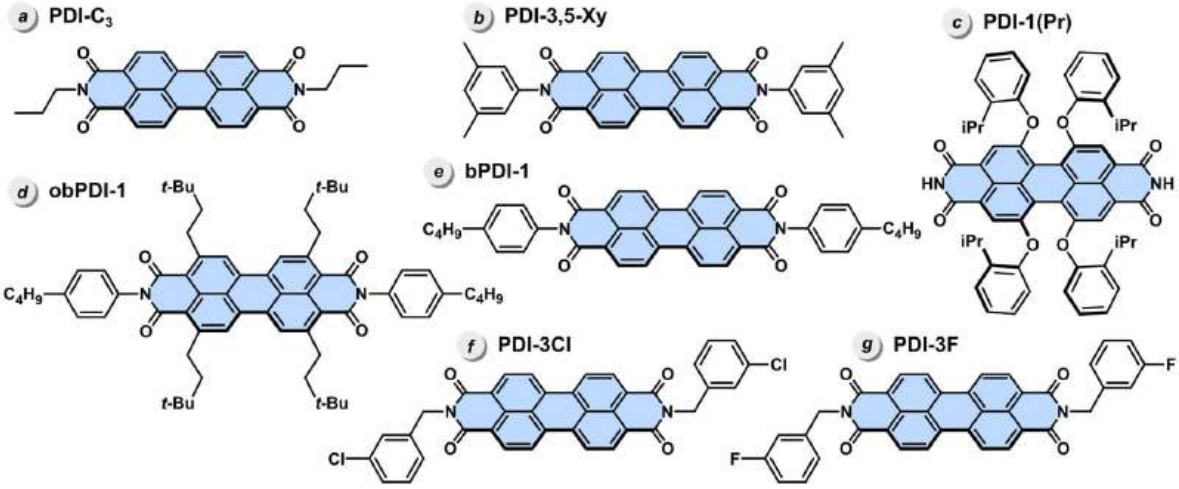

Figure 7. Chemical structure of selected PDI semiconductors.

While high-pressure and variable-temperature techniques have proven valuable for studying the structure–property relations in perovskites,[119–123] their application to organic semiconductors has remained unexplored. The reported studies on organic materials under extreme conditions often focus on specific aspects, such as the isolated effects of high pressure on either structure[124,125] or properties like photocurrent,[126,127] with only a few investigations considering both simultaneously.[86] The research focusing on semiconducting PDI derivatives, particularly their structural and optical responses to pressure and temperature changes, remains even more limited.[128] Nevertheless, several studies have highlighted the considerable potential of exploring these materials under non-ambient conditions.[62,64,71,129] For example, Huang *et al.* combined theoretical and experimental methods to analyze the structural, electronic, and optical properties of a monolayer organic molecular crystal of *N,N'*-dimethyl-3,4,9,10-perylenetetracarboxylic diimide (Me-PTCDI) under pressure up to 14.60 GPa.[129] They observed a pronounced red shift in PL emission under high pressure.

2. Aims of the thesis

The primary aim of this doctoral dissertation was to investigate how external stimuli, specifically high pressure and variable temperature, influence the structure and properties of selected organic semiconductors, with the overarching goal of deepening the understanding of fundamental structure–property relationships in these compounds.

This objective was achieved through comprehensive structural investigations of selected PDIs under ambient (0.1 MPa and 296±3 K), high-pressure, and variable-temperature conditions, to identify pressure- and temperature-induced structural transformations. Subsequently, complementary optical spectroscopy studies, including UV-Vis-NIR absorption and photoluminescence measurements, were employed to establish correlations between molecular structure and photophysical properties. Moreover, the influence of different substituents on structure and properties was studied by comparing PDIs functionalized at the *imide* position with either a phenyl group (PTCDI-Ph) or alkyl chains of varying lengths (PDI-C_n, where n = 5–8, Figure 8). A key contribution of this work is the discovery of novel polymorphs of PDIs and the characterization of their responses to external stimuli. Together, these findings provide critical insights into the polymorphism, adaptability, and structure–property relationships of this important class of organic semiconductors.

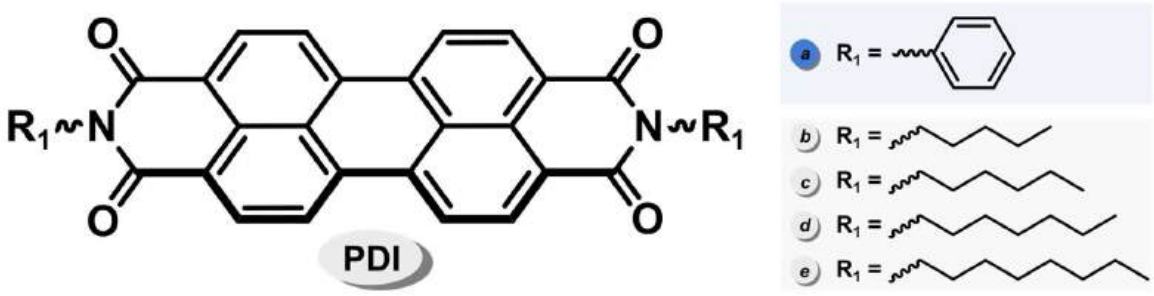

Figure 8. Perylene diimides studied within this thesis.

I also investigated other organic semiconductors, including the widely studied polymer PTB7. Specifically, I examined the influence of pressure as well as different film preparation methods on its optical absorption.

My PhD research has resulted in eight articles. Four of these (articles **A1**–**A4**), which focus on perylene diimides (**A1**–**A3**) and the polymer PTB7 (**A4**), represent my main scientific achievements. These four papers are listed below and discussed in detail in the *Results* and *Discussion* sections, with copies provided in Appendices **A1**–**A4**.

This doctoral dissertation is based on the following scientific articles:

A1 **P. Ratajczyk**, S. Sobczak, P. Woźny, A. Wcisło, T. Poręba, A. Katrusiak,
Unlocking the sensing potential of phenyl-substituted perylene diimides under extreme conditions, J. Mater. Chem. C, **2023**, 11, 11055-11065, DOI: 10.1039/D3TC01146A.

A2 **P. Ratajczyk**, S. Sobczak, M. Andrzejewski, F. Marin, M. Marchini, L. Maini, A. Katrusiak,
Pressure- and temperature-driven transitions and conformational conversions of n-hexyl substituted perylene diimide (PDI-C6) crystals, J. Mater. Chem. C, **2025**, 13, 13509-13518, DOI: 10.1039/D5TC00809C.

A3 **P. Ratajczyk,** S. Sobczak, M. Andrzejewski, P. Woźny, L. Maini, A. Katrusiak,
The odd-even alkyl chain effect on the structure and optoelectronic properties of alkyl-substituted perylene diimide (PDI) derivatives at highly strained environments, **2025,** DOI: 10.26434/chemrxiv-2025-2fjc9.

A4 **P. Ratajczyk,** A. Katrusiak, K. A. Bogdanowicz, W. Przybył, P. Krysiak, A. Kwak, A. Iwan,
Mechanical strain, thermal and pressure effects on the absorption edge of an organic charge-transfer polymer for flexible photovoltaics and sensors, Mater. Adv., **2022**, 3, 2697-2705, DOI: 10.1039/D1MA01066B.

3. Experimental Methods

This section presents a general overview of the experimental procedures applied in my research, while detailed methodologies are presented in the individual articles **A1**–**A4**.

3.1. Crystallization

Due to the limited solubility of PDIs, specialized recrystallization methods are required to obtain single crystals suitable for structural analysis. For commercially available PDIs, single crystals were grown either by sublimation in a sealed glass tube (as in the case of PTCDI-Ph) or by solvothermal crystallization (for the PDI-C_n series). In the sublimation procedure, the PTCDI-Ph sample was placed at the bottom of a glass capillary, which was then flame-sealed. The bottom of the capillary was heated with a heat gun to approximately 673 K, leading to the formation of plate-like crystals above the level of the crude material. For the PDI-C_n compounds, single crystals were grown from supersaturated solutions, heated overnight in a solvothermal reactor, followed by slow cooling to room temperature.

3.2. High-pressure generation in a diamond-anvil cell

High-pressure structural and spectroscopic experiments were conducted using a modified Merrill-Bassett diamond-anvil cell (DAC, Figure 9).[130] The DAC consists of two opposing diamonds, with the sample placed between their polished culets in the central hole of a pre-indented metal gasket.[131] This setup enables the generation of extremely high pressures with relatively low mechanical force, typically applied using screws or a gas membrane. In the experiments described in this thesis, diamond culets with diameters of 0.7–0.8 mm were

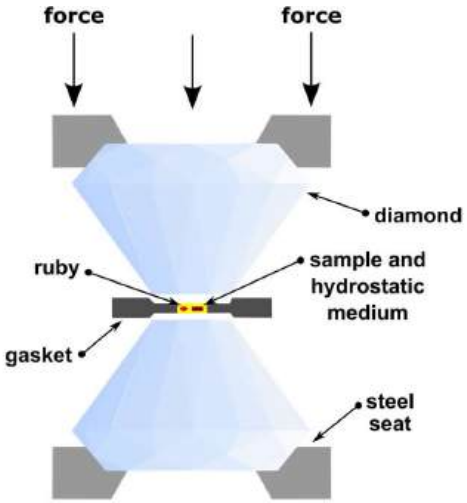

Figure 9. Schematic diagram of a DAC with a solid sample and a ruby chip inside a hole in the metal gasket.

employed. Owing to its versatility, the DAC allows for *in situ* investigation of a wide range of material properties, including structural, elastic, electric, and magnetic characteristics.

For all experiments, the DAC was prepared following a consistent protocol. A solid sample, a ruby for pressure calibration, and a pressure-transmitting medium were loaded into a spark-eroded hole (0.4–0.5 mm in diameter) in a 0.15–0.3 mm thick metal gasket (steel or tungsten). The pressure-transmitting medium, in this case a liquid, ensured efficient pressure transfer and maintained hydrostatic conditions. The only variation between experiments was the sample form: for structural studies, a single crystal of the compound was placed in the gasket hole, whereas for spectroscopic studies, a thin layer of the sample was deposited directly onto the diamond culet (see Section 3.4 for details). All samples were then isothermally compressed. The pressure was determined using the ruby-fluorescence method,[132,133] by measuring the redshift of the two characteristic ruby emission lines R1 and R2, with a Photon Control spectrometer, with an accuracy of 0.02 GPa.

3.3. Structural studies of single crystals

Structural studies were conducted separately at high-pressure and variable-temperature conditions. Single-crystal X-ray diffraction (SCXRD) experiments at various temperatures were performed using a SuperNova CCD diffractometer equipped with an X-ray micro-source or a Bruker D8 QUEST diffractometer. Both systems utilized Cu Kα radiation (λ = 1.54178 Å) and were equipped with an Oxford CryojetHT attachment for sample heating and cooling via a nitrogen gas stream. The temperature can be regulated to any value between 90–490 K.

High-pressure structural studies were conducted on single crystals at pressures up to 4.61 GPa. Experiments were performed at synchrotron facilities, including the European Synchrotron Radiation Facility (ESRF) in Grenoble, using a monochromatic X-ray beam with λ = 0.4099 Å, and the Swiss Light Source, employing radiation with λ = 0.4920 Å. In-lab four-circle diffractometers equipped with a Mo Kα X-ray source (λ =

0.71073 Å) were also used. For the in-lab measurements, the DAC was centered using the gasket shadowing method.[134]

Data collection and reduction were carried out using the CrysAlisPro or APEX5 software. Crystal structures were solved using programs SHELXT or SHELXS and refined with SHELXL,[135,136] all implemented within the OLEX2 interface.[137] The resulting crystallographic information files (CIFs) containing detailed data have been deposited in the CSD database.

3.4. UV-Vis-NIR and photoluminescence spectroscopy

Ultraviolet-Visible-Near Infrared (UV-Vis-NIR) absorption spectra under high-pressure conditions were recorded using a DAC equipped with low-fluorescence synthetic AII diamond anvils to minimize background signals. Sample layers were deposited on the diamond culet through three different methods (Figure 10):

1. Uniaxial compression: a small amount of the sample was placed on the diamond culet and pressed from above with a thick glass plate until a uniform layer formed (used in **A1**, **A3**, and **A4**, Figure 10a).
2. Solvent evaporation: a drop of the solution was placed on the culet, and the layer was formed after solvent evaporation (used in **A4**, Figure 10b).
3. Compression of solution: the solution was loaded into the DAC chamber, and the layer was formed as a precipitate after increasing the pressure (used in **A4**, Figure 10c).

For measurements involving PDIs, Daphne Oil 7575 was used as the pressure-transmitting medium, whereas for PTB7, glycerol was utilized. UV-Vis-NIR spectral measurements were performed using Jasco V-650 and V-770 spectrophotometers adapted for use with a DAC. The absorbance spectra were recorded at a scan speed of 200 nm min^{-1} across the wavelength range from 350 to 1200 nm.

The photoluminescence properties were measured using an Andor spectrometer. The materials were ground and loaded into the pressure chambers using a needle. Consistent with the absorption measurements, the DAC was equipped with type IIA diamond anvils, and Daphne Oil 7575 was used as the pressure-transmitting medium. For

high-temperature measurements, the sample was placed in a tube furnace. The PL properties of the PTCDI-Ph powder were measured by exciting the sample with a 411 nm LED light source, whereas the PDI-C_n (n = 5–8) derivatives were excited using a 450 nm diode.

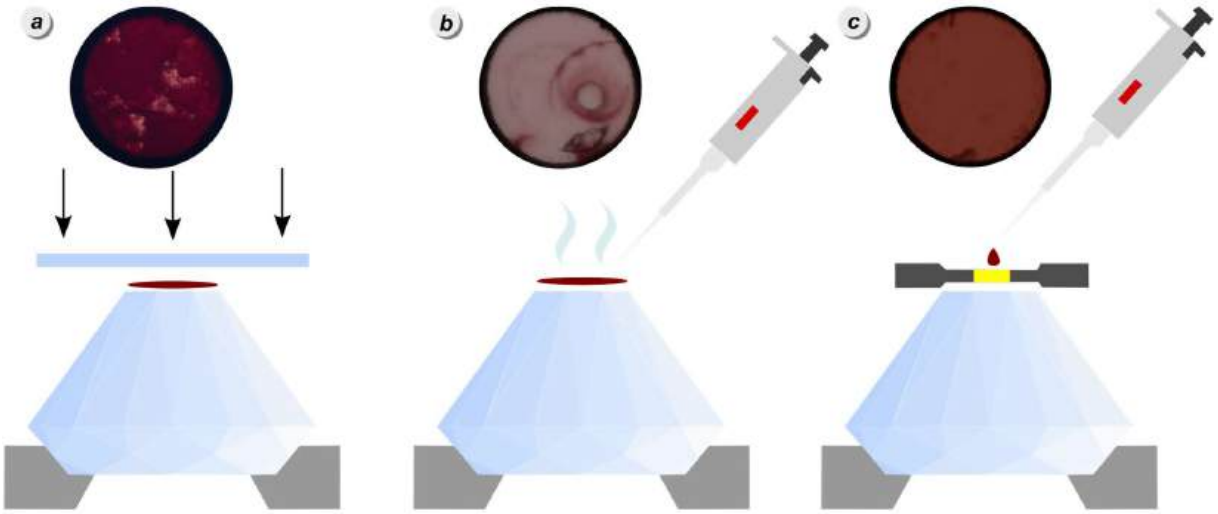

Figure 10. Representative images of the developed measurement layers accompanied by schematic diagrams illustrating the corresponding film preparation methods: (a) uniaxial compression of the solid material, (b) film formation via solvent evaporation, and (c) compression applied to the material in solution.

3.5. Complementary methods: DSC, PXRD, SEM and HSM

Differential scanning calorimetry (DSC) measurements were performed using a Thass DSC XP-10 apparatus for the PTCDI-Ph sample. Heating and cooling cycles were carried out at the rate of 5 K min^{-1} under the N_2 atmosphere. For the PDI-C_6 sample, a PerkinElmer PyrisDiamond DSC-7 equipped with a PII intracooler was used, also under the N_2 atmosphere, with the scanning rate of 20 K min^{-1}.

Powder X-ray diffraction (PXRD) measurements were conducted using a Bruker AXS D8 Advance diffractometer equipped with a Johansson monochromator (CuKα1 = 1.54060 Å) and a silicon-strip LynxEye detector.

Scanning electron microscopy (SEM) images were recorded using a Zeiss EVO 40 scanning electron microscope.

The hot-stage microscopy (HSM) analysis was performed using an OLYMPUS BX41 microscope equipped with a VISICAM 5.0 and a NIKON DS FI3 camera. A Linkam TMS-94 stage was used for temperature control.

4. Results

The performance of organic semiconductors critically depends on charge carrier mobility. It is influenced by intrinsic properties of the material, such as molecular structure and packing, extrinsic factors like the nature of defects, and external parameters including pressure and temperature.[15] My work aimed to investigate the influence of some of these effects on the optoelectronic properties of selected organic semiconductors. For this purpose, I studied representatives of both classes: small-molecule compounds, focusing on perylene diimide derivatives (articles **A1**–**A3**) and polymers, represented by PTB7 (**A4**).

Article **A1** investigates the structure and optoelectronic properties of PTCDI-Ph (Figure 8a), a perylene diimide N-substituted with a phenyl group, under external stimuli. The study utilized a combination of DSC, synchrotron and in-lab SCXRD, alongside UV-Vis-NIR absorption and PL spectroscopy to understand how structural deformations induced by high pressure and varying temperatures affect optical behavior of PTCDI-Ph. Article **A2** focuses on PDI-C_6, a PDI modified with an *n*-hexyl alkyl chain at the *imide* position (Figure 8c). This study explores its solid-state phase transitions under high pressure and varying temperatures, employing a combination of DSC, HSM, SCXRD and PXRD. Article **A3** presents the correlation between pressure-induced structural changes and variations in optical UV-Vis-NIR absorption and photoluminescence across a series of four PDIs with alkyl substituents of varying lengths at the *imide* positions (PDI-C_n, where n = 5–8), shown in Figure 8b–d. Experimental methods included high-pressure synchrotron and in-lab SCXRD, along with UV-Vis-NIR absorption and PL spectroscopy. Article **A4** presents an investigation of the impact of applied pressure and varied film preparation techniques on the absorption characteristics of the polymer PTB7. UV-Vis-NIR, SEM and PXRD techniques were used.

4.1. PTCDI-Ph (A1)

Calorimetric and X-ray diffraction studies presented in article **A1** reveal that PTCDI-Ph undergoes two phase transitions within the investigated pressure and temperature range (up to 3.55 GPa and between 130 and 573 K). Under ambient conditions, the compound crystallizes in the monoclinic space group $P2_1/c$ (phase II), with half of the PTCDI-Ph molecule in the asymmetric unit (Z' = 0.5). This structure is consistent with the previously reported single-point determination at 93 K and 0.1 MPa.[138] Phase II remains stable from at least 93 to 490 K and under compression up to 3.0 GPa. Above this pressure and temperature range, two additional polymorphs were observed: phase I, stable above 493 K, and phase III, which emerges above 3.0 GPa (Figure 3 in article **A1**). Due to the destructive nature of the transitions from phase II to phases I and III, only powder X-ray diffraction patterns were collected for phases I and III, and their crystal structures could not be determined.

A key conformational feature of PTCDI-Ph is the torsion angle of its terminal phenyl rings relative to the perylene core (C11-N1-C13-C18), of 58.5(9)° at 296 K and 0.1 MPa. The compression decreases this angle to 50.5(7)° at 2.85 GPa and simultaneously decreases π-π stacking distance from 3.523(7) Å at 0.1 MPa to 3.183(3) Å at 2.85 GPa, whereas heating generally increases the torsion angle and expands the d_π from 3.523(7) Å at 296 K to 3.59(5) Å at 490 K. Interestingly, the crystal displays negative linear compressibility (NLC) along the [100] direction up to 0.78 GPa (K = -6.1 TPa^{-1}) and also the negative thermal expansion (NTE) in the same direction (Figure 11). The NLC refers to an elastic elongation in one direction despite the application of hydrostatic pressure, while NTE describes a contraction upon heating, contrary to the typical thermal expansion of most materials (Figure 12).

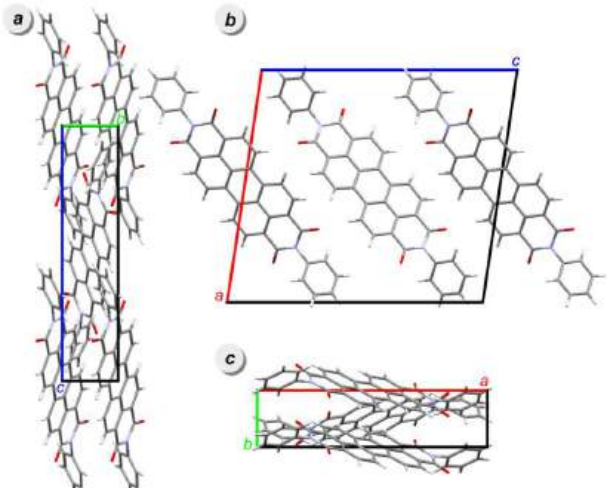

Figure 11. Arrangements of PTCDI-Ph molecules in the unit-cell along direction: (a) [100]; (b) [010]; and (c) [001], at 0.1 MPa.

Article **A1** also presents spectroscopic studies of solid PTCDI-Ph under high-pressure conditions. Up to 4.99 GPa, a pronounced bathochromic shift of approximately 33 nm GPa^{-1} is observed in the 630–793 nm range. This shift corresponds to a linear decrease in the band gap energy with increasing pressure, attributed to enhanced π–π stacking between adjacent perylene cores. These changes are accompanied by a visible color change of the PTCDI-Ph sample from red to black (Figure 13). This process is fully reversible, with the original color restored upon decompression. Photoluminescence (PL) measurements reveal that the PL properties are highly sensitive to both pressure and temperature. Heating causes a decrease in PL intensity and broadening of the emission bands, while compression induces a bathochromic shift of the emission maximum. These significant and reversible changes in PTCDI-Ph optical properties with pressure and temperature highlight its suitability as a highly stimuli-responsive organic material and multi-modal sensor for extreme conditions. Its pressure absolute sensitivity (S_a) can reach 8.33 nm GPa^{-1} and its temperature sensitivity can be up to 0.068 nm K^{-1}, outperforming many inorganic sensors, such as $YAlO_3$/ Cr^{3+}.[139]

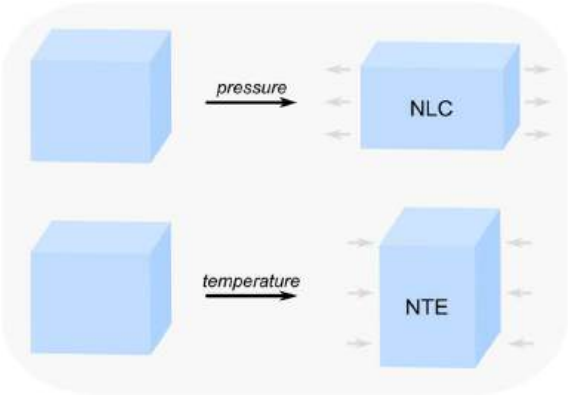

Figure 12. Negative linear compressibility – linear expansion along one direction (top), and negative thermal expansion – linear contraction along one direction upon heating (bottom).

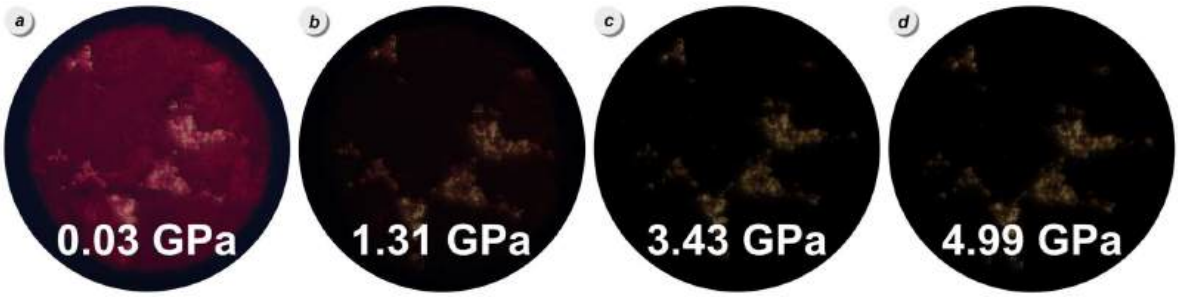

Figure 13. Photographs of visual changes in the PTCDI-Ph film under increasing pressure.

The research presented in **A1** demonstrates that the optoelectronic properties of PTCDI-Ph can be finely tuned by external stimuli, primarily through changes in π–π stacking distance and molecular conformation. This makes PTCDI-Ph a promising candidate for designing advanced organic electronic and optoelectronic devices, especially as a high-performance sensor for pressure and temperature.

4.2. PDI-C_6 (A2)

Article **A2** delves into the structural characteristics of PDI-C_6 under various conditions, including high pressure up to 4.61 GPa, as well as low and high temperatures in the range from 100 K up to 823 K. We identified five distinct polymorphs of PDI-C_6, all of which crystallize in the same triclinic space-group type $P\bar{1}$. At ambient conditions (phase I), the PDI-C_6 molecule is located on an inversion center ($Z' = 0.5$). The alkyl chains adopt an all-*antiperiplanar* conformation, with all relevant torsion angles approaching 180°. These observations are consistent with the structure reported by Madhu *et al.* at 173 K and 0.1 MPa.[140] Upon heating, the ambient phase I of PDI-C_6 transforms into phase II at 465 K, and subsequently, phase II transforms to phase III at 521 K. A notable structural change occurs in phase II, where perylene cores, initially arranged in parallel stacks in phase I, undergo a significant 33° scissor-opening rotation, coupled with conformational rearrangements of the alkyl chains (Figure 14). This behavior is consistent with observations for PDI-C_5, which exhibits a similar scissor-opening rotation upon transformation to high-temperature phase III.[62] The transition from phase II to phase III of PDI-C_6 is reconstructive, which has hindered the crystal-structure determination of phase III and only its unit-cell parameters have been established. Under high pressure,

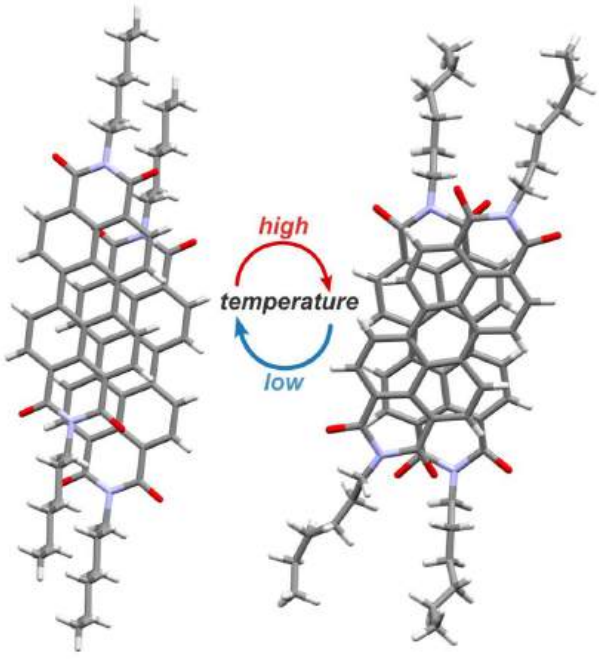

Figure 14. Molecular arrangement in phase I (left) and phase II (right) of PDI-C_6.

phase I of PDI-C_6 undergoes two other phase transitions: to phase IV at 1.22 GPa and further to phase V at 1.50 GPa. In phase IV, Z' increases from 0.5 to 1, and then decreases back to 0.5 in phase V. These pressure-induced transitions involve stepwise modifications of the *n*-hexyl substituent conformations, leading to the emergence of *synclinal* conformers with torsion angles close to ±60°. This conformational flexibility allows for more efficient molecular packing and effectively reduces the π-stacking distance by over 9% between 0.1 MPa and 4.61 GPa.

Hot-stage microscopy studies uncovered intriguing behavior of PDI-C_6 crystals during temperature-induced transitions between phases I and II. Upon heating, the transition from phase I to phase II shows propagation fronts, which lead to the formation of wrinkles on the crystal surface. During cooling, when the transition from phase II to phase I occurs, the PDI-C_6 crystals elongate, leading to the movement and bending of some crystals (Figure 2 in article **A2**). This behavior is the subject of our further research.

4.3. PDI-C_n (A3)

Article **A3** presents a correlation between the high-pressure structural and optoelectronic properties of four PDI-C_n derivatives (n = 5-8). At ambient conditions, all four PDI-C_n compounds crystallize in the triclinic space group type $P\bar{1}$, with comparable unit-cell parameters and Z' = 0.5. In their ambient phases, all compounds adopt *antiperiplanar* conformations in their alkyl chains, with all torsion angles close to 180°, except for PDI-C_7, in which its terminal carbon atoms are disordered. Importantly, the crystal structure of PDI-C_7 had not been previously determined. High-pressure single-crystal X-ray diffraction studies led to several previously unreported pressure-induced phases. Although the increasing pressure induces distinct phase transitions across the PDI-C_n series, several similarities emerge. Notably, all newly identified high-pressure phases crystallize in the same triclinic space group type $P\bar{1}$. Moreover, these pressure-induced transitions are associated with conformational changes in the alkyl chains, causing deviations of some torsion angles from 180°.

Measurements on PDI-C_5 up to 3.84 GPa revealed a phase transition from phase I to phase IV around 2 GPa. As previously mentioned, PDI-C_7 exhibits distinct structural

behavior compared to the other three PDI-C_n derivatives discussed in this dissertation. Notably, under ambient conditions the terminal methyl group of the *n*-heptyl substituent displays conformational disorder. In phase I of PDI-C_7, this disorder is manifested by two distinct torsion angles of the terminal carbon atoms: C16-C17-C18-C19A of ±78.8(8)° and C16-C17-C18-C19B of ±153(1)° at 0.1 MPa, with site occupancy factors (SOFs) of 0.596(14) and 0.404(14), respectively. Upon compression to 0.50 GPa, the disorder is eliminated, and the C16-C17-C18-C19 angle adopts a well-defined value of 175.1(9)°, indicating ordering of the alkyl chain in all-*antiperiplanar* conformation. Structural measurements were also performed down to 100 K to investigate the effect of temperature on this disorder. However, the effect of cooling is significantly weaker, and the disorder persists down to 100 K at least. The compression beyond 1.8 GPa resulted in a significant deterioration of diffraction-data quality, which hampered further X-ray diffraction experiments. At room temperature, PDI-C_8 undergoes two pressure-induced phase transitions. The first transition, from phase I to phase III occurs at 0.61 GPa, lower than the corresponding transitions in PDI-C_5 and PDI-C_6, indicating the significant role of the longer alkyl chains in accommodating the compression strain. The subsequent transition to phase IV occurs at 1.50 GPa and it involves an increase in the number of independent molecules in the unit cell, with Z' increasing from 0.5 to 1. As in the case of PDI-C_7, further compression beyond 1.6 GPa results in a marked deterioration of data quality, hampering the structure determination. The compression of phase I of PDI-C_8 revealed a NLC effect similar to that observed for PTCDI-Ph, but even more pronounced, with K = -37.6 TPa^{-1}. The observed structural changes were correlated with corresponding shifts in the absorption and emission spectra recorded under high-pressure conditions. All compounds exhibited bathochromic shifts, with the most pronounced effect observed for PDI-C_8, where the absorption edge redshifted by 84.4 nm GPa^{-1} and the PL band by 10.8 nm GPa^{-1}. The smallest absorption-edge shift, 46.9 nm GPa^{-1}, was observed for PDI-C_7, while the smallest PL band shift, 5.8 nm GPa^{-1}, was recorded for PDI-C_6.

4.4. PTB7 (A4)

Article **A4** focuses on polymer PTB7, for which the high-pressure optical properties were investigated. Thin films of PTB7, suitable for UV-Vis-NIR absorption spectroscopy, were prepared by three distinct methods on the diamond culet: (1) uniaxial compression of the powder, (2) solvent evaporation from a PTB7 solution, and (3) precipitation from a PTB7 solution under increasing pressure (Figure 10). The homogeneity of films from the first two methods was compared using SEM. These images revealed that films obtained by powder compression are uniform and homogeneous, whereas those prepared by evaporating dichloromethane exhibit patchy morphology with visible gaps and cracks, leading to heterogeneous defect patterns. It is important to note that solvent-based techniques, like methods (2) and (3) face practical limitations. A key issue for both methods is the poor solubility of many organic semiconductors, while method (3) is additionally restricted by a limited pressure range due to solvent crystallization.

Regardless of the preparation method, all PTB7 layers display a similar bathochromic shift of about 25 nm GPa^{-1} up to 5 GPa in their UV-Vis-NIR spectra. These changes progress linearly up to approximately 1 GPa, after which the rate of change significantly decreases, becoming several times smaller above 4 GPa.

5. Discussion

5.1. Structure of PDI derivatives under extreme conditions

High-pressure and variable-temperature structural investigations of five PDIs presented in this dissertation revealed several previously unreported polymorphs. The ambient phase II of PTCDI-Ph, which features a rigid phenyl substituent that can only rotate relative to the perylene core, demonstrates the highest stability, persisting from at least 93 up to 490 K, and under pressure up to 3.0 GPa (Figure 15). In contrast, the introduction of flexible alkyl substituents in the PDI-C_n compounds increases their susceptibility to the external stimuli of pressure. As a result, the first observed pressure-induced phase transitions for all PDI-C_n derivatives occur below 2.5 GPa. Within the PDI-C_n series, a clear trend was observed where longer alkyl chains correlate with lower pressures and

higher temperatures required for a transition to occur. For example, the first pressure-induced phase transition occurs at 2.17 GPa for PDI-C_5, 1.22 GPa for PDI-C_6, and 0.61 GPa for PDI-C_8 (Figure 15). PDI-C_7 deviates slightly from this trend, exhibiting an ordering of its alkyl chains at 0.50 GPa without significant changes in the unit-cell parameters. The temperature-induced transitions follow the opposite trend, occurring at 385 K for PDI-C_5,[62] 465 K for PDI-C_6, 486 K for PDI-C_7,[36,143] and 497 K for PDI-C_8.[143] Furthermore, the analysis reveals an odd-even effect in the number of observed transitions. This phenomenon, which can influence a wide range of physical properties, including melting point, solubility, and thermal expansion, occurs when the properties of a compound series alternate depending on whether a specific structural parameter, such as the number of carbon atoms, is odd or even.[144,145] In our studies, derivatives with an even number of carbon atoms (PDI-C_6 and PDI-C_8) undergo two pressure-induced phase transitions, whereas those with an odd number (PDI-C_5 and PDI-C_7) undergo only one. A different behavior is observed at high temperatures, where PDI-C_5, PDI-C_6, and PDI-C_7 each exhibit two transitions, while PDI-C_8 exhibits only one. Conversely, at low temperatures, the studied compounds proved highly stable, with no transitions detected down to 130 K for PTCDI-Ph or 100 K for PDI-C_6 and PDI-C_7. Among all derivatives, PDI-C_6 stands out as the most sensitive compound to external stimuli, undergoing two transitions under both high pressure and high temperature.

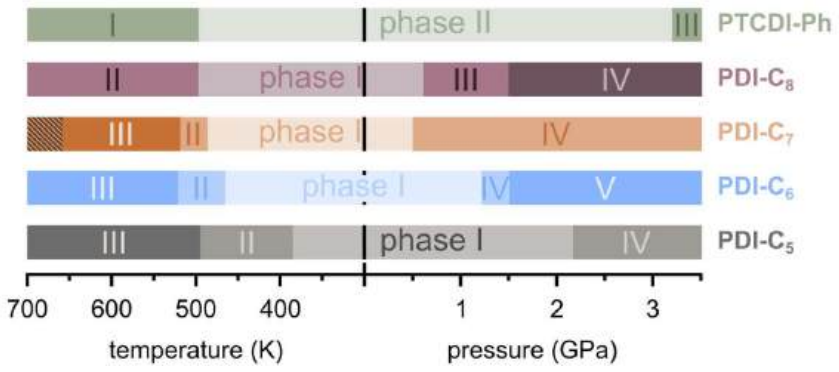

Figure 15. Temperature- and pressure- induced phase transitions in PTCDI-Ph and PDI-C_n, n = 5-8. The appearance of phases II and III in PDI-C_5,[62] phases II and III in PDI-C_7,[36,143] and phase II in PDI-C_8 has been previously reported in the literature.[143]

This odd-even behavior relates to the conformational flexibility of the alkyl substituents. Under pressure, the even-n chains of PDI-C_6 and PDI-C_8 are more prone to adopt *synclinal* conformations with some torsion angles close to ±60° (Figure 16b, d). It allows for more complex, multi-step packing adjustments. In contrast, the odd-n alkyls in PDI-C_5 and PDI-C_7 tend to maintain *antiperiplanar* conformations with all torsion angles close to 180°, resulting in simpler, single-step phase transitions under the studied pressure range (Figure 16a, c).

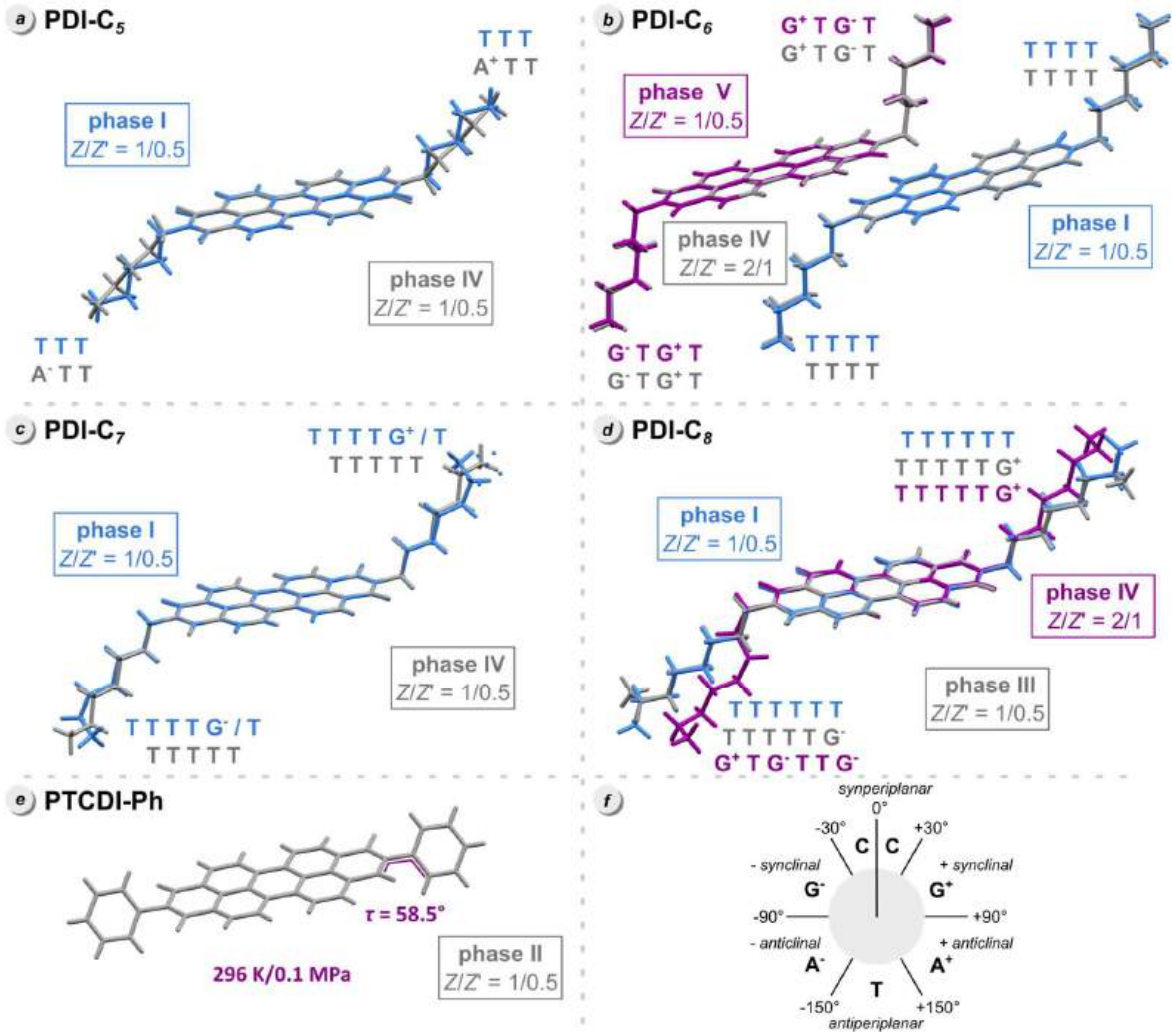

Figure 16. Conformational changes in PDI-C_5 (a), PDI-C_6 (b), PDI-C_7 (c), PDI-C_8 (d) molecules observed in pressure-induced phases, illustrated by superimposing the perylene cores; (e) PTCDI-Ph molecule highlighting the torsion angle that defines the rotation of the phenyl substituents; (f) legend presenting possible types of molecular conformations with the corresponding ranges of torsion angles and abbreviations.

To study the physical basis of the observed differences in phase stability, I analyzed the molecular volume (V_m) as a function of pressure and temperature (Figure 17). The rates of V_m change were determined within the pressure ranges corresponding to the occurrence of ambient phases (phase II for PTCDI-Ph and phase I for PDI-Cn) and across the whole measured pressure range (values highlighted with frames in Figure 17a). Among the ambient-pressure phases, PDI-C_8, which has the largest V_m at 0.1 MPa, exhibits the highest rate of V_m decrease. In general, as the initial V_m of the PDI derivatives decreases, the rate of its reduction also decreases, reaching the smallest value for PTCDI-Ph (−31.0 Å^3 GPa^{-1}). Thus, within the PDI-C_n series, the rate of V_m reduction increases systematically with the length of the alkyl chain. When comparing relative changes, V_m compresses at rates of approximately 5% GPa^{-1} for PDI-C_5, 4% GPa^{-1} for PDI-C_6, 6% GPa^{-1} for PDI-C_7, 8% GPa^{-1} for PDI-C_8, and 5% GPa^{-1} for PTCDI-Ph. Again, the highest rate is that of PDI-C_8 (Figure 17b).

The largest rate of temperature-induced V_m change is observed for PDI-C_6 (0.18 Å^3 K^{-1}), and the lowest rate for PTCDI-Ph (0.11 Å^3 K^{-1}). For comparison, I included data for PDIF-CN_2, a PDI derivative with both *imide* and *bay* substituents (CCDC deposition numbers: 1848554-1848559),[71] as it is currently the only other derivative with a reported series of variable-temperature structural studies. PDIF-CN_2 shows a rate of 0.15 Å^3 K^{-1}, however, this data is limited to temperatures up to 300 K. These macroscopic properties are fundamentally connected with the microscopic arrangement of the molecules—their crystal packing. The following analysis of the crystal packing will therefore provide a structural basis for the observed stability trends.

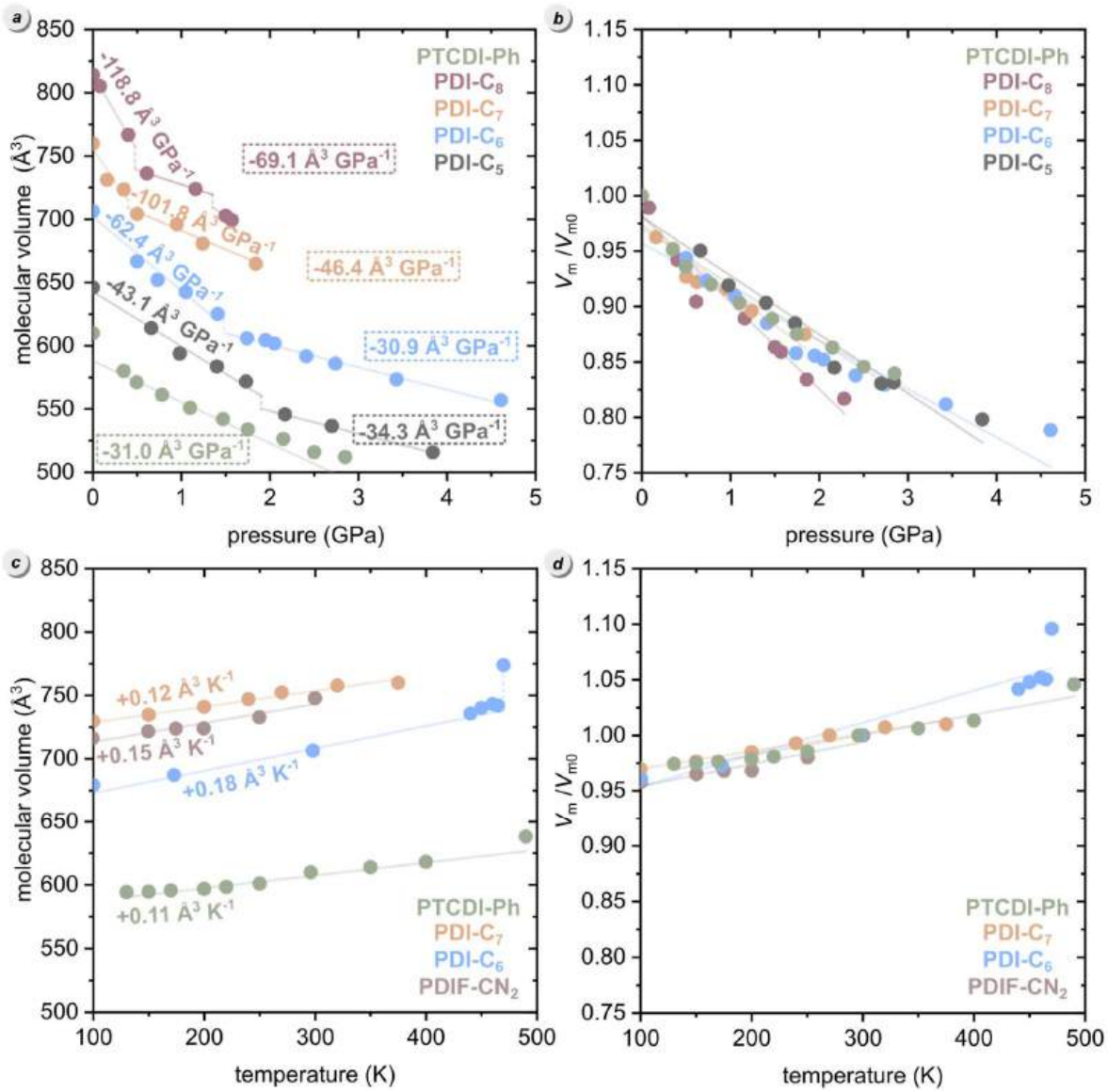

Figure 17. Pressure (a) and temperature (c) dependence of the molecular volume ($V_m = V/Z$, where V is the unit-cell volume and Z is the number of molecules in the unit cell), and the relative changes in V_m as a function of hydrostatic pressure (b) and temperature (d) for all PDI derivatives investigated in this thesis. For comparison, plots (c) and (d) also include data for PDIF-CN_2.[71] Vertical dashed lines indicate the phase transitions. The rates of V_m change were determined for the ambient-pressure phases and across the entire measured pressure range, with the later values given in frames in panel (a). For PTCDI-Ph, only a single value is shown, as data are available exclusively for the ambient phase II.

Understanding packing motifs is crucial, as they directly govern the intermolecular π-orbital overlap and, consequently, the charge transport properties that make PDIs promising organic semiconductors. While previous works, such as those by Maini *et al.*,[146] have attempted to classify PDI packing arrangements, a comprehensive understanding has been hindered by the limited availability of structural data, especially for polymorphs. Moreover, no structural information other than ours is currently available regarding the effects of high pressure on PDIs.

Analysis reveals that the investigated PDIs adopt two primary packing motifs at ambient conditions: a herringbone arrangement for PTCDI-Ph (Figure 18c) and lamellar π-π stacking for the PDI-C_n derivatives (Figure 18a). While high-pressure conditions do not significantly alter these overall packing motifs, some high-temperature phases undergo substantial rearrangements. Specifically, a pronounced scissor-like rotational motion of the molecules is observed in phase III of PDI-C_5 and phase II of PDI-C_6 (Figure 18b). However, the structural analysis remains incomplete, as the crystal structures of several high-pressure and high-temperature phases have not yet been determined. These include the high-pressure phase III of PTCDI-Ph, as well as the high-temperature phases for PTCDI-Ph (I), PDI-C_6 (III), PDI-C_7 (II, III), and PDI-C_8 (II).

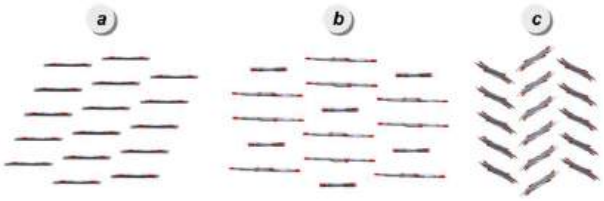

phase	I	II	III	IV	V
PDI-C_5	*a*	*a*	*b*	*a*	–
PDI-C_6	*a*	*b*	*a*	*a*	–
PDI-C_7	*a*	*a*	–	–	–
PDI-C_8	*a*	*b*	–	*a*	*a*
PTCDI-Ph	–	*c*	–	–	–

Figure 18. Crystal packing motifs observed in studied PDIs: (a) lamellar π-stacks with angle $Y = 0°$; (b) lamellar π-stacks with $Y \approx 30°$; and (c) herringbone π-stacks. The table summarizes the identified phases and their packing motifs (bottom).

To better describe these packing arrangements and the nature of rearrangements, the mutual orientation of neighboring molecules in a π-stacking column was characterized by three angles: *pitch* (*P*), *roll* (*R*),[147] and *yaw* (*Y*), as well as the π–π stacking distance (d_π). The *P* angle quantifies the displacement of adjacent molecules along their long molecular axis, while the *R* angle describes the relative shift along the short

molecular axis (see inset of Figure 19). The *Y* angle, introduced in this thesis, describes the rotation between adjacent perylene cores. It is measured along the z-axis of the perylene core and is defined as the torsion angle of $N_{molecule1}$-$centroid_{molecule1}$-$centroid_{molecule2}$-$N_{molecule2}$.

The analysis of these *P*, *R* (Figure 19) and *Y* angles reveals that while the packing is relatively rigid under most conditions, specific phase transitions are marked by abrupt changes in molecular orientation. At ambient conditions, the four PDI-C_n compounds exhibit similar packing arrangements, with *P* angles ranging from 42.0–43.5° (Figure 18a) and *R* angles from 20.0–22.1° (Figure 19c). These values differ significantly from those of PTCDI-Ph, where *P* is 6.78(18)°, and *R* is 28.08(7)°, highlighting its distinct packing motif. At ambient conditions, the *Y* angle is 0° for all PDI derivatives. Under pressure, the most significant change occurs in PDI-C_5 during its transition to phase IV at 2.17 GPa, where the *P* angle sharply decreases to 16.4(8)° and the *R* angle increases to 28.0(3)°. The *Y* angle remains equal to 0°. In contrast, the most pronounced thermal-induced rearrangement occurs in PDI-C_6 at 470 K. This transition from phase I to phase II corresponds to the previously described *scissor-like* motion and is quantified by changes in all three angles. The *Y* angle increases from 0° to ≈33°, while the *P* and *R* angles adopt distinct values depending on the relative orientation of neighboring *cis* and *trans* molecules. Specifically, the *P* angle increases to approximately 29° between two neighboring *cis* molecules and about 24° for neighboring *cis-trans* molecules (Figure 19b), while the *R* angle becomes ~20° and less than 6° for the respective pairs of molecules (Figure 19d).

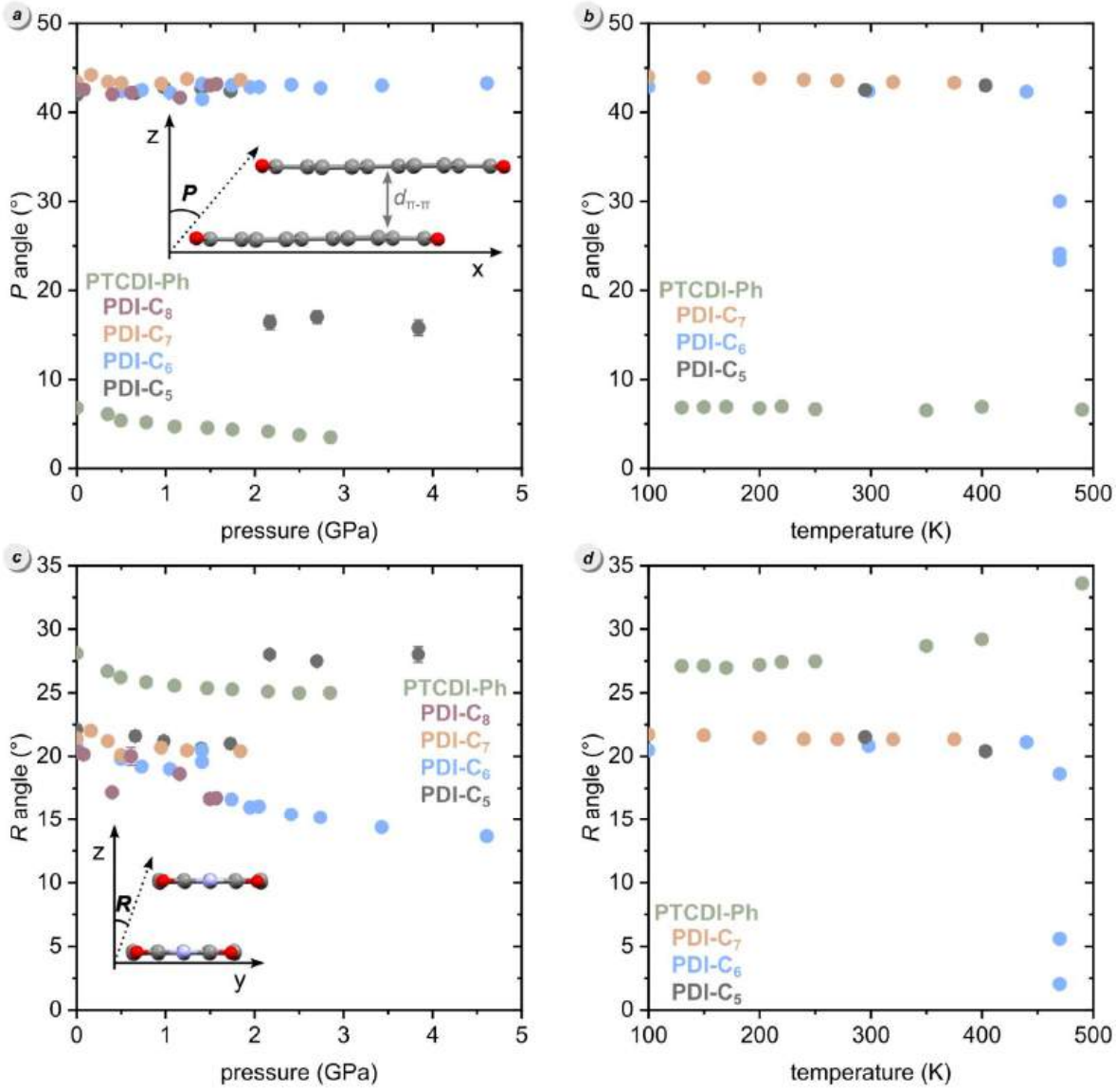

Figure 19. Pressure and temperature-induced changes in the *pitch* (a, b) and *roll* (c, d) angles. At 470 K, three data points are observed due to the increased number of molecules in the symmetry-independent part of the unit-cell ($Z' = 1.5$). The temperature-dependent angles calculated for PDI-C_5 are taken from the literature. The insets schematically describe the *pitch* (*P*) and *roll* (*R*) angles for the PDI cores projected along their short (a) and long (c) axes, respectively.

Figure 20 illustrates the correlation between the d_π distance and applied pressure (a) and temperature (b) for the studied PDI derivatives. According to the classification proposed by Janiak,[148] interplanar spacings around 3.3 Å indicate strong π–π interactions,

while those in the range of 3.6–3.8 Å are considered weak. At ambient pressure, the π–π stacking distances among the PDI-C_n derivatives are similar, between 3.360(8) Å in PDI-C_5 and 3.3882(9) Å in PDI-C_6. However, at a relatively low range of pressure above 0.15 GPa, their π-stacking distances begin to diverge visibly (Figure 20a). PTCDI-Ph initially exhibits the longest π–π stacking distance compared to the PDI-C_n series, equal to 3.523(7) Å at 0.1 MPa (Figure 21). This observation is consistent with previous reports, which demonstrated that PDIs N-substituted with alkyl have shorter π–π stacking distances than those functionalized with aromatic substituents. However, this difference becomes less pronounced under higher pressure, indicating a stronger compression response. The largest pressure-induced change in d_π is observed for PDI-C_8, with a rate of -0.11 Å GPa^{-1}, which correlates with the most pronounced redshift of the absorption edge among the studied compounds. Interestingly, the transition to phase IV in PDI-C_5 is accompanied by a sudden increase in the d_π distance, mirroring the abrupt changes observed in its *P* and *R* angles. The temperature-induced rate of change in d_π ranges from $2.73 \cdot 10^{-4}$ Å K^{-1} in PDI-C_7 to $3.48 \cdot 10^{-4}$ Å K^{-1} in PDI-C_6 (Figure 20b).

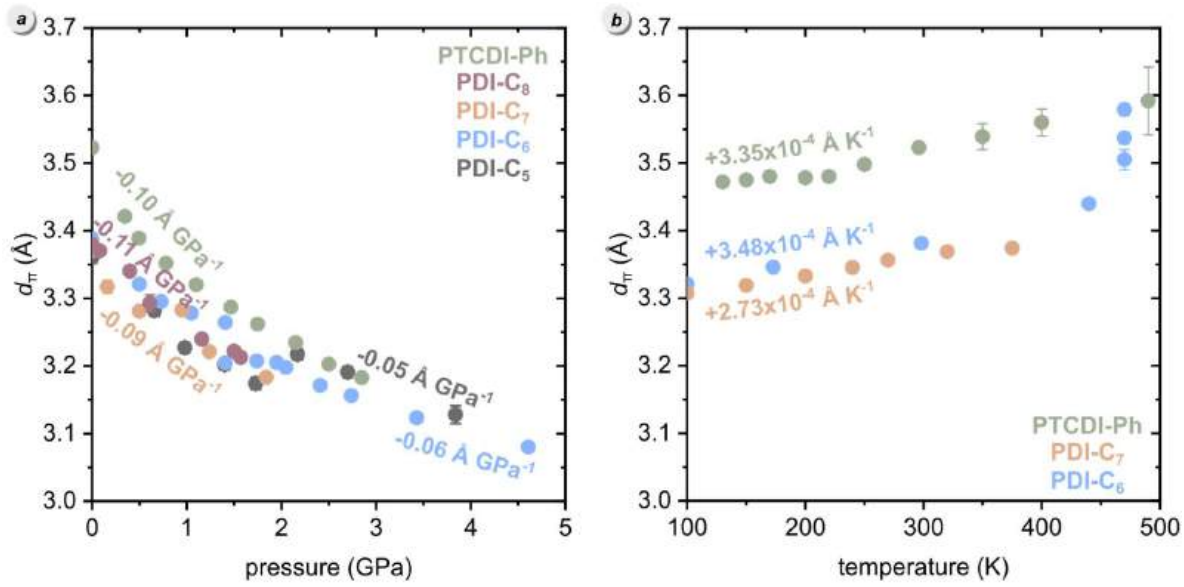

Figure 20. Distance d_π between π-stacked molecules as a function of pressure (a) and temperature (b) for studied PDIs. The rates calculated over the entire investigated pressure and temperature ranges are provided.

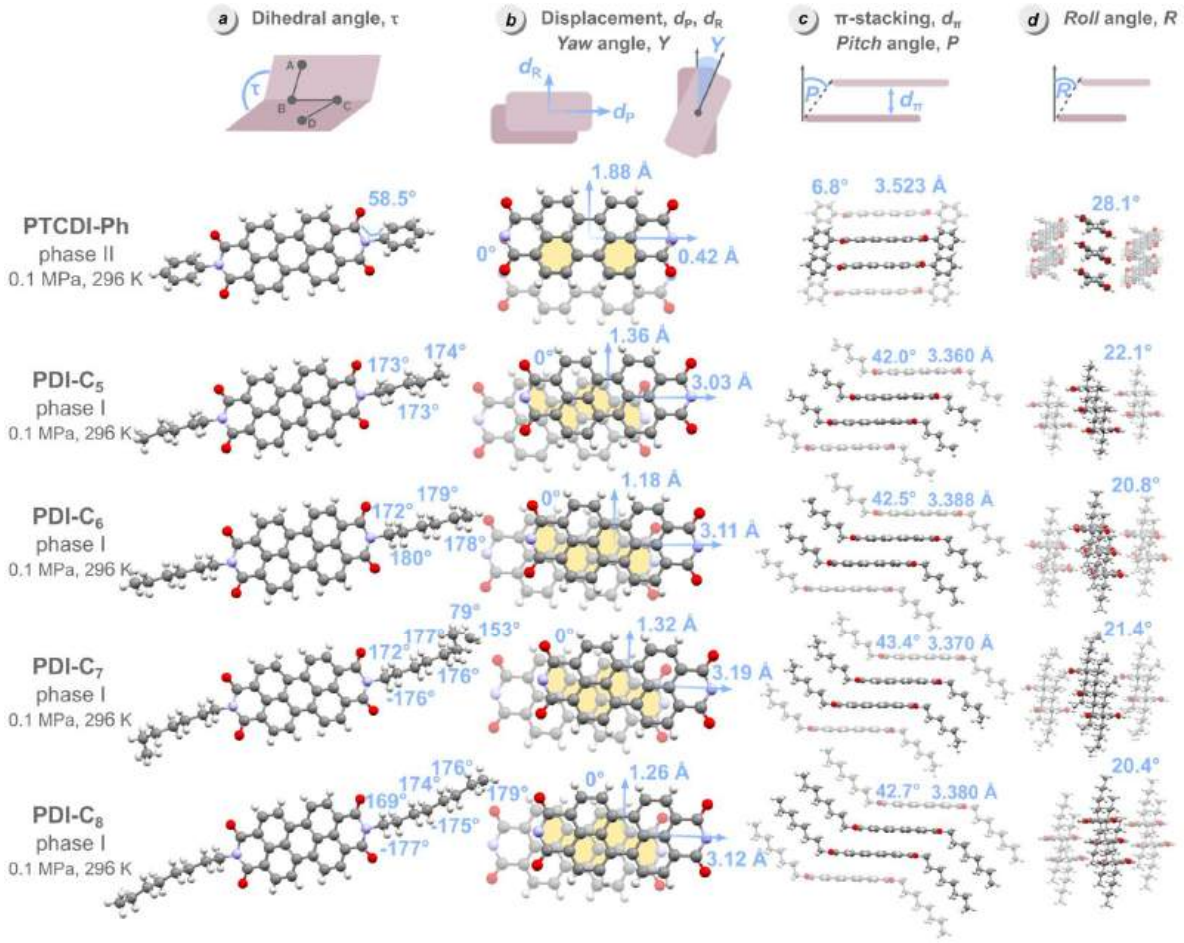

Figure 21. Crystal structures of the ambient phases of PDIs indicating the dihedral angle (τ) of the substituents (a); displacements between neighboring molecules and *yaw* angle (b); *pitch* angle and the π-stacking distance (c); *roll* angle between neighboring molecules in the π-stacking column.

5.2. High-pressure effects on photophysical properties of organic semiconductors

To gain deeper insight into the impact of structural transformations on the photophysical properties of organic semiconductors, we investigated the UV-Vis-NIR absorption spectra of six compounds discussed in this dissertation: PTCDI-Ph, PDI-C_5, PDI-C_6, PDI-C_7, PDI-C_8, and PTB7. All measurements presented in Figure 22 were performed on solid-state films prepared on diamond culets via the uniaxial compression method previously described in Section 3.4 (Figure 10a), and the pressure was then gradually increased.

With increasing pressure, all six compounds exhibit a progressive redshift in their absorption spectra, indicating a systematic reduction in band-gap energy (E_g, Figure 22). This was also visually apparent, as the crystals darkened under pressure. These changes were reversible, as the films returned to their original color upon decreasing the pressure.

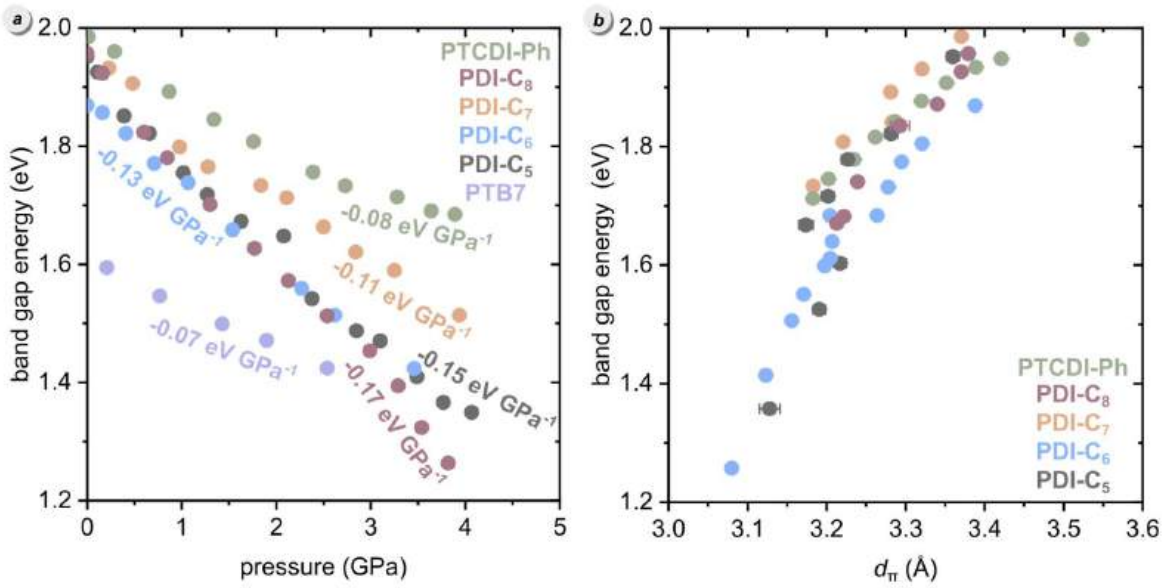

Figure 22. Pressure dependence of band-gap energy E_g for PTCDI-Ph, PDI-C_5, PDI-C_6, PDI-C_7, PDI-C_8, and PTB7 (a) and E_g as a function of d_π distances (b).

PTCDI-Ph and PDI-C_7 display the highest E_g values of 1.99 eV at 0.1 MPa, while PTB7 displays the lowest E_g of 1.59 eV at 0.21 GPa (Figure 22a). In terms of pressure sensitivity, PTB7 shows the smallest change in E_g with increasing pressure, with the dE_g/dp rate of -0.07 eV GPa^{-1}. Conversely, PDI-C_8 is most sensitive, with dE_g/dp of -0.17 eV GPa^{-1}. Among the PDI derivatives, PTCDI-Ph, known for its remarkable phase stability, shows the smallest rate of E_g change at -0.08 eV GPa^{-1}. The E_g reduction correlates with a shorter π-stacking distance d_π for all studied PDI derivatives (Figure 22b). For some compounds, such as PDI-C_5 and PDI-C_7, distinct drops in E_g are observed at phase transition points.

We also measured the photoluminescence of the PDI crystals under varying thermodynamic conditions. For PTCDI-Ph, the effects of temperature and pressure were investigated, whereas for the PDI-C_n (n = 5–8), only the influence of pressure was studied. All investigated materials exhibit a broad emission band in the NIR spectral range. Figure 23 presents the PL band centroid as a function of pressure for all five studied PDIs. The PL spectrum of PTCDI-Ph in phase II consists of two distinguishable emission bands: an intense band A at $\lambda \approx 680$ nm and a lower-intensity band B at $\lambda \approx 737$ nm. Only the shift of the intense band A is presented in Figure 23. Consistent with UV-Vis-NIR absorption shifts, PDI-C_8 displays the most pronounced redshift in its emission spectra, while PTCDI-Ph shows the smallest.

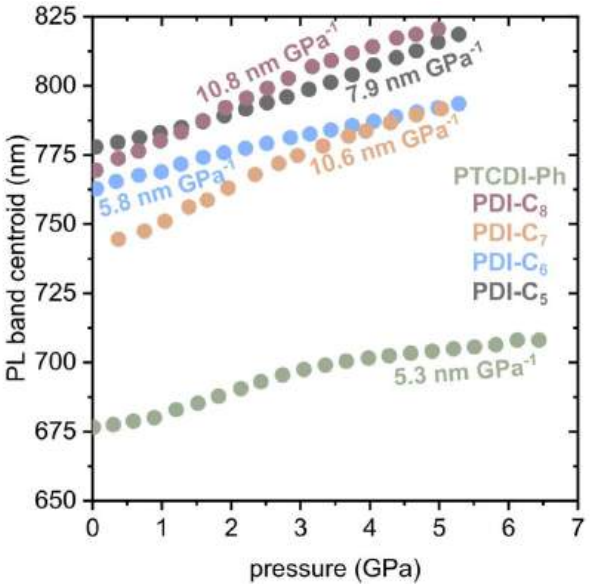

Figure 23. Pressure-induced PL bandshifts for PTCDI-Ph, PDI-C_5, PDI-C_6, PDI-C_7, and PDI-C_8. The shift rates calculated over all range of pressure investigated are given.

6. Conclusions

Studies presented in my dissertation bridge a gap in understanding the high-pressure and variable-temperature behavior of five perylene diimide (PDI) derivatives and the conjugated polymer PTB7. The selected PDIs include a homologous series of four alkyl-substituted compounds of various chain lengths (PDI-C_5, PDI-C_6, PDI-C_7, PDI-C_8) and one phenyl-substituted derivative (PTCDI-Ph), all functionalized at the *imide* positions. By employing a combination of experimental techniques, including in-lab and synchrotron single-crystal X-ray diffraction, differential scanning calorimetry, hot-stage microscopy, and UV-Vis-NIR absorption and photoluminescence spectroscopy under extreme conditions, this work provides detailed insights into the polymorphism, molecular packing, compressibility, thermal expansion and optical responses of these

representatives of organic semiconductors. These findings have been presented in a series of four articles.

X-ray diffraction and calorimetric studies revealed the rich polymorphic behavior of PDI derivatives under high-pressure and high-temperature conditions. Despite the experimental challenge posed by the low symmetry of the crystals, which often resulted in datasets with low completeness, this research successfully solved and refined a total of 64 single-crystal structures under various conditions, including 19 for PTCDI-Ph, 8 for PDI-C_5, 16 for PDI-C_6, 14 for PDI-C_7, and 7 for PDI-C_8. Among these, several previously unreported crystal phases were characterized: one phase for PDI-C_5 (IV); three for PDI-C_6 (II, IV and V); and two each for PDI-C_7 (I, IV) and PDI-C_8 (III, IV). Notably, all newly characterized high-pressure and high-temperature phases retain their ambient-pressure space group types. Under the studied conditions, PTCDI-Ph crystallizes in the monoclinic $P2_1/c$ space group, while the PDI-C_n series (where n = 5-8) crystallizes in the triclinic $P\bar{1}$ space group. Low-temperature studies down to 100 K on PTCDI-Ph, PDI-C_6, and PDI-C_7 revealed no phase transitions.

My further analysis of the PDI derivatives revealed several distinct trends. For instance, PTCDI-Ph, with its rigid phenyl substituent that can only rotate relative to the perylene core, demonstrates the highest phase stability. It is stable across a wide temperature range from 93 K up to 490 K at least, as well as at the high pressures up to 2.85 GPa. In contrast, more flexible alkyl-substituted PDI-C_n derivatives are susceptible to the external stimuli of temperature and pressure resulting in phase transitions in all of derivatives below 2.5 GPa. This behavior can be explained by their increased number of conformational degrees of freedom. Moreover, a clear relationship emerged between the length of alkyl chains in PDI-C_n and the conditions inducing the transitions. Longer alkyl chains correlate with lower pressures required to induce the transitions and with higher temperatures of the transitions at ambient pressure. This finding highlights the critical role of substituent flexibility in governing structural response to external stimuli. The odd-even effects, also identified within the PDI-C_n series, manifesting across properties such as the number of phase transitions, alkyl-chain conformational conversions, and compressibility, further highlight the tuning role of substituents for the properties of PDI derivatives. The strong anisotropy of the crystals is evident in in their varying

compressibility and thermal expansion along different crystal axes. A clear manifestation of this is the negative linear compressibility observed in PTCDI-Ph and PDI-C_8, where the crystal expands in one direction under hydrostatic pressure while contracting in others. Other features characteristic of this group of compounds have also been identified, such as the conformational disorder in PDI-C_7.

The macroscopic properties of PDI compounds, their phase stability and optical properties, have been related to microscopic structures. At ambient conditions, PTCDI-Ph adopts a herringbone motif, while the PDI-C_n derivatives form lamellar π–π stacking arrangements. These molecular arrangements allow for efficient π-stacking, which facilitates charge transport. While high-pressure conditions generally preserve these packing motifs, high-temperature transitions in some PDIs (e.g., PDI-C_5 and PDI-C_6) induce scissor-like rotations of molecules, leading to rearrangements within the π-stacking columns. To characterize these packing arrangements and transformations, I used three angles, *pitch*, *roll*, and *yaw*, along with the π–π stacking distance (d_π), to define the mutual orientation of neighboring molecules. Under pressure, d_π decrease is most pronounced in PDI-C_8, which correlates with its high compressibility and the most significant optical redshift.

I have also developed and compared different methods for measuring UV-Vis absorption in the diamond-anvil cell. The most effective technique proved to be the preparation of a solid sample layer by uniaxial compression. A general feature observed for the studied PDI derivatives investigated and polymer PTB7 is the pressure-induced band-gap narrowing, which results in reversible redshifts in their absorption and photoluminescence spectra. In the studied series, PDI-C_8 is the most sensitive to pressure, while PTCDI-Ph and PTB7 show the smallest responses.

In conclusion, the results obtained in my thesis demonstrate that the properties of organic semiconductors and their responses to external stimuli can be rationally tuned through careful molecular design. Substituent type, length, and flexibility determine both the structural adaptability and photophysical response. This knowledge provides a foundation for designing organic semiconductors with tailored properties for optoelectronic applications, including high-performance sensors and flexible devices.

These findings can guide the design of novel OSCs with improved mechanical resilience, tunable optical properties, and controlled molecular aggregation patterns for the charge-transport pathways.

7. References

(1) Yu, P. Y.; Cardona, M. *Fundamentals of Semiconductors*; Springer Berlin Heidelberg, 2005.

(2) Allard, S.; Forster, M.; Souharce, B.; Thiem, H.; Scherf, U. Organic Semiconductors for Solution-Processable Field-Effect Transistors (OFETs). *Angew. Chemie Int. Ed.* **2008**, *47* (22), 4070–4098. https://doi.org/10.1002/anie.200701920.

(3) *Semiconductor Materials for Solar Photovoltaic Cells*; Paranthaman, M. P., Wong-Ng, W., Bhattacharya, R. N., Eds.; Springer Series in Materials Science; Springer International Publishing: Cham, 2016; Vol. 218. https://doi.org/10.1007/978-3-319-20331-7.

(4) Hong, G.; Gan, X.; Leonhardt, C.; Zhang, Z.; Seibert, J.; Busch, J. M.; Bräse, S. A Brief History of OLEDs—Emitter Development and Industry Milestones. *Adv. Mater.* **2021**, *33* (9), 2005630. https://doi.org/10.1002/adma.202005630.

(5) Ren, A.; Wang, H.; Zhang, W.; Wu, J.; Wang, Z.; Penty, R. V.; White, I. H. Emerging Light-Emitting Diodes for next-Generation Data Communications. *Nat. Electron.* **2021**, *4* (8), 559–572. https://doi.org/10.1038/s41928-021-00624-7.

(6) Tang, Y.; Zhao, Y.; Liu, H. Room-Temperature Semiconductor Gas Sensors: Challenges and Opportunities. *ACS Sensors* **2022**, *7* (12), 3582–3597. https://doi.org/10.1021/acssensors.2c01142.

(7) Madelung, O. *Semiconductors: Data Handbook*; Springer Berlin Heidelberg: Berlin, Heidelberg, 2004. https://doi.org/10.1007/978-3-642-18865-7.

(8) Ho, P. K. H.; Kim, J.-S.; Burroughes, J. H.; Becker, H.; Li, S. F. Y.; Brown, T. M.; Cacialli, F.; Friend, R. H. Molecular-Scale Interface Engineering for Polymer Light-Emitting Diodes. *Nature* **2000**, *404* (6777), 481–484. https://doi.org/10.1038/35006610.

(9) Ostroverkhova, O. Organic Optoelectronic Materials: Mechanisms and Applications. *Chem. Rev.* **2016**, *116* (22), 13279–13412. https://doi.org/10.1021/acs.chemrev.6b00127.

(10) Garnier, F. Thin Film Transistors Based on Organic Conjugated Semiconductors. *Curr. Opin. Solid State Mater. Sci.* **1997**, *2* (4), 455–461. https://doi.org/10.1016/S1359-0286(97)80089-7.

(11) Köhler, A.; Bässler, H. *Electronic Processes in Organic Semiconductors: An Introduction*; John Wiley & Sons, 2015.

(12) Ding, L.; Jonforsen, M.; Roman, L. S.; Andersson, M. R.; Inganäs, O. Photovoltaic Cells with a Conjugated Polyelectrolyte. *Synth. Met.* **2000**, *110* (2), 133–140. https://doi.org/10.1016/S0379-6779(99)00284-2.

(13) Pochettino, A. The Photoconductivity of Anthracene. *Acad. Lincei Rend* **1906**, *15*, 355–363.

(14) Brütting, W. *Physics of Organic Semiconductors*; Brütting, W., Ed.; Wiley, 2005. https://doi.org/10.1002/3527606637.

(15) Coropceanu, V.; Cornil, J.; da Silva Filho, D. A.; Olivier, Y.; Silbey, R.; Brédas, J.-L. Charge Transport in Organic Semiconductors. *Chem. Rev.* **2007**, *107* (4), 926–952. https://doi.org/10.1021/cr050140x.

(16) Chen, Y.; Yan, C.; Dong, J.; Zhou, W.; Rosei, F.; Feng, Y.; Wang, L. Structure/Property Control in Photocatalytic Organic Semiconductor Nanocrystals. *Adv. Funct. Mater.* **2021**, *31* (36), 2104099. https://doi.org/10.1002/adfm.202104099.

(17) Bao, Z. Materials and Fabrication Needs for Low-Cost Organic Transistor Circuits. *Adv. Mater.* **2000**, *12* (3), 227–230. https://doi.org/10.1002/(SICI)1521-4095(200002)12:3<227::AID-ADMA227>3.0.CO;2-U.

(18) Jones, B. A.; Ahrens, M. J.; Yoon, M.; Facchetti, A.; Marks, T. J.; Wasielewski, M. R. High-Mobility Air-Stable N-Type Semiconductors with Processing Versatility: Dicyanoperylene-3,4:9,10-bis(Dicarboximides). *Angew. Chemie Int. Ed.* **2004**, *43* (46), 6363–6366. https://doi.org/10.1002/anie.200461324.

(19) Silinsh, E. A. *Organic Molecular Crystals*; Springer, Berlin, 1980.

(20) Myers, J. D.; Xue, J. Organic Semiconductors and Their Applications in Photovoltaic Devices. *Polym. Rev.* **2012**, *52* (1), 1–37. https://doi.org/10.1080/15583724.2011.644368.

(21) Spanggaard, H.; Krebs, F. C. A Brief History of the Development of Organic and Polymeric Photovoltaics. *Sol. Energy Mater. Sol. Cells* **2004**, *83* (2–3), 125–146. https://doi.org/10.1016/j.solmat.2004.02.021.

(22) Root, S. E.; Savagatrup, S.; Printz, A. D.; Rodriquez, D.; Lipomi, D. J. Mechanical Properties of Organic Semiconductors for Stretchable, Highly Flexible, and Mechanically Robust Electronics. *Chem. Rev.* **2017**, *117* (9), 6467–6499. https://doi.org/10.1021/acs.chemrev.7b00003.

(23) Lee, E. K.; Lee, M. Y.; Park, C. H.; Lee, H. R.; Oh, J. H. Toward Environmentally Robust

Organic Electronics: Approaches and Applications. *Adv. Mater.* **2017**, *29* (44), 1703638. https://doi.org/10.1002/adma.201703638.

(24) Bronstein, H.; Nielsen, C. B.; Schroeder, B. C.; McCulloch, I. The Role of Chemical Design in the Performance of Organic Semiconductors. *Nat. Rev. Chem.* **2020**, *4* (2), 66–77. https://doi.org/10.1038/s41570-019-0152-9.

(25) Chiang, C. K.; Fincher, C. R.; Park, Y. W.; Heeger, A. J.; Shirakawa, H.; Louis, E. J.; Gau, S. C.; MacDiarmid, A. G. Electrical Conductivity in Doped Polyacetylene. *Phys. Rev. Lett.* **1977**, *39* (17), 1098–1101. https://doi.org/10.1103/PhysRevLett.39.1098.

(26) Cui, W.; Chen, F.; Li, Y.; Su, X.; Sun, B. Status and Perspectives of Transparent Conductive Oxide Films for Silicon Heterojunction Solar Cells. *Mater. Today Nano* **2023**, *22*, 100329. https://doi.org/10.1016/j.mtnano.2023.100329.

(27) Thompson, S. E.; Parthasarathy, S. Moore's Law: The Future of Si Microelectronics. *Mater. Today* **2006**, *9* (6), 20–25. https://doi.org/10.1016/S1369-7021(06)71539-5.

(28) Li, R.; Hu, W.; Liu, Y.; Zhu, D. Micro- and Nanocrystals of Organic Semiconductors. *Acc. Chem. Res.* **2010**, *43* (4), 529–540. https://doi.org/10.1021/ar900228v.

(29) Anthony, J. E. Addressing Challenges. *Nat. Mater.* **2014**, *13* (8), 773–775. https://doi.org/10.1038/nmat4034.

(30) Gryn'ova, G.; Lin, K.-H.; Corminboeuf, C. Read between the Molecules: Computational Insights into Organic Semiconductors. *J. Am. Chem. Soc.* **2018**, *140* (48), 16370–16386. https://doi.org/10.1021/jacs.8b07985.

(31) Facchetti, A. Semiconductors for Organic Transistors. *Mater. Today* **2007**, *10* (3), 28–37. https://doi.org/10.1016/S1369-7021(07)70017-2.

(32) Xue, R.; Zhang, J.; Li, Y.; Li, Y. Organic Solar Cell Materials toward Commercialization. *Small* **2018**, *14* (41), 1801793. https://doi.org/10.1002/smll.201801793.

(33) Ando, S.; Murakami, R.; Nishida, J.; Tada, H.; Inoue, Y.; Tokito, S.; Yamashita, Y. N-Type Organic Field-Effect Transistors with Very High Electron Mobility Based on Thiazole Oligomers with Trifluoromethylphenyl Groups. *J. Am. Chem. Soc.* **2005**, *127* (43), 14996–14997. https://doi.org/10.1021/ja055686f.

(34) Mei, J.; Diao, Y.; Appleton, A. L.; Fang, L.; Bao, Z. Integrated Materials Design of Organic Semiconductors for Field-Effect Transistors. *J. Am. Chem. Soc.* **2013**, *135* (18), 6724–6746. https://doi.org/10.1021/ja400881n.

(35) Huang, C.; Barlow, S.; Marder, S. R. Perylene-3,4,9,10-Tetracarboxylic Acid Diimides: Synthesis, Physical Properties, and Use in Organic Electronics. *J. Org. Chem.* **2011**, *76*

(8), 2386–2407. https://doi.org/10.1021/jo2001963.

(36) Struijk, C. W.; Sieval, A. B.; Dakhorst, J. E. J.; Van Dijk, M.; Kimkes, P.; Koehorst, R. B. M.; Donker, H.; Schaafsma, T. J.; Picken, S. J.; Van de Craats, A. M.; Warman, J. M.; Zuilhof, H.; Sudholter, E. J. R. Liquid Crystalline Perylene Diimides: Architecture and Charge Carrier Mobilities. *J. Am. Chem. Soc.* **2000**, *122* (45), 11057–11066. https://doi.org/10.1021/ja000991g.

(37) Cao, J.; Yang, S. Progress in Perylene Diimides for Organic Solar Cell Applications. *RSC Adv.* **2022**, *12* (12), 6966–6973. https://doi.org/10.1039/d1ra08484d.

(38) Zhan, X.; Facchetti, A.; Barlow, S.; Marks, T. J.; Ratner, M. A.; Wasielewski, M. R.; Marder, S. R. Rylene and Related Diimides for Organic Electronics. *Adv. Mater.* **2011**, *23* (2), 268–284. https://doi.org/10.1002/adma.201001402.

(39) Jung, B. J.; Tremblay, N. J.; Yeh, M. L.; Katz, H. E. Molecular Design and Synthetic Approaches to Electron-Transporting Organic Transistor Semiconductors. *Chem. Mater.* **2011**, *23* (3), 568–582. https://doi.org/10.1021/cm102296d.

(40) Kozma, E.; Catellani, M. Perylene Diimides Based Materials for Organic Solar Cells. *Dye. Pigment.* **2013**, *98* (1), 160–179. https://doi.org/10.1016/j.dyepig.2013.01.020.

(41) Schmidt-Mende, L.; Fechtenkötter, A.; Müllen, K.; Moons, E.; Friend, R. H.; MacKenzie, J. D. Self-Organized Discotic Liquid Crystals for High-Efficiency Organic Photovoltaics. *Science.* **2001**, *293* (5532), 1119–1122. https://doi.org/10.1126/science.293.5532.1119.

(42) Li, C.; Wonneberger, H. Perylene Imides for Organic Photovoltaics: Yesterday, Today, and Tomorrow. *Adv. Mater.* **2012**, *24* (5), 613–636. https://doi.org/10.1002/adma.201104447.

(43) Weil, T.; Vosch, T.; Hofkens, J.; Peneva, K.; Müllen, K. The Rylene Colorant Family—Tailored Nanoemitters for Photonics Research and Applications. *Angew. Chemie Int. Ed.* **2010**, *49* (48), 9068–9093. https://doi.org/10.1002/anie.200902532.

(44) Anthony, J. E.; Facchetti, A.; Heeney, M.; Marder, S. R.; Zhan, X. N-Type Organic Semiconductors in Organic Electronics. *Adv. Mater.* **2010**, *22* (34), 3876–3892. https://doi.org/10.1002/adma.200903628.

(45) Kardos, M. Über Einige Aceanthrenchinon- Und 1.9-Anthracen-Derivate. *Berichte der Dtsch. Chem. Gesellschaft* **1913**, *46* (2), 2086–2091. https://doi.org/10.1002/cber.191304602126.

(46) Greene, M. Perylene Pigments. In *High Performance Pigments*; Wiley, 2001; pp 249–261. https://doi.org/10.1002/3527600493.ch16.

(47) Kazmaier, P. M.; Hoffmann, R. A Theoretical Study of Crystallochromy . Quantum M2MSH0. *J. Am. Chem. Soc.* **1994**, *116*, 9684–9691.

(48) Huang, C.; Barlow, S.; Marder, S. R. Perylene-3,4,9,10-Tetracarboxylic Acid Diimides: Synthesis, Physical Properties, and Use in Organic Electronics. *J. Org. Chem.* **2011**, *76* (8), 2386–2407. https://doi.org/10.1021/jo2001963.

(49) Tang, C. W. Two-Layer Organic Photovoltaic Cell. *Appl. Phys. Lett.* **1986**, *48* (2), 183–185. https://doi.org/10.1063/1.96937.

(50) Zhang, G.; Feng, J.; Xu, X.; Ma, W.; Li, Y.; Peng, Q. Perylene Diimide-Based Nonfullerene Polymer Solar Cells with over 11% Efficiency Fabricated by Smart Molecular Design and Supramolecular Morphology Optimization. *Adv. Funct. Mater.* **2019**, *29* (50), 1906587.

(51) Zhang, B.; Zhao, Y.; Xu, C.; Feng, C.; Li, W.; Qin, X.; Lv, M.; Luo, X.; Qin, X.; Li, A.; He, Z.; Wang, E. Perylene Diimide-Based Low-Cost and Thickness-Tolerant Electron Transport Layer Enables Polymer Solar Cells Approaching 19% Efficiency. *Adv. Funct. Mater.* **2024**, *34* (34), 2400903. https://doi.org/10.1002/adfm.202400903.

(52) Zhang, Z.-G.; Qi, B.; Jin, Z.; Chi, D.; Qi, Z.; Li, Y.; Wang, J. Perylene Diimides: A Thickness-Insensitive Cathode Interlayer for High Performance Polymer Solar Cells. *Energy Environ. Sci.* **2014**, *7* (6), 1966. https://doi.org/10.1039/c4ee00022f.

(53) Feng, L.; Xiang, Y.; Li, Z.; Li, Q.; Dong, H.; Yan, S.; Xu, B.; Hou, J. Non-Ionic Perylene-Diimide Polymer as Universal Cathode Interlayer for Conventional, Inverted, and Blade-Coated Organic Solar Cells. *Angew. Chemie* **2024**, *136* (43), e202410857. https://doi.org/10.1002/ange.202410857.

(54) Mai, T. L. H.; Sun, Z.; Kim, S.; Jeong, S.; Lee, S.; Park, J.; Yang, C. Open-Air, Green-Solvent Processed Organic Solar Cells with Efficiency Approaching 18% and Exceptional Stability. *Energy Environ. Sci.* **2024**, *17* (19), 7435–7444. https://doi.org/10.1039/D4EE01944J.

(55) Gao, L.; Wang, H.; Guo, Q.; Wang, Z.; Yuan, F.; Zhou, E. D-A-D Typed Fused-Ring Perylene Diimide: A Cathode Interface Material for Efficient Inverted Perovskite Solar Cells. *Chem. Eng. J.* **2024**, *480*, 148277. https://doi.org/10.1016/j.cej.2023.148277.

(56) Kim, H. S.; Cho, Y.; Lee, H.; Kim, S.; Jung, E. D.; Noh, Y. W.; Park, S.; Cho, S.; Lee, B. R.; Yang, C.; Song, M. H. Vacuum-Assisted Reforming Cathode Interlayer Orientation for Efficient and Stable Perovskite Solar Cells. *Nano Energy* **2024**, *125*, 109584. https://doi.org/10.1016/j.nanoen.2024.109584.

(57) Zhou, W.; Liu, G.; Yang, B.; Ji, Q.; Xiang, W.; He, H.; Xu, Z.; Qi, C.; Li, S.; Yang, S.; Xu, C. Review on Application of Perylene Diimide (PDI)-Based Materials in Environment: Pollutant Detection and Degradation. *Sci. Total Environ.* **2021**, *780*, 146483. https://doi.org/10.1016/j.scitotenv.2021.146483.

(58) Liu, Z.-R.; Rill, R. L. N,N′-Bis[3,3′-(Dimethylamino)Propylamine]-3,4,9,10-Perylenetetracarboxylic Diimide, a Dicationic Perylene Dye for Rapid Precipitation and Quantitation of Trace Amounts of DNA. *Anal. Biochem.* **1996**, *236* (1), 139–145. https://doi.org/10.1006/abio.1996.0142.

(59) Gao, X.; Wu, X.; Wu, Z.; Gao, J.; Liu, Z. Organic Solar Cells Based on Molecular Perylene Diimides-Type Nonfullerene Acceptors: Achievements, Challenges and the Future. *Sci. China Chem.* **2025**, *68*, 3359–3375. https://doi.org/10.1007/s11426-024-2406-9.

(60) Würthner, F.; Stepanenko, V.; Chen, Z.; Saha-Möller, C. R.; Kocher, N.; Stalke, D. Preparation and Characterization of Regioisomerically Pure 1,7-Disubstituted Perylene Bisimide Dyes. *J. Org. Chem.* **2004**, *69* (23), 7933–7939. https://doi.org/10.1021/jo048880d.

(61) Liu, Z.; Wu, Y.; Zhang, Q.; Gao, X. Non-Fullerene Small Molecule Acceptors Based on Perylene Diimides. *J. Mater. Chem. A* **2016**, *4* (45), 17604–17622. https://doi.org/10.1039/C6TA06978A.

(62) Marin, F.; Tombolesi, S.; Salzillo, T.; Yaffe, O.; Maini, L. Thorough Investigation on the High-Temperature Polymorphism of Dipentyl-Perylenediimide: Thermal Expansion vs. Polymorphic Transition. *J. Mater. Chem. C* **2022**, *10* (20), 8089–8100. https://doi.org/10.1039/d1tc06132a.

(63) Williams, M. L.; Brown, P. J.; Palmer, J. R.; Young, R. M.; Wasielewski, M. R. Structure-Dependent Triplet State Formation in Fluorinated Perylenediimide Single Crystal Polymorphs. *J. Phys. Chem. C* **2024**, *128* (4), 1603–1611. https://doi.org/10.1021/acs.jpcc.3c07470.

(64) Mizuguchi, J. Electronic Characterization of N,N′-Bis(2-Phenylethyl)Perylene-3,4:9, 10-Bis(Dicarboximide) and Its Application to Optical Disks. *J. Appl. Phys.* **1998**, *84* (8), 4479–4486. https://doi.org/10.1063/1.368699.

(65) Hartnett, P. E.; Margulies, E. A.; Matte, H. S. S. R.; Hersam, M. C.; Marks, T. J.; Wasielewski, M. R. Effects of Crystalline Perylenediimide Acceptor Morphology on Optoelectronic Properties and Device Performance. *Chem. Mater.* **2016**, *28* (11), 3928–

3936. https://doi.org/10.1021/acs.chemmater.6b01230.

(66) Sharma, S. M.; Sikka, S. K. Pressure Induced Amorphization of Materials. *Prog. Mater. Sci.* **1996**, *40* (1), 1–77. https://doi.org/10.1016/0079-6425(95)00006-2.

(67) Volek, T. S.; Verkamp, M. A.; Ruiz, G. N.; Staat, A. J.; Li, B. C.; Rose, M. J.; Eaves, J. D.; Roberts, S. T. Slowed Singlet Exciton Fission Enhances Triplet Exciton Transport in Select Perylenediimide Crystals. *J. Am. Chem. Soc.* **2024**, *146* (43), 29575–29587. https://doi.org/10.1021/jacs.4c09923.

(68) Pinto, R. M.; Maçôas, E. M. S.; Neves, A. I. S.; Raja, S.; Baleizão, C.; Santos, I. C.; Alves, H. Effect of Molecular Stacking on Exciton Diffusion in Crystalline Organic Semiconductors. *J. Am. Chem. Soc.* **2015**, *137* (22), 7104–7110. https://doi.org/10.1021/ja512886h.

(69) Cruz-Cabeza, A. J.; Reutzel-Edens, S. M.; Bernstein, J. Facts and Fictions about Polymorphism. *Chem. Soc. Rev.* **2015**, *44* (23), 8619–8635. https://doi.org/10.1039/C5CS00227C.

(70) Groom, C. R.; Bruno, I. J.; Lightfoot, M. P.; Ward, S. C. The Cambridge Structural Database. *Acta Crystallogr. Sect. B Struct. Sci. Cryst. Eng. Mater.* **2016**, *72* (2), 171–179. https://doi.org/10.1107/S2052520616003954.

(71) Stoeckel, M.; Olivier, Y.; Gobbi, M.; Dudenko, D.; Lemaur, V.; Zbiri, M.; Guilbert, A. A. Y.; D'Avino, G.; Liscio, F.; Migliori, A.; Ortolani, L.; Demitri, N.; Jin, X.; Jeong, Y.; Liscio, A.; Nardi, M.; Pasquali, L.; Razzari, L.; Beljonne, D.; Samorì, P.; Orgiu, E. Analysis of External and Internal Disorder to Understand Band-Like Transport in N-Type Organic Semiconductors. *Adv. Mater.* **2021**, *33* (13), 2007870. https://doi.org/10.1002/adma.202007870.

(72) Bernstein, J. Crystal Growth, Polymorphism and Structure-Property Relationships in Organic Crystals. *J. Phys. D. Appl. Phys.* **1993**, *26* (8B), B66–B76. https://doi.org/10.1088/0022-3727/26/8B/010.

(73) Chung, H.; Diao, Y. Polymorphism as an Emerging Design Strategy for High Performance Organic Electronics. *J. Mater. Chem. C* **2016**, *4* (18), 3915–3933. https://doi.org/10.1039/c5tc04390e.

(74) Diao, Y.; Lenn, K. M.; Lee, W.-Y.; Blood-Forsythe, M. A.; Xu, J.; Mao, Y.; Kim, Y.; Reinspach, J. A.; Park, S.; Aspuru-Guzik, A.; Xue, G.; Clancy, P.; Bao, Z.; Mannsfeld, S. C. B. Understanding Polymorphism in Organic Semiconductor Thin Films through Nanoconfinement. *J. Am. Chem. Soc.* **2014**, *136* (49), 17046–17057.

https://doi.org/10.1021/ja507179d.

(75) Kim, W.; Kim, J. K.; Kim, E.; Ahn, T. K.; Wang, D. H.; Park, J. H. Conflicted Effects of a Solvent Additive on PTB7:PC 71 BM Bulk Heterojunction Solar Cells. *J. Phys. Chem. C* **2015**, *119* (11), 5954–5961. https://doi.org/10.1021/jp510996w.

(76) Liang, Y.; Xu, Z.; Xia, J.; Tsai, S.; Wu, Y.; Li, G.; Ray, C.; Yu, L. For the Bright Future—Bulk Heterojunction Polymer Solar Cells with Power Conversion Efficiency of 7.4%. *Adv. Mater.* **2010**, *22* (20), E135–E138. https://doi.org/10.1002/adma.200903528.

(77) Dubrovinsky, L.; Dubrovinskaia, N.; Prakapenka, V. B.; Abakumov, A. M. Implementation of Micro-Ball Nanodiamond Anvils for High-Pressure Studies above 6 Mbar. *Nat. Commun.* **2012**, *3* (1), 1163. https://doi.org/10.1038/ncomms2160.

(78) Katrusiak, A. Lab in a DAC - High-Pressure Crystal Chemistry in a Diamond-Anvil Cell. *Acta Crystallogr. Sect. B Struct. Sci. Cryst. Eng. Mater.* **2019**, *75*, 918–926. https://doi.org/10.1107/S2052520619013246.

(79) Baun, W. L. X-ray diffraction study of straight chain (C1 TO C14) carboxylic acids. *J. Phys. Chem.* **1961**, *65* (12), 2122–2126.

(80) Todd, F. C. Changes in the X-Ray Diffraction Pattern of Nitrobenzene Produced by an Electric Field, Changes in Temperature and Circulation. *Phys. Rev.* **1933**, *44* (10), 787–793. https://doi.org/10.1103/PhysRev.44.787.

(81) De Bretteville, A.; McBain, J. W. X-Ray Diffraction Investigation of Sodium Stearate from Room Temperature to the Melting Point. *J. Chem. Phys.* **1943**, *11* (9), 426–429. https://doi.org/10.1063/1.1723868.

(82) De Bretteville, A. An X-Ray High Temperature Camera. *Rev. Sci. Instrum.* **1942**, *13* (11), 481–483. https://doi.org/10.1063/1.1769946.

(83) Bridgman, P. W. *The Physics Of High Pressure*; G. Bell And Sons Ltd., London, 1949.

(84) Weir, C. E.; Lippincott, E. R.; Van Valkenburg, A.; Bunting, E. N. Infrared Studies in the 1- to 15-Micron Region to 30,000 Atmospheres. *J. Res. Natl. Bur. Stand. Sect. A Phys. Chem.* **1959**, *63A* (1), 55–62. https://doi.org/10.6028/jres.063A.003.

(85) Jamieson, J. C.; Lawson, A. W.; Nachtrieb, N. D. New Device for Obtaining X-Ray Diffraction Patterns from Substances Exposed to High Pressure. *Rev. Sci. Instrum.* **1959**, *30* (11), 1016–1019. https://doi.org/10.1063/1.1716408

(86) Liang, J.; Ju, C.; Liu, Z.; Li, H.; Karina, A.; Eklund, T.; Zheng, W.; Amann-Winkel, K.; Cai, W.; Wagner, M.; Qiu, Z.; Weil, T.; Müllen, K. Fluorescence of Helical Molecular Springs Under High Pressure. *Angew. Chemie Int. Ed.* **2025**, *64* (21), e202500923.

https://doi.org/10.1002/anie.202500923.

(87) Zakharov, B. A.; Boldyreva, E. V. A High-Pressure Single-Crystal to Single-Crystal Phase Transition in DL-Alaninium Semi-Oxalate Monohydrate with Switching-over Hydrogen Bonds. *Acta Crystallogr. Sect. B Struct. Sci. Cryst. Eng. Mater.* **2013**, *69* (3), 271–280. https://doi.org/10.1107/S2052519213011676.

(88) Marciniak, J.; Bąkowicz, J.; Dobrowolski, M. A.; Dziubek, K. F.; Kaźmierczak, M.; Paliwoda, D.; Rajewski, K. W.; Sobczak, S.; Stachowicz, M.; Katrusiak, A. Most Frequent Organic Interactions Compressed in Toluene. *Cryst. Growth Des.* **2016**, *16* (3), 1435–1441. https://doi.org/10.1021/acs.cgd.5b01538.

(89) Zakharov, B. A.; Boldyreva, E. V. High Pressure: A Complementary Tool for Probing Solid-State Processes. *CrystEngComm* **2019**, *21* (1), 10–22. https://doi.org/10.1039/c8ce01391h.

(90) Boldyreva, E. V. High-Pressure Diffraction Studies of Molecular Organic Solids. A Personal View. *Acta Crystallogr. Sect. A Found. Crystallogr.* **2008**, *64* (1), 218–231. https://doi.org/10.1107/S0108767307065786.

(91) Kong, L.; Liu, G.; Gong, J.; Hu, Q.; Schaller, R. D.; Dera, P.; Zhang, D.; Liu, Z.; Yang, W.; Zhu, K.; Tang, Y.; Wang, C.; Wei, S.-H.; Xu, T.; Mao, H. Simultaneous Band-Gap Narrowing and Carrier-Lifetime Prolongation of Organic–Inorganic Trihalide Perovskites. *Proc. Natl. Acad. Sci.* **2016**, *113* (32), 8910–8915. https://doi.org/10.1073/pnas.1609030113.

(92) Liu, G.; Kong, L.; Gong, J.; Yang, W.; Mao, H.; Hu, Q.; Liu, Z.; Schaller, R. D.; Zhang, D.; Xu, T. Pressure-Induced Bandgap Optimization in Lead-Based Perovskites with Prolonged Carrier Lifetime and Ambient Retainability. *Adv. Funct. Mater.* **2017**, *27* (3), 1604208. https://doi.org/10.1002/adfm.201604208.

(93) Zhang, L.; Liu, C.; Wang, L.; Liu, C.; Wang, K.; Zou, B. Pressure-Induced Emission Enhancement, Band-Gap Narrowing, and Metallization of Halide Perovskite Cs 3 Bi 2 I 9. *Angew. Chemie Int. Ed.* **2018**, *57* (35), 11213–11217. https://doi.org/10.1002/anie.201804310.

(94) Zurek, E.; Grochala, W. Predicting Crystal Structures and Properties of Matter under Extreme Conditions via Quantum Mechanics: The Pressure Is On. *Phys. Chem. Chem. Phys.* **2015**, *17* (5), 2917–2934. https://doi.org/10.1039/C4CP04445B.

(95) Allan, D. R. Exploring Crystal Structure-Physical Property Relationships with Pressure. *IUCrJ* **2024**, *11* (Pt 4), 438–439. https://doi.org/10.1107/S205225252400602X.

(96) Desiraju, G. R. Crystal Engineering: A Holistic View. *Angew. Chemie Int. Ed.* **2007**, *46* (44), 8342–8356. https://doi.org/10.1002/anie.200700534.

(97) Ratajczyk, P.; Sobczak, S.; Katrusiak, A. High-Pressure Structure and Properties of N , N -Dimethylformamide (DMF). *Cryst. Growth Des.* **2019**, *19* (2), 896–901. https://doi.org/10.1021/acs.cgd.8b01452.

(98) Patyk, E.; Podsiadło, M.; Katrusiak, A. CH···N Bonds and Dynamics in Isostructural Pyrimidine Polymorphs. *Cryst. Growth Des.* **2015**, *15* (8), 4039–4044. https://doi.org/10.1021/acs.cgd.5b00657.

(99) Oganov, A. R.; Lyakhov, A. O.; Valle, M. How Evolutionary Crystal Structure Prediction Works—and Why. *Acc. Chem. Res.* **2011**, *44* (3), 227–237. https://doi.org/10.1021/ar1001318.

(100) Sobczak, S.; Ratajczyk, P.; Katrusiak, A. High-pressure Nucleation of Low-Density Polymorphs**. *Chem. – A Eur. J.* **2021**, *27* (24), 7069–7073. https://doi.org/10.1002/chem.202005121.

(101) Allen, F. H.; Taylor, R. Research Applications of the Cambridge Structural Database (CSD). *Chem. Soc. Rev.* **2004**, *33* (8), 463. https://doi.org/10.1039/b309040j.

(102) Wang, C.; Dong, H.; Jiang, L.; Hu, W. Organic Semiconductor Crystals. *Chem. Soc. Rev.* **2018**, *47* (2), 422–500. https://doi.org/10.1039/C7CS00490G.

(103) Cozzi, F.; Bacchi, S.; Filippini, G.; Pilati, T.; Gavezzotti, A. Synthesis, X-ray Diffraction and Computational Study of the Crystal Packing of Polycyclic Hydrocarbons Featuring Aromatic and Perfluoroaromatic Rings Condensed in the Same Molecule: 1,2,3,4-Tetrafluoronaphthalene, -anthracene and -phenanthrene. *Chem. – A Eur. J.* **2007**, *13* (25), 7177–7184. https://doi.org/10.1002/chem.200700267.

(104) Anthony, J. E.; Brooks, J. S.; Eaton, D. L.; Parkin, S. R. Functionalized Pentacene: Improved Electronic Properties from Control of Solid-State Order. *J. Am. Chem. Soc.* **2001**, *123* (38), 9482–9483. https://doi.org/10.1021/ja0162459.

(105) Jurchescu, O. D.; Meetsma, A.; Palstra, T. T. M. Low-Temperature Structure of Rubrene Single Crystals Grown by Vapor Transport. *Acta Crystallogr. Sect. B Struct. Sci.* **2006**, *62* (2), 330–334. https://doi.org/10.1107/S0108768106003053.

(106) Campbell, R. B.; Robertson, J. M.; Trotter, J. The Crystal Structure of Hexacene, and a Revision of the Crystallographic Data for Tetracene. *Acta Crystallogr.* **1962**, *15* (3), 289–290. https://doi.org/10.1107/S0365110X62000699.

(107) Li, R.; Hu, W.; Liu, Y.; Zhu, D. Micro- and Nanocrystals of Organic Semiconductors.

Acc. Chem. Res. **2010**, *43* (4), 529–540. https://doi.org/10.1021/ar900228v.

(108) Yao, Z.-F.; Wang, J.-Y.; Pei, J. Control of π–π Stacking via Crystal Engineering in Organic Conjugated Small Molecule Crystals. *Cryst. Growth Des.* **2018**, *18* (1), 7–15. https://doi.org/10.1021/acs.cgd.7b01385.

(109) Wang, C.; Dong, H.; Hu, W.; Liu, Y.; Zhu, D. Semiconducting π-Conjugated Systems in Field-Effect Transistors: A Material Odyssey of Organic Electronics. *Chem. Rev.* **2012**, *112* (4), 2208–2267. https://doi.org/10.1021/cr100380z.

(110) Wang, C.; Dong, H.; Li, H.; Zhao, H.; Meng, Q.; Hu, W. Dibenzothiophene Derivatives: From Herringbone to Lamellar Packing Motif. *Cryst. Growth Des.* **2010**, *10* (9), 4155–4160. https://doi.org/10.1021/cg100863q.

(111) Dong, H.; Wang, C.; Hu, W. High Performance Organic Semiconductors for Field-Effect Transistors. *Chem. Commun.* **2010**, *46* (29), 5211. https://doi.org/10.1039/c0cc00947d.

(112) Payne, M. M.; Parkin, S. R.; Anthony, J. E.; Kuo, C.-C.; Jackson, T. N. Organic Field-Effect Transistors from Solution-Deposited Functionalized Acenes with Mobilities as High as 1 Cm 2 /V·s. *J. Am. Chem. Soc.* **2005**, *127* (14), 4986–4987. https://doi.org/10.1021/ja042353u.

(113) Geng, Y.; Li, H.-B.; Wu, S.-X.; Su, Z.-M. The Interplay of Intermolecular Interactions, Packing Motifs and Electron Transport Properties in Perylene Diimide Related Materials: A Theoretical Perspective. *J. Mater. Chem.* **2012**, *22* (39), 20840. https://doi.org/10.1039/c2jm33369d.

(114) Hädicke, E.; Graser, F. Structures of Three Perylene-3,4,9,10-Bis(Dicarboximide) Pigments. *Acta Crystallogr. Sect. C Cryst. Struct. Commun.* **1986**, *42* (2), 195–198. https://doi.org/10.1107/S0108270186096816.

(115) Mizuguchi, J.; Tojo, K. Crystal Structure of N,N'-Bis(3,5-Xylyl)Perylene-3,4:9,10-Bis(Dicarboxi-Mide),C40H26N2O4. *Zeitschrift für Krist. - New Cryst. Struct.* **2001**, *216* (1–4), 397–398. https://doi.org/10.1524/ncrs.2001.216.14.397.

(116) Stolte, M.; Hecht, R.; Xie, Z.; Liu, L.; Kaufmann, C.; Kudzus, A.; Schmidt, D.; Würthner, F. Crystal Engineering of 1D Exciton Systems Composed of Single- and Double-Stranded Perylene Bisimide J-Aggregates. *Adv. Opt. Mater.* **2020**, *8* (18), 2000926. https://doi.org/10.1002/adom.202000926.

(117) Zhang, B.; Lyskov, I.; Wilson, L. J.; Sabatini, R. P.; Manian, A.; Soleimaninejad, H.; White, J. M.; Smith, T. A.; Lakhwani, G.; Jones, D. J.; Ghiggino, K. P.; Russo, S. P.; Wong, W. W. H. FRET-Enhanced Photoluminescence of Perylene Diimides by

Combining Molecular Aggregation and Insulation. *J. Mater. Chem. C* **2020**, *8* (26), 8953–8961. https://doi.org/10.1039/D0TC02108C.

(118) Zugenmaier, P.; Duff, J.; Bluhm, T. L. Crystal and Molecular Structures of Six Differently with Halogen Substituted Bis (Benzylimido) Perylene. *Cryst. Res. Technol.* **2000**, *35* (9), 1095–1115. https://doi.org/10.1002/1521-4079(200009)35:9<1095::AID-CRAT1095>3.0.CO;2-5.

(119) Szafrański, M.; Katrusiak, A. Mechanism of Pressure-Induced Phase Transitions, Amorphization, and Absorption-Edge Shift in Photovoltaic Methylammonium Lead Iodide. *J. Phys. Chem. Lett.* **2016**, *7* (17), 3458–3466. https://doi.org/10.1021/acs.jpclett.6b01648.

(120) Jaffe, A.; Lin, Y.; Karunadasa, H. I. Halide Perovskites under Pressure: Accessing New Properties through Lattice Compression. *ACS Energy Lett.* **2017**, *2* (7), 1549–1555. https://doi.org/10.1021/acsenergylett.7b00284.

(121) Szafrański, M.; Katrusiak, A. Photovoltaic Hybrid Perovskites under Pressure. *J. Phys. Chem. Lett.* **2017**, *8* (11), 2496–2506. https://doi.org/10.1021/acs.jpclett.7b00520.

(122) Saski, M.; Sobczak, S.; Ratajczyk, P.; Terlecki, M.; Marynowski, W.; Borkenhagen, A.; Justyniak, I.; Katrusiak, A.; Lewiński, J. Unprecedented Richness of Temperature- and Pressure-Induced Polymorphism in 1D Lead Iodide Perovskite. *Small* **2024**, *20* (38), 2403685. https://doi.org/10.1002/smll.202403685.

(123) Mączka, M.; Sobczak, S.; Ratajczyk, P.; Leite, F. F.; Paraguassu, W.; Dybała, F.; Herman, A. P.; Kudrawiec, R.; Katrusiak, A. Pressure-Driven Phase Transition in Two-Dimensional Perovskite MHy 2 PbBr 4. *Chem. Mater.* **2022**, *34* (17), 7867–7877. https://doi.org/10.1021/acs.chemmater.2c01533.

(124) Zhou, W.; Aslandukov, A.; Minchenkova, A.; Hanfland, M.; Dubrovinsky, L.; Dubrovinskaia, N. Structural Transformations and Stability of Benzo[a]Pyrene under High Pressure. *IUCrJ* **2025**, *12* (Pt 1), 16–22. https://doi.org/10.1107/S2052252524010455.

(125) Pakhomova, A.; Han, M.; Poreba, T.; Mezouar, M. Polymorphism of Pyrene on Compression to 35 GPa in a Diamond Anvil Cell. *Commun. Chem.* **2024**, *7* (1), 209. https://doi.org/10.1038/s42004-024-01294-0.

(126) Rang, Z.; Haraldsson, A.; Kim, D. M.; Ruden, P. P.; Nathan, M. I.; Chesterfield, R. J.; Frisbie, C. D. Hydrostatic-Pressure Dependence of the Photoconductivity of Single-

Crystal Pentacene and Tetracene. *Appl. Phys. Lett.* **2001**, *79* (17), 2731–2733. https://doi.org/10.1063/1.1410878.

(127) Liu, C. Y.; Bard, A. J. Pressure-Induced Insulator-Conductor Transition in a Photoconducting Organic Liquid-Crystal Film. *Nature* **2002**, *418* (6894), 162–164. https://doi.org/10.1038/nature00875.

(128) Oleson, A.; Zhu, T.; Dunn, I. S.; Bialas, D.; Bai, Y.; Zhang, W.; Dai, M.; Reichman, D. R.; Tempelaar, R.; Huang, L.; Spano, F. C. Perylene Diimide-Based Hj- and HJ-Aggregates: The Prospect of Exciton Band Shape Engineering in Organic Materials. *J. Phys. Chem. C* **2019**, *123* (33), 20567−20578
. https://doi.org/10.1021/acs.jpcc.9b04429.

(129) Li, R.; Wang, M.; Zhao, H.; Bian, Z.; Wang, X.; Cheng, Y.; Huang, W. Pressure Effect on Electronic and Excitonic Properties of Purely J-Aggregated Monolayer Organic Semiconductor. *J. Phys. Chem. Lett.* **2020**, *11* (15), 5896−5901. https://doi.org/10.1021/acs.jpclett.0c01809.

(130) Merrill, L.; Bassett, W. A. Miniature Diamond Anvil Pressure Cell for Single Crystal X-Ray Diffraction Studies. *Rev. Sci. Instrum.* **1974**, *45* (2), 290–294. https://doi.org/10.1063/1.1686607.

(131) Katrusiak, A. High-Pressure Crystallography. *Acta Crystallogr. Sect. A Found. Crystallogr.* **2008**, *64* (1), 135–148. https://doi.org/10.1107/S0108767307061181.

(132) Mao, H. K.; Xu, J.; Bell, P. M. Calibration of the Ruby Pressure Gauge to 800 Kbar under Quasi-hydrostatic Conditions. *J. Geophys. Res. Solid Earth* **1986**, *91* (B5), 4673–4676. https://doi.org/10.1029/JB091iB05p04673.

(133) Forman, R. A.; Piermarini, G. J.; Barnett, J. D.; Block, S. Pressure Measurement Made by the Utilization of Ruby Sharp-Line Luminescence. *Science.* **1972**, *176* (4032), 284–285. https://doi.org/10.1126/science.176.4032.284.

(134) *High-Pressure Crystallography*; Katrusiak, A., McMillan, P., Eds.; Springer Netherlands: Dordrecht, 2004. https://doi.org/10.1007/978-1-4020-2102-2.

(135) Sheldrick, G. M. A Short History of SHELX. *Acta Crystallogr. Sect. A Found. Crystallogr.* **2008**, *64* (1), 112–122. https://doi.org/10.1107/S0108767307043930.

(136) Sheldrick, G. M. Crystal Structure Refinement with SHELXL . *Acta Crystallogr. Sect. C Struct. Chem.* **2015**, *71* (1), 3–8. https://doi.org/10.1107/s2053229614024218.

(137) Dolomanov, O. V.; Bourhis, L. J.; Gildea, R. J.; Howard, J. A. K.; Puschmann, H. OLEX2: A Complete Structure Solution, Refinement and Analysis Program. *J. Appl. Crystallogr.*

2009, *42* (2), 339–341. https://doi.org/10.1107/S0021889808042726.

(138) Sato, K.; Mizuguchi, J. N , N ′-Diphenylperylene-3,4:9,10-Bis(Dicarboximide). *Acta Crystallogr. Sect. E Struct. Reports Online* **2006**, *62* (11), o5008–o5009. https://doi.org/10.1107/S1600536806041845.

(139) Barnett, J. D.; Block, S.; Piermarini, G. J. An Optical Fluorescence System for Quantitative Pressure Measurement in the Diamond-Anvil Cell. *Rev. Sci. Instrum.* **1973**, *44* (1), 1–9. https://doi.org/10.1063/1.1685943.

(140) Pitchaimani, J.; Kundu, A.; Anthony, S. P.; Moon, D.; Madhu, V. Facile Synthetic Route for Direct Access of Perylenediimide Single Crystals in High Yield through In Situ Crystallization. *ChemistrySelect* **2020**, *5* (6), 2070–2074. https://doi.org/10.1002/slct.201904347.

(141) Briseno, A. L.; Mannsfeld, S. C. B.; Reese, C.; Hancock, J. M.; Xiong, Y.; Jenekhe, S. A.; Bao, Z.; Xia, Y. Perylenediimide Nanowires and Their Use in Fabricating Field-Effect Transistors and Complementary Inverters. *Nano Lett.* **2007**, *7* (9), 2847–2853. https://doi.org/10.1021/nl071495u.

(142) Okamoto, T.; Kumagai, S.; Fukuzaki, E.; Ishii, H.; Watanabe, G.; Niitsu, N.; Annaka, T.; Yamagishi, M.; Tani, Y.; Sugiura, H.; Watanabe, T.; Watanabe, S.; Takeya, J. Robust, High-Performance n-Type Organic Semiconductors. *Sci. Adv.* **2020**, *6* (18). https://doi.org/10.1126/sciadv.aaz0632.

(143) Kuznetsova, L. I.; Piryazev, A. A.; Anokhin, D. V.; Mumyatov, A. V.; Susarova, D. K.; Ivanov, D. A.; Troshin, P. A. Disubstituted Perylene Diimides in Organic Field-Effect Transistors: Effect of the Alkyl Side Chains and Thermal Annealing on the Device Performance. *Org. Electron.* **2018**, *58*, 257–262. https://doi.org/10.1016/j.orgel.2018.03.026.

(144) Kalita, N.; Deka, P.; Ghosh, I.; Kalita, K. J.; Gogoi, A.; Malla Reddy, C.; Thakuria, R. Odd–Even Effect Controls Twist-Elasticity of an Organic Fluorophore in Cocrystals Prepared Using Mechanochemistry. *J. Mater. Chem. C* **2025**, *13* (21), 10769–10779. https://doi.org/10.1039/D5TC00313J.

(145) Lei, T.; Wang, J.-Y.; Pei, J. Roles of Flexible Chains in Organic Semiconducting Materials. *Chem. Mater.* **2014**, *26* (1), 594–603. https://doi.org/10.1021/cm4018776.

(146) Marin, F.; Zappi, A.; Melucci, D.; Maini, L. Self-Organizing Maps as a Data-Driven Approach to Elucidate the Packing Motifs of Perylene Diimide Derivatives. *Mol. Syst. Des. Eng.* **2023**, *8* (4), 500–515. https://doi.org/10.1039/D2ME00240J.

(147) Curtis, M. D.; Cao, J.; Kampf, J. W. Solid-State Packing of Conjugated Oligomers: From π-Stacks to the Herringbone Structure. *J. Am. Chem. Soc.* **2004**, *126* (13), 4318–4328. https://doi.org/10.1021/ja0397916.

(148) Janiak, C. A Critical Account on π–π Stacking in Metal Complexes with Aromatic Nitrogen-Containing Ligands. *J. Chem. Soc. Dalt. Trans.* **2000**, No. 21, 3885–3896. https://doi.org/10.1039/b003010o.

8. PhD candidate's scientific achievements

Scientific articles described within this thesis:

1. **Ratajczyk, P.**, Sobczak, S., Woźny, P., Wcisło, A., Poręba, T., Katrusiak, A., Unlocking the sensing potential of phenyl-substituted perylene diimides under extreme conditions, *J. Mater. Chem. C,* 2023, 11, 11055-11065.
2. **Ratajczyk, P.**, Sobczak, S., Andrzejewski, M., Marin, F., Marchini, M., Maini, L., Katrusiak, A, Pressure- and temperature-driven transitions and conformational conversions of n-hexyl substituted perylene diimide (PDI-C6) crystals, *J. Mater. Chem. C,* 2025, 13, 13509-13518.
3. **P. Ratajczyk,** S. Sobczak, M. Andrzejewski, P. Woźny, L. Maini, A. Katrusiak, The odd-even alkyl chain effect on the structure and optoelectronic properties of alkyl-substituted perylene diimide (PDI) derivatives at highly strained environments, 2025, DOI: 10.26434/chemrxiv-2025-2fjc9
4. **Ratajczyk, P.**, Katrusiak, A., Bogdanowicz, K. A., Przybył, W., Krysiak, P., Kwak, A., Iwan, A., Mechanical strain, thermal and pressure effects on the absorption edge of an organic charge-transfer polymer for flexible photovoltaics and sensors. *Mater. Adv.,* 2022, 3, 2697-2705.

Additional scientific articles not included in the thesis:

1. Saski, M., Sobczak, S., **Ratajczyk, P.**, Terlecki, M., Marynowski, W., Borkenhagen, A., Justyniak, I., Katrusiak, A., Lewiński, J., Unprecedented Richness of Temperature- and Pressure-Induced Polymorphism in 1D Lead Iodide Perovskite, *Small*, 2024, 20, 2403685.

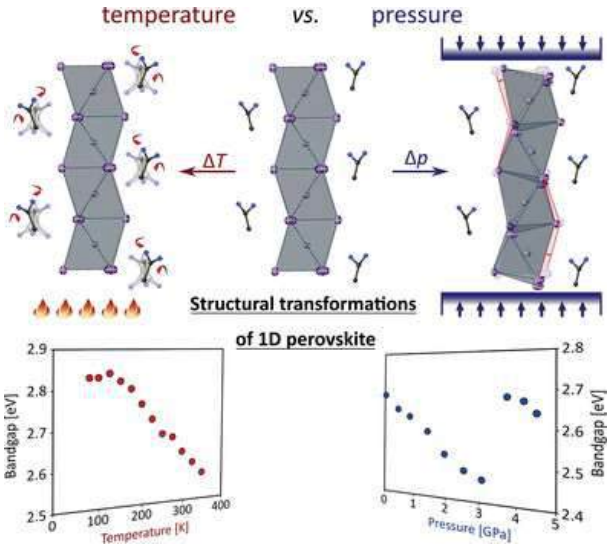

2. Bogdanowicz, K. A., Lalik, S., **Ratajczyk, P.**, Katrusiak, A., Krysiak, P., Pawłowska, A. I., Marzec, M., Iwan, A., A new look at imines and their mixture with PC71BM for organic, flexible photovoltaics, *Sci. Rep.,* 2023, 13, 13240.

3. Szczepaniak, G., Jeong, J., Kapil, K., Dadashi-Silab, S., Yerneni, S. S., **Ratajczyk, P.**, Lathwal, S., Schild, D.J., Das, S. R., Matyjaszewski, K., Open-air green-light-driven ATRP enabled by dual photoredox/copper catalysis. *Chem. Sci.*, 2022, 13, 11540-11550.

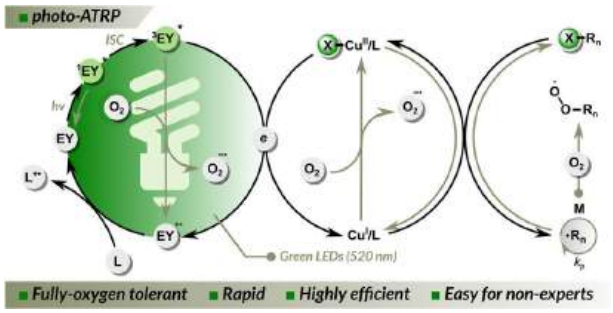

4. Mączka, M., Sobczak, S., **Ratajczyk, P.**, Leite, F. F., Paraguassu, W., Dybała, F., Herman, A. P., Kudrawiec, R., Katrusiak, A., Pressure-Driven Phase Transition in Two-Dimensional Perovskite MHy_2PbBr_4. *Chem. Mater.*, 2022, 34, 17, 7867−7877.

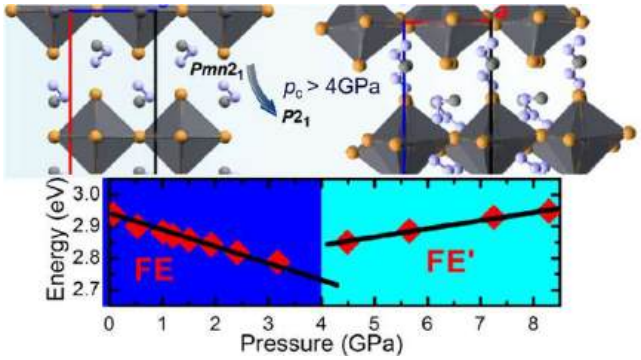

5. Sobczak, S., **Ratajczyk, P.**, Katrusiak, A., Squeezing out the catalysts: the sustainable approach to disulfide bond exchange in aryl disulfides. *ACS Sustain. Chem. Eng.*, 2021, 9, 7171−7178.

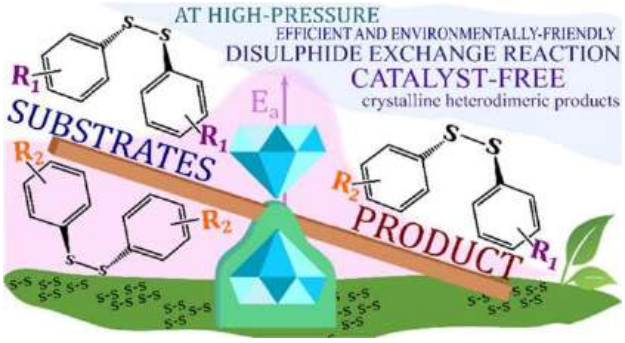

6. Sobczak, S., **Ratajczyk, P.**, Katrusiak, A., High-pressure nucleation of low-density polymorphs. *Chem. Eur. J.*, 2021, 27, 7069-7073.

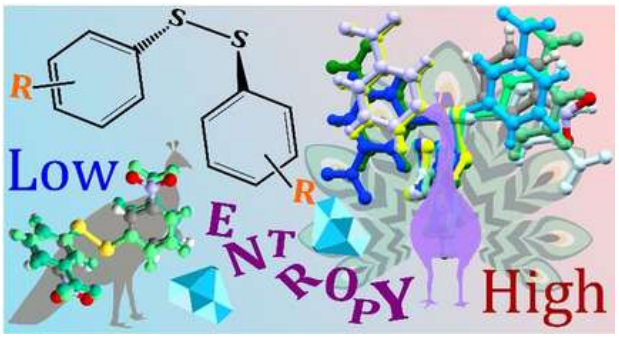

7. Sobczak, S., Półrolniczak, A., **Ratajczyk, P.**, Cai, W., Gładysiak, A., Nikolayenko, V. I., Castell, D., Barbour, L., Katrusiak, A., Large Negative Linear Compressibility of a Porous Molecular Co-Crystal. *Chem. Commun.*, 2020, 56, 4324-4327.

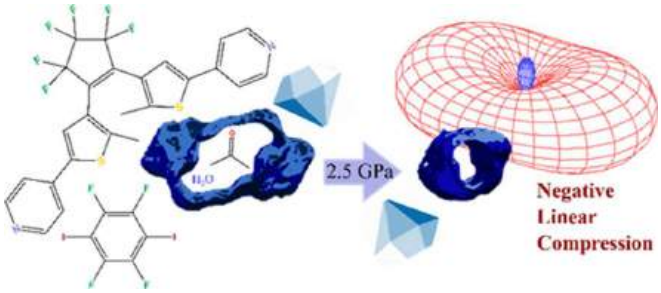

8. **Ratajczyk P.**, Sobczak S., Katrusiak A., High-Pressure Structure and Properties of *N,N*-Dimethylformamide (DMF). *Cryst. Growth Des.*, 2018, 19, 896–901.

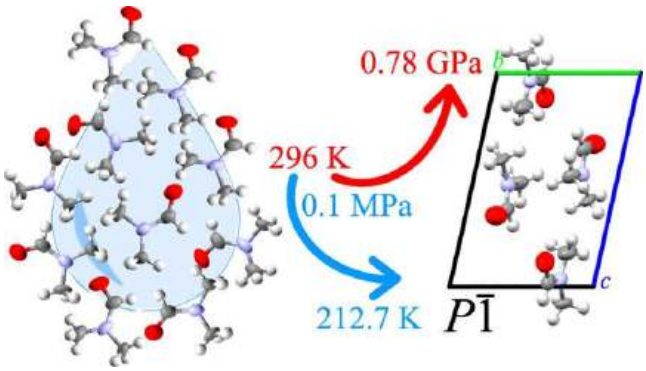

Conferences

1. **P. Ratajczyk**, S. Sobczak, M. Andrzejewski, P. Woźny, L. Maini, A. Katrusiak, *Pressure-induced structural changes and their impact on the properties of alkyl-substituted perylene diimides,* 35th European Crystallographic Meeting, 25–29.08.2025 Poznań, Poland (poster)
2. **P. Ratajczyk**, S. Sobczak, M. Andrzejewski, M. Marchini, F. Marin, L. Maini, A. Katrusiak, *Pressure- and temperature-driven polymorphism in PDI-C6*, 34th European Crystallographic Meeting, 26–30.08.2024 Padua, Italy (poster)
3. **P. Ratajczyk**, S. Sobczak, T. Poręba, A. Katrusiak, *Access to new properties of perylene diimide derivative through extreme conditions*, 26th Congress and General

Assembly of the International Union of Crystallography, 22–29.08.2023 Melbourne, Australia (poster)

4. **P. Ratajczyk**, S. Sobczak, P. Woźny, A. Wcisło, T. Poręba, A. Katrusiak, *Revealing the structure-property relationship of phenyl-substituted perylene diimide derivative (PTCDI-Ph) under extreme conditions*, 64 Konwersatorium Krystalograficzne, 5–7.07.2023 Wrocław, Poland (poster)
5. **P. Ratajczyk**, S. Sobczak, A. Katrusiak, *Pressure-induced disulfides exchange reactions with catalyst elimination*, ACS Fall 2022, 21–25.08.2022 Chicago, USA (poster)
6. **P. Ratajczyk**, S. Sobczak, A. Katrusiak, *High-Entropy Nucleation for Low-Density Polymorphs*, 14th Frolic Goats Workshop on High-Pressure Diffraction, 19–20.04.2021 online (oral presentation)
7. **P. Ratajczyk**, S. Sobczak, A. Półrolniczak, A. Katrusiak, *Large negative linear compressibility of a porous co-crystal of 1,2-bis[2-methyl-5-(pyridyl)-3thienyl] cyclopentene with 1,4-diiodotetrafluorobenzene*, 13th Frolic Goats Workshop on High-Pressure Diffraction, 04–05.05.2020 online (oral presentation)
8. **P. Ratajczyk**, S. Sobczak, A. Katrusiak, *Pressure-induced disulfide metathesis reactions*, Joint Polish-German Crystallographic Meeting 2020, 24–27.02.2020 Wrocław, Poland (poster)
9. **P. Ratajczyk**, S. Sobczak, A. Katrusiak, *Spektrometria masowa metodą identyfikacji produktów reakcji wysokociśnieniowych*, 62 Polish Chemical Society Meeting, 02–06.09.2019 Warsaw, Poland (oral presentation)
10. **P. Ratajczyk**, S. Sobczak, A. Katrusiak, *Mass spectrometry as a simple method for identification products of high-pressure reactions*, 12th Frolic Goats Workshop on High-Pressure Diffraction, 14–16.04.2019 Poznań, Poland (poster)
11. **P. Ratajczyk**, S. Sobczak, A. Katrusiak, *Wysokociśnieniowa i niskotemperaturowa struktura dimetyloformamidu (DMF)*, X Poznań Scientific Conference: Chemistry - Science and Industry, 30.11.2018, Poznań, Poland (oral presentation)
12. **P. Ratajczyk**, S. Sobczak, A. Katrusiak, *Wysokociśnieniowa i Niskotemperaturowa Struktura Dimetyloformamidu (DMF)*, 60th Polish Crystallographic Meeting, 27–29.06.2018 Wrocław, Poland (poster)

13. **P. Ratajczyk**, S. Sobczak, A. Katrusiak, *Struktura Wysokociśnieniowa Dimetyloformamidu*, 59th Polish Crystallographic Meeting, 28–30.06.2017 Wroclaw, Poland (poster)

Scientific internships

- **01.07–30.09.2022** Internship in Prof. Matyjaszewski's group at Carnegie Mellon University in Pittsburgh, USA, financed by the Kosciuszko Foundation
- **05.09–02.10.2021** ESRF/ILL International Student Summer Programme on X-Ray and Neutron Science, Matters at Extremes group, European Synchrotron Radiation Facility, Grenoble, France

Research projects

- **11.2020–10.2024** Principal investigator, Polish Ministry of Education and Science grant: DIAMENTOWY GRANT (No. 0160/DIA/2020/49) *W poszukiwaniu wydajniejszych organicznych materiałów fotowoltaicznych - od modyfikacji chemicznych po wpływ warunków ekstremalnych* (219 863 PLN)

Prizes and Awards

- **01.2025** Dr Jan Kulczyk Scholarship Award
- **02.2024** Marshal of the Wielkopolska Region Award "Wielkopolska for Planet 2030"
- **11.2022** AMU Foundation scholarship for Ph.D. students for the 2022/2023 academic year
- **04.2022** Kosciuszko Foundation award in Exchange Program to the United States
- **02.2021** Prize of the Minister of Education and Science for outstanding academic achievement
- **12. 2019** Prize of the Minister of Science and Higher Education for outstanding academic achievement

9. Scientific articles included in this dissertation

Article A1

Unlocking the sensing potential of phenyl-substituted perylene diimides under extreme conditions

Paulina Ratajczyk, Szymon Sobczak, Przemysław Woźny, Angelika Wcisło, Tomasz Poręba, Andrzej Katrusiak

Journal of Materials Chemistry C, 2023, 11, 11055-11065, DOI: 10.1039/D3TC01146A

Journal of Materials Chemistry C

ROYAL SOCIETY OF CHEMISTRY

PAPER

View Article Online
View Journal | View Issue

Check for updates

Cite this: J. Mater. Chem. C, 2023, 11, 11055

Unlocking the sensing potential of phenyl-substituted perylene diimides under extreme conditions†

Paulina Ratajczyk, [a] Szymon Sobczak, *[a] Przemysław Woźny, [a] Angelika Wcisło, [a] Tomasz Poręba [b] and Andrzej Katrusiak *[a]

Received 31st March 2023,
Accepted 5th June 2023

DOI: 10.1039/d3tc01146a

rsc.li/materials-c

Phenyl-substituted perylene diimide (PTCDI-Ph) derivatives are prospective organic, electronic and optoelectronic materials. In this study, the effects of modified intermolecular interactions and molecular conformations on the energy gap and the optical properties of PTCDI-Ph were explored at high pressure and various temperatures by calorimetry, X-ray diffraction, UV-vis absorption, and photoluminescence spectroscopy. Below 498 K, PTCDI-Ph transforms from phase I to phase II, which is stable down to 93 K at least. Above 3.0 GPa, phase II transforms into phase III. The compressed intermolecular distance between perylene cores linearly narrows the band gap, due to the intensified π–π stacking. The negative linear compressibility of the crystal along [100] coincides with the negative thermal expansion in this direction. Owing to the strong pressure and temperature dependence of the luminescence spectrum, the PTCDI-Ph derivatives constitute a promising class of highly stimuli-responsive elastic organic materials with broad potential for tailoring their optoelectronic properties through physical and chemical modifications.

Introduction

Owing to their low cost, low molecular weight, high electron mobility, and excellent chemical and thermal stability, perylene-3,4,9,10-tetracarboxylic acid diimide derivatives, often referred to as perylene diimides (PDIs), are intensely studied for use in electronic devices, such as organic field-effect transistors (OFETs),[1–5] organic light-emitting diodes (OLEDs),[6,7] organic photovoltaics (OPVs),[8–11] and dye-sensitized solar cells (DSSCs).[12,13] An important advantage of PDIs over traditional photovoltaic materials is the possibility of modifying their physical, optical, electronic, and aggregation properties by chemical functionalization at the *imide*, *ortho*, and *bay* core positions (Fig. S1 in the ESI†).[13] The introduction of different substituents at the *imide* position strongly affects the solubility and aggregation of PDIs, but less so for their absorption and emission. Modification of HOMO and LUMO orbital energy levels, and thus the band gap energy, plays a crucial role in determining the power-conversion efficiency (PCE) of PDIs, and can be achieved by introducing an electron-donating substituent at the *bay* core position. Different electron-donor or -acceptor groups at the *bay* positions of the perylene core were shown to modulate the electronic and optical properties.[14] Halogen substituents improve their solubility, facilitating PDI processing and making them suitable for solar-cell applications. For example, 1,(6)7-dibromo-*N*,*N*′-diacetyl PDI is well soluble in organic solvents, while its analogue without Br is not.[15] The solubility of PDIs in halogenated solvents, commonly used to prepare the active layer in bulk-heterojunction (BHJ) solar cells,[16] can be improved by introducing long alkyl or aryl substituents at the *imide* and *bay* core positions,[9] while the incorporation of the hydrophilic moieties at the *imide* positions yields water-soluble PDIs.[17,18] The π–π stacking of the perylene cores (Fig. 1), which governs the crystal packing and electron mobility, can also be altered by introducing appropriate steric hindrance between the bulky substituents.[9] All these factors can be employed to design the PDI structure, optimized for its physical, chemical, and optoelectronic properties, which are necessary to maximize the high PCE.

A significant challenge in the development of novel organic semiconductors is their polymorphism, illustrating the effect of aggregation and interactions on the properties of compounds; hence the recent research in the field of perylenediimide-based organic semiconductors (PDIs-OSCs) has explored the mechanisms of molecular aggregation not only in terms of chemical derivatives,[4,19–21] but also by temperature changes.[22,23] It is well known that mechanical impact on soft organic materials, particularly in the form of thin films, can strain the PDI-OSC

[a] Faculty of Chemistry, Adam Mickiewicz University, Universytetu Poznańskiego 8, 61-614 Poznań, Poland. E-mail: szymon.sobczak@amu.edu.pl, katran@amu.edu.pl
[b] European Synchrotron Radiation Facility, 71 Avenue des Martyrs, 38000 Grenoble, France

† Electronic supplementary information (ESI) available. CCDC 2253183–2253201. For ESI and crystallographic data in CIF or other electronic format see DOI: https://doi.org/10.1039/d3tc01146a

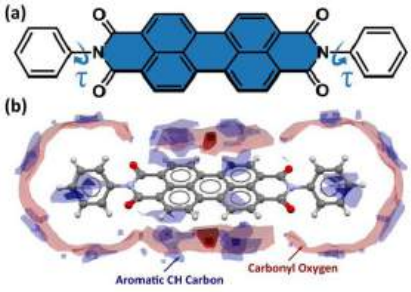

Fig. 1 Molecular structure of *N,N′*-diphenyl-3,4,9,10-perylenedicarboximide (PTCDI-Ph) (a) with the perylene core coloured in blue and with an indicated soft C11–N1–C13–C18 torsion angle (τ); and (b) the closest interaction map indicating the strongest intermolecular interactions types formed at 0.1 MPa/296 K.

structure and affect its quantum efficiency. The associated structural changes (molecular conformation, π–π stacking, *etc.*) can distort the n-type semiconducting properties. Thus, the understanding of structure–property relationships is vital for developing next-generation electronic devices.

In recent years, techniques employing high-pressure and various temperatures have been successfully used to investigate and model strain-induced changes in inorganic and hybrid perovskites.[24–26] However, organic photovoltaic materials were only sporadically studied under extreme conditions.[27–29] To the best of our knowledge, few studies have focused on specific aspects of semiconducting perylene diimide derivatives, such as their structural or optical response to pressure and temperature changes.[22,23,30,31] These scarce comprehensive studies significantly increased the understanding of the structure–property relationships as a function of temperature and pressure. In our present study, we employed the varying-temperature and high-pressure synchrotron and in-lab X-ray diffraction techniques, alongside differential scanning calorimetry (DSC), UV-vis absorption, and photoluminescence (PL) spectroscopy to explore the effects of structural deformations under external stimuli on the opto-electronic properties of a chemically and thermally stable phenyl-substituted PDI derivative, *N,N′*-diphenyl-3,4,9,10-perylenedicarboximide (PTCDI-Ph). In light of our results, PTCDI-Ph is a promising material for highly efficient organic electronic and optoelectronic devices.[32–34]

Results and discussion

Under room conditions (296 K/0.1 MPa), PTCDI-Ph crystallizes in monoclinic phase II, space group $P2_1/c$, with the molecule located on the inversion centre ($Z' = 0.5$). The perylene-diimide skeleton of PTCDI-Ph is flat, but the terminal phenyl rings are rotated off the plane by 58.5°: this rotation is measured by the torsion angle C11–N1–C13–C18, denoted τ (Fig. 1a). The rotation of phenyl substituents is crucial for π-electron coupling in the alternative systems of conjugated bonds. Several examples in the literature demonstrate that flattening of conjugated systems increases π-electron coupling, whereas the off-plane rotations of substituents hamper the electron mobility.[35–37] Furthermore, the τ angle reflects the intermolecular interactions within the structure, specifically the stacking distance ($d_{\pi-\pi}$) and stacking displacements (α_{agg} and β_{agg}), which are key factors for the charge-transfer characteristics. In phase II, the PTCDI-Ph molecules are π–stacked into columns along the crystal [010] direction, as shown in Fig. 2 (*cf.* S3 in the ESI†). Hydrogen bonds CH···O dominate the interactions between the neighbouring columns (Fig. 2). This type of aggregation stabilizes the structure of phase II in a remarkable temperature range from 490 K down to 93 K at least,[38] as well as at a high pressure to 2.85 GPa (Fig. 3). We have corroborated different

Szymon Sobczak

Dr. Szymon Sobczak, an adjunct at Adam Mickiewicz University, devotes his efforts to understanding pressure-induced transformations across a range of materials, from molecular crystals to MOFs and perovskites. His current research centers on the correlation between structural deformations and changes in physicochemical properties of materials, highlighting the significant role of pressure and varied-temperature conditions. His contributions to the field are marked by innovative approaches, such as developing a sustainable method for disulfide exchange replacing the conventional catalyst with pressure, and protocol for obtaining kinetic polymorphs recoverable at ambient conditions. His investigations of the mechanical behavior of coordination polymers provides a new dimension to the design of flexible and transformable frameworks.

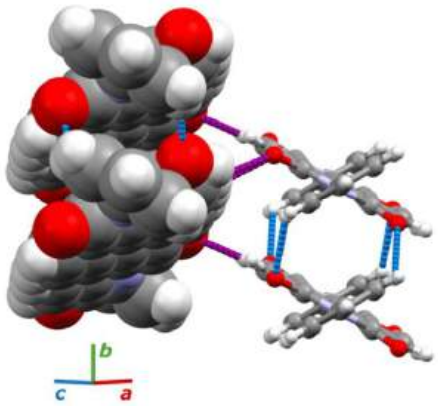

Fig. 2 Aggregation of molecules in PTCDI-Ph phase II: one column is drawn in the space-filling style and the other as balls-and-sticks. The CH···O contacts between π-stacked molecules are blue and those between adjacent columns are purple.

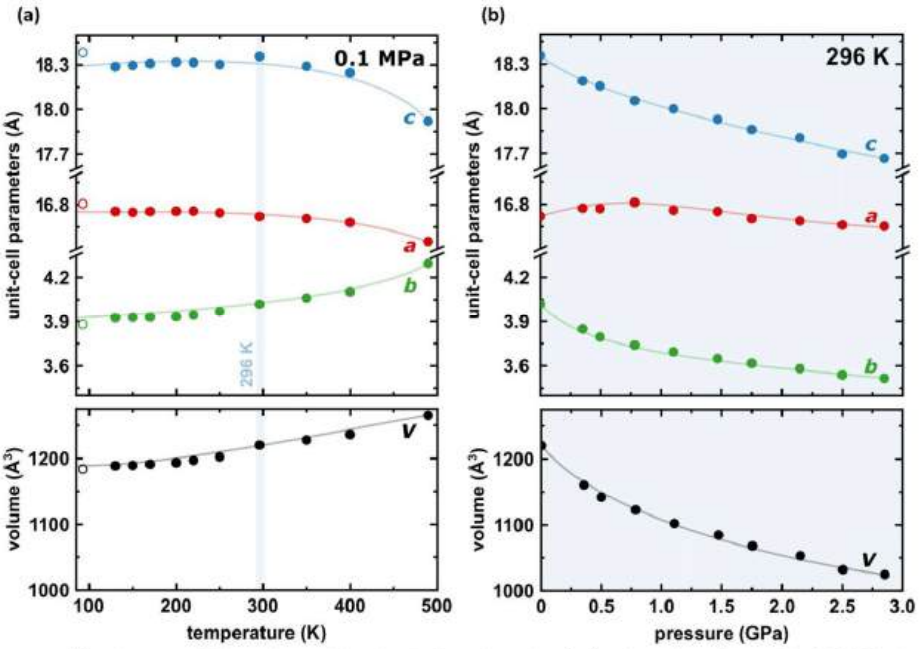

Fig. 3 Temperature (a) and pressure (b) dependence of the unit-cell dimensions *a*, *b*, *c* (top) and its volume (bottom) for PTCDI-Ph phase II. Open symbols mark the data previously reported by Sato and Mizuguchi.[38] The estimated standard deviations (ESDs) are smaller than plotted symbols. The blue highlight indicate the data measured at 296 K. The changes in monoclinic angle β are shown in Fig. S5 in the ESI.†

structural and physicochemical properties within its phase-stability region using various techniques, including the effects of temperature (490 K to 130 K), and high-pressure probed by in-house and synchrotron X-ray diffraction (up to 3.55 GPa), differential scanning calorimetry (from 200 to 573 K), photoluminescence (293 to 573 K and up to 6.44 GPa), and UV-vis spectra (up to 4.99 GPa). The results are presented in the following paragraphs.

Thermal expansion

The result of our systematic study on the temperature dependence of PTCDI-Ph is consistent with the previously reported single-point structure determination at 93 K/0.1 MPa.[38] Notably, the PTCDI-Ph phase II crystals exhibit unusual changes in the sign of thermal expansion upon cooling: above room temperature, the crystal shrinks in directions [100] and [001], and the expected elongation with an increase in temperature is observed only along direction [010], as shown in Fig. 3. However, the thermal expansion is strongly non-linear, and below room temperature, the linear thermal expansions become positive in all directions (Fig. S7a, ESI†). The observed changes in the thermal expansion of the crystal can be connected with its strongly anisotropic structure. The CH···O contacts; CH2···O1 and CH3···O1 (Fig. S2 in the ESI†), on the H-donor site formed in the plane of the perylene–imide skeleton with adjacent molecules, effectively support the structure perpendicular to direction [010] (Fig. 2). At low temperatures, the *N*-substituted phenyl group rotates to a lower τ angle from $\tau = 58.5(7)^\circ$ at 296 K to $55.7(3)^\circ$ at 93 K (Fig. 4a), which coincides with the negative thermal expansion along direction [100]: from 130 to 296 K, the lattice parameter *a* shrinks by −0.035 Å (*cf.* Table S1, ESI†). The packing of PTCDI-Ph phase II correlates with the phenyl position, the most non-planar molecular fragment (Fig. 4a), and in fact, the calculated intermolecular potentials[39,40] indicate a reduction in total packing energy from −294 kJ mol^{-1} at 296 K/0.1 MPa to −295.5 kJ mol^{-1} at 130 K. This modifies the PTCDI-Ph optoelectronic properties, as described by Kasha's theory,[41–43] further extended by Spano explicitly for PDI dimers.[23] The main contribution to the cohesion forces comes from the π–π stacking (−170 kJ mol^{-1} at 296 K/0.1 MPa) and H-bonds (about 10% for the carbonyl O1 atom and 5% for the O2 of the total energy). Thus hydrogen bonds CH···O account for over 15% of the crystal cohesion forces (*cf.* Fig. S4, ESI†).

According to Kasha,[42] a blue-shifted absorption maximum and suppressed radiative decay rate occur for molecular dimers stacked face-to-face or in a card-pack arrangement, while those stacked head-to-tail exhibit a red-shifted absorption maximum and enhanced radiative decay rate. These dimers are known as H-aggregates and J-aggregates, respectively. The arrangements of the interacting molecules in the linear chain can be differentiated by the packing angle describing the shift between molecules, and thus for the H-aggregates α_{agg} approximates 90° and for J-aggregates $\alpha_{agg} = 0^\circ$.[44] However, in certain packing

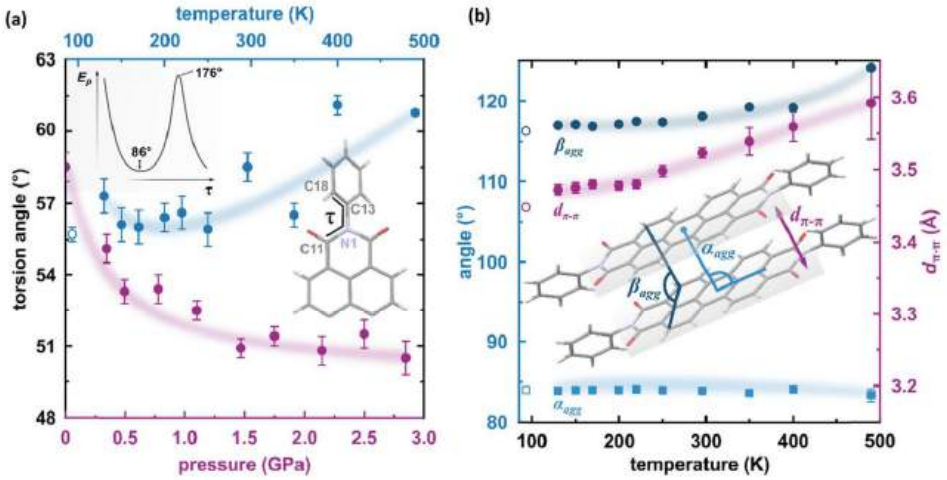

Fig. 4 (a) Change of the torsion angle τ (C11–N1–C13–C18) as a function of temperature (blue symbols), and pressure (purple symbols) in the PTCDI-Ph molecule. An open symbol refers to the previously reported structure by Sato and Mizuguchi.[31] Inset: Potential energy of the isolated PTCDI-Ph molecule with rotation around one torsion angle (another τ was fixed at 55.92° as derived from the X-ray measurement). (b) Packing arrangements in PTCDI-Ph phase II at varying temperatures: purple circles mark the distance between π-stacked molecules ($d_{\pi-\pi}$) and blue symbols represent the packing angles (α_{agg} and β_{agg}). The α_{agg} denotes the angle formed by the imide N-atom, perylene core centroid, and the centroid of the closest molecule from the same stack, and the β_{agg} is the angle between two C-atoms (C3 and C9) of one perylene core and a carbon atom (C9) of the neighbouring molecule.

arrangements, such as in π-stacks, the distance between the rigid backbone of the molecules is close enough (when $d_{\pi-\pi} < 3.5$ Å) to allow for significant wave-function overlap and the emergence of short-range interactions.[45] In such stacks, the exciton bandwidth and curvature at the band centre are determined by interference between short-range coupling, due to the wave-function overlap and long-range Coulomb coupling arising from transition dipole–dipole interactions.[23,44] This, sometimes unfavoured interference, can result in an unusual situation where the chromophore aggregate displays monomer-like properties (null aggregates).[23,44] This situation was described as a characteristic of PDIs, where the positive long-range coupling may induce H-aggregate behaviour, whereas counteracting short-range coupling can induce J-aggregate behaviour, combining into so-called HJ-aggregate properties.[23]

To correlate the changes in the optoelectronic properties of PTCDI-Ph with the inclination from an ideal π-stack in our solid-state structures, we adopted the descriptors α_{agg} and β_{agg} analogous to the pitch and roll angles developed by Curtis *et al.* (*cf.* Tables S6 and S7 in the ESI†).[46] The α_{agg} inclination translates adjacent stacked molecules relative to one another in the direction of the long molecular axis while β_{agg} inclination translates the molecules along the short molecular axis (Fig. 4b). Our analysis of the temperature-induced changes in the aggregation of PTCDI-Ph molecules revealed that below room temperature (296 K), the π-stacking geometry is hardly affected: α_{agg} increases by 0.09°, while β_{agg} decreases by 1.57° in the 296–93 K range; the distance between molecules decreases quite significantly, from 3.523(7) Å at 296 K to 3.448(2) Å at 93 K. According to our calculations, this process is connected to the phenyl rotation, influencing the potential energy, E_p (Fig. 4a and Fig. S10, ESI†).

Above 300 K, adjacent π-stacked molecules significantly shift as the thermal motions build up progressively. This process is clearly visible as the elongation of the unit-cell direction *b*, directly related to the stacking distance. Although the expansion of the unit-cell increases above 350 K, the intermolecular CH···O distances hardly change, confirming their important role in the stability of phase II (Fig. S2, ESI†). The thermally-induced strain is compensated by the rotation of the terminal phenyl ring towards the lower-energy conformation (Fig. 4a and Fig. S10, ESI†). This conformational alteration elongates the $d_{\pi-\pi}$ distance, which at 490 K is 3.59(5) Å. Simultaneously, α_{agg} decreases while β_{agg} increases, which may be interpreted as the packing adjustment towards the J-aggregate.

The considerable interest in developing materials with tunable luminescence susceptible to physical parameter changes, such as temperature and pressure,[47–51] inspired us to measure the photoluminescence of PTCDI-Ph crystals subjected to varying thermodynamic conditions. The PL spectrum of PTCDI-Ph in phase II consists of two distinguishable emission bands: an intense band A at $\lambda \approx 680$ nm and a lower intensity band B at $\lambda \approx 737$ nm (Fig. 5). When the system is heated, the overall luminescence intensity of both bands decreases by 53% (at 473 K), but the relative intensity of band B compared to A evolves monotonically.[52] This observation is consistent with the previous investigation by Spano *et al.*[23] Above 350 K, the emission band starts to broaden and at 490 K, its full width at half maximum (FWHM) doubles, compared to the room temperature. Above this point, the discontinuous change in the PL spectrum shape marks a phase transition to high-temperature

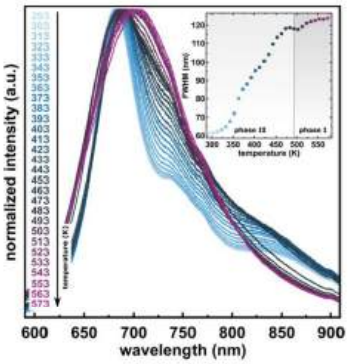

Fig. 5 Normalized emission spectra of the PTCDI-Ph heating cycle up to 573 K after excitation at λ = 411 nm. Inset: Changes of the full-width at half maximum (FWHM) upon phase transition at high temperature.

phase I. This phase transformation, additionally confirmed by our powder diffraction data (Fig. 12), is reversible upon cooling. The absence of hysteresis and the DSC peak shape (Fig. 6) indicate a second-order character of this phase transition.

As the temperature continues to increase up to 523 K, the emission intensities of overlapped bands with a maximum at $\lambda \approx 692$ nm increase, which can be linked to the change from an oblique head-to-tail structure to the head-to-tail card-pack aggregation, which involves a change in the π–π intermolecular stacking. In phase I at 523 K, thermal quenching is observed again and continues up to 573 K. The hypsochromic shift of the emission bands at higher temperatures confirms intensified head-to-tail stacking in phase I.[53]

The observed changes in luminescence, such as the increased emission intensity and the generation of one broad-band, may be attributed to the changes in the excited energy levels and the occurrence of phosphorescence ($T \rightarrow S_0$) at the expense of fluorescence ($S_1 \rightarrow S_0$) due to the altered packing and defects appearing when the crystal transforms to phase I.[53]

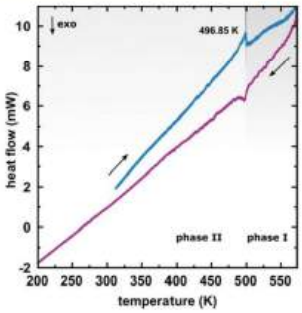

Fig. 6 Differential scanning calorimetry (DSC) thermogram of PTCDI-Ph in the heating and cooling cycles.

High-pressure behaviour

The X-ray diffraction data collected up to 3.55 GPa at room temperature (Table 2) show that phase II can be compressed to about 2.85 GPa without any signs of phase transition. However, the measurement at 3.20 GPa revealed a symmetry change: the unit-cell angles α and γ deviate from 90°, indicating a transition to the triclinic system (phase III). Due to this symmetry reduction, single crystals were twinned and broken, which hampered the structural analysis above 2.85 GPa and allowed only for the collection of the powder diffraction pattern of phase III (Fig. 11).

The molecular volume of a PTCDI-Ph crystal compressed to 2.85 GPa decreases by about −16% (the compressibility and Birch–Murnaghan coefficients are provided in the ESI†). Over this pressure range, the unit-cell parameters are compressed: a by −0.4%, b by −12.5% and c by −3.8% (Fig. 3b). The strongest compressibility in the [010] direction correlates with a decrease in the distance between weakly-bonded π-stacked perylene cores. The $d_{\pi-\pi}$ distance changes from 3.523(7) Å at 0.1 MPa to 3.183(3) Å at 2.85 GPa. Interestingly, below 0.78 GPa, the crystal exhibits negative linear compressibility (NLC) along [100]. Negative compressibility is an unusual elastic response when the crystal becomes longer in one direction, despite increased hydrostatic pressure.[54–56] In PTCDI-Ph, NLC exists only up to 0.78 GPa, above which it reverses to the positive linear compressibility along the [100] direction. This phenomenon can be rationalized by the presence of a wine-rack motif of CH···O bonded PTCDI-Ph molecules.[55,56] Such a mechanism arises from the soft CH9···O2 bond formed between stacked molecules, parallel to the [010] direction, and the much stronger CH2···O1 bond, linking the molecules from adjacent columns. Furthermore, compression reduces the τ angle to 50.5° at 2.85 GPa, as the PTCDI-Ph molecule becomes flatter (Fig. 4a). The PTCDI-Ph molecules tied by the intramolecular interactions are forced to reduce the $d_{\pi-\pi}$ distance (Fig. 7). Also, the H-aggregating properties are enhanced when the material is compressed as α_{agg} increases to 86° at 2.85 GPa. Such structural changes are mirrored in the absorption-band shifts observed at high pressure. By measuring the UV-vis spectra of the PTCDI-Ph crystals compressed in the DAC chamber, we determined the pressure dependence of the absorption edge (Fig. 8a). At 0.03 GPa the absorption edge of PTCDI-Ph at about 629 nm corresponds to the energy band gap of around 1.97 eV, which is comparable with the results reported by Ichikawa and co-workers.[57] Up to 4.99 GPa, a strong bathochromic shift is approximately 33 nm GPa^{-1} in the 630–793 nm range. As the pressure increases, the crystal visibly changes its colour from red to black (Fig. 8b). This change is fully reversible, and after reducing the pressure, the original colour returns. The determined optical energy gap (E_g), plotted as a function of pressure in Fig. 8b, shows that the bandgap narrows linearly, from 1.97 eV at 0.03 GPa to 1.56 eV at 4.99 GPa. After releasing pressure, the absorption-edge values are very close to the initial ones. Importantly, we do not observe significant changes in the absorption-edge shift above the phase transition; the bandgap continues to narrow linearly.

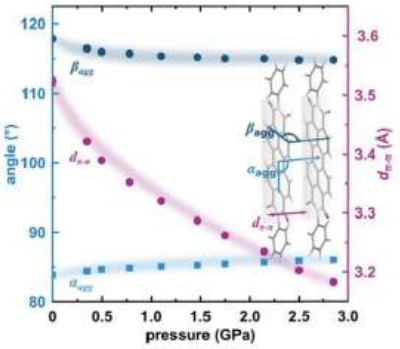

Fig. 7 Changes in the packing of PTCDI-Ph phase II under compression (b): purple circles mark the distance between π-stacked molecules ($d_{\pi-\pi}$) and blue symbols represent the packing angles α_{agg} and β_{agg} (*c.f.* Fig. 4).

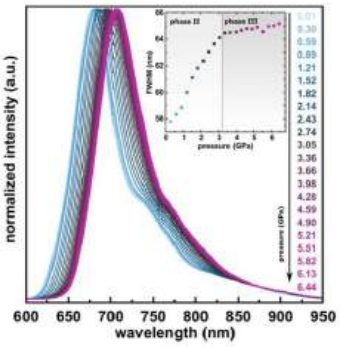

Fig. 9 Normalized emission spectra of PTCDI-Ph in the compression cycle up to 6.44 GPa after excitation at λ = 410 nm. Inset: Changes in the full-width at half maximum (FWHM) of the band.

The photoluminescence properties of PTCDI-Ph crystals at high pressure were investigated using excitation at λ = 411 nm, which correlates with the broad absorption band at 400–600 nm (Fig. 9). The resulting emission spectra show a broad band in the range of 600–950 nm with the peak maximum at $\lambda \approx$ 679 nm (band A) and at $\lambda \approx$ 750 nm (band B), with a total FWHM of approximately 57.44 nm at 0.01 GPa. A gradual bathochromic shift of the PTCDI-Ph emission band was observed during the compression cycle. The band centroid of PTCDI-Ph phase II bands A and B shifts almost linearly with a rate of 6.26 nm GPa^{-1} up to 3 GPa (Fig. S8a in the ESI†). However, above the transition from phase II to phase III, the bathochromic shift drastically decreases and above 3.2 GPa, bands A and B change with a rate of 2.09 nm GPa^{-1}. Within phase III the bandwidth further broadens with a rate of 0.20 nm GPa^{-1}, to 65.17 nm at 6.5 GPa, compared to the maximum FWHM value of 64.11 nm in phase II just before the transition.

Pressure and temperature sensing

The astonishing optoelectronic properties and excellent chemical and thermal stability are the prerequisites desired for the potential application of PTCDI-Ph as an extreme condition sensor (*cf.* Experimental section). To investigate the sensing performance of PTCDI-Ph, we have calculated the absolute sensitivity (S_a) parameter separately for high pressure up to 6.44 GPa (Fig. 10a) and for high temperature up to 450 K (Fig. 10a). We fitted the experimentally assigned shift of the band A centroid (MP) as a function of the stimuli (E) using empirical polynomial functions (*cf.* Fig. S8 and S9 in the ESI†) and calculated the sensitivity

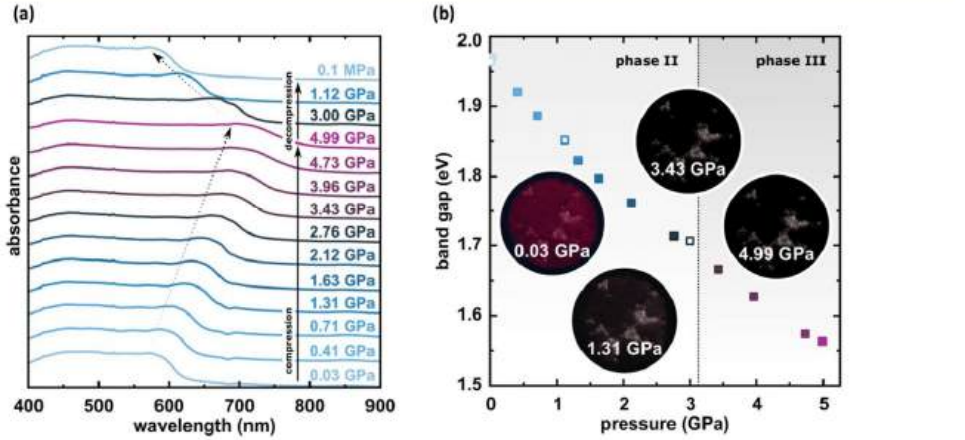

Fig. 8 Pressure evolution of the (a) absorption spectra and (b) optical band gap; closed and open symbols correspond to the compression and decompression runs, respectively. The inserted photos show the PTCDI-Ph film prepared for measurements of UV-vis spectra at 0.03, 1.31, 3.43 and 4.99 GPa, showing the darkening of the sample as the pressure increases.

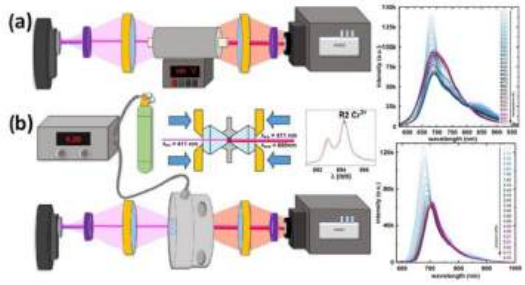

Fig. 10 Schematic drawings of experimental setups with PTCDI-Ph crystals applied as (a) high-temperature and (b) high-pressure sensors. The accompanying plots illustrate the shifts in the respective luminescence spectra (cf. Fig. 5 and 9).

response to external stimuli using the following equation:

$$S_a = \frac{\partial MP}{\partial E},$$

for which we found a high degree of correlation in both ranges: for high pressure $R^2 > 0.99$ and for elevated temperatures $R^2 > 0.98$.

Up to this point, the most extensively investigated group for high potential as temperature and pressure sensors were inorganic materials containing rare earth ions.[58–67] However, due to the high cost of rare-earth elements, other less expensive, safe, and stable carbon-based alternatives that can act as high-performance contactless sensors are intensively sought. For comparison, the S_a values obtained for PTCDI-Ph are considerably higher than those reported for other luminescence-based temperature sensors in the literature (Table 1 and Table S8 in the ESI†). PTCDI-Ph exhibits a remarkable sensitivity to temperature up to 370 K, where the S_a parameter reaches 0.068 nm K^{-1}. Above this temperature, the sensitivity gradually decreases, through the values of 0.065, 0.055, and 0.045 nm K^{-1} observed for 380, 400, and 420 K, respectively. While there is a limited number of reports[68] on contactless thermometers based on the band shift at varying temperatures, our study highlights the broad operating temperature range of PTCDI-Ph (up to 450 K), low-temperature quenching, high signal stability, and its satisfactory sensitivity and repeatability.

Table 1 Comparison of the most sensitive shift-based sensors under extreme conditions of temperature (nm K^{-1}) and pressure (nm GPa^{-1})

Host/emitting ion	Sensitivity line shift, S_a		Ref.
	nm K^{-1}	nm GPa^{-1}	
PTCDI-Ph	6.8×10^{-2}	8.33	This work
YVO_4/Er^{3+}	5.16×10^{-3}	1.766	58
$SrFCl/Sm^{2+}$	2.36×10^{-3}	1.11	59
$BaLi_2Al_2Si_2N_6/Eu^{2+}$	—	1.58	60
Y_2SiO_5/Pr^{3+}	—	1.04	61
$Y_2Ge_{0.10}Si_{0.90}O_5/Pr^{3+}$	—	1.28	61
$YAlO_3/Cr^{3+}$	7.6×10^{-3}	0.70	62
$NaBiF_4/Er^{3+}$	—	0.8	63
Bi_2MoO_6/Er^{3+}, Tm^{3+}, Yb^{3+}	8.5×10^{-3}	—	64
SrB_4O_7/Eu^{2+}	4.8×10^{-4}	0.17	65
SrB_4O_7/Sm^{2+}	1×10^{-4}	0.255	69–71
YPO_4/Tm^{3+}	—	0.8	66
Al_2O_3/Cr^{3+}	6.2×10^{-3}	0.365	72

Similarly high performance was observed at high pressure, where the S_a parameter of PTCDI-Ph increases dramatically from ambient conditions, for which S_a = 1.34 nm GPa^{-1}, to 1.76 GPa where it reaches a maximum value of 8.33 nm GPa^{-1}. Within this range (up to 1.76 GPa), the sensing performance of PTCDI-Ph significantly exceeds most of the described inorganic sensors, for which the pressure sensitivity is not higher than 3 nm GPa^{-1}.[73,74] Although the structural changes related to the phase transition decrease above 3.2 GPa, the S_a value at 5.19 GPa (S_a = 1.88 nm GPa^{-1}) is still much higher than the sensitivity reported for most of the inorganic sensors. In the pressure range between 5.19 and 6.44 GPa, the high S_a value is restored, increasing to 5.43 nm GPa^{-1}.

The photoluminescence quantum yield (Φ) is a crucial factor in determining the performance of luminescent materials. We calculated the quantum yield using the following equation:

$$\Phi = \frac{I_S}{E_R - E_S} \times 100\%,$$

where Φ is the quantum yield, I_S is the integrated intensity of luminescence, and E_R and E_S are the intensities of LED excitation radiation scattered on the reference material (La_2O_3) and intensities of the excitation light scattered on the investigated sample, respectively. The difference in the scattered light between the reference and sample provides information on the number of photons absorbed by the material. Our calculations show that under ambient conditions, the value of Φ is 0.56%. The low value of the quantum yield can be attributed to the high absorption of the radiation and low probability of energy transfer to the emission center of the investigated material. Notably, the Φ value strictly depends on various factors, such as the functional substituents at atom N1, type of aggregation, solvents and concentration.[75–78] Despite the low Φ value, the application of PTCDI-Ph as a sensor material is advantageous owing to the large shift value and excellent sensitivity parameter for the investigated temperature and pressure conditions.

Conclusions

Our study shows that PTCDI-Ph is a highly stable n-type semiconductor with impressive phase stability, attributed to the strong π–π interactions between the perylene cores and CH···O bonds that further stabilize the crystal structure. Phase II is stable in a wide range of temperatures up to 490 K and compression up to 3.0 GPa. We also characterized two distinct phases above this range: phase I stable above 493 K, and phase III stable above 3.0 GPa. These findings provide new insights into the behaviour of PTCDI-Ph under extreme conditions, highlighting the potential of PTCDI-Ph as a stable optoelectronic stimuli-responsive organic luminophore, whose properties can be tailored through chemical modifications and physical stimuli. For the PTCDI-Ph phase II crystals subjected to the temperature and pressure stimuli, the observed energy gap and luminescence clearly show the importance of the π-stacking

distance, prevailing over other structural transformations. Consequently, the pitch-and-roll model[46] has been extended to the pitch–roll–squeeze model, which stresses the importance of intermolecular π–π and p–p orbital overlaps.[79]

Due to the specific pattern of the H-bonds between the π-stacked columns, the crystals of PTCDI-Ph exhibit the negative linear compressibility and negative thermal expansion, both in the same direction [100]. The high rigidity in the direction perpendicular to soft π-stacks sustains the non-radiative pathways upon application of external stimuli (high pressure/temperature). The significant structural changes impacting the molecular aggregation have been correlated with its luminescence as a function of temperature and pressure. The properties of PTCDI-Ph and its chemical inertness are ideal for multimodal-sensor applications. In particular, its sensitivity in the range of up to 1.76 GPa, where S_a = 1.34 nm GPa^{-1}, and temperatures up to 350 K, for which S_a is 0.068 nm K^{-1}, significantly outperforms those of most of the previously described inorganic sensors.

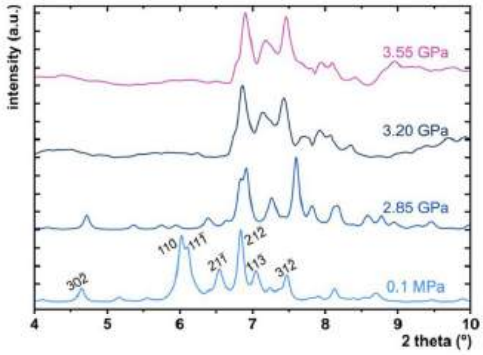

Fig. 11 PXRD collected for PTCDI-Ph phase II at 0.1 MPa, 2.85 and 3.20 GPa as well as phase III at 3.55 GPa. The measurements were performed using synchrotron X-ray diffraction (λ = 0.4099 Å). Patterns for 0.1 MPa and 2.85 GPa are the calculated diffractograms from single-crystal measurements.

Experimental methods

Materials

N,*N*′-Diphenyl-3,4,9,10-perylenedicarboximide of 98% purity was purchased from Merck and further purified by sublimation at 650 K in a sealed glass tube (*cf.* Section S1 in the ESI†). The attempts to recrystallize PTCDI-Ph in various solvents, including methanol, ethanol, chloroform, dimethylformamide (DMF), dimethyl sulfoxide (DMSO), hexane, ethyl acetate, and dichloromethane, using moderate heating (up to 100 °C) and stirring did not succeed due to insufficient dissolution.

High-pressure X-ray diffraction

High-pressure X-ray diffraction measurements were performed in a membrane-driven diamond-anvil cell (DAC). A single crystal of PTCDI-Ph together with a small ruby, used as a pressure calibrant,[80,81] were mounted inside a 0.3 mm hole in a steel gasket. The remaining volume was filled with a mixture of methanol:ethanol (4 : 1), used as the pressure-transmitting medium.[82] The single crystal of PTCDI-Ph was isothermally compressed up to 3.78 GPa. The in-situ high-pressure synchrotron X-ray diffraction data were measured at the ID15B beamline at the European Synchrotron Radiation Facility in Grenoble.[83] A monochromatic X-ray beam with a wavelength of 0.4099 Å was used, and a single ω-scan $\pm 32^\circ$ strategy was applied. Unfortunately, the phase transition between phases II and III led to the destruction and partial amorphization of the single crystal, and above 3.5 GPa we were able to collect only powder diffraction patterns (Fig. 11).

In this case, the collected diffraction images have been summed up using PyMCA, and subsequently integrated into powder diffraction patterns with Dioptas software. The CrysAlisPro software was used for data collection and reduction.[84] The crystal structures were solved and refined with SHELX software implemented in Olex2.[85,86] The crystallographic data and experimental details are summarized in Table 2 and Table S12 in the ESI† and have been deposited in CIF format in the Cambridge Crystallographic Database with numbers CCDC 2253183–2253192.† Structural illustrations were prepared using the program Mercury 2021.3.0.[87]

Varied-temperature X-ray diffraction

The low- and high-temperature single-crystal measurements were performed on SuperNova and Xcalibur diffractometers, respectively, with a microfocus source (CuKα = 1.54178 Å) and an Oxford CryojetHT (allowing for measurements in the range of 90–490 K). A series of six measurements for the cooled and three for the heated sample between 130 and 490 K were collected. The resulting data were then processed as described above for the high-pressure experiments. The final crystal data are summarized in Table 2 and Table S11 in the ESI† and have been deposited in the CCDC with numbers 2253193–2253201.† As the phase transformation between phases II and I occurs slightly above the capabilities of the Cryojet, we could only collect a powder diffractogram of phase I at 493 K (Fig. 12).

High-pressure optical absorption

The ultraviolet-visible (UV-vis) spectra of the solid-state PTCDI-Ph layer were recorded using a Merrill-Bassett diamond-anvil cell equipped with diamond IIA anvils. The diamond culets were 0.8 mm in diameter. The gasket was made of 0.1 mm thick tungsten foil with a sparked-eroded hole 0.45 mm in diameter. The PTCDI-Ph layer was prepared on the diamond culet: a small amount of the sample was strongly pressed by a thick glass plate until it smashed into a uniform layer. Daphne Oil 7575 was used as the pressure-transmitting medium. The UV-vis spectra of PTCDI-Ph at high pressure were recorded with a Jasco V-770 spectrophotometer adapted for use with a DAC. The absorbance was measured at a scan speed of 200 nm min^{-1} in the 400–900 nm range.

High-temperature and high-pressure photoluminescence

The photoluminescence properties (*i.e.*, emission spectra, PL) of the PTCDI-Ph powder were measured by exciting the samples

Table 2 Selected crystallographic data for PTCDI-Ph phase II as a function of temperature and pressure

	Unit cell					
p/T	a (Å)	b (Å)	c (Å)	β (°)	V (Å^3)	D_x (g cm^{-3})
0.1 MPa/130 K	16.755(5)	3.9243(13)	18.288(4)	98.69(2)	1188.7(6)	1.516
0.1 MPa/296 K	16.72(4)	4.0187(8)	18.355(3)	98.55(6)	1220(3)	1.477
0.1 MPa/490 K	16.52(3)	4.344(4)	17.92(4)	97.10(19)	1276(4)	1.411
0.35 GPa/296 K	16.773(19)	3.8482(6)	18.186(3)	98.64(6)	1160.5(14)	1.553
2.85 GPa/296 K	16.644(13)	3.5187(2)	17.670(3)	98.14(4)	1024.4(8)	1.759

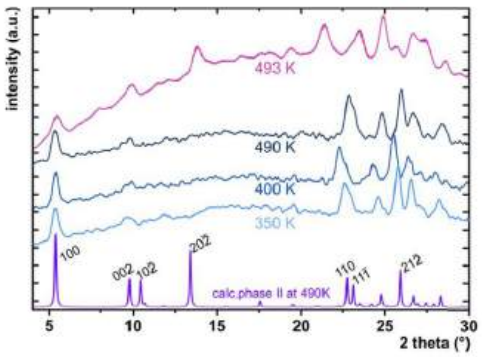

Fig. 12 High-temperature PXRD of PTCDI-Ph (phase II at 350, 400 and 490 K and phase I at 493 K) measured with Cu Kα, and the pattern at the bottom with indicated *hkl* planes is the calculated diffractogram from the single-crystal measurements collected at 490 K.

with a 411 nm LED light with the use of an Andor Shamrock 500 spectrometer coupled with a silicon CCD detector (Fig. 10). For high-temperature measurements, the sample was placed in a tube-furnace. The high-pressure measurements were performed in a membrane diamond-anvil cell equipped with diamond IIA anvils. Daphne Oil 7575 assured the hydrostatic pressure up to 4.78 GPa.[88,89] All photoluminescence data were corrected for the apparatus response, *i.e.*, the emission spectrum of the SLS201L light source provided by the manufacturer, and the emission spectrum of the SLS201L light source measured on the CCD detector. Photoluminescence quantum yield was measured using an integrating sphere, λ_{LED} = 411 nm, as an excitation source, and an Andor spectrometer as the detector.

Differential scanning calorimetry

The PTCDI-Ph was characterized by differential scanning calorimetry (DSC) using Thass DSC XP-10 apparatus. The measurement in a heating (from ambient temperature to 573 K) and cooling (from 573 K to 200 K) cycle at a rate of 5 K min^{-1} was carried out under a N_2 atmosphere.

Ab initio calculations

The potential energy (E_p) of the isolated PTCDI-Ph molecule depending on rotation about one torsion angle was calculated using the Gaussian 16 program, Revision C.01[90] by applying the B3LYP basis set 6-311++g(2d,2p). Atomic positions were first retrieved from the CIF file for the measurement collected at 296 K/0.1 MPa and optimized with one of the torsion angles fixed at τ = 55.92°. All H-atoms were renormalized. The energy values in hartee were converted to kJ mol^{-1} (1 hartee is 2625 kJ mol^{-1}). All HOMO and LUMO energy levels (Tables S9 and S10 in the ESI†) were calculated using MOPAC 2016 and the PM6 method.[91]

Author contributions

Methodology: P. R., S. S., P. W., T. P., and A. K.; investigation: P. R., S. S., P. W., A. W., and T. P.; resources: P. W., T. P., and A. K.; data curation and formal analysis: P. R., S. S., P. W., and T. P.; conceptualization: S. S.; supervision and validation: S. S. and A. K.; visualization: P. R.; funding acquisition: P. R. and A. K.; original draft preparation: P. R., S. S., and A. K.; and review and editing: all authors. All the authors have given their approval to the final version of the manuscript.

Conflicts of interest

There are no conflicts of interest to declare.

Acknowledgements

The authors acknowledge the European Synchrotron Radiation Facility (ESRF) for the provision of synchrotron radiation facilities. P. R. is a recipient of the Adam Mickiewicz University Foundation scholarship for the 2022/2023 academic year and is grateful to the Polish Ministry of Education and Science (Diamentowy Grant DI2019/0160/49) for their financial support.

Notes and references

1 F. Würthner, *Angew. Chem., Int. Ed.*, 2001, **40**, 1037–1039.
2 B. A. Jones, M. J. Ahrens, M. H. Yoon, A. Facchetti, T. J. Marks and M. R. Wasielewski, *Angew. Chem., Int. Ed.*, 2004, **43**, 6363–6366.
3 B. J. Jung, N. J. Tremblay, M. L. Yeh and H. E. Katz, *Chem. Mater.*, 2011, **23**, 568–582.
4 X. Zhan, A. Facchetti, S. Barlow, T. J. Marks, M. A. Ratner, M. R. Wasielewski and S. R. Marder, *Adv. Mater.*, 2011, **23**, 268–284.
5 A. S. Molinari, H. Alves, Z. Chen, A. Facchetti and A. F. Morpurgo, *J. Am. Chem. Soc.*, 2009, **131**, 2462–2463.

6 P. Ranke, I. Bleyl, J. Simmerer, D. Haarer, A. Bacher and H. W. Schmidt, *Appl. Phys. Lett.*, 1997, **71**, 1332–1334.
7 M. A. Angadi, D. Gosztola and M. R. Wasielewski, *Mater. Sci. Eng., B*, 1999, **63**, 191–194.
8 Z. Liu, Y. Wu, Q. Zhang and X. Gao, *J. Mater. Chem. A*, 2016, **4**, 17604–17622.
9 E. Kozma and M. Catellani, *Dyes Pigm.*, 2013, **98**, 160–179.
10 A. J. Breeze, A. Salomon, D. S. Ginley, B. A. Gregg, H. Tillmann and H. H. Hörhold, *Appl. Phys. Lett.*, 2002, **81**, 3085–3087.
11 L. Schmidt-Mende, A. Fechtenkötter, K. Müllen, E. Moons, R. H. Friend and J. D. MacKenzie, *Science*, 2001, **293**, 1119–1122.
12 C. Li and H. Wonneberger, *Adv. Mater.*, 2012, **24**, 613–636.
13 G. Zhang, J. Zhao, P. C. Y. Chow, K. Jiang, J. Zhang, Z. Zhu, J. Zhang, F. Huang and H. Yan, *Chem. Rev.*, 2018, **118**, 3447–3507.
14 F. Würthner, V. Stepanenko, Z. Chen, C. R. Saha-Möller, N. Kocher and D. Stalke, *J. Org. Chem.*, 2004, **69**, 7933–7939.
15 C. Huang, S. Barlow and S. R. Marder, *J. Org. Chem.*, 2011, **76**, 2386–2407.
16 A. Sharenko, C. M. Proctor, T. S. Van Der Poll, Z. B. Henson, T. Q. Nguyen and G. C. Bazan, *Adv. Mater.*, 2013, **25**, 4403–4406.
17 Y. Liu, K. R. Wang, D. S. Cuo and B. P. Jiang, *Adv. Funct. Mater.*, 2009, **19**, 2230–2235.
18 H. Li and O. S. Wenger, *Angew. Chem.*, 2022, **134**, e202110491.
19 R. M. Pinto, E. M. S. Maçôas, A. I. S. Neves, S. Raja, C. Baleizão, I. C. Santos and H. Alves, *J. Am. Chem. Soc.*, 2015, **137**, 7104–7110.
20 M. Gsänger, J. H. Oh, M. Könemann, H. W. Höffken, A. M. Krause, Z. Bao and F. Würthner, *Angew. Chem., Int. Ed.*, 2010, **49**, 740–743.
21 B. A. Jones, A. Facchetti, M. R. Wasielewski and T. J. Marks, *J. Am. Chem. Soc.*, 2007, **129**, 15259–15278.
22 F. Marin, S. Tombolesi, T. Salzillo, O. Yaffe and L. Maini, *J. Mater. Chem. C*, 2022, **10**, 8089–8100.
23 A. Oleson, T. Zhu, I. S. Dunn, D. Bialas, Y. Bai, W. Zhang, M. Dai, D. R. Reichman, R. Tempelaar, L. Huang and F. C. Spano, *J. Phys. Chem. C*, 2019, **123**, 20567–20578.
24 M. Szafrański and A. Katrusiak, *J. Phys. Chem. Lett.*, 2016, **7**, 3458–3466.
25 F. Capitani, C. Marini, S. Caramazza, P. Postorino, G. Garbarino, M. Hanfland, A. Pisanu, P. Quadrelli and L. Malavasi, *J. Appl. Phys.*, 2016, **119**, 185901.
26 M. Mączka, S. Sobczak, P. Ratajczyk, F. F. Leite, W. Paraguassu, F. Dybała, A. P. Herman, R. Kudrawiec and A. Katrusiak, *Chem. Mater.*, 2022, **34**, 7867–7877.
27 P. Ratajczyk, A. Katrusiak, K. A. Bogdanowicz, W. Przybył, P. Krysiak, A. Kwak and A. Iwan, *Mater. Adv.*, 2022, **3**, 2697–2705.
28 S. Bergantin, M. Moret, G. Buth and F. P. A. Fabbiani, *J. Phys. Chem. C*, 2014, **118**, 13476–13483.
29 M. Knaapila and S. Guha, *Rep. Prog. Phys.*, 2016, **79**, 066601.
30 R. Li, M. Wang, H. Zhao, Z. Bian, X. Wang, Y. Cheng and W. Huang, *J. Phys. Chem. Lett.*, 2020, **11**, 5896–5901.
31 H. Zhao, Y. Zhao, Y. Song, M. Zhou, W. Lv, L. Tao, Y. Feng, B. Song, Y. Ma, J. Zhang, J. Xiao, Y. Wang, D. H. Lien, M. Amani, H. Kim, X. Chen, Z. Wu, Z. Ni, P. Wang, Y. Shi, H. Ma, X. Zhang, J. Bin Xu, A. Troisi, A. Javey and X. Wang, *Nat. Commun.*, 2019, **10**, 5589.
32 L. Huang, F. Zhu, C. Liu, H. Wang, Y. Geng and D. Yan, *Org. Electron.*, 2010, **11**, 195–201.
33 A. S. Komolov, E. F. Lazneva, N. B. Gerasimova, Y. A. Panina, A. V. Baramygin and S. A. Pshenichnyuk, *Phys. Solid State*, 2016, **58**, 1901–1905.
34 J. Yang, D. Yan and T. S. Jones, *Chem. Rev.*, 2015, **115**, 5570–5603.
35 S. R. Byrn, D. Y. Curtin and I. C. Paul, *J. Am. Chem. Soc.*, 1972, **94**, 890–898.
36 N. Casati, A. Kleppe, A. P. Jephcoat and P. Macchi, *Nat. Commun.*, 2016, **7**, 1–8.
37 M. Anioła and A. Katrusiak, *Cryst. Growth Des.*, 2015, **15**, 764–770.
38 K. Sato and J. Mizuguchi, *Acta Crystallogr., Sect. E: Struct. Rep. Online*, 2006, **62**, 5008–5009.
39 A. Gavezzotti, *Acc. Chem. Res.*, 1994, **27**, 309–314.
40 A. Gavezzotti and G. Filippini, *J. Phys. Chem.*, 1994, **98**, 4831–4837.
41 E. G. Mcrae and M. Kasha, *J. Chem. Phys.*, 1958, **28**, 721–722.
42 M. Kasha, *Radiat. Res.*, 1963, **20**, 55–70.
43 M. Kasha, H. R. Rawls and M. A. El-Bayoumi, *Pure Appl. Chem.*, 1965, **11**, 371–392.
44 N. J. Hestand and F. C. Spano, *Chem. Rev.*, 2018, **118**, 7069–7163.
45 N. J. Hestand and F. C. Spano, *Acc. Chem. Res.*, 2017, **50**, 341–350.
46 M. D. Curtis, J. Cao and J. W. Kampf, *J. Am. Chem. Soc.*, 2004, **126**, 4318–4328.
47 T. Chen, Y.-J. Ma and D. Yan, *Adv. Funct. Mater.*, 2023, **33**, 2214962.
48 S. Liu, Y. Lin and D. Yan, *Sci. Bull.*, 2022, **67**, 2076–2084.
49 F. Nie, K. Z. Wang and D. Yan, *Nat. Commun.*, 2023, **14**, 1654.
50 B. Lu, Y. Zhang, X. Yang, K. Wang, B. Zou and D. Yan, *J. Mater. Chem. C*, 2018, **6**, 9660–9666.
51 Y. Yang, X. Yang, X. Fang, K. Z. Wang and D. Yan, *Adv. Sci.*, 2018, **5**, 1–8.
52 F. C. Spano, *Acc. Chem. Res.*, 2010, **43**, 429–439.
53 P. O. J. Scherer and S. F. Fischer, *Chem. Phys.*, 1984, **86**, 269–283.
54 A. B. Cairns and A. L. Goodwin, *Phys. Chem. Chem. Phys.*, 2015, **17**, 20449–20465.
55 M. Anioła, A. Katrusiak and R. Kia, *CrystEngComm*, 2012, **14**, 6424–6427.
56 J. Marciniak and A. Katrusiak, *J. Phys. Chem. C*, 2017, **121**, 22303–22309.
57 M. Ichikawa, S. Deguchi, T. Onoguchi, H. G. Jeon and G. D. R. Banoukepa, *Org. Electron.*, 2013, **14**, 464–468.
58 M. Runowski, T. Zheng, P. Woźny and P. Du, *Dalton Trans.*, 2021, **50**, 14864–14871.
59 B. Lorenz, Y. R. Shen and W. B. Holzapfel, *High Pressure Res.*, 1994, **12**, 91–99.

60 Y. Wang, T. Seto, K. Ishigaki, Y. Uwatoko, G. Xiao, B. Zou, G. Li, Z. Tang, Z. Li and Y. Wang, *Adv. Funct. Mater.*, 2020, **30**, 2001384.
61 M. Sójka, M. Runowski, P. Woźny, L. D. Carlos, E. Zych and S. Lis, *J. Mater. Chem. C*, 2021, **9**, 13818–13831.
62 J. D. Barnett, S. Block and G. J. Piermarini, *Rev. Sci. Instrum.*, 1973, **44**, 1–9.
63 M. A. Antoniak, S. J. Zelewski, R. Oliva, A. Żak, R. Kudrawiec and M. Nyk, *ACS Appl. Nano Mater.*, 2020, **3**, 4209–4217.
64 T. Zheng, M. Runowski, N. Stopikowska, M. Skwierczyńska, S. Lis, P. Du and L. Luo, *J. Alloys Compd.*, 2022, **890**, 161830.
65 T. Zheng, M. Runowski, P. Rodríguez-Hernández, A. Muñoz, F. J. Manjón, M. Sójka, M. Suta, E. Zych, S. Lis and V. Lavín, *Acta Mater.*, 2022, **231**, 117886.
66 M. Runowski, A. Shyichuk, A. Tymiński, T. Grzyb, V. Lavín and S. Lis, *ACS Appl. Mater. Interfaces*, 2018, **10**, 17269–17279.
67 M. Runowski, P. Woźny, N. Stopikowska, Q. Guo and S. Lis, *ACS Appl. Mater. Interfaces*, 2019, **11**, 4131–4138.
68 P. Woźny, K. Soler-Carracedo, N. Stopikowska, I. R. Martín and M. Runowski, *J. Mater. Chem. C*, 2023, **11**, 4792–4807.
69 F. Datchi, R. Letoullec and P. Loubeyre, *J. Appl. Phys.*, 1997, **81**, 3333–3339.
70 A. Lacam, *High Pressure Res.*, 1990, **5**, 782–784.
71 A. You, M. Be and I. In, *J. Appl. Phys.*, 1989, **66**, 366–372.
72 A. Katrusiak, *Int. Tables Crystallogr.*, 2018, 156–173.
73 T. Zheng, L. Luo, P. Du, S. Lis, U. R. Rodríguez-Mendoza, V. Lavín, I. R. Martín and M. Runowski, *Chem. Eng. J.*, 2022, **443**, 136414.
74 T. Zheng, M. Sójka, P. Woźny, I. R. Martín, V. Lavín, E. Zych, S. Lis, P. Du, L. Luo and M. Runowski, *Adv. Opt. Mater.*, 2022, **10**, 2201055.
75 N. Tang, J. Zhou, L. Wang, M. Stolte, G. Xie, X. Wen, L. Liu, F. Würthner, J. Gierschner and Z. Xie, *Nat. Commun.*, 2023, **14**, 1922.
76 X. Xu, A. Austin, S. E. Mylon, J. Plenge and J. M. Szarko, *ChemPhysChem*, 2017, **18**, 2430–2441.
77 N. I. Georgiev, A. I. Said, R. A. Toshkova, R. D. Tzoneva and V. B. Bojinov, *Dyes Pigm.*, 2019, **160**, 28–36.
78 K. Nagarajan, A. R. Mallia, V. S. Reddy and M. Hariharan, *J. Phys. Chem. C*, 2016, **120**, 8443–8450.
79 H. Q. Le, M. Rusek and A. Katrusiak, *J. Phys. Chem. C*, 2023, **127**, 4310–4318.
80 G. J. Piermarini, S. Block, J. D. Barnett and R. A. Forman, *J. Appl. Phys.*, 1975, **46**, 2774–2780.
81 H. K. Mao, J. Xu and P. M. Bell, *J. Geophys. Res.*, 1986, **91**, 4673.
82 R. J. Angel, M. Bujak, J. Zhao and G. Diego, *J. Appl. Crystallogr.*, 2007, **40**, 26–32.
83 T. Poręba, D. Comboni, M. Mezouar, G. Garbarino and M. Hanfland, *J. Phys.: Condens. Matter*, 2022, **35**, 054001.
84 Agilent, *CrysAlis PRO*, Agilent Technologies Ltd, Yarnton, Oxfordshire, England, 2014.
85 G. M. Sheldrick, *Acta Crystallogr., Sect. A: Found. Crystallogr.*, 2008, **64**, 112–122.
86 O. V. Dolomanov, L. J. Bourhis, R. J. Gildea, J. A. K. Howard and H. Puschmann, *J. Appl. Crystallogr.*, 2009, **42**, 339–341.
87 C. F. Macrae, P. R. Edgington, P. McCabe, E. Pidcock, G. P. Shields, R. Taylor, M. Towler and J. Van De Streek, *J. Appl. Crystallogr.*, 2006, **39**, 453–457.
88 D. Staško, J. Prchal, M. Klicpera, S. Aoki and K. Murata, *High Pressure Res.*, 2020, **40**, 525–536.
89 K. Murata and S. Aoki, *Rev. High Pressure Sci. Technol.*, 2016, **26**, 3–7.
90 M. J. Frisch, G. W. Trucks, H. B. Schlegel, G. E. Scuseria, M. A. Robb, J. R. Cheeseman, G. Scalmani, V. Barone, G. A. Petersson, H. Nakatsuji, X. Li, M. Caricato, A. V. Marenich, J. Bloino, B. G. Janesko, R. Gomperts, B. Mennucci, H. P. Hratchian, J. V. Ortiz, A. F. Izmaylov, J. L. Sonnenberg, D. Williams-Young, F. Ding, F. Lipparini, F. Egidi, J. Goings, B. Peng, A. Petrone, T. Henderson, D. Ranasinghe, V. G. Zakrzewski, J. Gao, N. Rega, G. Zheng, W. Liang, M. Hada, M. Ehara, K. Toyota, R. Fukuda, J. Hasegawa, M. Ishida, T. Nakajima, Y. Honda, O. Kitao, H. Nakai, T. Vreven, K. Throssell, J. A. Montgomery, Jr., J. E. Peralta, F. Ogliaro, M. J. Bearpark, J. J. Heyd, E. N. Brothers, K. N. Kudin, V. N. Staroverov, T. A. Keith, R. Kobayashi, J. Normand, K. Raghavachari, A. P. Rendell, J. C. Burant, S. S. Iyengar, J. Tomasi, M. Cossi, J. M. Millam, M. Klene, C. Adamo, R. Cammi, J. W. Ochterski, R. L. Martin, K. Morokuma, O. Farkas, J. B. Foresman and D. J. Fox, *Gaussian 16 (Revision C.01)*, Gaussian, Inc., Wallingford CT, 2016.
91 J. J. P. Stewart, *MOPAC2016, Stewart Computational Chemistry*, Colorado Springs, CO, 2016.

Article A2

Pressure- and temperature-driven transitions and conformational conversions of n-hexyl substituted perylene diimide (PDI-C6) crystals

Paulina Ratajczyk, Szymon Sobczak, Michał Andrzejewski, Francesco Marin, Marianna Marchini, Lucia Maini, Andrzej Katrusiak

Journal of Materials Chemistry C, 2025, **13**, 13509-13518, DOI: 10.1039/D5TC00809C

Journal of Materials Chemistry C

ROYAL SOCIETY OF CHEMISTRY

PAPER

View Article Online
View Journal

Cite this: DOI: 10.1039/d5tc00809c

Pressure- and temperature-driven transitions and conformational conversions of *n*-hexyl substituted perylene diimide (PDI-C_6) crystals†

Paulina Ratajczyk, [a] Szymon Sobczak, [a] Michał Andrzejewski, [b] Francesco Marin, [c] Marianna Marchini, [c] Lucia Maini *[c] and Andrzej Katrusiak *[a]

Perylene diimides (PDIs) are organic semiconductors with properties suitable for applications in electronic devices. This study presents a comprehensive investigation of **PDI-C_6**, a perylene diimide modified with an *n*-hexyl alkyl chain at the imide position, under non-ambient conditions, with a focus on the rich diagram of structurally varying phases and their anisotropic strain. Five distinct polymorphs of **PDI-C_6** have been found. The ambient phase I transforms to phase II at 465 K, which at 521 K transforms to phase III. The perylene cores arranged in parallel stacks in phase I rotate in the scissor-opening motion by 33° in phase II. Under high pressure, phase I transforms to phase IV at 1.22 GPa and to phase V at 1.50 GPa. The transitions between phases I, IV and V stepwise modify the conformation of the *n*-hexyl substituents. Surprisingly, all five polymorphs are of space-group type $P\bar{1}$, which is unprecedented as the symmetry of phases usually involves the space-group changes. These findings significantly enhance our understanding of the structural transformations of next-generation electronic materials and highlight the role of crystal engineering in constructing novel organic semiconductors with high sensitivity to environmental stimuli.

Received 24th February 2025,
Accepted 23rd May 2025

DOI: 10.1039/d5tc00809c

rsc.li/materials-c

Introduction

Organic charge-transfer complexes and π-conjugated compounds are prospective materials for efficiently harvesting solar energy, proposed in response to the pressing demand for new environment-friendly sustainable energy sources. Presently, the mass production of silicon and hybrid-perovskite solar photovoltaic (SPV) panels poses significant drawbacks. Silicon panels are expensive and energy-demanding in production, their disposal is environment polluting and recycling difficult and expensive; the main problems connected to the presently innovative hybrid perovskites, such as $[CH_3NH_3]PbI_3$ ($MAPbI_3$), are their contents of metals, often poisonous and contaminating the environment both at the production and disposal stages, not to mention a relatively high susceptibility to humidity, temperature changes and stress. The mass production of Si-based panels threatens the environment and biosphere and more environment-friendly materials are intensely sought.[1,2]

Organic materials are attractive due to their practically infinite ways of modifications and tuning properties, production and disposal. π-Conjugated molecular materials have recently attracted significant attention in the field of organic electronics due to their potential for practical applications, driven by the promising combination of superior charge carrier mobility and robust stability.[3] Recent extensive research has focused on designing and synthesizing new materials, understanding their structures, properties and emerging opportunities for developing innovative devices.[4] Compared to their inorganic counterparts, organic semiconductors offer not only high efficiency of the photoelectric conversion but also new qualities, including high flexibility and light weight, making them attractive for next-generation electronic devices,[5,6] such as photovoltaic tapes and foils for highly flexible photovoltaic panels and tissues, apart from substituting the roof and other panels. The envisaged applications for the organic photovoltaics (OPVs) panels can be similar to those already witnessed for similar organic light-emitting diodes (OLEDs) and organic thin-film transistors (OTFTs).[7–10]

Thermal expansion, compressibility and polymorphism are key issues for organic semiconductors, because different crystal

[a] Faculty of Chemistry, Adam Mickiewicz University, Uniwersytetu Poznańskiego 8, 61-614 Poznań, Poland. E-mail: katran@amu.edu.pl
[b] Paul Scherrer Institute, Forschungsstrasse 111, Villigen, CH-5232, Switzerland
[c] Department of Chemistry "G. Ciamician", University of Bologna, via Selmi 2, 40126 Bologna, Italy. E-mail: l.maini@unibo.it

† Electronic supplementary information (ESI) available. CCDC 2421994, 2422224, 2412030, 2421130 and 2412018–2412029. For ESI and crystallographic data in CIF or other electronic format see DOI: https://doi.org/10.1039/d5tc00809c

forms of the same compound can significantly vary in properties additionally modified by the temperature and pressure-induced strain.[11,12] Molecular engineering through chemical synthesis is a direct method to tailor the optoelectronic properties of materials,[13,14] but they may be enhanced or deteriorated by the monotonic changes and phase transitions. The synthesis process is usually time-consuming, labor-intensive and expensive, but the polymorphism of products can improve or diminish envisaged applications.[15,16] Most organic semiconductors crystallize in two or more polymorphic forms with different molecular packings in solid state,[17–21] leading to different properties.[22,23] The electronic, optical, mechanical, and charge transport properties of organic materials are heavily dependent on molecular packing, which is governed by various types of strong and weak intermolecular interactions.[24,25] Thus, investigating and controlling crystal structures and polymorphism is crucial for tailoring optical and electrical properties of organic semiconductors. Application of pressure and high- or low-temperature efficiently modifies intermolecular interactions and reveal the polymorphic behaviour of molecular compounds.[26,27] Including this important physical variables in the study of organic materials opens new exciting opportunities for investigating and developing high-performance semiconductors for optoelectronic devices.[28–30]

Perylene-3,4,9,10-tetracarboxydiimides, commonly known as perylene diimides (PDIs) are a class of compounds with polyaromatic π-conjugated flat molecules. PDIs offer a number of attractive characteristics, including high photo- and thermal-stability along with chemical inertness,[31] and have been extensively studied as semiconductors for OFETs,[32–35] and OPVs.[36–38] The properties of these n-type semiconducting materials can be efficiently modified through appropriate functionalization of the PDI core, achieved either by introducing different substituents at the imide N-atom or by modifying the core at the *bay* or *ortho* positions.[39] Such substitutions effectively alter crystal packing and solubility, influencing the optical and electrochemical properties.[36,40] Particularly effective, in the context of enhanced solubility, is the imide-site substitution by long alkyl chains. Several PDI systems with different alkyl chain length are known, but their polymorphic behaviour remains underinvestigated.[41–44]

Here, we present our study on *N*,*N*′-dihexyl-3,4,9,10-perylenedicarboximide (denoted as **PDI-C$_6$**), a commercially available PDI derivative functionalized with a hexyl alkyl moiety at the imide position (Scheme 1). The UV-Vis spectrum shows the high absorbance (Fig. S1, ESI†) characteristic of highly efficient photovoltaic materials. Although two high-temperature transitions of **PDI-C$_6$** were reported,[32–35] they have not been thoroughly investigated, and the structures of those phases remain unknown. Recently, Madhu and coworkers reported the crystal structure of **PDI-C$_6$** phase I at 173 K, revealing its one-dimensional (1D) columns, characteristic of PDI alkyl derivatives, stabilized by π–π stacking and C–H···O hydrogen bonding interactions.[45] Some of PDIs, such as PDI-C$_5$, have been studied at both room and high temperature, showing intriguing phase transitions, including polymorph obtained at 494 K that is characterized by a criss-cross arrangement of the aromatic cores.[46,47] However, high-pressure studies of perylene diimides, and other organic photovoltaic (OPV) materials remain exceptionally rare.[9,48–53] To fill this gap, we explored the polymorphism of **PDI-C$_6$** at various temperatures and high pressure by combining multiple techniques, including synchrotron and in-lab X-ray diffraction, as well as differential scanning calorimetry (DSC).

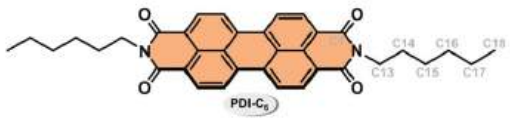

Scheme 1 Structural formula of *N*,*N*′-dihexyl-3,4,9,10-perylenedicarboximide (**PDI-C$_6$**).

Results and discussion

Previous calorimetric studies of **PDI-C$_6$** revealed two phase transitions during heating, occurring around 464 and 519 K, and two during cooling, at 494 and 409 K,[34] but they were not further investigated. To maintain consistent labelling with that previously introduced for PDI-C$_5$,[47] a PDI derivative with an *n*-pentyl chain, we will refer to the form stable under room conditions (296 K/0.1 MPa) as phase I, with subsequent phases labelled according to their order of appearance.

PDI-C$_6$ at room conditions

At room conditions, **PDI-C$_6$** phase I crystallizes in the triclinic space group $P\bar{1}$, with the **PDI-C$_6$** molecule located on an inversion center (Z' = 0.5). This observation agrees with the structure reported by Madhu *et al.* at 173 K (CSD refcode: TIXTUS).[45] In this structure, the molecules π-stacked into columns along the [100] crystal direction (Fig. S2, ESI†). The distance between π-stacked molecular cores ($d_{\pi-\pi}$) at room conditions is 3.3809(15) Å, somewhat shorter than the typical range 3.4–3.6 Å usually reported for π-stacked aggregates.[54]

The perylene core of the PDI molecules is planar, while the alkyl chains protrude off the plane in *trans* conformation. The inclination of the *n*-hexyl chain to the perylene core can be described by torsion angle C1–N1–C13–C14 (τ_1), while the conformation of the alkyl chains is characterized by four torsion angles (Scheme 1): N1–C13–C14–C15 (τ_2), C13–C14–C15–C16 (τ_3), C14–C15–C16–C17 (τ_4) and C15–C16–C17–C18 (τ_5). In analogy to the ethane-like molecules, the hexyl chain conformers can be represented using four-letter descriptors.[55] In phase I, the alkyl chains adopt *anti-anti-anti-anti* conformation denoted by descriptor AAAA, corresponding to angles τ_2, τ_3, τ_4, τ_5 all approaching 180°. The conformations involving *gauche*$^+$ and *gauche*$^-$ torsions (60° and −60°, respectively), present in subsequent phases, are denoted *e.g.* G$^+$AG$^-$A. The eclipsed conformation (*E*) describes a molecular arrangement in which adjacent methylene or methyl groups are in close

proximity, with the torsion angles between 0° and ± 30°, or close to 120°. The overall packing consists of alternating layers, with interdigitated alkyl chains and layers composed of rigid aromatic cores.

Temperature effect on PDI-C_6

The thermal behaviour of **PDI-C_6** has been investigated by several complementary techniques, including differential scanning calorimetry (DSC); thermogravimetric analysis (TGA); hot-stage microscopy (HSM); variable-temperature synchrotron X-ray powder diffraction (VT-PXRD) and in-lab single-crystal X-ray diffraction (VT-SCXRD). These methods allowed us to explore a broad temperature range from 100 K up to the decomposition at 823 K with TGA (in a N_2 atmosphere, Fig. S3 in ESI†) or at 673 K using VT-PXRD (in air).

During the heating cycle, according to the DSC thermogram, phase I transforms to phase II at $T_{I\rightarrow II}$ = 465 K, and at $T_{II\rightarrow III}$ = 521 K phase II transforms to phase III (Fig. 1). These transitions are consistent with the VT-SCXRD and HSM. The thermograms collected for the **PDI-C_6** cooled at a rate of 20 K min^{-1} indicate that the transitions from phase III to phase II and from phase II to phase I are reversible, as previously reported.[34]

The HSM revealed intriguing behaviour during the heating and cooling of the crystals related to the transition between phases I and II. The transitions occurred at slightly different temperatures for individual crystals, which is characteristic of 1st-order reconstructive transitions. The phase I to phase II transition observed upon heating was characterized by clearly visible propagating fronts that induced wrinkle formation on the crystal surface (as visible for crystal 1 in Fig. 2a and b). A different behaviour was observed upon cooling, at approx. 392 K, all the **PDI-C_6** needles elongated (Fig. 2c and d), leading to the movement, jumping and bending of some crystals (Fig. S18e and f, ESI†). Similar polymorphism and thermomechanical behaviour were observed for other organic semiconducting materials.[56,57] These macroscopic changes in single-crystal morphology can be attributed to the mutual rotation of the perylene cores, where the transformation of stress accumulated due to molecular rearrangement is converted into mechanical force.[47]

Our VT-PXRD analysis shows that, on approaching the transition to phase II, simultaneously the reflections of both

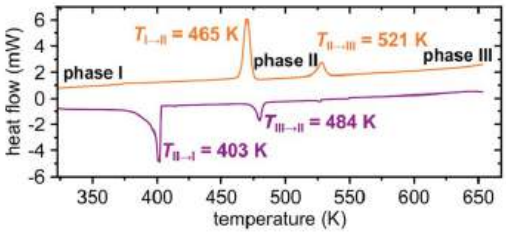

Fig. 1 Differential scanning calorimetry (DSC) thermogram of **PDI-C_6** in the heating (top) and cooling (bottom) cycles. Temperatures of phase transitions are indicated.

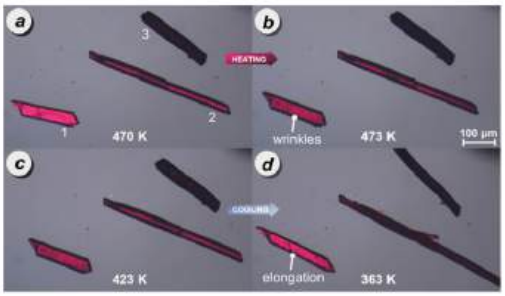

Fig. 2 Hot stage microscopy of **PDI-C_6** crystals during the heating cycle: (a) phase I at 470 K, (b) transition from phase I to phase II at 473 K; and during cooling cycle: (c) phase II at 423 K, (d) transition from phase II to phase I at 363 K, reshaping the crystals. Additional images are provided in Fig. S18 and S19 of the ESI.†

phases II and III appear, while above $T_{II\rightarrow III}$, at 538 K only phase III is present (Fig. 3). The coexistence of phases II and III is evident from two distinct reflections at 2θ below 1.25° in the PXRD pattern collected at 475 K (Fig. S4, ESI†). Because the transition from phase I to phase II is accompanied by a strong deformation, the unexpected appearance of phase III at 469 K can be associated with this strong mechanical effect 'pulling' small portions of the crystals into the adjacent higher-temperature phase III. The observation of phases outside their stability regions is occasionally experienced for other compounds, too, *e.g.* resorcinol or benzimidazole.[58,59] This recourse of a portion of the fine-powder sample to phase III at 469 K contrasts with all our experiments on single crystals and DSC measurements, all of which transformed to phase II, as expected. Upon cooling, phase III demonstrates strong hysteresis, persisting up to 353 K, when a simultaneous transition into phases II and I occurs (Fig. S9, ESI†). This extended hysteresis of phase III in the cooling run may result from a substantial thermal contraction, as indicated by thermal-expansion tensor plot (Table S7, ESI†), potentially hindering the spatial reorganization of molecules during the transition to phases II/I. Notably, a significant difference is observed in the phase transition temperature across different thermal analyses (*cf.* Fig. S8, ESI†). This suggests that crystal morphology, particularly crystal size, plays a crucial role in influencing the kinetics of phase transition events, as it was observed for other materials.[60]

In order to better understand the structural changes and the temperature effect on **PDI-C_6** crystals, we performed a series of VT-SCXRD experiments up to 470 K. Heating phase I from 100 K to $T_{I\rightarrow II}$, gradually elongates the unit-cell parameters a_I and c_I (the index indicates the phase). Parameter b_I initially elongates up to 338 K; on further heating to 430 K this trend is reversed and b_I shortens; and between 430 K and 465 K, b_I hardly changes with temperature (Fig. 4a). This unexpected behaviour can be attributed to the conformational changes of the *n*-hexyl chains. The π-conjugated stacking columns of **PDI-C_6**

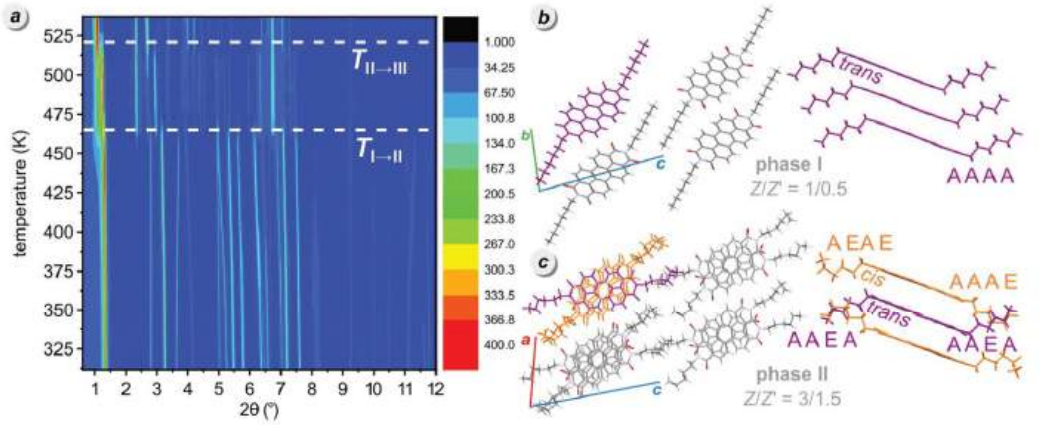

Fig. 3 (a) Temperature-resolved powder X-ray diffractograms of **PDI-C_6** upon heating (left). The dashed lines indicate the transition temperatures identified in the DSC measurement: $T_{I\to II}$ = 465 K and $T_{II\to III}$ = 521 K. The color scale represents intensity variations. Crystal structures of **PDI-C_6** phase I (b) and II (c) showing: the packing arrangement along the 1D columnar alignment (left) and the columnar stacking, including conformer descriptors (right). Molecules located at the inversion center with a *trans* conformation are depicted in purple, while those in general positions with a *cis* conformation are shown in orange.

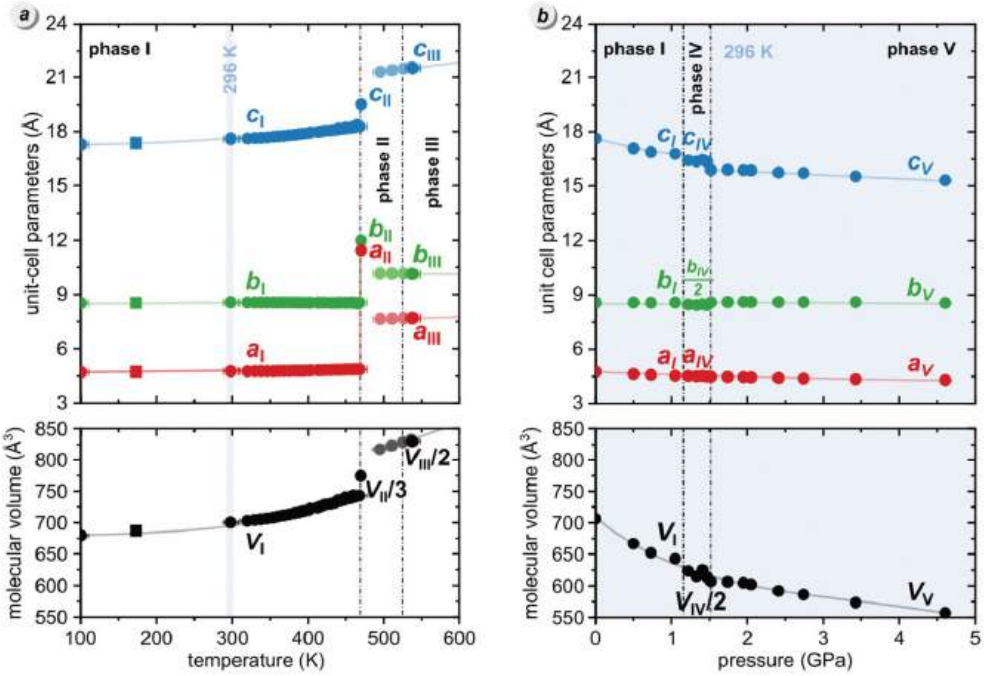

Fig. 4 Temperature (a) and pressure (b) dependence of the unit-cell dimensions *a*, *b*, *c* (top) and molecular volume (V_m = *V*/*Z*, bottom) of **PDI-C_6**. Estimated standard deviations (ESDs) are smaller than plotted symbols. The data at 173 K (squares) were taken from Madhu *et al.*[45] The unit-cell parameters of phase III determined during the cooling cycle are marked with a lighter color. The data measured at 296 K is highlighted in blue. Lines joining the points are for guiding the eye only. The triclinic angles are plotted in Fig. S21 (ESI†).

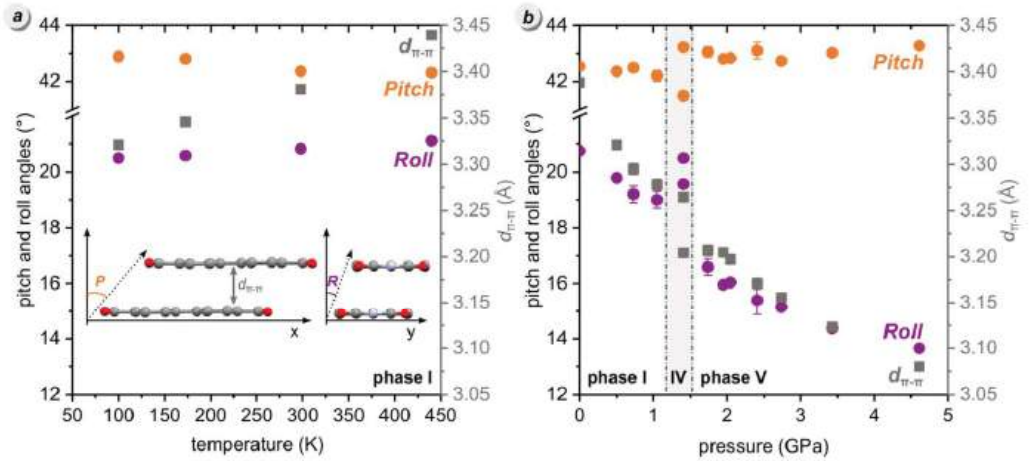

Fig. 5 Temperature (a) and pressure (b) effects on the π-stacking of **PDI-C$_6$** molecules under pressure: orange and purple symbols represent the pitch and roll angles and grey squares mark the distance between π-stacked molecules ($d_{\pi-\pi}$).[61] Inset: Graphical representation of *P*, *R* and $d_{\pi-\pi}$. The alkyl substituents and H-atoms are skipped for clarity. The corresponding numerical values can be found in Tables S2 and S10 of the ESI.†

molecules aligned along direction a_I in phase I can be described by the pitch and roll inclinations relative to the ideal cofacial π-stack, as reported by Curtis *et al.*[61] In this analysis, the pitch (*P*) angle corresponds to the displacement caused by the shift of adjacent molecules along the long molecular axis, whereas the roll (*R*) angle refers to the relative shift between adjacent molecules perpendicular to the long axis of the molecule (or along its short molecular axis). As the temperature increases in phase I, the *P* angle decreases from 42.88(6)° at 100 K to 42.31(4)° at 440 K, while the *R* angle slightly increases from 20.49(7)° to 21.11(5)° over the same temperature range (Fig. 5a). The distance between π-stacked molecular planes ($d_{\pi-\pi}$) increases from 3.321(2) Å at 100 K up to 3.4397(13) Å at 440 K (Table S2, ESI†). The calculated volumetric thermal expansion coefficient (α_V) in the 100–354 K range, is 162 × 10^{-6} K^{-1}, which is close to the typical value of 170 × 10^{-6} K^{-1} observed for organic compounds.[62] However, between 368 K and 461 K, the α_V increases sharply, reaching 446 × 10^{-6} K^{-1}, which is nearly three times the value observed in the previous temperature range (see the ESI† for more details).

The phase transition from phase **I** to phase II fractures the single crystals, which complicated the accurate determination of high-temperature structures. Despite these difficulties, we successfully solved the structure of phase II at 470 K, revealing its triclinic symmetry of space group $P\bar{1}$. The unit-cell parameters of **PDI-C$_6$** phase II closely resemble those of high-temperature phase III of PDI-C$_5$ (*a* = 11.624 Å, *b* = 11.617 Å, *c* = 17.415 Å, α = 98.21°, β = 71.25°, γ = 116.06°, CSD refcode: DICMUX01) and its number of molecules in the unit cell (*Z* = 3) is the same.[47] These similarities extend to the molecular packing and in **PDI-C$_6$** phase II one molecule lies at an inversion center, while the other occupies a general position. The alkyl chains of the C_i-symmetric molecule are in *trans* conformation (*i.e.* they protrude to the opposite sides of PDI core), whereas the alkyl chains in the molecule at general position are *cis* (they protrude to the same side). The *trans*-molecule adopts the AAEA conformation, while the *cis* molecule has AAAE and AEAE conformers (Fig. 3c). Within the columns, every two parallel *cis*-molecules are followed by a *trans*-molecule, whose perylene core is rotated by approximately 33° about the column axis and slightly tilted relative to the

Table 1 Selected crystallographic data of **PDI-C$_6$** phases I, II, III, IV and V (*cf.* Tables S16 and S17 in ESI for details)

		Unit cell								
p (GPa)/*T* (K)	Phase	*a* (Å)	*b* (Å)	*c* (Å)	α (°)	β (°)	γ (°)	*V* (Å^3)	*Z*/*Z*′	$d_{\pi-\pi}$ (Å)
0.0001/298	I	4.7568(10)	8.5487(16)	17.576(2)	81.678(14)	84.850(15)	83.169(16)	700.3(2)	1/0.5	3.3809(15)
0.0001/470	II	11.443(7)	11.988(8)	19.506(9)	96.05(5)	73.16(5)	114.90(6)	2323(3)	3/1.5	3.579(8)
0.0001/537	III	7.676(2)	10.148(1)	21.559 (2)	84.35(2)	83.34(4)	90.52(3)	1665.5(5)	2/1	—
1.41/296	IV	4.5308(1)	16.9532(3)	17.887(1)	66.484(3)	95.489(2)	96.287(1)	1250.21(8)	2/1	3.2643(6) 3.2044(5)
1.95/296	V	4.4643(1)	8.6151(1)	15.8664(8)	90.750(3)	92.236(3)	97.490(1)	604.46(3)	1/0.5	3.2049(6)

cis-molecules. This results in an alternating sequence of two molecules *cis*, criss-cross π-stacked to one molecule *trans*, followed by two molecules *cis*, *etc.* Above 521 K, the strong reconstructive transition hampered our attempts to determine the structure of **PDI-C$_6$** phase III. The unit-cell parameters of phase III are reported in Table 1.

PDI-C$_6$ under pressure

High-pressure single-crystal X-ray diffraction measurements were performed on **PDI-C$_6$** at room temperature, up to 4.61 GPa. The discontinuities in the unit-cell dimensions as well as the doubling of parameter b_I at 1.22 GPa and its subsequent halving at 1.52 GPa evidence two pressure-induced phase transitions (Fig. 4b). Phase I is stable up to 1.05 GPa and then transforms to phase IV, which at 1.52 GPa transforms to phase V. The high-pressure phases IV and V are of the same triclinic space group type $P\bar{1}$ as phases I, II and III. In phases I and V, the asymmetric part of the unit cell comprises half of the **PDI-C$_6$** molecule, while $Z' = 1$ in phase IV. The crystallographic data are summarized in Table 1 and the crystal and experimental data are detailed in Table S16 in ESI.†

The compression of the phase I significantly reduces the a_I and c_I dimensions, which is associated with decreased π–π distances and deformations of the alkyl chains. The parameter b_I is hardly affected by the pressure and upon the compression to 0.73 GPa, it decreases by only −0.14%. Interestingly, at 1.05 GPa, just before the transition to phase IV, the b_I is approximately +0.01% longer compared to its length at 0.1 MPa. These changes correlate with variations in the shortest hydrogen bond $CH_4\cdots O_2$, which shortens from 2.4752(15) Å at 0.1 MPa to 2.37(3) Å at 0.73 GPa, before lengthening slightly to 2.39(2) Å at 1.05 GPa. At 0.1 MPa, the *P* angle is 42.53° and the *R* angle is 20.75°. The compression of phase I from 0.1 MPa to 1.05 GPa of **PDI-C$_6$** has a small impact on the *P* angle, reducing it by only 0.33°. In contrast, the changes of the *R* angle and π–π stacking distance ($d_{\pi-\pi}$) are much more pronounced. The compression to 1.05 GPa decreases the *R* angle by 1.75° and shortens the $d_{\pi-\pi}$ distance to 3.278(6) Å from 3.3882(4) Å measured at 0.1 MPa (Fig. 5b).

The unit cell of phase IV clearly corresponds to that of phase I, as evident from compression of parameters (Fig. 4b) and the structural comparison presented in Fig. 6. The nearly monotonic compression of *a* reflects the gradual contraction of π–π stacking distance between adjacent **PDI-C$_6$** molecules within the stacks. The unit-cell vectors of phases I (a_I, b_I, c_I) and IV (a_{IV}, b_{IV}, c_{IV}) are related by the following eqn (1):

$$\begin{pmatrix} a_{IV} \\ b_{IV} \\ c_{IV} \end{pmatrix} = \begin{pmatrix} -1 & 0 & 0 \\ 0 & -2 & 0 \\ 0 & -1 & 1 \end{pmatrix} \begin{pmatrix} a_I \\ b_I \\ c_I \end{pmatrix} \quad (1)$$

Apart from doubling of the *b* parameter ($b_{IV} = 2b_I$), the transition from phase I to IV leads to an abrupt reduction of the c'_{IV} parameter by −2.20%, which can be recalculated in relation to the c_I parameter of phase I with the eqn (2):

$$c'_{IV} = \sqrt{c_{IV}^2 + b_{IV}^2/4 - c_{IV} b_{IV} \cos\alpha_{IV}} \quad (2)$$

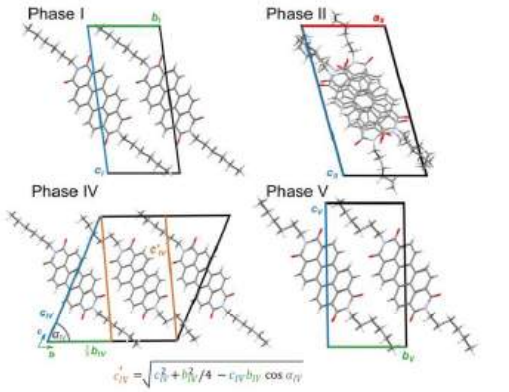

Fig. 6 Lattice relations between phases I (0.1 MPa/298 K), II (0.1 MPa/470 K), IV (1.41 GPa/296 K), and V (1.95 GPa/296 K) in **PDI-C$_6$**, illustrated for maintained orientations of the π-stacked molecules; the orange axes in phase IV indicate the corresponding directions in phases I and V.

The transformation to phase IV releases the structural strain accumulated during compression by lowering the crystal symmetry and doubling the number of independent molecules. As a result, due to conformational alternation of the *n*-hexyl chains, the Z' in phase IV increases from 0.5 to 1. One of the molecules retains C_i symmetry, maintaining the AAAA conformation of alkyl chains, as observed before in phase I, with τ_2–τ_5 torsion angles close to 180°. The other molecule adopts a *gauche*$^+$/*gauche*$^-$ (G^+/G^-) conformation, where τ_3 and τ_5 remain near 180°, while τ_2 and τ_4 twist to approximately ±60°. Consequently, the conformers descriptors for two independent molecules present in phase IV are AAAA/AAAA and G^+AG^-A/G^-AG^+A (Fig. 7). The discrimination of molecules into two independent conformers affects their π-stacking in phase IV and significantly impacts the elastic response of the crystal. The pressure-induced deformation of the AAAA stacks follows the trends observed in phase I, with the *P* angle decreasing by 0.71°, and $d_{\pi-\pi}$ by 0.42% compared to their values at 1.05 GPa. Under the same conditions, the *R* angle increases by 1.5°. The accommodation of new conformers G^+AG^-A/G^-AG^+A requires the *P* angle to increase by 1.73° and *R* angle to decrease by 0.93°, compared to the AAAA conformer at 1.41 GPa. As a result, the enhanced flexibility of G^+AG^-A/G^-AG^+A conformers allows for more efficient packing and the $d_{\pi-\pi}$ distance shorter by 1.84% compared to that between conformers AAAA at 1.41 GPa.

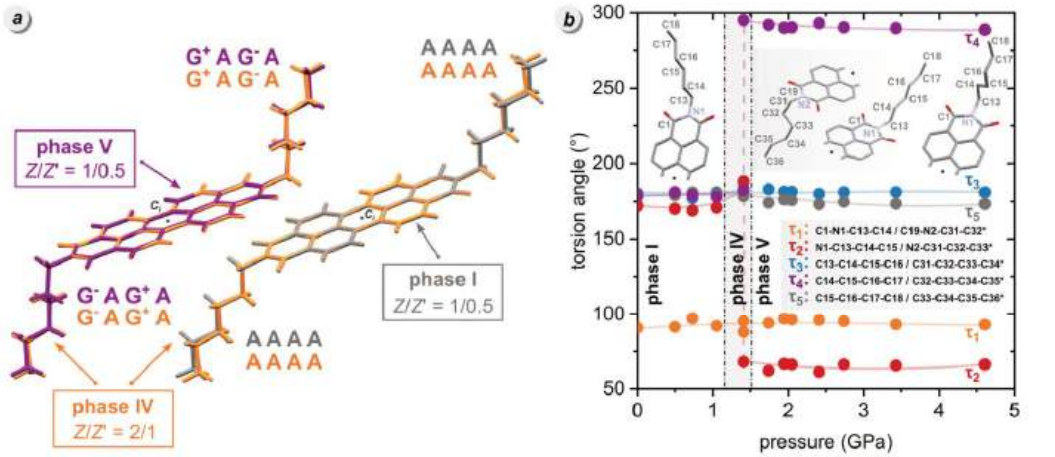

Fig. 7 Conformational changes in **PDI-C$_6$** molecules in phases I (grey), IV (orange) and V (violet) illustrated by (a) superimposing fragment of the perylene core, and (b) torsion angles τ_{1-5} plotted as a function of pressure. In the description of the torsion angles, asterisks refer to the atoms in phase IV. Hydrogen atoms are omitted for clarity.

At 1.5 GPa, a drop in the parameter c_{IV} length and the halving of the parameter b_{IV} mark another phase transition, changing the unit-cell vectors to resemble those of phase I:

$$\begin{pmatrix} a_V \\ b_V \\ c_V \end{pmatrix} = \begin{pmatrix} -1 & 0 & 0 \\ 0 & -1/2 & 0 \\ 0 & -1/2 & 1 \end{pmatrix} \begin{pmatrix} a_{IV} \\ b_{IV} \\ c_{IV} \end{pmatrix} \quad (3)$$

In phase V, the Z' number is reduced back to 0.5, and all molecules adopt the G$^+$AG$^-$A/G$^-$AG$^+$A conformation (Fig. 7). As the pressure increases from 1.74 to 4.61 GPa, the a_V parameter shortens by −4.12%, and c_V by −3.62%, while parameter b_V is hardly reduced (−0.48%). This unusual effect results from the preserved characteristic motif of π-stacking into columns, similarly as in phase I. The G$^+$AG$^-$A/G$^-$AG$^+$A conformation effectively accommodates compression, as evidenced by a negligible change in $d_{\pi-\pi}$ distance up to 2.1 GPa. Above this pressure, $d_{\pi-\pi}$ decreases significantly with compression, by 9.09% at 4.61 GPa compared to 0.1 MPa. The deformation of the π-stacked columns in phase V becomes more pronounced, with the P angle increasing by 0.22° and the R angle decreasing by 2.95° between 1.74 and 4.61 GPa (Table S10, ESI†).

Conclusions

We comprehensively investigated the solid-state phase transitions of the semiconductor **PDI-C$_6$**, employing a combination of differential scanning calorimetry, hot-stage microscopy, and X-ray diffraction under high pressure and various temperatures. Our research highlights an unprecedented polymorphic diversity of **PDI-C$_6$**, identifying reversible transformations between five distinct polymorphic forms. This includes two high-temperature polymorphs, previously observed only through DSC analysis, and two new high-pressure phases. Notably, all identified polymorphs crystallize in the same triclinic space-group type $P\bar{1}$.

The transition from phase I to phase II involves a scissor-like rotation of the perylene cores, accompanied by a significant conformational rearrangement of the alkyl chains. However, the structure retains its 1D columnar π-stacking and the interdigitation of the alkyl chains. **PDI-C$_6$** phase II is isomorphic to phase III of PDI-C$_5$. The close structural relationship is further evidenced by similar mechano-responsive behaviour of crystals upon cooling from phase II back to phase I, when single crystals move, jump and reshape. Due to the reconstructive phase transition, the structure of phase III could not be determined; however, we were able to establish the unit-cell parameters and characterize its thermal contraction upon cooling. This significant thermal strain may hinder the spatial rearrangement of molecules, leading to a high hysteresis upon cooling as observed in the VT-PXRD.

The volume changes observed in **PDI-C$_6$** phase I on lowering the temperature from 298 to 100 K, on average, correspond to the compression from ambient pressure to *ca.* 0.5 GPa, fulfilling pressure-temperature correspondence rule.[63] Conversely, in the temperature range from 100 to 440 K, the **PDI-C$_6$** phase I follows the rule of the inverse relation of the thermal expansion and compressibility, exemplified by thermal expansion along [z],[64] which corresponds to the strongest compressibility in the same direction. While the thermal phase transition from phase I to II is dominated by the rotation of the aromatic core, the experimental and theoretical computations consistently indicate that the conformational flexibility of the *n*-hexyl substituents at the imide position is the driving factor of pressure-induced phase transitions. The stepwise emergence of conformers G$^+$AG$^-$A/G$^-$AG$^+$A during compression in phase IV, where

half of the molecules preserve the conformation AAAA/AAAA, while in phase V all molecules adopt the $G^{+}AG^{-}A/G^{-}AG^{+}A$ conformation, indicates that such conformational conversion facilitates more efficient molecular packing and thus effectively reduces the π-stacking distance by 9.09% between 0.1 MPa and 4.61 GPa.

Experimental methods

Crystallization

PDI-C_6 was purchased from Aldrich and used without additional purification. Single crystals of **PDI-C_6** were obtained using a solvothermal reactor. The process involved preparing a supersaturated solution of **PDI-C_6** in toluene, *p*-xylene, CH_2Cl_2, or $CHCl_3$, heating it to 453 K (or 373 K for chlorinated solvents) overnight, and then gradually cooling it to room temperature.

Differential scanning calorimetry (DSC)

The DSC measurement was performed with PerkinElmer PyrisDiamond DSC-7 equipped with a PII intracooler, in N_2 atmosphere and a scanning speed of 20 K min^{-1}. The temperatures of phase transitions were determined using the method of intersecting slope and baseline lines.

Hot-stage microscopy (HSM)

The HSM analysis was performed using an OLYMPUS BX41 microscope equipped with a VISICAM 5.0 and a NIKON DS FI3 camera. A Linkam TMS-94 stage was used for the temperature control. The images were taken under polarized light to highlight modifications in the crystals due to solid-state transition, with a 40× magnification.

Variable-temperature single-crystal X-ray diffraction (VT-SCXRD)

The single-crystal measurements were performed on Xcalibur diffractometers with microfocus sources (CuKα = 1.54178 Å and MoKα = 0.71073 Å) and an Oxford Cryojet attachment. For data collection and processing, the CrysAlisPro software was employed. The crystal structures were initially solved using SHELXT and subsequently refined using SHELXL within the Olex2 suite.[65,66] All non-H atoms were refined with anisotropic thermal parameters. H atoms were located in the difference Fourier map and from the molecular geometry. All crystal structures were analysed and compared using the software Mercury.[67] We conducted measurements at 100, 298, 440 and 470 K. Additionally, we determined the unit-cell parameters between 450 and 465 K from quick-experiments. The final crystal data are summarized in Table 1 and have been deposited in the CCDC with numbers 2421994, 2422224, 2412030 and 2421130.†

Variable temperature X-ray powder diffraction (VT-PXRD)

VT-PXRD experiments were conducted in the 312–537 K range at the ALBA Synchrotron and Powder Diffraction beamline BL04-MSPD equipped with the High-throughput Position Sensitive Detector (PSD) MYTHEN and an FMB Oxford hot air blower. Indexing of the high-temperature phases was achieved using a 30-second X-ray exposure, λ = 0.41235(1) Å, over the 2θ range of 0.8°–15°. Fig. 3a presents the VT-PXRD patterns obtained upon heating the material, while Fig. S9 (ESI†) contains a temperature-resolved diffractogram collected during cooling the **PDI-C_6** powder. Indexing of the PXRD data collected at 499 K was hampered. However, we successfully indexed the data collected at 537 K, which allowed the determination of the triclinic primitive unit-cell parameters of high-temperature polymorph III of **PDI-C_6**. Furthermore, the data for **PDI-C_6** phase III at 537 K were refined using Pawley fitting in Topas-Academic V5 (TOPAS).[68] The final crystallographic data are summarized in Table 1.

High-pressure single-crystal X-ray diffraction

All high-pressure experiments were conducted using a modified Merrill-Bassett diamond anvil cell (DAC) with diamond anvils supported on steel discs.[69] The diamond culets were 0.8 mm in diameter. The gasket was made of 0.3 mm thick tungsten foil with spark-eroded holes 0.4 mm in diameter. Strongly elongated thin plate crystals were prepared by cutting them to the dimensions required for the experimental chamber. The DAC chamber was loaded with the single-crystal sample and a ruby chip. Daphne Oil 7575 was used as the pressure-transmitting medium to maintain hydrostatic conditions.[70,71] Subsequently, the DAC was closed and compressed. Pressure was generated by controlled tightening of three screws. The experimental details are shown in Fig. S20 of the ESI.† Pressure was calibrated before and after the measurement using the ruby fluorescence method with the Photon Control spectrometer, affording an accuracy of 0.02 GPa.[72,73] Single-crystal X-ray diffraction measurements were conducted on a 4-circle diffractometer equipped with a CCD detector and MoKα X-ray source (λ = 0.71073 Å) and with synchrotron radiation (see below Synchrotron X-ray Diffraction Measurements for details). The DAC chamber was centered using the gasket-shadowing method.[74] The CrysAlisPro software (ver. 43.98a) was used for the data collection, reduction and absorption correction. The structures were solved with direct methods using SHELXS and refined using least-squares methods with SHELXL, all within the Olex2 software suite.[66,75] Anisotropic displacement parameters were applied to all non-hydrogen atoms. The hydrogen atoms were initially identified through different Fourier maps and recalculated based on the molecular geometry after each refinement cycle. In-lab X-ray diffraction measurements were conducted at pressures of 1.05, 1.74 and 2.41 GPa. Additionally, quick experiments were carried out at 1.22, 1.33, 1.47, and 1.52 GPa, where only the unit-cell parameters were determined. All reference images collected during the diffraction measurements were consistent, testifying that no transformations took place during these experiments.

Synchrotron X-ray diffraction measurements

X-ray diffraction measurements were performed at the Materials Science beamline of the Swiss Light Source[76] using synchrotron radiation of approx. 0.4920 Å, focused and collimated to 150 μm (exact wavelengths were placed in Table S16, ESI†). High-pressure diffraction data was collected for single crystals of the **PDI-C$_6$** systems placed in a DAC in a steel gasket (thickness ~90 μm and a hole diameter 250 μm). A ruby fluorescent method was used to determine pressure inside the DAC. Daphne Oil 7575 was used as a pressure transmitting medium. We conducted measurements at 0.1 MPa, 0.5, 0.73, 1.41, 1.95, 2.05, 2.74, 3.43, and 4.61 GPa. The final crystal data from high-pressure measurements are summarized in Table 1 (*cf.* Table S16, ESI†) and have been deposited in CIF format in the Cambridge Crystallographic Database with numbers CCDC 2412018–2412029 (from in-lab and synchrotron measurements).†

Author contributions

Sample preparation: F. M., L. M., investigation and analysis of high-pressure and high-temperature SCXRD: P. R., S. S., M. A., F. M., A. K.; investigation and analysis of DSC, HSM, VT-PXRD: F. M., M. M., L. M.; theoretical investigation: M. A.; funding acquisition: P. R., L. M., A. K.; visualization: P. R., supervision: S. S., L. M., A. K.; original draft preparation: P. R., S. S., L. M., A. K.; review and editing: all authors. All the authors have given their approval to the final version of the manuscript.

Data availability

Data for this article, Have been included as part of the ESI,† and the crystallographic data for compound **PDI-C$_6$** has been deposited at the CCDC with numbers 2421994, 2422224, 2412030 and 2421130 (varied-temperature data) and 2412018–2412029 (high-pressure data) and can be obtained in the form of CIF files from https://www.ccdc.cam.ac.uk/.

Conflicts of interest

There are no conflicts to declare.

Acknowledgements

We are grateful to Dr Nicola Casati for providing access to the synchrotron at PSI, Villigen. PR is grateful to the Polish Ministry of Education and Science (Diamentowy Grant DI2019/0160/49) for their financial support.

Notes and references

1 S. Preet and S. T. Smith, *J. Cleaner Prod.*, 2024, **448**, 141661.
2 X. Wang, X. Tian, X. Chen, L. Ren and C. Geng, *Sol. Energy Mater. Sol. Cells*, 2022, **248**, 111976.
3 W. Wu, Y. Liu and D. Zhu, *Chem. Soc. Rev.*, 2010, **39**, 1489–1502.
4 A. B. Koren, M. D. Curtis, A. H. Francis and J. W. Kampf, *J. Am. Chem. Soc.*, 2003, **125**, 5040–5050.
5 L. Zang, Y. Che and J. S. Moore, *Acc. Chem. Res.*, 2008, **41**, 1596–1608.
6 S. Park, T. Kim, S. Yoon, C. W. Koh, H. Y. Woo and H. J. Son, *Adv. Mater.*, 2020, **32**, 1–29.
7 C. Wang, H. Dong, W. Hu, Y. Liu and D. Zhu, *Chem. Rev.*, 2012, **112**, 2208–2267.
8 H. Dong, X. Fu, J. Liu, Z. Wang and W. Hu, *Adv. Mater.*, 2013, **25**, 6158–6183.
9 P. Ratajczyk, S. Sobczak, P. Woźny, A. Wcisło, T. Poręba and A. Katrusiak, *J. Mater. Chem. C*, 2023, **11**, 11055–11065.
10 G. Zhang, F. R. Lin, F. Qi, T. Heumüller, A. Distler, H. J. Egelhaaf, N. Li, P. C. Y. Chow, C. J. Brabec, A. K. Y. Jen and H. L. Yip, *Chem. Rev.*, 2022, **122**, 14180–14274.
11 Y. G. Zhen, H. L. Dong, L. Jiang and W. P. Hu, *Chin. Chem. Lett.*, 2016, **27**, 1330–1338.
12 M. Mas-Torrent and C. Rovira, *Chem. Rev.*, 2011, **111**, 4833–4856.
13 M. Zambianchi, L. Favaretto, M. Durso, C. Bettini, A. Zanelli, I. Manet, M. Gazzano, L. Maini, D. Gentili, S. Toffanin, F. Gallino, M. Muccini, M. Cavallini and M. Melucci, *J. Mater. Chem. C*, 2015, **3**, 121–131.
14 L. Maini, F. Gallino, M. Zambianchi, M. Durso, M. Gazzano, K. Rubini, D. Gentili, I. Manet, M. Muccini, S. Toffanin, M. Cavallini and M. Melucci, *Chem. Commun.*, 2015, **51**, 2033–2035.
15 D. Liu, C. Li, S. Niu, Y. Li, M. Hu, Q. Li, W. Zhu, X. Zhang, H. Dong and W. Hu, *J. Mater. Chem. C*, 2019, **7**, 5925–5930.
16 J. Bernstein, *Polymorphism in molecular crystals*, OxfordUniversity Press, New York, 2002.
17 H. Chung and Y. Diao, *J. Mater. Chem. C*, 2016, **4**, 3915–3933.
18 Y. Diao, K. M. Lenn, W. Y. Lee, M. A. Blood-Forsythe, J. Xu, Y. Mao, Y. Kim, J. A. Reinspach, S. Park, A. Aspuru-Guzik, G. Xue, P. Clancy, Z. Bao and S. C. B. Mannsfeld, *J. Am. Chem. Soc.*, 2014, **136**, 17046–17057.
19 C. Wang, Y. Yu, Z. Chai, F. He, C. Wu, Y. Gong, M. Han, Q. Li and Z. Li, *Mater. Chem. Front.*, 2019, **3**, 32–38.
20 P. Pandey, N. Demitri, L. Gigli, A. M. James, F. Devaux, Y. H. Geerts, E. Modena and L. Maini, *Cryst. Growth Des.*, 2022, **22**, 1680–1690.
21 I. de Oliveira Martins, F. Marin, E. Modena and L. Maini, *Faraday Discuss.*, 2022, **235**, 490–507.
22 C. Cappuccino, L. Catalano, F. Marin, G. Dushaq, G. Raj, M. Rasras, R. Rezgui, M. Zambianchi, M. Melucci, P. Naumov and L. Maini, *Cryst. Growth Des.*, 2020, **20**, 884–891.
23 C. Cappuccino, S. Canola, G. Montanari, S. G. Lopez, S. Toffanin, M. Melucci, F. Negri and L. Maini, *Cryst. Growth Des.*, 2019, **19**, 2594–2603.
24 G. R. Desiraju, *Crystal engineering: the design of organic solids*, Elsevier Science Publishers B.V., Amsterdam, 1989.
25 C. Gao, X. Li, Y. Qu, R. Dai, Z. Wang, H. Li and Z. Zhang, *J. Phys. Chem. C*, 2019, **123**, 8731–8739.
26 E. V. Boldyreva, *Acta Crystallogr., Sect. A:Found. Crystallogr.*, 2008, **64**, 218–231.
27 A. Katrusiak, *Cryst. Res. Technol.*, 1991, **26**, 523–531.

28 Y. S. Guan, Z. Zhang, J. Pan, Q. Yan and S. Ren, *J. Mater. Chem. C*, 2017, **5**, 12338–12342.
29 M. Szafrański and A. Katrusiak, *J. Phys. Chem. Lett.*, 2017, **8**, 2496–2506.
30 M. Szafrański and A. Katrusiak, *J. Phys. Chem. Lett.*, 2016, **7**, 3458–3466.
31 A. Datar, K. Balakrishnan and L. Zang, *Chem. Commun.*, 2013, **49**, 6894–6896.
32 T. B. Singh, S. Erten, S. Günes, C. Zafer, G. Turkmen, B. Kuban, Y. Teoman, N. S. Sariciftci and S. Icli, *Org. Electron.*, 2006, **7**, 480–489.
33 R. Centore, L. Ricciotti, A. Carella, A. Roviello, M. Causà, M. Barra, F. Ciccullo and A. Cassinese, *Org. Electron.*, 2012, **13**, 2083–2093.
34 L. I. Kuznetsova, A. A. Piryazev, D. V. Anokhin, A. V. Mumyatov, D. K. Susarova, D. A. Ivanov and P. A. Troshin, *Org. Electron.*, 2018, **58**, 257–262.
35 J. Mei, Y. Diao, A. L. Appleton, L. Fang and Z. Bao, *J. Am. Chem. Soc.*, 2013, **135**, 6724–6746.
36 E. Kozma and M. Catellani, *Dyes Pigm.*, 2013, **98**, 160–179.
37 C. Li and H. Wonneberger, *Adv. Mater.*, 2012, **24**, 613–636.
38 W. S. Shin, H. H. Jeong, M. K. Kim, S. H. Jin, M. R. Kim, J. K. Lee, J. W. Lee and Y. S. Gal, *J. Mater. Chem.*, 2006, **16**, 384–390.
39 C. Huang, S. Barlow and S. R. Marder, *J. Org. Chem.*, 2011, **76**, 2386–2407.
40 F. Marin, A. Zappi, D. Melucci and L. Maini, *Mol. Syst. Des. Eng.*, 2023, **8**, 500–515.
41 H. Langhals, S. Demmig and T. Potrawa, *J. Prakt. Chem.*, 1991, **333**, 733–748.
42 A. J. McKerrow, E. Buncel and P. M. Kazmaier, *Can. J. Chem.*, 1993, **71**, 390–398.
43 M. Carmen Ruiz Delgado, E. G. Kim, D. A. Da Silva Filho and J. L. Bredas, *J. Am. Chem. Soc.*, 2010, **132**, 3375–3387.
44 Y. Geng, H. Bin Li, S. X. Wu and Z. M. Su, *J. Mater. Chem.*, 2012, **22**, 20840–20851.
45 J. Pitchaimani, A. Kundu, S. P. Anthony, D. Moon and V. Madhu, *ChemistrySelect*, 2020, **5**, 2070–2074.
46 E. Hadicke and F. Graser, *Acta Crystallogr.*, 1986, **42**, 189–195.
47 F. Marin, S. Tombolesi, T. Salzillo, O. Yaffe and L. Maini, *J. Mater. Chem. C*, 2022, **10**, 8089–8100.
48 P. Ratajczyk, A. Katrusiak, W. Bogdanowicz, K. A. Przybył, P. Krysiak, A. Kwak and A. Iwan, *Mater. Adv.*, 2022, **3**, 2697–2705.
49 K. A. Bogdanowicz, S. Lalik, P. Ratajczyk, A. Katrusiak, P. Krysiak, A. I. Pawłowska, M. Marzec and A. Iwan, *Sci. Rep.*, 2023, **13**, 13240.
50 W. Shi, T. Deng, G. Wu, K. Hippalgaonkar, J. S. Wang and S. W. Yang, *Adv. Mater.*, 2019, **31**, 1–8.
51 M. Knaapila and S. Guha, *Rep. Prog. Phys.*, 2016, **79**, 066601.
52 S. Bergantin, M. Moret, G. Buth and F. P. A. Fabbiani, *J. Phys. Chem. C*, 2014, **118**, 13476–13483.
53 R. Li, M. Wang, H. Zhao, Z. Bian, X. Wang, Y. Cheng and W. Huang, *J. Phys. Chem. Lett.*, 2020, **11**, 5896–5901.
54 R. Thakuria, N. K. Nath and B. K. Saha, *Cryst. Growth Des.*, 2019, **19**, 523–528.
55 A. Półrolniczak, S. Sobczak and A. Katrusiak, *J. Mater. Chem. C*, 2023, **11**, 16992–17002.
56 M. Dharmarwardana, R. P. Welch, S. Kwon, V. K. Nguyen, G. T. McCandless, M. A. Omary and J. J. Gassensmith, *Chem. Commun.*, 2017, **53**, 9890–9893.
57 M. Dharmarwardana, S. Pakhira, R. P. Welch, C. Caicedo-Narvaez, M. A. Luzuriaga, B. S. Arimilli, G. T. McCandless, B. Fahimi, J. L. Mendoza-Cortes and J. J. Gassensmith, *J. Am. Chem. Soc.*, 2021, **143**, 5951–5957.
58 F. Safari and A. Katrusiak, *J. Phys. Chem. C*, 2021, **125**, 23501–23509.
59 W. Zieliński and A. Katrusiak, *Cryst. Growth Des.*, 2013, **13**, 696–700.
60 A. Katrusiak, M. Rusek, M. Dušek, V. Petříček and M. Szafrański, *J. Phys. Chem. Lett.*, 2023, **14**, 3111–3119.
61 M. D. Curtis, J. Cao and J. W. Kampf, *J. Am. Chem. Soc.*, 2004, **126**, 4318–4328.
62 A. van der Lee and D. G. Dumitrescu, *Chem. Sci.*, 2021, **12**, 8537–8547.
63 M. Kaźmierczak, E. Patyk-Kaźmierczak and A. Katrusiak, *Cryst. Growth Des.*, 2021, **21**, 2196–2204.
64 R. M. Hazen and L. W. Finger, *Comparative Crystal Chemistry: Temperature, Pressure, Composition and the Variation of Crystal Structure*, Wiley, London, 1982.
65 G. M. Sheldrick, *Acta Crystallogr. Sect. C Struct. Chem.*, 2015, **71**, 3–8.
66 O. V. Dolomanov, L. J. Bourhis, R. J. Gildea, J. A. K. Howard and H. Puschmann, *J. Appl. Crystallogr.*, 2009, **42**, 339–341.
67 C. F. MacRae, I. Sovago, S. J. Cottrell, P. T. A. Galek, P. McCabe, E. Pidcock, M. Platings, G. P. Shields, J. S. Stevens, M. Towler and P. A. Wood, *J. Appl. Crystallogr.*, 2020, **53**, 226–235.
68 A. A. Coelho, *J. Appl. Crystallogr.*, 2018, **51**, 210–218.
69 L. Merrill and W. A. Bassett, *Rev. Sci. Instrum.*, 1974, **45**, 290–294.
70 D. Staško, J. Prchal, M. Klicpera, S. Aoki and K. Murata, *High Press. Res.*, 2020, **40**, 525–536.
71 K. Murata and S. Aoki, *Rev. High Press. Sci. Technol./Koatsuryoku No Kagaku Gijutsu*, 2016, **26**, 3–7.
72 G. J. Piermarini, S. Block, J. D. Barnett and R. A. Forman, *J. Appl. Phys.*, 1975, **46**, 2774–2780.
73 H. K. Mao, J. Xu and P. M. Bell, *J. Geophys. Res.*, 1986, **91**, 4673.
74 A. Budzianowski and A. Katrusiak, *High-Pressure Crystallographic*, 2004, vol. 140, pp. 101–112.
75 G. M. Sheldrick, *Acta Crystallogr., Sect. A:Found. Crystallogr.*, 2008, **64**, 112–122.
76 P. R. Willmott, D. Meister, S. J. Leake, M. Lange, A. Bergamaschi, M. Böge, M. Calvi, C. Cancellieri, N. Casati, A. Cervellino, Q. Chen, C. David, U. Flechsig, F. Gozzo, B. Henrich, S. Jäggi-Spielmann, B. Jakob, I. Kalichava, P. Karvinen, J. Krempasky, A. Lüdeke, R. Lüscher, S. Maag, C. Quitmann, M. L. Reinle-Schmitt, T. Schmidt, B. Schmitt, A. Streun, I. Vartiainen, M. Vitins, X. Wang and R. Wullschleger, *J. Synchrotron Radiat.*, 2013, **20**, 667–682.

Article A3

The odd-even alkyl chain effect on the structure and optoelectronic properties of alkyl-substituted perylene diimide (PDI) derivatives at highly strained environments

P. Ratajczyk, S. Sobczak, M. Andrzejewski, P. Woźny, L. Maini, A. Katrusiak

2025, DOI: 10.26434/chemrxiv-2025-2fjc9

The odd-even alkyl chain effect on the structure and optoelectronic properties of alkyl-substituted perylene diimide (PDI) derivatives at highly strained environments

Paulina Ratajczyk, Szymon Sobczak, Michał Andrzejewski, Przemysław Woźny, Lucia Maini, Andrzej Katrusiak

P. Ratajczyk, S. Sobczak, P. Woźny, A. Katrusiak
Faculty of Chemistry, Adam Mickiewicz University, Uniwersytetu Poznańskiego 8, 61-614 Poznań, Poland

M. Andrzejewski
Paul Scherrer Institute, Forschungsstrasse 111, Villigen CH-5232, Switzerland

L. Maini
Department of Chemistry "G. Ciamician", University of Bologna, via Pietro Gobetti 85, 40129 Bologna, Italy

Funding: Polish Ministry of Education and Science (Diamentowy Grant DI2019/0160/49), National Science Center of Poland (grant no. 2023/51/D/ST5/00579), IDUB program (Initiative of Excellence - Research University)

Keywords: crystal structure, high pressure, perylene diimides, phase transitions, structure-property relationships, UV-Vis and PL spectroscopies

When subjected to a highly strained environment, such as high pressure, perylene diimides N-substituted with alkyl chains PDI-C_n (n = 5–8) reveal a combination of structural and optoelectronic responses directed by the odd-even alkyl chain effect. Their phase transitions as well as absorption and emission properties have been systematically analyzed by synchrotron and in-lab X-ray diffraction, UV-Vis, and photoluminescence spectroscopy, complemented by theoretical calculations. Their packing interactions, dominated by π-stacking and weak C-H···O interactions, lead to strikingly similar crystal structures, all

belonging to the triclinic space group $P\bar{1}$. Their distinct polymorphic behavior under high pressure is regulated by the alkyl chain length and conformations, and at high temperatures by the scissor-like opening and closing movement of parallel π-stacked molecules. The most susceptible to external stimuli are the even-PDIs, PDI-C_6 and PDI-C_8, which transform between three phases under high pressure. Compression of π-stacking distances induces a significant bathochromic shift in absorption and emission spectra, most prominently redshifting the absorption edge in PDI-C_8 by 84.4 nm GPa^{-1}. These findings provide valuable insights into the mechanism behind structure-property relations for one of the most promising classes of organic semiconductors and underscore the role of the odd-even effect in organic semiconductors combined with the potential of strain engineering for optimizing material performance.

1. Introduction

In recent years, the growing concern for environmental issues has led to a more intense search for sustainable energy solutions derived from renewable sources.[1] Organic solar cells (OSCs) stand out among the various photovoltaic technologies for their unique advantages, such as affordability, light weight, excellent mechanical flexibility, low production costs, and the ability to tune electronic energy levels through organic synthesis.[2–5] Despite significant recent progress, the enhancement of power conversion efficiency (PCE) of organic photovoltaics (OPVs) remains an ongoing challenge. The highest reported PCE of single-junction OSCs has surpassed 19 %, but this falls short compared to perovskite counterparts, which have achieved an impressive PCE of more than 25 %.[6,7] This significant efficiency gap between OSCs and perovskite solar cells requires further attention and research efforts.

The properties of materials are fundamentally linked to their atomic structure.[8] The development of X-ray crystallography revolutionized the understanding of these connections, enabling the detailed investigation of structure-property relationships. Such insights are essential for designing new materials with tailored functionalities. Over the years, this field has witnessed significant growth, encompassing the study of a variety of physicochemical properties, such as magnetism, electrical conductivity, and optical properties. By manipulating thermodynamic conditions, such as pressure or temperature, it is possible to tune a wide range of material properties in a controlled manner.[9] In particular, applying high pressure offers an efficient means of modifying crystal structures: it shortens interatomic distances, alters bonding patterns and electronic orbitals, and shifts energy levels, thereby opening new routes to enhance the performance of both organic and inorganic solids.[10,11] Moreover, pressure- and temperature-driven phase transitions often yield novel structures with improved or entirely new functionalities—for instance, high pressure has been shown to increase carrier mobility and photoconductivity in pentacene and rubrene crystals.[12,13] Over the past decade, compression has also been extensively employed to explore the structure-property relations of various types of perovskites.[14–18] One-, two-, and three-dimensional halide perovskites have been studied upon compression, revealing a variety of novel phenomena including pressure-induced phase transitions,[11,17,19] metallization,[20,21] band-gap modulation,[22–24] enhanced photoluminescence (PL) intensity[18,25] and improved electric conductivity.[26] Despite these advances, high-pressure studies on structure-property relations of organic photovoltaic materials remain relatively rare,[27,28] providing an exciting opportunity for further exploration and discovery.

Perylene-3,4,9,10-tetracarboxylic acid diimides (PDIs) and their derivatives represent a highly promising class of organic photovoltaic materials thanks to their strong electron-accepting ability, efficient charge-transport properties, and remarkable photo-, thermal-, and chemical stability.[29,30] These properties make PDIs a viable alternative to fullerene-based n-type semiconductors.[2] Beyond their intrinsic stability, PDIs exhibit strong light absorption in the visible spectrum and can be readily modified through chemical substitution, making them versatile building blocks for optoelectronic applications. The use of perylene materials in OSCs was pioneered by Tang in 1986,[31] and since then, PDIs have been extensively investigated, with steady improvements in their efficiency.[2] The physicochemical properties of PDIs can be tuned through chemical modifications, such as the introduction of alkyl or aryl substituents at the *imide*, *bay*, or *ortho* positions of the PDI core,[32] with these modifications exerting a profound influence on the resulting molecular packing and structural variability.[33] Of particular relevance is the introduction of alkyl chains of varying length, as a discrete geometry of terminal methyl groups gives rise to pronounced differences in intermolecular contacts, packing density, and long-range order, depending on whether the number of methylene units in the side chain is odd or even.[34] Even-numbered alkyl chains generally facilitate more compact and symmetric molecular packing,[35,36] resulting in higher packing densities,[37,38] elevated melting points,[38,39] changes in solubility,[40] and increased crystallinity,[37] whereas odd-numbered chains introduce local packing frustration and disorder,[35,41–45] often leading to less efficient intermolecular contacts and lower thermal stability. This odd-even alternation, first recognized in simple *n*-alkanes and liquid crystals, has since been demonstrated to have profound consequences for the structure and function of advanced optoelectronic materials,[46–48] including organic field-effect transistors,[34,49,50] self-assembled monolayers,[50–52] and layered perovskite semiconductors.[41] In π-conjugated systems, the odd–even effect has been shown to regulate not only crystal symmetry and phase stability, but also electronic coupling, charge carrier mobility, and photophysical response.[44,45,53,54] For example, recent studies on fluoranthene-fused imide dimers have revealed needle-like crystal morphology and higher crystallinity for derivatives with even-numbered alkyl chains. Similarly, in 2,7-dialkyl-substituted BTBT derivatives with alkyl chains of n = 5–10, the hole mobility in solution-processed field-effect transistors systematically oscillates with side-chain length: even-numbered derivatives exhibit superior mobility compared to odd-numbered ones, whereas for longer chains ($n > 10$), this trend is reversed.[55,56]

Although the odd–even effect of alkyl chains has been extensively documented in simple n-alkanes, liquid crystals, and selected organic semiconductors, its explicit role in PDI derivatives under conditions of high strain—such as elevated pressure and temperature—remains largely unexplored. Previous studies have focused on individual PDIs or related systems, but a systematic comparison linking alkyl chain parity to crystal packing, phase stability, and optoelectronic responses under external stimuli is still lacking. This leaves an important gap in understanding how subtle chemical modifications translate into structure–property relationships in technologically relevant organic semiconductors.

In this study, we explore the odd-even effects at high pressure in a series of four perylene diimide derivatives with alkyl substituents of varying lengths at the *imide* positions (PDI-C_n, n = 5–8, **Figure 1**), namely *N*,*N*′-dipentyl-3,4,9,10-perylenedicarboximide (PDI-C_5), *N*,*N*′-dihexyl-3,4,9,10-perylenedicarboximide (PDI-C_6), *N*,*N*′-diheptyl-3,4,9,10-perylenedicarboximide (PDI-C_7), and *N*,*N*′-dioctyl-3,4,9,10-perylenedicarboximide (PDI-C_8). The crystal structures of phase I (stable at room conditions) are already known for PDI-C_5, -C_6, and -C_8, whereas that of of PDI-C_7, is reported here for the first time.The structure of PDI-C_5 was originally characterized at room temperature by Hädicke and Graser,[57] later its thermal expansion behavior and high-temperature polymorphs were investigated by Maini et al.[58] Madhu et al. determined the crystal structures of PDI-C_6 and PDI-C_8, together with their absorption and fluorescence properties over the 353–523 K range.[59] The high-pressure and variable-temperature phase transition of PDI-C_6 was subsequently investigated by us.[60] The crystal structure of PDI-C_8 was first described by Xia et al. at 173 K,[61] followed by Okamoto et al. at 298 K.[62] Troshin et al. conducted a systematic study on the PDI-C_n series (n = 4–12), focusing on the influence of side-chain length and thermal annealing on the electrical performance of organic field-effect transistors (OFETs) which highlighted the presence of polymorphic phases at high temperature for the compounds.[63] While these prior studies have contributed important insight, they have not addressed the role of subtle structural phenomena—most notably, the so-called "odd–even effect"—on the structure–property relations in this family of organic semiconductors.

The present study significantly extends the investigation by correlating strain-induced structural deformations with the alkyl-chain length and the resulting variations in optical absorption and photoluminescence across all four PDIs. Our experimental methods include high-pressure synchrotron and in-lab single-crystal X-ray diffraction, along with UV-Vis absorption and PL spectroscopy.

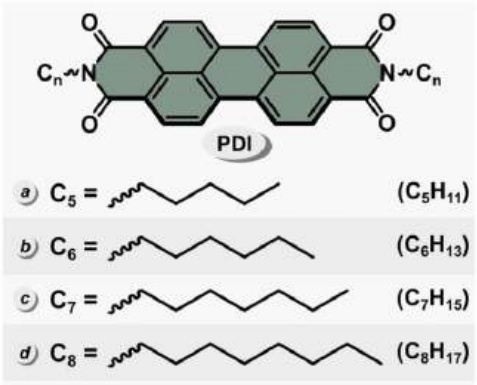

Figure 1. Molecular structures of the investigated N-substituted PDIs, abbreviated as: PDI-C_5 (a), PDI-C_6 (b), PDI-C_7 (c), and PDI-C_8 (d).

2. Results and discussion

2.1. PDI-C_n at room pressure

At ambient conditions (296 K, 0.1 MPa), all four perylene diimides (PDI-C_5, -C_6, -C_7, and -C_8) form isostructural crystals of the triclinic space group type $P\bar{1}$, with comparable unit-cell parameters and half of the PDI molecule in the asymmetric unit ($Z' = 0.5$, Figure S1). The PDI-C_n molecules are π-stacked in characteristic columns running along the [100] direction. The π–π stacking distance ($d_{\pi\text{-}\pi}$) in the investigated series ranges from 3.361(8) Å (in PDI-C_5) to 3.3882(9) Å (in PDI-C_6). In all cases, the neighboring π-stacked columns are stabilized by weak C-H···O interactions. The perylene cores of the molecules are planar, while the alkyl chains protrude out of the plane in the *trans* configuration. To describe the chain conformations, which depend on 3 to 6 torsion angles (τ) depending on the chain length, we adopt a simplified notation using letter descriptors: T (*antiperiplanar*, $\tau = \pm 150$ to 180°), G^+ (*synclinal*$^+$, $\tau = 30$ to 90°) and G^- (*synclinal*$^-$, $\tau = -30$ to -90°), A^+ (*anticlinal*$^+$, $\tau = 90$ to 150°), A^- (*anticlinal*$^+$, $\tau = -90$ to -150°), and C (*synperiplanar*, $\tau = 0$ to ±30°).

2.2. PDI-C_n at high pressure

Pressure-induced structural changes in PDI-C_n were investigated using single-crystal X-ray diffraction **(Figure 2)**. Additionally, the effects of pressure on the optoelectronic properties were explored using UV-Vis absorption and photoluminescence spectroscopy, measured on PDI-C_n crystals compressed in a diamond anvil cell (DAC). Experimental details are provided in the Supporting Information (SI).

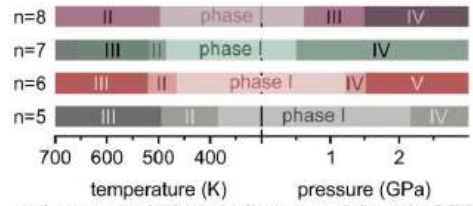

Figure 2. Temperature- and pressure-induced phase transitions in PDI-C_n (n = 5–8).

2.2.1 *N,N'*-Dipentyl-3,4,9,10-perylenedicarboximide (PDI-C5)

The high-temperature investigations on PDI-C_5 reported recently show that this material undergoes two transitions to phases II and III at 385 and 494 K, respectively.[58] All three polymorphs I, II, and III crystallize in the triclinic space group $P\bar{1}$ (CCDC numbers: 2127829-2127831). Our investigations also confirmed earlier reports that PDI-C_5 decomposes before melting, and therefore no melting point can be determined for this compound.[58]

In phase I at room temperature, the PDI-C_5 molecule is located at an inversion center (Z' = 0.5) and the n-pentyl alkyl chains adopt an *antiperiplanar-antiperiplanar-antiperiplanar* (TTT) conformation. The transition between phases I and II induces minor structural changes, primarily affecting the alkyl substituent conformation, from TTT/TTT to TA^+A^+/TA^-A^-. The latter transformation to phase III involves much more pronounced conformational changes leading to an increase in Z' from 0.5 to 1.5. In phase III, one of the PDI-C_5 molecules retains its position at an inversion center with alkyl chains protruding in a *trans* configuration. The other molecule sits at the general position, which allows the release of compression strain by modifying the alkyl chain configuration from *trans* to *cis*. Thus, in phase III, the C_i-symmetric *trans*-molecule adopts an $A^-A^+A^-/A^+A^-A^+$ conformation, while the *cis*-molecule adopts the $A^-A^-A^+/TG^+T$ conformation.

High-pressure single-crystal X-ray diffraction measurements were performed on PDI-C_5 up to 3.84 GPa. Compression of phase I reveals that the most compressible unit-cell parameters are a_I and c_I, primarily due to a reduction of the soft π-stacking distance and deformation of the alkyl chains, respectively. These changes lead to more compact molecular packing, as confirmed by a molecular volume (V_m) reduction of 11.50 % at 1.73 GPa. Specifically, a_I, representing the centroid-to-centroid distance between adjacent PDI-C_5 molecules, decreases by 5.50 % while c_I by 4.94 %, while the least compressible b_I direction contracts by only 1.72 % on compression to 1.73 GPa. At 2 GPa, a discontinuity in the unit-cell parameters, accompanied by a notable reduction in V_m, indicates a phase transition to the high-pressure phase IV **(Figure 3a)**. Further compression of phase IV to 3.84 GPa reveals that the largest relative reductions in the unit-cell parameters occur along the a_{IV} and c_{IV} directions,

consistent with the behavior observed in phase I. However, the linear compressibilities along these directions are notably smaller: a_{IV} is reduced by 3.23 %, and c_{IV} contracts by 3.07 %. The b_{IV} direction remains the least compressible, decreasing by only 0.43 % up to 3.84 GPa. The considerably lower compressibility values suggest that the structure of phase IV is characterized by a highly efficient packing arrangement, in which compression is absorbed mainly through minor conformational adjustments rather than substantial decreases in intermolecular separations. This interpretation is reinforced by the observed V_m reduction of about 5.5%, nearly half of that recorded for phase I under compression.

The monotonic compression of phase I enhances electrostatic interactions between adjacent molecules. At 0.1 MPa, the electrostatic repulsion –CH(δ^+)···(δ^+)HC– is compensated mainly by dispersion and polarization energies, and the electrostatic energy even is reduced by half between ambient pressure and 0.66 GPa. Beyond this point, a subtle centroid contraction (19.52 → 19.26 Å) increases electrostatic repulsion, triggering the phase transition as the alkyl chains adopt more favorable conformations. The *antiperiplanar*-conformer rotates, and τ_1 = (N1–C13–C14–C15) lowers from 173(2)° to 145(3)° (Figure S6), shifting it to an *anticlinal* conformation, while τ_2 and τ_3 maintain values close to 180°. As a result, the conformation changes from TTT/TTT in phase I to A^+TT/A^-TT in phase IV **(Figure 4a)**. Interestingly, after the transition, the trend of rising electrostatic energy resumes, and at the maximum applied pressure of 3.84 GPa, the intermolecular distance approaches the value observed under ambient conditions. This behavior indicates the possibility of additional structural conversion, although likely beyond the hydrostatic limit of the pressure-transmitting medium (PTM) employed in this study. On the other hand, the most stable part of the PDI-C_5 crystal structure is the PDI core, π-stacked through numerous interactions involving carbon atoms and, after the transition, also through newly formed O···O and N···O interactions (Figure S22).

We also analyzed the packing of PDI-C_5 in terms of *pitch* (*P*) and *roll* (*R*) inclinations relative to an ideal cofacial π-stack **(Figure 5)**.[67] The *pitch* angle describes the translation of adjacent molecules in the direction of the long molecular axis, while the *roll* angle along the short molecular axis. In phase I of PDI-C_5 at ambient pressure, the *P* angle is 42.0(3)°, the *R* angle is 22.1(4)°, and the interplanar distance $d_{\pi\text{-}\pi}$ is 3.360(8) Å (Figure 5a and Table S7). Compression to 1.73 GPa does not have a significantly influence on the *P* and *R* angles, but the $d_{\pi\text{-}\pi}$ decreases by 5.5 %. In contrast, the transition to phase IV involves conformational rearrangements of the alkyl chains, lowering the *P* angle to 16.4(8)° and increasing the *R* angle to 28.0(3)° at 2.17 GPa. Notably, the $d_{\pi\text{-}\pi}$ separation expands to 3.217(8) Å (vs. 3.174(9)

Å at 1.73 GPa). Upon further compression to 3.84 GPa, the *P* and *R* angles remain unchanged, while $d_{\pi-\pi}$ decreases by only 2.8%, far less than in phase I. This suggests that π-stacking plays a diminished role in accommodating strain within phase IV.

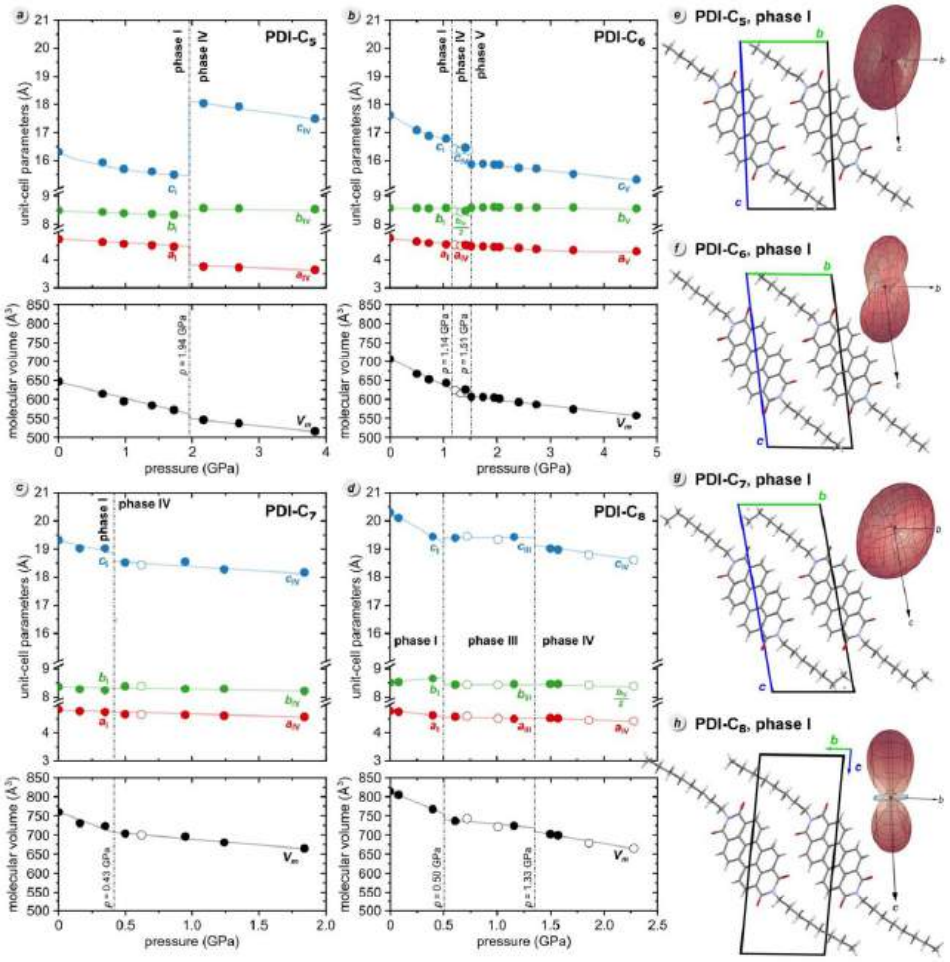

Figure 3. Pressure dependence of the unit-cell dimensions *a*, *b*, *c* (top) and molecular volume ($V_m = V/Z$, where *V* is the unit-cell volume and *Z* is the number of molecules in a unit cell, bottom) for PDI-C_5 (a), PDI-C_6 (b), PDI-C_7 (c), and PDI-C_8 (d). The estimated standard deviations (ESDs) are smaller than the plotted symbols. Unfilled symbols represent data from quick experiments in which only the unit-cell parameters were determined. Arrangements of PDI-C_5 (e), -C_6 (f), -C_7 (g), and -C_8 (h) molecules in the unit-cell along directions [100] with

graphical representations of compressibility tensors for phases I are shown on the right (cf. Figures S7-S9 and Tables S2-S6 in SI for details).

2.2.2 *N,N'*-Dihexyl-3,4,9,10-perylenedicarboximide (PDI-C_6)

Previous studies using DSC and X-ray diffraction at high pressure and varied temperatures revealed the existence of five distinct phases of PDI-C_6.[60] These include two high-temperature phases II and III, forming at 465 K and 521 K, as well as two high-pressure phases IV and V, stable above 1.22 GPa and 1.50 GPa, respectively (Figure 3b). All phases, I–V, crystallize in the triclinic space group $P\bar{1}$. It is also known that phase I remains stable during cooling down to at least 100 K.[60]

The crystal structure of PDI-C_6 phase I closely resembles that of PDI-C_5 phase I—exhibiting very similar unit-cell dimensions, with $Z' = 0.5$ in both cases. At high temperature, phase I transforms into phase II, with Z' increasing from 0.5 in phase I to 1.5 in phase II by accommodating PDI-C_6 molecules in both *cis* and t*rans* conformations. Moreover, despite the similarities between phases I and high-temperature phases II of PDI-C_6 and III of PDI-C_5, the mechanism of the phase transition appears to be similar. The conformations of the alkyl chains in the *trans* PDI-C_6 molecule are $TTA^{+}T/TTA^{-}T$, while in the *cis* molecule, the alkyl chains can be denoted with $TTTC/TA^{+}TG^{-}$. Above 521 K, a strong reconstructive transition occurs, significantly impacting single-crystal quality, and hindering the structural determination of phase III.

High-pressure single-crystal X-ray diffraction measurements on PDI-C_6 up to 4.61 GPa reveal that the first phase transition occurs already at 1.22 GPa, indicating that much less stress is required to induce the structural rearrangement of PDI-C_6 phase I than in PDI-C_5 phase I. Compression of PDI-C_6 phase I, similarly to the compression of PDI-C_5, leads to the most pronounced contractions of parameters a_I and c_I, while b_I remains the least compressible direction for both materials. The transition to high-pressure phase IV above 1.22 GPa doubles the b axis and shrinks c by 2.2 %, while a continues decreasing with no noticeable anomaly at the phase transition. Such changes arise from conformational change, switching from the TTTT/TTTT alkyl chain conformation to $G^{+}TG^{-}T/G^{-}TG^{+}T$ (Figure 4b). At 1.52 GPa, a new discontinuity in the compressibility of the unit-cell dimensions appears, characterized by a drop in c and a halving of b, indicating another phase transition to phase V. Upon transformation to phase V, the structural strain accumulated during compression is relieved by lowering the crystal symmetry and changing the Z' to 0.5. As the pressure increases up to 4.61 GPa, parameter a_V shortens by 4.41 % and parameter c_V is contracted by 3.52 %, while b_V is

marginally reduced (0.38 %). Compared to PDI-C_5, pressure effects in PDI-C_6 have a weaker impact on angle *P*, but much stronger on angle *R* (Figure 5b). Despite these differences, the overall change in $d_{\pi\text{-}\pi}$ for PDI-C_6 resembles that in PDI-C_5, reaching 9.1 % up to 3.5 GPa.

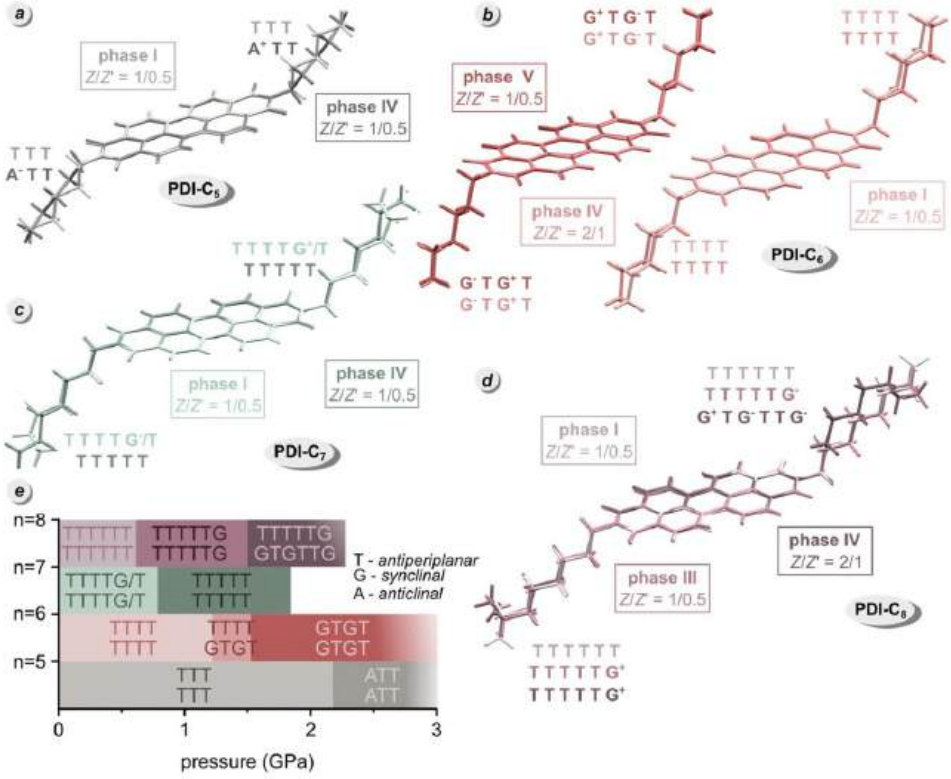

Figure 4. Conformational changes in PDI-C_5 (a), PDI-C_6 (b), PDI-C_7 (c), PDI-C_8 (d) molecules observed in pressure-induced phases; (e) summarizes these conformational variations across all PDI-C_n phases.

2.2.3. *N,N'*- Diheptyl-3,4,9,10-perylenedicarboximide (PDI-C_7)

The crystal structure of PDI-C_7 has not been previously reported. However, calorimetric studies indicate that phase I remains stable up to 486 K, above which it undergoes a solid-solid phase transition.[63,68] A subsequent phase transition occurs at 518 K, followed by melting at 658 K (Figure S12). These high-temperature solid phases will be labeled as phase II and III, respectively.

At room conditions, PDI-C_7 (phase I) crystallizes in triclinic space group $P\bar{1}$, with the molecule lying on an inversion center ($Z' = 0.5$). At 296 K/0.1 MPa, all methylene groups in

alkyl moiety are bonded in *antiperiplnar-antiperiplanar* fashion, except for the terminal methyl group which displays positional disorder with site occupancy factors of 0.596(14) and 0.404(14). The torsion angles involving the terminal carbons (τ_5) are ±78.8(8)° and ±153(1)°, respectively. Thus, the *n*-heptyl substituent is disordered between the TTTTG$^+$ and TTTTT conformations. With increasing pressure, the disorder disappears at 0.50 GPa, and τ_5 becomes 175.1(9)°, indicating the TTTTT conformers (Figure 4c). This structural as well as conformational change allows phase I to remain stable up to at least 1.84 GPa. The influence of low temperature is much less pronounced than the effect of compression and the disorder of the terminal methyl group is preserved down to 100 K (Figure S11).

The compression of phase I is strongly anisotropic. Initially, from 0.1 MPa to 0.35 GPa, the c_I parameter exhibits the most substantial contraction. Above 0.5 GPa, when the disorder is extinguished, a more uniform contraction of all unit-cell parameters is observed. Specifically, from 0.50 GPa to 1.84 GPa, the a_{IV}, b_{IV}, and c_{IV} parameters decrease by 2.21 %, 1.97 %, and 1.89 %, respectively, and V_m decreases by 5.58 %. At 0.1 MPa, the P and R angles of PDI-C_7 are 43.42(3)° and 21.41(4)°, respectively, and they hardly change with increasing pressure. The $d_{\pi\text{-}\pi}$ distance decreases by 5.6 % over the pressure range from 0.1 MPa to 1.84 GPa, at a similar rate as in PDI-C_5 and PDI-C_6. Based on these results, we anticipate that PDI-C_7 undergoes an isostructural transition between disordered phase I and ordered phase IV. It is possible that the transition proceeds through the supercritical region with no sharp boundary between phases. Compression above 2 GPa deteriorated the quality of PDI-C_7 measurements, preventing the collection of single-crystalline data at higher pressures.

2.2.4. *N,N'*-Dioctyl-3,4,9,10-perylenedicarboximide (PDI-C_8)

Previously reported calorimetric studies revealed that PDI-C_8 undergoes a phase transition at 497 K to a high-temperature phase labelled as phase II.[63] High-pressure single-crystal X-ray diffraction experiments on PDI-C_8, performed at room temperature up to 2.28 GPa (Figure 3d), revealed two pressure-induced phase transitions: at 0.61 GPa to phase III and at 1.50 GPa to phase IV, marked by abrupt changes in molecular volume and unit-cell parameters. All identified phases of PDI-C_8, like in PDI-C_5, -C_6, and -C_7, crystallize in triclinic space group type $P\bar{1}$. Notably, the transition to phase III occurs at a much lower pressure than in PDI-C_6 and PDI-C_5, indicating a significant role of the alkyl substituents conformation in compensating the compression strain. The transition to phase IV increases the Z' from 0.5 to 1 and, analogously to the transformation between phases I and IV observed in PDI-C_6, a

doubling of parameter b. Further compression beyond 2.5 GPa led to a deterioration in PDI-C_8 measurements quality, as also observed in PDI-C_7.

In phase I, where the alkyl chains adopt an TTTTTT/TTTTTT conformation, the V_m decreases significantly from 814.05(8) Å^3 at 0.1 MPa to 766.80(16) Å^3 at 0.40 GPa. This reduction of V_m by 5.8 % is primarily driven by the compression of unit-cell parameters a_I and c_I, which decrease by 3.1 % and 4.2 %, respectively. Interestingly, compression to 0.40 GPa leads to elongation of the b_I axis by 1.7 % (K = -37.6 TPa^{-1}, Table S6). This counterintuitive effect, known as negative linear compressibility (NLC),[69] differs significantly from the behaviour observed in other alkyl-substituted PDIs, however a similar effect has also been reported for another member of the PDI family, phenyl substituted perylene diimide PTCDI-Ph (K = -6.1 TPa^{-1}; pressure range 0–0.78 GPa).[27] The transition to phase III has the most pronounced effect on the terminal methyl group, which adopts $\tau_6 = \pm 72.8(7)°$, altering the alkyl conformation to TTTTTG$^+$/TTTTTG$^-$. The compressibility of phase IV, which is stable above 1.3 GPa, resembles that of phase I, with a_{IV} and b_{IV} being slightly reduced, while the parameter c_{IV} undergoes a pronounced contraction. Conformational changes in phase IV are associated with an increase in Z' from 0.5 to 1, where one alkyl chain maintains the TTTTTG$^+$ conformation, and the opposite alkyl chain adopts a G$^+$TG$^-$TTG$^-$ conformation (Figure 4d).

At 0.1 MPa, the P and R angles of PDI-C_8 are 42.70(3)° and 20.38(4)°, respectively, similar to those observed for other investigated PDI-C_n. Up to 1.5 GPa, compression only slightly affects the P angle. However, in phase IV, the P angle becomes wider indicating sliding of molecules along the longer molecular axis. The R angle shows more pronounced pressure induced changes: it decreases by 3.21° in phase I (from 0.1 MPa to 0.4 GPa), increases by 2.83° during the phase I to III transition, then decreases by 1.38° within phase III, followed by a further decrease of 1.96° during the transition from phase III to IV. The $d_{\pi\text{-}\pi}$ decreases by 4.94 % overall between 0.1 MPa and 1.57 GPa.

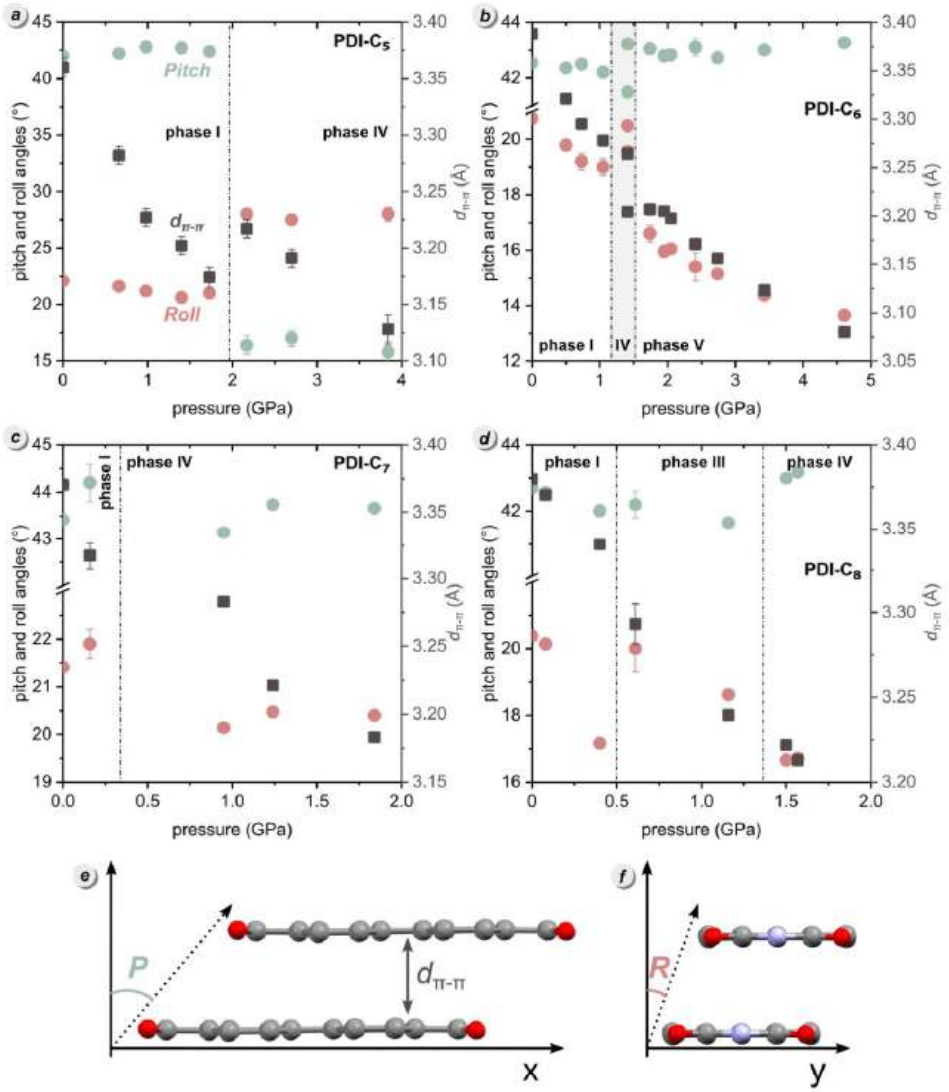

Figure 5. π-Stacking parameters of molecules PDI-C_5 (a), PDI-C_6 (b), PDI-C_7 (c), PDI-C_8 (d) under pressure: pink and green symbols represent the *pitch* (e) and *roll* (f) angles and grey squares mark the $d_{\pi-\pi}$ distance.[67] Angles *P* and *R*, as well as distance $d_{\pi-\pi}$ are illustrated in (e) and (f), where the π-stacked molecules are projected along their shortest and longest in-plane axes, while alkyl substituents and H atoms are omitted for clarity. Where not indicated, the ESDs are smaller than the plotted symbols.

2.3. Optoelectronic responses of PDI-C_n

To investigate the pressure-induced changes of the band-gap energy (E_g), we performed UV-Vis absorption spectroscopy experiments on solid PDI-C_5, PDI-C_6, PDI-C_7, and PDI-C_8 under compression up to ~4 GPa and following decompression. All four PDI-C_n exhibit a progressive redshift in their absorption spectra with increasing pressure, causing the PDI-C_n films to darken visibly from red to black **(Figure 6)**. These redshifts are fully reversible upon pressure release, with the films returning to their original color. The pressure dependence of the E_g is shown in **Figure 7**.

At ambient conditions, the absorption edges for PDI-C_5, -C_6, -C_7, and -C_8 are 636, 664, 625, and 634 nm, respectively, corresponding to the E_g of approximately 1.95, 1.87, 1.99, and 1.96 eV (Table S10-S13). The E_g of PDI-C_5 exhibits a monotonic decrease at a rate of approximately 0.14 eV GPa^{-1} up to 2.08 GPa. Following a phase transition, a small discontinuity in the E_g is observed, with the decrease continuing at a slightly reduced rate of 0.12 eV GPa^{-1}. PDI-C_6 shows a consistent linear decrease in the E_g at a rate of 0.13 eV GPa^{-1} across the measured pressure range (0.1 MPa to 3.46 GPa). PDI-C_7 displays an initial rapid decrease at 0.18 eV GPa^{-1}, followed by a drop at 0.70 GPa, and a subsequent decrease at 0.12 eV GPa^{-1}. This discontinuity occurs in the pressure region where the ordering of C_7 chains is observed. The pressure-induced E_g behavior of PDI-C_7 deviates from the trend observed for its analogs PDI-C_5, -C_6, and -C_8 (Figure 7). Finally, PDI-C_8 exhibits a linear decrease in the E_g throughout the compression cycle at a rate of 0.17 eV GPa^{-1}. Of the four studied derivatives, PDI-C_8 demonstrates the largest overall change in E_g, with a total decrease of approximately 0.69 eV up to 3.82 GPa.

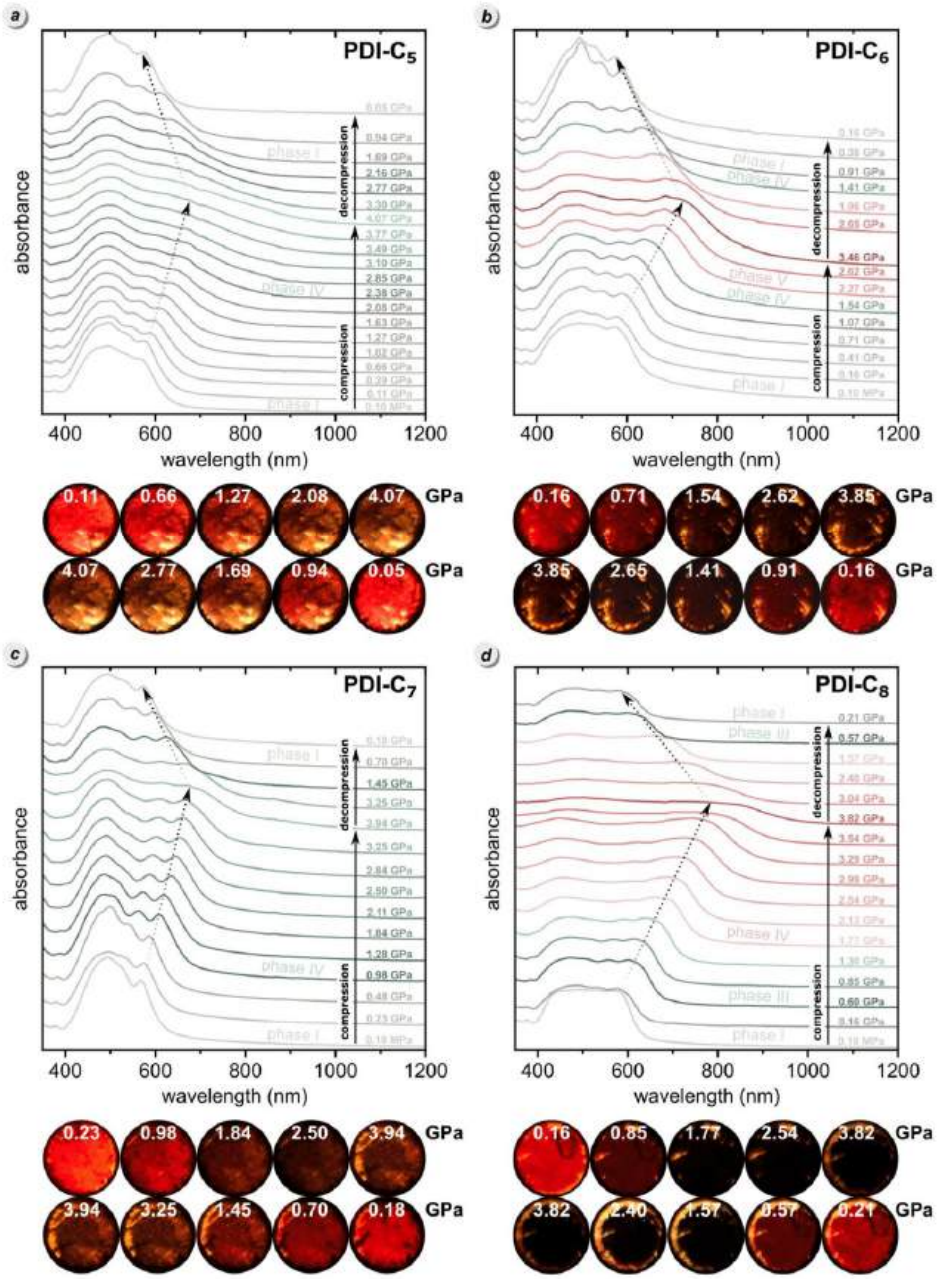

Figure 6. Pressure evolution of the absorption spectra of PDI-C_5 (a), PDI-C_6 (b), PDI-C_7 (c), and PDI-C_8 (d). Corresponding images of thin-film samples under increasing pressure (top) and upon pressure release (bottom) are shown below the respective plots.

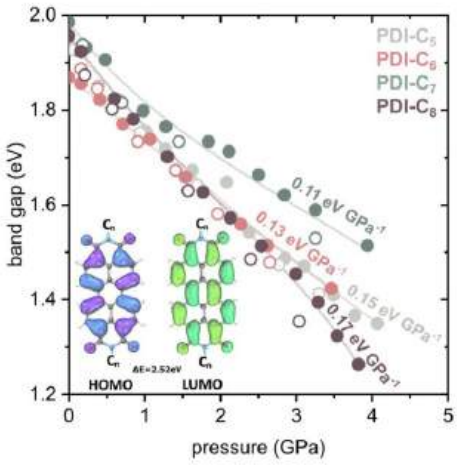

Figure 7. Pressure dependence of band-gap energy E_g for PDI-C_5, PDI-C_6, PDI-C_7, and PDI-C_8. Filled and unfilled symbols represent the compression and decompression runs, respectively. Inset: Frontier molecular orbitals (HOMO and LUMO) of the studied PDI derivatives. The HOMO (highest occupied molecular orbital) and LUMO (lowest unoccupied molecular orbital) are predominantly localized on the PDI core, illustrating the main chromophoric unit responsible for the optical properties. ΔE refers to HOMO-LUMO gap.

According to our quantum-mechanical calculations, the HOMO–LUMO gap for the investigated PDI molecules with varying alkyl chain lengths is approximately 2.52 eV (Figure 7 and Table S14). It is important to emphasize that these calculations were performed for isolated molecules in the gas phase and, as such, inherently neglect key factors present in condensed phases, including intermolecular interactions, crystal packing effects, and dielectric screening from the surrounding medium. These factors can significantly modulate the energies of frontier orbitals and thus alter the HOMO–LUMO gap. In order to bypass this limitation, additional calculations in CrystalExplorer were performed to provide an analysis of intermolecular interactions (Figure S20 and Table S16, S17). Nevertheless, the calculated values are consistent with previously reported HOMO–LUMO gaps for related PDI derivatives, which typically fall within the range of 2.0 to 2.5 eV, depending on the specific nature and length of the substituents as well as the electronic environment.[30] In our study, the alkyl chains attached to the PDI core function primarily as solubilizing groups. Similarly, our results indicate that while variations in alkyl chain length and conformation in PDI derivatives strongly affect physicochemical properties such as solubility, molecular packing, and possibly thermal stability, they do not substantially alter the electronic structure of the PDI

chromophore or its optical absorption profile. This distinction aligns well with the literature on both chlorophyll and organic dyes, where peripheral alkyl substituents modulate material processing and intermolecular interactions without significantly perturbing the intrinsic electronic transitions governing light absorption. For example, studies on PDIs and related rylene dyes consistently report that substituents improve solubility and crystalline order but leave π-π* transitions localized on the core largely unchanged. Likewise, work on chlorophyll analogues underscores the minor role of the phytol tail in electronic excitation, emphasizing its contribution to environment-induced modulation instead of intrinsic spectral shifts.

2.4. High-pressure photoluminescence (PL)

We investigated the PL properties of PDI-C_5, -C_6, -C_7, and -C_8 materials under both ambient and high-pressure conditions. We observed that the relative intensity of the emission and excitation spectra varies with the length of the alkyl chain **(Figure 8)**. For all compounds, the excitation spectra for the emission band at λ = 700 nm exhibit a broad band in the 220–500 nm range, while the emission spectra show a broad red –NIR band (600–850 nm) upon excitation at λ = 370 nm. At ambient pressure, the excitation band maximum shifts depending on the alkyl chain length: 360 nm for PDI-C_5, 368 nm for PDI-C_6, 373 nm for PDI-C_7, and 370 nm for PDI-C_8. A similar trend is observed for the emission band maxima, which occur at 703 nm for PDI-C_5, 696 nm for PDI-C_6, 685 nm for PDI-C_7, and 689 nm for PDI-C_8, indicating a chain-length-dependent modulation of the PL characteristics.

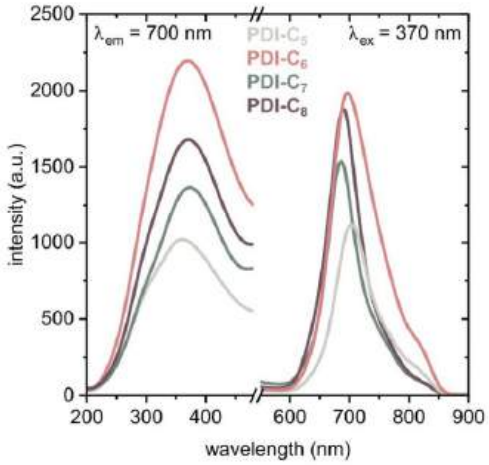

Figure 8. Emission and excitation spectra for the PDI-C_n materials at ambient conditions.

Subsequently, the PL properties of the PDI-C_n excited with the $\lambda = 450$ nm diode were examined up to ~5 GPa using DAC. All investigated materials exhibited a broad emission band in the NIR spectral range **(Figure 9)**. The initial shift of the emission band maximum observed in the DAC can be attributed to the influence of the pressure-transmitting medium. Compression of PDI-C_5 phase I causes a small decrease in PL intensity (Figure S14a). After the transition to phase IV, the emission band remains almost constant, but overall the integrated PL intensity increases, likely due to band broadening—i.e., the full width at half maximum (FWHM) increases with pressure (Figure S17a). Spectral shifts observed in phase IV significantly exceed the changes in the PL spectrum observed in phase I, reaching 8.9 and 6.1 nm GPa^{-1}, respectively (Figure S16a). The band centroid was calculated using a quadratic polynomial fit (i.e., a second-order polynomial function) as described in **Equation 1**:

$$y = ax^2 + bx + c \quad (1)$$

where a is 0.48, b is 5.31 and c is 777.44, and R^2 is 0.999. Based on the fitted function, we have calculated the relative sensitivity (S_r) for the band shift parameter using **Equation 2**:

$$S_r = 100\% \frac{1}{\lambda} \left| \frac{d\lambda}{dp} \right| \quad (2)$$

where λ is the band centroid position and p is the pressure value. For PDI-C_5, the emission band shifted by ≈40 nm across the pressure range with sensitivity increasing from 0.70 % GPa^{-1} at 0.05 GPa to 1.25 % GPa^{-1} at 5.29 GPa. Notably, PDI-C_5 was the only derivative exhibiting stable luminescence intensity coupled with an increase in relative sensitivity over the investigated pressure range.

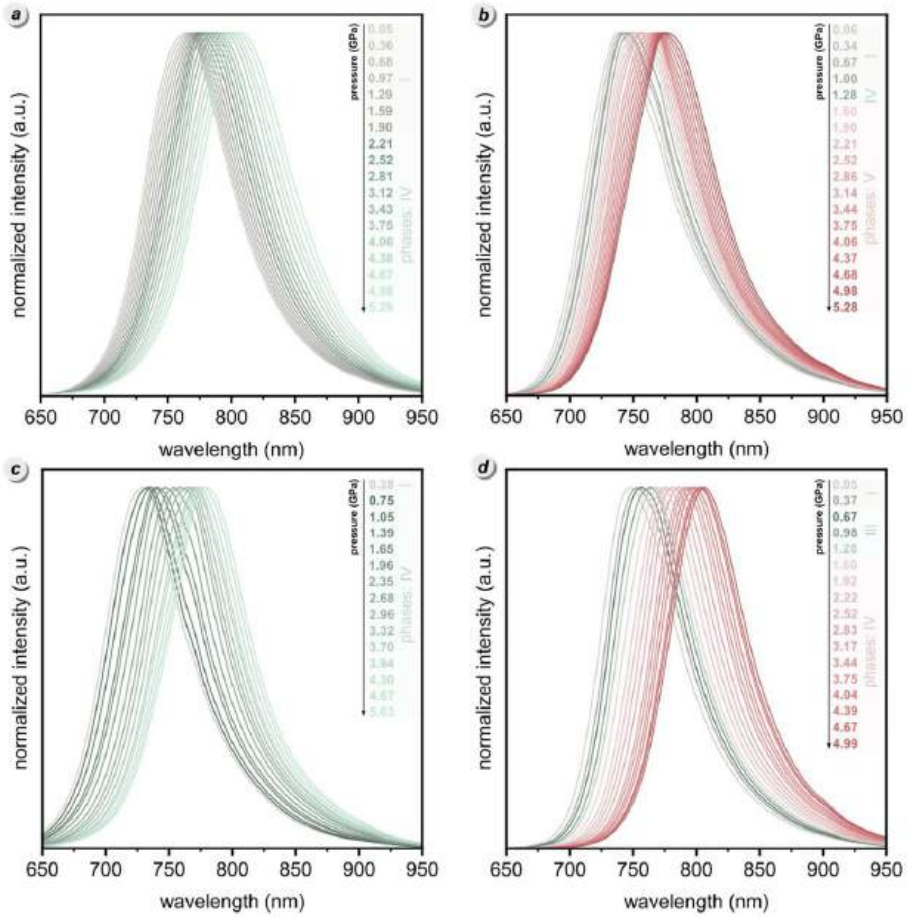

Figure 9. Normalized emission spectra of PDI-C_5 (a), PDI-C_6 (b), PDI-C_7 (c), and PDI-C_8 (d) during the compression cycles.

The longer alkyl chain in PDI-C_6 causes more prominent pressure effects in the emission spectra. The PL intensity for PDI-C_6 in phases I and IV is only negligibly affected by compression, but after the transition to phase V, the PL intensity increases markedly (Figure S14b). The emission band maximum shifts by 29.5 nm, resulting in the polynomial function (Equation 1) with parameters $a = -0.27$, $b = 7.21$, and $c = 762.70$. The S_r decreased from 0.85 % GPa^{-1} to ≈ 0.61 % GPa^{-1} at 5.28 GPa (Equation 2). Phase transitions do not affect the spectral shift of the emission band, which assumes 5.75 nm GPa^{-1} (Figure S16b), but the FWHM increases in phases I and IV, reaching its maximum at 2.5 GPa in phase V.

For PDI-C_7, the luminescence intensity decreased monotonically up to 1 GPa, when the transition to phase IV occurs. This phase transition pressure is shifted compared to that

determined by structural investigations, likely due to the faster compression rates employed during luminescence measurements. Above this pressure, the intensity declined gradually up to ≈4 GPa, accompanied by significant band broadening. The redshift of the PL band of PDI-C_7 is almost linear from 745 to ~780 nm ($\Delta\lambda \approx 47$ nm) at 5.03 GPa, following the quadratic function (Equation 1) with parameters $a = -0.76$, $b = 14.70$, and $c = 737.45$. The sensitivity (S_r) decreased from 1.90 % GPa^{-1} to 0.89 % GPa^{-1}, while the FWHM remained nearly constant. The phase transition point between phases I and IV can be detected only as a small deviation of the PL intensity (Figure S14c).

The transitions between phases I, III, and IV of PDI-C_8 are not reflected in the PL intensity (Figure S14d). It gradually decreases until the complete transition to phase IV, after which the PL intensity starts to increase above 3.4 GPa. The rate of spectral shift changes from 12 nm GPa^{-1} up to 2.8 GPa to 7.6 nm GPa^{-1} at higher pressure. In PDI-C_8, the FWHM of the emission band is useful for the detection of different phases. In contrast to other parameters, it is constant for phase I then decreases drastically during compression of phase III and increases when phase IV is compressed (Figure S17d). PDI-C_8 displays the most pronounced redshift in emission spectra, consistent with its absorption behavior, with a total shift of 51.1 nm between 0.1 MPa and 4.99 GPa **(Figure 10)**, fitting the polynomial (Equation 1) with $a = -0.66$, $b = 14.10$, and $c = 767.68$. The sensitivity decreased linearly from 1.82 % GPa^{-1} at ambient pressure to 0.91 % GPa^{-1} at 5 GPa (Equation 2). Figure 10 shows that longer alkyl substituents induce a greater redshift in the emission spectra. However, PDI-C_6 is an exception, exhibiting the smallest observed shift.

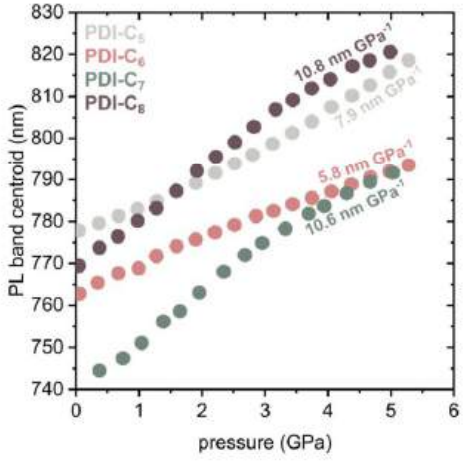

Figure 10. Pressure-induced PL bandshift for PDI-C_5, -C_6, -C_7, and -C_8.

2.5. The odd-even effect in PDI-C_n series

We have observed an odd-even effect in the PDI-C_n series, manifested in several ways. For the even-n alkyl derivatives, two pressure-induced phase transitions are observed, whereas odd-n alkyl chains exhibit only a single transition (Figure 2a). The even-n alkyls are conformationally more flexible under pressure, while the odd-n chains remain relatively rigid (Figure 2b). In the even-n alkyls, the *synclinal* conformers appear at higher pressures, whereas they are absent in the odd-n chains. Notably, in PDI-C_7, the *synclinal* conformations are present in the disordered ambient phase but disappear under elevated pressure. A direct consequence of this behavior is that up to 2 GPa, the volume is more compressed for even-n analogues than for odd ones **(Figure 11)**. The small linear compressibility along *b* of PDI-C_6 and the negative linear compressibility of PDI-C_8 contrasts with the larger linear compressibilities along *b* in PDI-C_5 and PDI-C_7; also, PDI-C_5 and PDI-C_7 elongate along *b* at the transitions to higher-pressure phases, whereas in PDI-C_6 and PDI-C_8 the transitions result in jumpwise shortening of the *b* parameter. This behaviour is consistent with the stronger effect of pressure on the even alkyl substituents, which stronger compensate the effect of the external stimuli. Moreover, the odd–even effect is also reflected in the π–π stacking distance at ambient pressure, with $d_{\pi-\pi}$ being longer for the even-n alkyls and shorter for the odd ones (the inset in Figure 12a). In contrast, the pressure-induced shifts of the absorption edge and PL bands did not reveal any discernible odd–even effect. It is plausible that the odd–even effects in the PDI-C_n series arise from the position of the terminal methyl, either sticking out or closer to the molecular planes, respectively. Consequently, the even-n alkyl substituents are more prone to yield under compression.

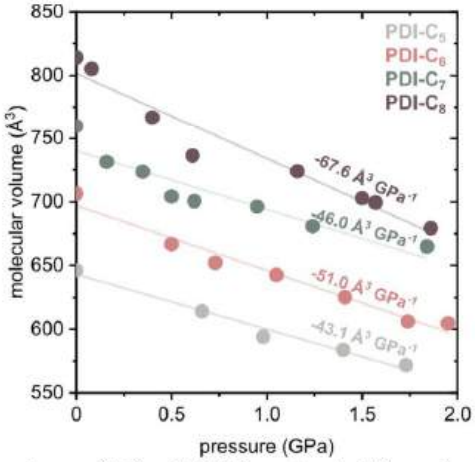

Figure 11. Molecular volumes (V_m) of PDI-C_n extracted from single-crystal measurments plotted as a function of pressure up to 2 GPa.

2.6. Comparative structural analysis in the PDI-C_n series

From our systematic studies on the PDI-C_n (n = 5–8) series, several conclusions can be drawn about structural transformations as a function of temperature and pressure. The most apparent systematic changes are:

- For all the PDI-C_n compounds, the π-stacking distance is reduced with the average rate of 0.08 Å GPa^{-1}; for PDI-C_5, the $d_{\pi\text{-}\pi}$ distance abruptly increases by nearly 0.04 Å at the phase transition (2.17 GPa), whereas for PDI-C_6 it decreases by 0.06 Å at 1.41 GPa **(Figure 12a)**;
- All PDI-C_n compounds assume the all-T conformation in phase I; an exception is the disordered conformation of PDI-C_7 in phase I, including the all-T conformer as the minor disorder component; the pressure-induced transformations lead to other conformers (Figure 4e);
- Pressure influences the arrangement of π-stacks; while it has a minimal effect on the displacement of adjacent molecules along their long molecular axis, measured by the relatively stable angle *P*. Pressure effect on the displacement along the short molecular axis is more pronounced and angle R decreases toward the ideal cofacial π-stacking arrangement. However, PDI-C_5 exempts from this trend, by significantly decreasing angle *P* by 26° and increasing angle *R* by 7° at the transition to phase IV at 2.17 GPa;
- Changes in $d_{\pi\text{-}\pi}$ correlate with changes in angle *R*; they both decrease with increasing pressure, e.g. in PDI-C_6, the decrease in angle *R* mirrors that of $d_{\pi\text{-}\pi}$; conversely, in PDI-C_5, the unexpected increase in *R* angles coincides with an increase in $d_{\pi\text{-}\pi}$;
- The increasing alkyl-chain length correlates with lower pressures and higher temperatures required for the transitions to occur – for example, phase I of PDI-C_5 is destabilized at 2.17 GPa, of PDI-C_6 at 1.22 GPa and of PDI-C_8 at 0.61 GPa; an exception is observed for PDI-C_7, where the alkyl chains gradually order below 0.50 GPa, without detectible phase-transition anomaly.
- As expected, the π-stacking distance $d_{\pi\text{-}\pi}$ correlates with the band gap energy E_g; Figure 12 shows the distance $d_{\pi\text{-}\pi}$ as a function of pressure and the E_g values as a function of $d_{\pi\text{-}\pi}$ distances in the PDI-C_n series.

The compressibility of the crystals visualized by the graphical representation of the compressibility tensors in Figures 3(e-h) consistently indicates the smallest compression along the CH···O bonded π-stacking columns in all the PDI-C_5 – PDI-C_8 crystals, respectively, in their phase I. In phase I of PDI-C_8, the crystals exhibit the negative linear

compressibility, which can be connected to the largest absorption of the external stimuli by the longest alkyl chains in this compound. This trend of the least-compressed unit-cells parameters b (parallel to the π-stacked columns) continues also in the high-pressure phases. The small or even negative compressions along b correlate with the reduction of the *roll R* angles in PDI-C_5, PDI-C_6 and PDI-C_8 (Figure 5). In other words, the molecular cores gradually become more parallel to the (100) plane, or more perpendicular to the π-stacking columns, which counteracts the compression along the b direction. Noteworthy, the reduction in the *roll* angle is the largest in PDI-C_8, consistently with the direction of the negative linear compressibility. However, in PDI-C_7, the R angle exemps from this trend and it somewhat increases with pressure for the only measurement performed within the exceptionally narrow phase I. On one hand, this increased R angle in phase I of PDI-C_7 crystal corresponds to its compressibility considerably larger than those in PDI-C_5, PDI-C_6 and PDI-C_8 (Figure 3). On the other hand, the increased R angle in phase I of PDI-C_7 and its still highest stiffness along b shows that the compression of the PDI derivatives is a complex process involving multiple strutural parameters.

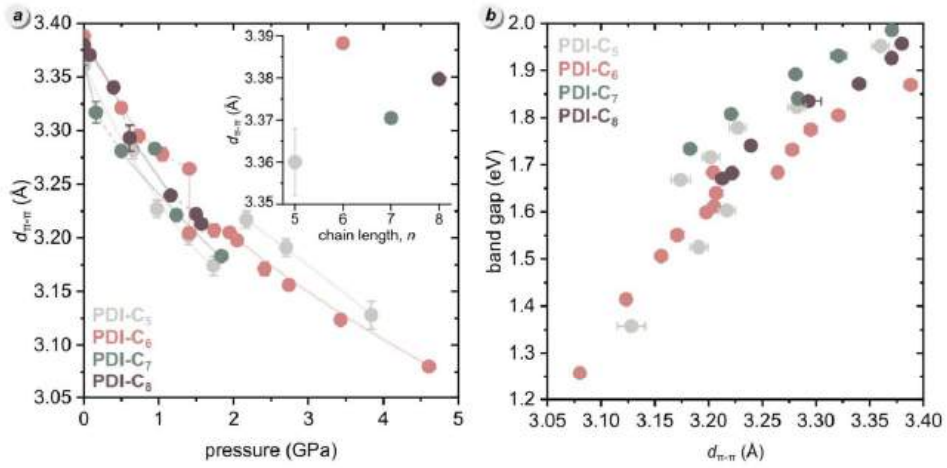

Figure 12. (a) π-π stacking distance ($d_{π-π}$) as a function of pressure for PDI-C_n. Inset: $d_{π-π}$ at 0.1 MPa for PDI-C_n with n = 5–8. (b) E_g as a function of $d_{π-π}$ for PDI-C_n.

3. Conclusion

This study elucidates the polymorphic behavior and solid-state phase transitions of four N-substituted alkyl chain perylene diimides (PDI-C_n, n = 5–8). All identified phases consistently exhibit a triclinic space group type $P\bar{1}$ across a broad range of temperatures and pressures.

Among the studied PDIs, PDI-C_6 displays the richest polymorphism with five distinct crystalline phases. At ambient conditions, all PDI-C_n crystallize in an isostructural arrangement. The crystal of PDI-C_7 is the least prone to transformations, exhibiting only changes of its *n*-heptyl disorder. All pressure-induced structural transformations in PDI-C_n, n = 5–8, are primarily attributed to deformations within the alkyl chains, directly influencing the intermolecular interactions and packing. Under high pressure, no scisors-like transformations previously reported for the high-temperature phase II in PDI-C_6, and in phase III in PDI-C_5, have been observed. The pressure-dependent optical studies revealed significant redshifts in absorption and emission spectra, such as a remarkable shift of 303 nm for PDI-C_8 absorption between 0.1 MPa and 3.54 GPa. Modifications in the length and conformation of the alkyl chains do not significantly affect the shape and spatial distribution of the frontier molecular orbitals (HOMO and LUMO). The electronic density of these orbitals remains predominantly localized on the PDI core, indicating that the alkyl substituents act mainly as steric and solubilizing groups without substantially perturbing the core's electronic structure. This observation allows us to conclude that the optical and electronic properties associated with the frontier orbitals are governed primarily by the PDI chromophore itself, and not by the peripheral alkyl chains. PL spectroscopic analysis further confirms this conclusion and enabled us to precise detection of pressure-induced phase transitions in PDI derivatives, particularly through band broadening caused by energy-level splitting and altered π-π interactions in high-pressure phases. Among the PDI-C_n series, PDI-C_5 emerges as the most promising candidate for optical manometry due to its stable luminescence intensity, strong pressure response, and uniquely increasing relative sensitivity as a function of pressure. By combining the high-pressure diffraction and optical data, we established a clear correlation between structural modifications and optical responses. These findings advance our understanding of PDI behavior under extreme conditions, demonstrating the efficacy of pressure as a powerful tool to precisely tune the optical and structural properties of materials.

[CCDC ###### contains the supplementary crystallographic data for this paper. These data can be obtained free of charge from The Cambridge Crystallographic Data Centre via www.ccdc.cam.ac.uk/data_request/cif.]

Acknowledgements

We are grateful to Dr. Nicola Casati for providing access to a synchrotron at PSI, Villigen. This work was supported by the Polish Ministry of Education and Science (Diamentowy

Grant DI2019/0160/49) and National Science Center of Poland (grant no. 2023/51/D/ST5/00579).

Data Availability Statement

((include as appropriate, including link to repository))

Received: ((will be filled in by the editorial staff))
Revised: ((will be filled in by the editorial staff))
Published online: ((will be filled in by the editorial staff))

References

[1] Y. Liu, B. Liu, C. Q. Ma, F. Huang, G. Feng, H. Chen, J. Hou, L. Yan, Q. Wei, Q. Luo, Q. Bao, W. Ma, W. Liu, W. Li, X. Wan, X. Hu, Y. Han, Y. Li, Y. Zhou, Y. Zou, Y. Chen, Y. Li, Y. Chen, Z. Tang, Z. Hu, Z. G. Zhang, Z. Bo, *Sci. China Chem.* **2022**, *65*, 224.

[2] J. Cao, S. Yang, *RSC Adv.* **2022**, *12*, 6966.

[3] S. Gu, H. Neugebauer, N. S. Sariciftci, **2007**, 1324.

[4] B. Kippelen, J. L. Brédas, *Energy Environ. Sci.* **2009**, *2*, 251.

[5] J. Miao, Y. Wang, J. Liu, L. Wang, *Chem. Soc. Rev.* **2022**, *51*, 153.

[6] J. Fu, P. W. K. Fong, H. Liu, C. S. Huang, X. Lu, S. Lu, M. Abdelsamie, T. Kodalle, C. M. Sutter-Fella, Y. Yang, G. Li, *Nat. Commun.* **2023**, *14*, 1760.

[7] A. J. Gillett, A. Privitera, R. Dilmurat, A. Karki, D. Qian, A. Pershin, G. Londi, W. K. Myers, J. Lee, J. Yuan, S. J. Ko, M. K. Riede, F. Gao, G. C. Bazan, A. Rao, T. Q. Nguyen, D. Beljonne, R. H. Friend, *Nature* **2021**, *597*, 666.

[8] D. R. Allan, *IUCrJ* **2024**, *11*, 438.

[9] A. Katrusiak, *Acta Crystallogr. Sect. A Found. Crystallogr.* **2008**, *64*, 135.

[10] L. Zhang, Y. Wang, J. Lv, Y. Ma, *Nat. Rev. Mater.* **2017**, *2*, 1.

[11] A. Jaffe, Y. Lin, C. M. Beavers, J. Voss, W. L. Mao, H. I. Karunadasa, *ACS Cent. Sci.* **2016**, *2*, 201.

[12] Z. Rang, A. Haraldsson, D. M. Kim, P. P. Ruden, M. I. Nathan, R. J. Chesterfield, C. D. Frisbie, *Appl. Phys. Lett.* **2001**, *79*, 2731.

[13] Z. Rang, M. I. Nathan, P. P. Ruden, V. Podzorov, M. E. Gershenson, C. R. Newman, C. D. Frisbie, *Appl. Phys. Lett.* **2005**, *86*, 1.

[14] G. Liu, L. Kong, J. Gong, W. Yang, H. Mao, Q. Hu, Z. Liu, R. D. Schaller, D. Zhang, T. Xu, *Adv. Funct. Mater.* **2017**, *27*, 1604208.

[15] Y. Wang, X. Lü, W. Yang, T. Wen, L. Yang, X. Ren, L. Wang, Z. Lin, Y. Zhao, *J. Am. Chem. Soc.* **2015**, *137*, 11144.

[16] M. Szafrański, A. Katrusiak, *J. Phys. Chem. Lett.* **2016**, *7*, 3458.

[17] M. Szafrański, A. Katrusiak, *J. Phys. Chem. Lett.* **2017**, *8*, 2496.

[18] M. Mączka, S. Sobczak, P. Ratajczyk, F. F. Leite, W. Paraguassu, F. Dybała, A. P. Herman, R. Kudrawiec, A. Katrusiak, *Chem. Mater.* **2022**, *34*, 7867.

[19] M. Saski, S. Sobczak, P. Ratajczyk, M. Terlecki, W. Marynowski, A. Borkenhagen, I. Justyniak, A. Katrusiak, J. Lewiński, *Small* **2024**, *2403685*, 1.

[20] A. Jaffe, Y. Lin, W. L. Mao, H. I. Karunadasa, *J. Am. Chem. Soc.* **2017**, *139*, 4330.

[21] L. Zhang, C. Liu, L. Wang, C. Liu, K. Wang, B. Zou, *Angew. Chemie - Int. Ed.* **2018**, *57*, 11213.

[22] Q. Li, Y. Wang, W. Pan, W. Yang, B. Zou, J. Tang, Z. Quan, *Angew. Chemie - Int. Ed.* **2017**, *56*, 15969.

[23] L. Zhang, L. Wu, K. Wang, B. Zou, *Adv. Sci.* **2019**, *6*, 2.

[24] G. Liu, L. Kong, P. Guo, C. C. Stoumpos, Q. Hu, Z. Liu, Z. Cai, D. J. Gosztola, H. K. Mao, M. G. Kanatzidis, R. D. Schaller, *ACS Energy Lett.* **2017**, *2*, 2518.

[25] T. Yin, B. Liu, J. Yan, Y. Fang, M. Chen, W. K. Chong, S. Jiang, J. L. Kuo, J. Fang, P. Liang, S. Wei, K. P. Loh, T. C. Sum, T. J. White, Z. X. Shen, *J. Am. Chem. Soc.* **2019**, *141*, 1235.

[26] J. A. Aramburu, P. García-Fernández, N. R. Mathiesen, J. M. Garcia-Lastra, M. Moreno, *J. Phys. Chem. C* **2018**, *122*, 5071.

[27] P. Ratajczyk, S. Sobczak, P. Woźny, A. Wcisło, T. Poręba, A. Katrusiak, *J. Mater. Chem. C* **2023**, *11*, 11055.

[28] Q. Wang, H. Zhang, Y. Zhang, C. Liu, Y. Han, Y. Ma, C. Gao, *High Press. Res.* **2014**, *34*, 355.

[29] C. Huang, S. Barlow, S. R. Marder, *J. Org. Chem.* **2011**, *76*, 2386.

[30] F. Würthner, *Chem. Commun.* **2004**, 1564.

[31] C. W. Tang, *Appl. Phys. Lett.* **1986**, *48*, 183.

[32] E. Kozma, M. Catellani, *Dye. Pigment.* **2013**, *98*, 160.

[33] F. Marin, A. Zappi, D. Melucci, L. Maini, *Mol. Syst. Des. Eng.* **2023**, *8*, 500.

[34] T. Lei, J.-Y. Wang, J. Pei, *Chem. Mater.* **2014**, *26*, 594.

[35] F. Tao, S. L. Bernasek, *Chem. Rev.* **2007**, *107*, 1408.

[36] A. D. Bond, *New J. Chem.* **2004**, *28*, 104.

[37] L. Ding, H.-B. Li, T. Lei, H.-Z. Ying, R.-B. Wang, Y. Zhou, Z.-M. Su, J. Pei, *Chem. Mater.* **2012**, *24*, 1944.

[38] R. Boese, H.-C. Weiss, D. Bläser, *Angew. Chemie Int. Ed.* **1999**, *38*, 988.

[39] V. R. Thalladi, R. Boese, H.-C. Weiss, *J. Am. Chem. Soc.* **2000**, *122*, 1186.

[40] S. Inoue, H. Minemawari, J. Tsutsumi, M. Chikamatsu, T. Yamada, S. Horiuchi, M. Tanaka, R. Kumai, M. Yoneya, T. Hasegawa, *Chem. Mater.* **2015**, *27*, 3809.

[41] S. Wang, M. Mandal, H. Zhang, D. W. Breiby, O. Yildiz, Z. Ling, G. Floudas, M. Bonn, D. Andrienko, H. I. Wang, P. W. M. Blom, W. Pisula, T. Marszalek, *J. Am. Chem. Soc.* **2024**, *146*, 19128.

[42] T. Kato, T. Uryu, H. Kihara, A. Fujishima, J. M. J. Frechet, *Macromolecules* **1992**, *25*, 6836.

[43] L. Tu, W. Che, S. Li, X. Li, Y. Xie, Z. Li, *J. Mater. Chem. C* **2021**, *9*, 12124.

[44] Y. Liu, K. Xian, R. Gui, K. Zhou, J. Liu, M. Gao, W. Zhao, X. Jiao, Y. Deng, H. Yin, Y. Geng, L. Ye, *Macromolecules* **2022**, *55*, 133.

[45] A. Ananiadou, M. Alagiannis, M. Steinhart, K. Skobridis, G. Floudas, *J. Phys. Chem. C* **2022**, *126*, 16409.

[46] G. H. Roche, G. Bruckner, D. G. Dumitrescu, J. J. E. Moreau, A. van der Lee, G. Wantz, O. J. Dautel, *Adv. Electron. Mater.* **2022**, *8*, 2100265.

[47] S. Wang, M.-Z. Wei, G.-C. Hu, C.-K. Wang, G.-P. Zhang, *Org. Electron.* **2017**, *49*, 76.

[48] S. Inoue, T. Higashino, K. Nikaido, R. Miyata, S. Matsuoka, M. Tanaka, S. Tsuzuki, S. Horiuchi, R. Kondo, R. Sagayama, R. Kumai, D. Sekine, T. Koyanagi, M. Matsubara, T. Hasegawa, *Adv. Sci.* **2024**, *11*, 2308270.

[49] P.-T. Wu, H. Xin, F. S. Kim, G. Ren, S. A. Jenekhe, *Macromolecules* **2009**, *42*, 8817.

[50] P. Stoliar, R. Kshirsagar, M. Massi, P. Annibale, C. Albonetti, D. M. de Leeuw, F. Biscarini, *J. Am. Chem. Soc.* **2007**, *129*, 6477.

[51] A. Liang, K. Ma, Y. Gao, L. Dou, *Small Struct.* **2022**, *3*, 2100173.

[52] X. Li, J. M. Hoffman, M. G. Kanatzidis, *Chem. Rev.* **2021**, *121*, 2230.

[53] Y. Arakawa, Y. Ishida, T. Shiba, K. Igawa, S. Sasaki, H. Tsuji, *CrystEngComm* **2022**, *24*, 1877.

[54] Z. Jin, B. Song, X. Chen, L. Shi, F. Zhao, P. Gao, C. Zhang, B. Hu, *J. Mater. Chem. A* **2025**, *13*, 15189.

[55] K. Takimiya, S. Shinamura, I. Osaka, E. Miyazaki, *Adv. Mater.* **2011**, *23*, 4347.

[56] H. Ebata, T. Izawa, E. Miyazaki, K. Takimiya, M. Ikeda, H. Kuwabara, T. Yui, *J. Am.*

Chem. Soc. **2007**, *129*, 15732.

[57] E. Hädicke, F. Graser, *Acta Crystallogr. Sect. C Cryst. Struct. Commun.* **1986**, *42*, 189.

[58] F. Marin, S. Tombolesi, T. Salzillo, O. Yaffe, L. Maini, *J. Mater. Chem. C* **2022**, *10*, 8089.

[59] J. Pitchaimani, A. Kundu, S. P. Anthony, D. Moon, V. Madhu, *ChemistrySelect* **2020**, *5*, 2070.

[60] P. Ratajczyk, S. Sobczak, M. Andrzejewski, F. Marin, M. Marchini, L. Maini, A. Katrusiak, *J. Mater. Chem. C* **2025**, *13*, 13509.

[61] A. L. Briseno, S. C. B. Mannsfeld, C. Reese, J. M. Hancock, Y. Xiong, S. A. Jenekhe, Z. Bao, Y. Xia, *Nano Lett.* **2007**, *7*, 2847.

[62] T. Okamoto, S. Kumagai, E. Fukuzaki, H. Ishii, G. Watanabe, N. Niitsu, T. Annaka, M. Yamagishi, Y. Tani, H. Sugiura, T. Watanabe, S. Watanabe, J. Takeya, *Sci. Adv.* **2020**, *6*, eaaz0632.

[63] L. I. Kuznetsova, A. A. Piryazev, D. V. Anokhin, A. V. Mumyatov, D. K. Susarova, D. A. Ivanov, P. A. Troshin, *Org. Electron.* **2018**, *58*, 257.

[64] M. Hasegawa, N. Sato, *Mol. Cryst. Liq. Cryst. Sci. Technol. Sect. A Mol. Cryst. Liq. Cryst.* **1997**, *296*, 409.

[65] S. Tatemichi, M. Ichikawa, T. Koyama, Y. Taniguchi, *Appl. Phys. Lett.* **2006**, *89*, 138.

[66] E. Hädicke, F. Graser, *Acta Crystallogr. Sect. C Cryst. Struct. Commun.* **1986**, *42*, 195.

[67] M. D. Curtis, J. Cao, J. W. Kampf, *J. Am. Chem. Soc.* **2004**, *126*, 4318.

[68] C. W. Struijk, A. B. Sieval, J. E. J. Dakhorst, M. Van Dijk, P. Kimkes, R. B. M. Koehorst, H. Donker, T. J. Schaafsma, S. J. Picken, A. M. Van de Craats, J. M. Warman, H. Zuilhof, E. J. R. Sudholter, *J. Am. Chem. Soc.* **2000**, *122*, 11057.

[69] E. Patyk-Kaźmierczak, M. Kaźmierczak, *Chem. Commun.* **2024**, *60*, 10310.

Supporting Information

Supporting Information is available from the Wiley Online Library or from the author.

The odd-even alkyl chain effect on the structure and optoelectronic properties of alkyl-substituted perylene diimide (PDI) derivatives at highly strained environments

PDI-C_nH_{2n+1} (denoted PDI-C_n, n = 5–8) exhibit remarkable polymorphic diversity under high pressure and high temperature, transforming within the same space-group type $P\bar{1}$. The alkyl-chain length correlates with the temperature and reversly correlates with the pressure of phase transitions.

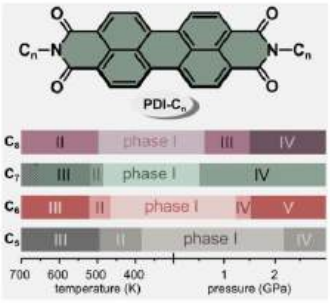

Article A4

Mechanical strain, thermal and pressure effects on the absorption edge of an organic charge-transfer polymer for flexible photovoltaics and sensors

Paulina Ratajczyk, Andrzej Katrusiak, Krzysztof A Bogdanowicz, Wojciech Przybył, Piotr Krysiak, Anna Kwak, Agnieszka Iwan

Materials Advances, 2022, 3, 2697-2705, DOI: 10.1039/D1MA01066B

Materials Advances

ROYAL SOCIETY OF CHEMISTRY

COMMUNICATION

View Article Online
View Journal

Check for updates

Cite this: DOI: 10.1039/d1ma01066b

Received 13th November 2021,
Accepted 11th February 2022

DOI: 10.1039/d1ma01066b

rsc.li/materials-advances

Mechanical strain, thermal and pressure effects on the absorption edge of an organic charge-transfer polymer for flexible photovoltaics and sensors†

Paulina Ratajczyk, [a] Andrzej Katrusiak, *[a] Krzysztof A. Bogdanowicz, [b] Wojciech Przybył, [b] Piotr Krysiak, [b] Anna Kwak [b] and Agnieszka Iwan *[b]

Mechanical and thermal strains in organic photovoltaic layers deposited on poly(ethylene terephthalate) (PET) and glass substrates and the resulting effect on the bandgap energy have been determined for the organic charge-transfer polymer PTB7. Its strong bathochromic shift of the absorption spectra under pressure also depends on the layer preparation method. The effects of different solvents and PTB7 concentrations on agglomerate formation were also studied. A perfect linear dependence of the concentration *vs.* absorbance was observed up to 1.81 × 10^{-7} M for chlorobenzene or *o*-dichlorobenzene solution. The thermal image monitoring of the current response at an increasing potential showed a linear current-to-voltage tendency, indicating that the conductive behaviour of the polymer depends on the substrate used in PET/ITO/PTB7/Ag/ITO/PET and glass/ITO/PTB7/Ag/ITO/glass devices. The PTB7 layer on the PET/ITO substrate displays superior mechanical properties suitable for flexible photovoltaic panels exposed to strain and deformations.

Introduction

New photovoltaic (PV) materials are intensively sought for operation, efficiency, and performance improvement, as well as for improving the mechanical properties and resistance to damage. Such materials would enable wider applications of photovoltaic cells, a goal that is directly connected to environmental protection. While most of the currently available photovoltaic panels are based on silicon technologies as well as other covalent and ionic materials, organic compounds offer significant advantages, such as a low production cost, easy processing (*e.g.*, the formation of thin layers through painting or spraying any-shaped surfaces), practically infinite means of chemical modifications aimed at improving the efficiency, durability, and good elastic performance for applications in flexible screens, panels and cloth.[1] The organic polymer flexible panels are light, cheap to produce and easily disposed of.

At present, organic/polymer solar cells are being widely investigated in a few main directions: (i) the application of new polymers, copolymers or small compounds in the active layer of PV devices,[2–7] (ii) the application of graphene, graphene oxide, their chemical modifications, carbon nanotubes, fullerenes and non-fullerenes, and their derivatives either as an active layer or as an interlayer in PV devices,[8–14] (iii) the application of new polymers or graphene as flexible substrates in PV devices[15–17] and (iv) the application of new polymers as hole transporting layers (HTLs), instead of poly(3,4-ethylenedioxythiophene) polystyrene sulfonate (PEDOT:PSS), in PV devices.[18,19]

To construct the active layer in polymer photovoltaic devices, poly(3-hexylthiophene) (P3HT) and poly[*N*-9″-heptadecanyl-2,7-carbazole-*alt*-5,5-(4′,7′-di-2-thienyl-2′,1′,3′-benzothiadiazole)] (PCDTBT) have been widely investigated as donor materials. Theoretical studies from 2008 predicted "realistically achievable" power conversion efficiency (PCE) values of *ca.* 15% for fully optimized donor–acceptor bulk heterojunction (BHJ) organic solar cells.[20] The basic questions to be addressed centre on the relationships between the chemical and physical compositions of interlayer materials and their energetic and electrical properties on nanometre length scales, often in environments with the complexity of the working solar cell platform.

Most recently, various strategies have been used for optimizing the organic/polymeric solar cells, *e.g.*: (i) in order to manipulate the molecular interactions of the binary blend, environmentally friendly solvents were used as the third component of the active layer;[21] (ii) efficient deposition techniques for perovskites and charge transport layers such as doctor-blade coating, slot-die coating, screen printing, and spray deposition strategies contributed to the significant development of large-area perovskite solar modules;[22] (iii) small-molecule donor–acceptor mixtures were used as stable device architectures

[a] *Faculty of Chemistry, Adam Mickiewicz University, Uniwersytetu Poznańskiego 8, 61-614 Poznań, Poland. E-mail: katran@amu.edu.pl*
[b] *Military Institute of Engineer Technology, Obornicka 136, 50-961 Wroclaw, Poland. E-mail: iwan@witi.wroc.pl*

† Electronic supplementary information (ESI) available. See DOI: 10.1039/d1ma01066b

without intermediate electrode layers;[23] (iv) a broad family of organoboron small molecular donors/acceptors and organoboron polymer donors/acceptors became an important class of organic photovoltaic materials;[5] (v) the stability of organic solar cells was significantly increased *via* material design, device engineering of the active layers, employing an inverted geometry, optimizing the buffer layers, and using stable electrodes and encapsulation materials;[7] (vi) several printing techniques improved the production of large-area flexible transparent conductive films (TCFs);[24] (vii) novel nanomaterials were designed and developed, including carbon nanotubes, graphene and their composites, which are now the main materials for flexible and transparent thin-film electrodes;[17,25,26] and (viii) radioactive sources were used to generate photonic light in scintillators as converters of ionizing radiation to electricity in photovoltaic cells.[27]

Poly[[4,8-bis[(2-ethylhexyl)oxy]benzo[1,2-*b*:4,5-*b*′]dithio-phene-2,6-diyl][3-fluoro-2-[(2-ethylhexyl)oxy]carbonyl]thieno [3,4-*b*]thiophenediyl] (PTB7) (Fig. 1) presently gives some of the highest reported efficiencies (PCE = 8.92%) for PTB7:$PC_{71}BM$ BHJ solar cells in the presence of 3.0 v% 1,8-diiodooctane (DIO) and 1 wt% polystyrene (PS).[28] For the inverted architecture indium tin oxide (ITO)/poly[(9,9-bis(3′-(*N*,*N*-dimethylamino)propyl)-2,7-fluorene)-*alt*-2,7-(9,9-dioctylfluorene)] (PFN)/PTB7:$PC_{71}BM$/MoO_3/Al, the power conversion efficiency was found to be 9.15% (for standard BHJ solar cell ITO/PEDOT:PSS/PTB7:$PC_{71}BM$/PFN/Ca, PCE = 8.24%).[29] However, this efficiency is still far from the theoretical value of PCE, which is equal to 15%. One of the proposed ways to achieve or even exceed the theoretical value of PCE is the construction of tandem perovskite cells with ITO/SnO_2/$CsPbI_2Br$/P3HT/MoO_3/Ag/PFN-Br/PTB7-Th:IEICO-4F/MoO_3/Ag architectures containing poly[[2,6′-4,8-di(5-ethylhexylthienyl)benzo[1,2-*b*;3,3-*b*]dithiophene]{3-fluoro-2[(2-ethylhexyl)carbonyl]thieno[3,4-*b*]thiophenediyl}] (PTB7-Th) as a component of the hole transporting material (HTM) layer with PCE = 17.24%.[30]

Murray *et al.* described the ITO/HTL/PTB7:$PC_{71}BM$/LiF/Al architecture for polymer solar cells, where graphene oxide (GO) or PEDOT:PSS was used as the HTL.[31] Devices with GO exhibited a PCE equal to 7.5%, indicating a 5-fold enhancement in the thermal aging lifetime and a 20-fold enhancement in the humid ambient lifetime *versus* analogous PEDOT:PSS-based devices.

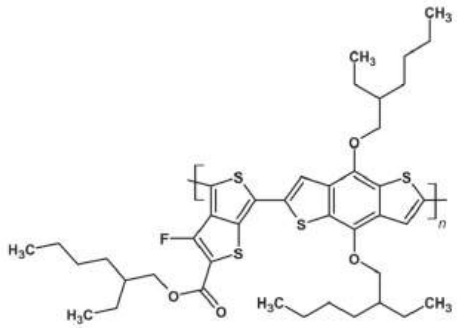

Fig. 1 Molecular structure of PTB7.

It should be emphasized that polymer solar cells based only on PTB7 are utilized in the inverted device with the ITO/ZnO/PTB7/MoO_3/Ag architecture, and the PCE value is only 0.14%, indicating almost no photovoltaic performance.[32] For solar cells with an active layer based on PTB7:$PC_{71}BM$ or PTB7:$PC_{71}BM$:DIO, the PCE values are 4.74% and 7.41%, respectively.

In addition to modifying the solar cell architecture, scientists are studying the selected electrochemical parameters of PTB7:$PC_{71}BM$ in detail to understand the differences in behaviour of this mixture compared to P3HT:PCBM. For example, Park *et al.* discovered that, at the PTB7:$PC_{71}BM$ interface, the interface dipole and band bending were not observed due to their identical charge neutrality levels. On the other hand, a large interfacial dipole was observed at the P3HT:$PC_{61}BM$ interface. It was found that the photovoltaic energy gaps (EPVG) were 1.10 eV and 0.90 eV for PTB7:$PC_{71}BM$ and P3HT:$PC_{61}BM$, respectively, inducing a larger open-circuit voltage in PTB7:$PC_{71}BM$ than that in P3HT:$PC_{61}BM$.[33] Jin *et al.* investigated the transient THz conductivities of PTB7 and P3HT blended with $PC_{71}BM$ using ultrafast THz spectroscopy.[34] They demonstrated that the carrier–carrier interactions at higher density play a significant role in decreasing the charge carrier mobility in PTB7:$PC_{71}BM$. Transient absorption spectroscopy of PTB7:$PC_{71}BM$ blends containing a broad range of acceptor contents (0.01–50% by weight)[35] showed that with the increase in the polaron signal $PC_{71}BM$ concentrations of more than 10%, most polarons are generated within 200 fs, while for lower acceptor concentrations, the polaron signal increases gradually over ~1 ps, with most polarons generated after 200 fs.

Detailed studies on the selected properties of PTB7 led to new solutions for improving the charge mobility and morphology of PTB7. For example, Savikhin *et al.* studied the effect of high-temperature annealing on the properties of PTB7 and PTB7:fullerene blends and revealed that annealing at a moderate temperature (260 °C) improves the PTB7 morphology and optoelectronic properties.[36] Although high-temperature annealing (290 °C) also improves the morphology, it caused poorer optoelectronic properties as an effect of aliphatic side chain modification in PTB7, increased electronic disorder and decreased mobility. It was found that solar irradiation modifies the chemical structure of PTB7 and affects the device photostability.

Kettle *et al.* studied the chemical degradation of PTB7 by X-ray photoelectron spectroscopy (XPS)[37] and demonstrated that PTB7 seems to be essentially unstable when illuminated in air. XPS studies were used to confirm that the rapid photodegradation process occurs due to changes in the chemical structure of PTB7. The transient magnetic field effects of photoexcitation in PTB7 were studied by Huynh *et al.*[38]

Among the considerable number of techniques employed for studying solar cell properties in recent years, high-pressure techniques have been used to reveal the impressive potential of photovoltaics based on perovskites.[39–46] Pressure is a fundamental thermodynamic variable that can induce a variety of

structural changes, such as phase transitions,[47] Jahn–Teller interplay with the lattice strain,[48] and amorphization.[49,50] Generally, high-pressure studies are ideal for understanding the structure–property relationship,[51] as they provide fundamental insight into the structural, optoelectronic, and magnetic properties of materials and thus can guide the design of new photovoltaic materials with desired properties. An important feature of photovoltaic materials, generally used in the form of thin and thick layers, is the effect of strain on the absorption and current-generation efficiency. Strain can be generated in the layer-deposition process due to the layer–substrate interactions, as governed by the different multilayer thermal expansions in photovoltaic panels, the bending strain in flexible devices and other effects in the production process and specific applications in different environments. Furthermore, the operation of solar cells occurs with significant temperature changes that can amplify stress, which may completely alter the structure and optoelectronic properties of the materials, affecting their performance. Nowadays, strain engineering is increasingly used to tailor optoelectronic functionalities.[52,53] To our knowledge, no pressure effects have been described for the absorption edge of organic photovoltaic materials. Therefore, we have undertaken this study on the photovoltaic polymer PTB7. Apart from the photovoltaic performance, we also continue to be interested in finding new materials for pressure sensors. Our present study includes the effects of solvents and additives on the morphological, optical, mechanical and electrical behaviours of the created PTB7 layer. We have shown that the PTB7-based panels endow flexible and adaptive multilayer systems offering sufficient performance of the bulk and interfaces for their operation under the strain required in flexible, wearable and exposed products under extreme conditions. Such a performance can result not only from high stretchability, but also from autonomous self-healing capabilities.

Results and discussion

The solubility of PTB7 was assessed through ultrasonication for 60 minutes with 1.0 mg of the sample and 1 mL of the solvent in a vial. Then, the vials were put aside for another 60 minutes, and the observations were noted. These tests showed good solubility in chlorinated solvents such as dichloroethane, dichloromethane and *o*-dichlorobenzene (*o*-DCB). Since PTB7 is a polymeric material, it requires more time to fully dissolve; hence, we left the compound overnight, and the ultrasonication was repeated.

UV-vis in solution

First, a UV-vis study was performed for the solutions in chlorobenzene (CB) and *o*-DCB. The basic spectra in CB and *o*-DCB at a concentration of 6.62×10^{-3} mg mL^{-1} displayed a typical PTB7 shape with very similar absorption maxima for both solutions (Fig. 2). In the spectra, there are three main bands with maxima at 300, 621, and 680 nm.

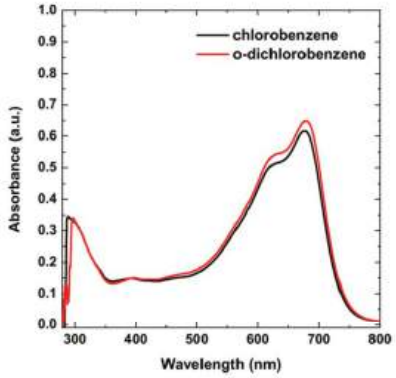

Fig. 2 UV-vis spectra of PTB7 in chlorobenzene and *o*-dichlorobenzene.

To establish the possible agglomerate formation depending on the type of solvent, we investigated a wide range of concentrations (Fig. 3), from 5.3×10^{-9} to 2.56×10^{-7} M (6.67×10^{-4} to 3.22×10^{-2} mg mL^{-1}), within the limit of 2.1 absorbance units. Following the changes in spectra, the ratios of the integrated intensities of the bands at 621 and 680 nm were compared. We found that the normalized signal for 680 nm reflected a change in the proportion from 1.21 : 1/1.19 : 1 to nearly 1.10 : 1/1.06 : 1 for chlorobenzene/*o*-chlorobenzene. According to Zhang *et al.*, this direction of change is due to

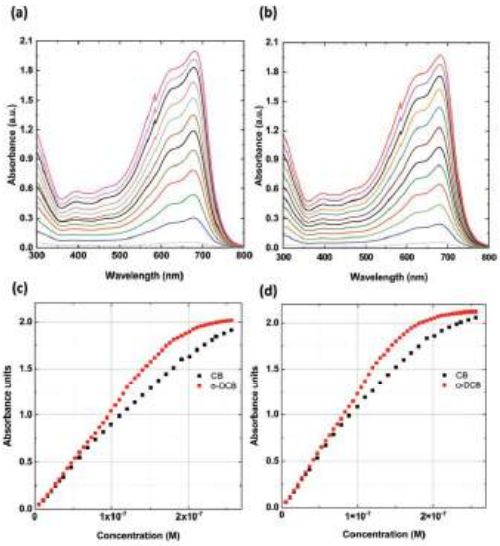

Fig. 3 UV-vis spectra of PTB7 in (a) CB and (b) *o*-DCB for selected concentrations from 5.30×10^{-9} to 2.81×10^{-7} M. The calibration curve based on UV-vis absorbance spectra recorded on single bands at (c) 680 nm (d) and 629 nm for different concentrations of PTB7 in CB and *o*-DCB.

the reduced polymer ordered aggregation in solution that occurs upon increasing the concentration.[32] In our study, disordered aggregation was observed for concentrations above 1.81×10^{-7} M (2.28×10^{-2} mg mL^{-1}), which was evident for the solution in *o*-DCB. Thus, an almost perfect linear dependence of the concentration *vs.* absorbance was observed up to 1.81×10^{-7} M (2.28×10^{-2} mg mL^{-1}) for both solvents, with only a small discrepancy for the CB solution. This shows that the dipole-moment change from 1.54 D (CB) to 2.14 D (*o*-DCB) influences the in-solution aggregation ordering of the PTB7 polymer, resulting in a stronger disorder at higher concentrations. This relationship indicates that the dipole moment of solvent molecules has a similar effect on aggregation as the addition of DIO to the CB solution.[32]

High-pressure spectroscopy

UV-vis spectra of the solid-state PTB7 layers were obtained using a Merrill–Bassett diamond-anvil cell (DAC) equipped with diamond anvils IIA. The PTB7 layers were deposited on the diamond culet through three methods:

(i) The PTB7 layer deposited by uniaxial compression: after placing a small amount of the sample on the diamond culet, it was strongly pressed from above by a thick glass plate until it fused into a uniform layer (Fig. 4d).

(ii) The PTB7 layer deposited by solvent evaporation: a drop of the PTB7 solution in dichloromethane, chlorobenzene or 1,2-dichlorobenzene was placed on the culet, and the layer was formed after solvent evaporation (Fig. 4b, c and 5).

(iii) The PTB7 layer deposited by the solution under high pressures: the solution of PTB7 in dichloromethane was loaded into the DAC chamber, and the layer was formed as a precipitate after increasing the pressure (Fig. 4a).

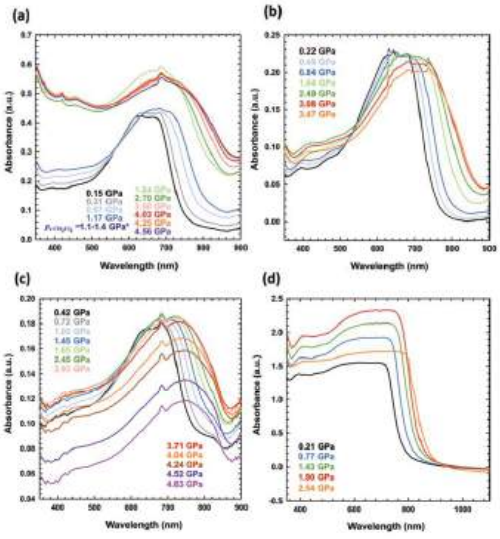

Fig. 4 High-pressure absorbance spectra of PTB7 measured for (a) a solution of PTB7 in dichloromethane (the sample was liquid up to 1.25 GPa, when dichloromethane freezes at 296 K),[61,62] (b) a PTB7 layer on one culet, formed upon evaporation of dichloromethane, (c) the same layer as in (b), but on two diamond culets, and (d) a layer pressed on one culet.

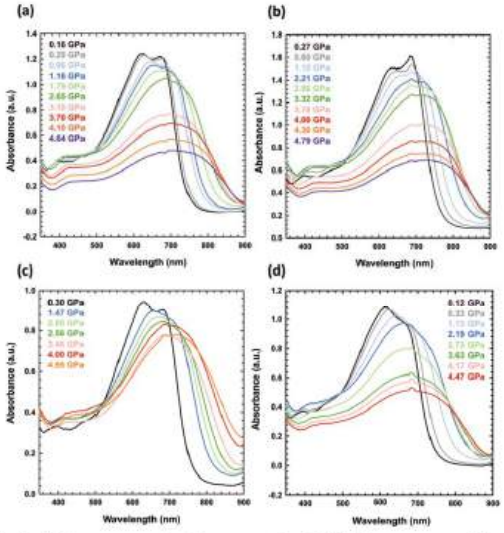

Fig. 5 High-pressure absorbance spectra of PTB7 layers prepared from the solutions after the evaporation of the following solvents: (a) CB, (b) *o*-DCB, (c) a CB–DIO mixture, and (d) an *o*-DCB–DIO mixture. The concentration of each solution was 10 mg mL^{-1}.

When measuring the absorbance spectrum of PTB7 dissolved in dichloromethane above the freezing pressure of dichloromethane (above 1.25 GPa), a clear jump-like increase was observed in the absorbance (Fig. 4a). This jump is associated with the precipitation of small grains of PTB7 extruded from dichloromethane upon crystallization. The crystallization of the solvent in the DAC chamber is clearly visible through the microscope, but this process significantly increases the scattering of the probing-beam light on the tiny grains of PTB7 dispersed in the sample. We also observed this effect for other freezing solutions.

The UV-vis spectra measured in the DAC for PTB7 layers prepared using different methods (i–iii) display similar strong bathochromic pressure effects (Fig. 6). The absorption edges up to 5 GPa are shifted by approximately 25 nm GPa^{-1} in the range 700–870 nm. It is a characteristic of all spectra series that, in the initial increased pressure ranges up to approximately 1 GPa, the absorption edge shift is linearly dependent on pressure. Then, above 1 GPa, $d\lambda/dp$ gradually decreases, and above 4 GPa, $d\lambda/dp$ is several times smaller compared to that in the range from 0.1 MPa to 1 GPa.

This finding correlates with the tendency of PTB7 to form aggregates, which are known to cause red absorption.[54,55] In a

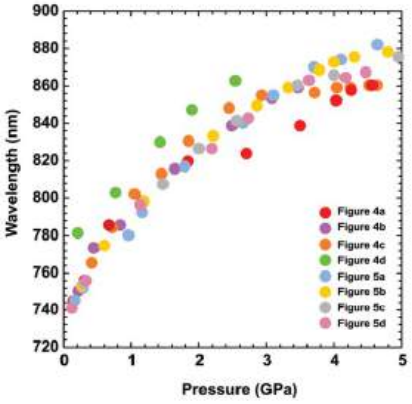

Fig. 6 The absorption edge as a function of pressure, depending on the PTB7 preparation method. As described in the plot, the different colours refer to the data in Fig. 4 and 5.

photoluminescence study, Hedley *et al.* revealed that small nanoaggregates of polymer chains can enhance the red absorption range above 600 nm, which they connected to micro-aggregation.[56]

Scanning electron microscopy (SEM) images were recorded to inspect the homogeneity of the prepared layers: (i) PTB7 powder compressed into the culet (Fig. S2a in the ESI†) and (ii) a layer formed by evaporation of dichloromethane (Fig. S2b in the ESI†). The SEM images allowed us to determine that the thickness of the layer formed by pressing the powdered product into the diamond was approximately 15 μm. The PTB7 layers formed *via* solvent evaporation were much thinner. The SEM micrographs show that the surface of the PTB7 layers formed by powder compression is homogenous and uniform, whereas the layers formed by dichloromethane evaporation consist of small patches with gaps and cracks that cause various patterns of defects in the deposited film.

X-ray powder diffraction (XRD) measurements (Fig. S3 in the ESI†) were used to confirm that both samples (i) prepared by pressing PTB7 and (ii) obtained by evaporating the solvent were amorphous.

The heat generated by the electric current in a through-plane thin layer was registered through thermal imaging. The experiment includes thermographic images that were each registered at the end of 3 minute intervals, when a stable state was reached for a constant current and temperature. To assess the electrical and thermal behaviours of PTB7 compounds, the change in the thermal signature was registered while applying an external potential. Two devices were constructed with the following configurations: (a) glass/ITO/PTB7/Ag/ITO/glass and (b) PET/ITO/PTB7/Ag/ITO/PET. These configurations differ based on the glass and PET substrates. In both devices, the thin PTB7 layers display nearly linear current-to-voltage dependences (Fig. 7), which confirms that the polymer is an electric conductor. The electric resistance of glass-supported

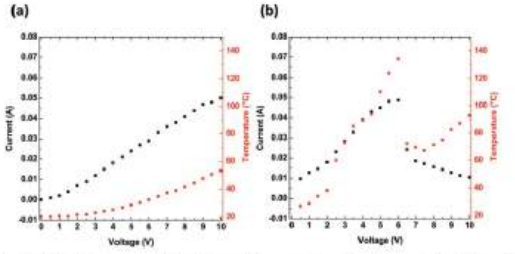

Fig. 7 Electric current (black) and temperature (red) as a function of applied voltage for devices composed of (a) glass/ITO/PTB7/Ag/ITO/glass and (b) PET/ITO/PTB7/Ag/ITO/PET.

PTB7 was 178.5 Ω and that of PET-supported PTB7 was 119.1 Ω. The difference is related to the pixeled glass support giving a longer conductive pathway than in the case of the PET/ITO support. However, for PET-supported PTB7, the lower resistance resulted in a larger current, causing a higher temperature, which in turn led to a drastic decline in the current above 6 V/136 °C. Nevertheless, high temperatures observed in the thermal images suggest the progressive degradation of the device, although at a lower pace.

The thermal response, culminating at approximately 53 °C for glass devices and at 136 °C for PET-supported PTB7 devices, shows an approximate logarithmic dependence on the voltage. For the flexible support, a higher temperature affects the organic layers and reduces their performance. According to the thermal images (Fig. 8), the edges of the device are most affected and overheated compared to the other regions. Defects located along the edges are most likely the cause of overheating and subsequent degradation of the PTB7 layers. In the present form, the PET-supported device performs well up to approximately 5 V.

Thermally induced pressure effect on the energy gap in PTB7

The thermal expansion of the PTB7 layers can generate compression due to the smaller thermal expansion of the substrate. The pressure (Δp) required to compensate for the difference in the dimensions of the PTB7 layer and the glass substrate can be assessed using the formula $\Delta p = \Delta L \cdot K/3$, where K is the difference between the bulk moduli of PTB7 and glass and ΔL is the difference in the linear dimensions of the PTB7 layer and the glass substrate. These approximate calculations result in E_g changes of 10^{-4} eV K^{-1}. Thus, a temperature change of 100 K would result in the narrowing of the PTB7 bandgap by 0.1 eV in the glass substrate device.

Mechanical properties

An important property of materials that are used to build elastic organic devices is their resistance to mechanical deformations. We have studied the mechanical properties of samples composed of a layered structure of poly(ethylene-terephthalate) (PET), indium-tin oxide (ITO) and PTB7. We prepared the devices by coating single and double layers of PTB7 through the spin coating technique. The samples were 0.17 mm thick.

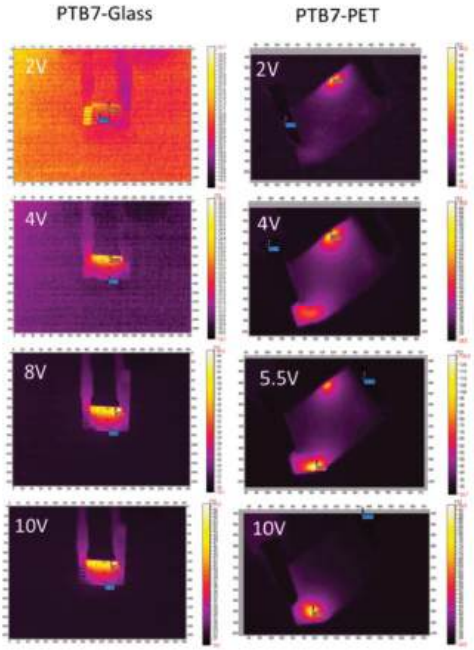

Fig. 8 Thermal images for glass/ITO/PTB7/Ag/ITO/glass and PET/ITO/PTB7/Ag/ITO/PET devices.

The selected mechanical properties of these devices are summarized in Fig. 9 and Table S1 in the ESI.† The devices break under the average stress values of 93(8) MPa for the single-layer and 155(8) MPa for the double-layer PTB7 versions. The maximum elongations before breaking, equal to $\Delta L_{max}/L_o \times 100\%$, were (113 ± 38)% and (111 ± 14)% for single and double layers of PTB7, respectively.

The correlation between the stretching force and elongation (Fig. 10) drastically differs for the single- and double-coated PET/ITO samples in the multilayer substrate devices. For all samples, the tests revealed both elastic and plastic behaviours,

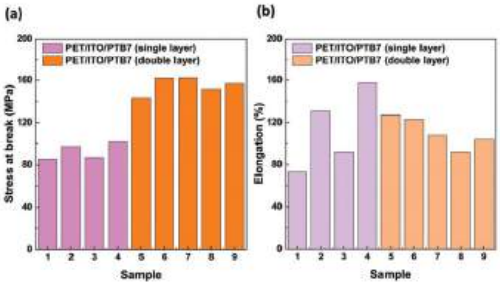

Fig. 9 (a) Stress at break and (b) elongation at break for PET/ITO/PTB7 single layer (samples no. 1–4) and double layer (no. 5–9) devices.

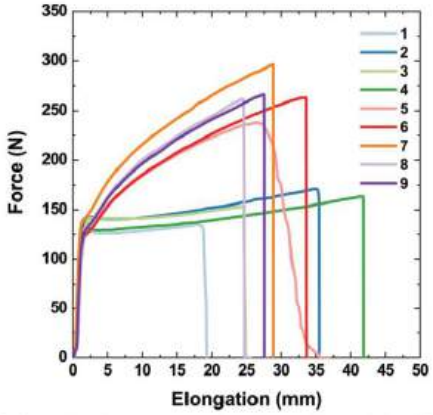

Fig. 10 Stretching force values as a function of elongation for PET/ITO/PTB7 single layer (samples 1–4) and double layer (5–9) devices.

with the transition reaching approximately 2 mm elongation (approximately 0.8% of the initial length) at a force of approx. 135 N (79 MPa), consistent with the elastic properties of the PET/ITO support. After reaching the transition, the PTB7 single-coated samples became fully plastic and elongated until they broke with a negligible increase in the applied force. The plastic deformations of the samples with double-layer PTB7 clearly differed from those with the single layer. The force–elongation dependence for double-layer PTB7 deviated from the typical plastic behaviour due to the effect of the approximately 100 N force enhancement that occurred before reaching the break point. This shows that the double layer of PTB7 adds an elastic component to the typical plastic behaviour, increasing the value of the applied force and the value of the stress at the breaking point. The PTB7 double layer reduced the breaking-point elongation to an average value of 29.3 mm (samples 5–9) compared to an average value of 37 mm for the PTB7 single-layer samples 2 and 4. This change is connected to the higher values of the stretching force and the breaking point for the PTB7 double-layer samples (on average 250 N) compared to the PTB7 single-layer samples (150 N). However, the PTB7 single-layer samples 1 and 3 broke at the lowest elongation values of 19 and 25 mm, respectively. In the case of the 5th sample, a slight deviation from the normal behaviour was attributed to the imperfection of the PET/ITO support probably caused by the cutting process.

Experimental

Materials

Poly[[4,8-bis[(2-ethylhexyl)oxy]benzo[1,2-*b*:4,5-*b*′]dithiophene-2,6-diyl][3-fluoro-2-[(2-ethylhexyl)carbonyl]thieno[3,4-*b*]thiophenediyl]], commonly abbreviated as PTB7, was purchased from Ossila Ltd (Sheffield, UK). Solvents and 1,8-diiodooctane (DIO) were of reagent grade and were obtained from Aldrich Chemical Co. (Saint Louis, MO, USA).

Methods

High-pressure experiments were performed using a Merrill–Bassett diamond-anvil cell (DAC)[57] modified by mounting the diamond anvils directly on steel backing supports with conical windows. The gasket was made of 0.1 mm thick tungsten foil or steel with sparked-eroded holes of 0.4 to 0.5 mm in diameter. The gaskets were preindented to 0.05 mm. The pressure was calibrated using the ruby fluorescence method.[58,59] The ultraviolet-visible (UV-vis) spectra of PTB7 at high pressure were recorded using Jasco V-650 and Jasco V-770 spectrophotometers adapted for using a DAC. The absorbance was measured at a scan speed of 200 nm min^{-1} in the 350–1100 nm or 350–900 nm range. In compression experiments, the pressure-transmitting medium was glycerol.

The basic transmission UV-vis spectra of PTB7 in solution were acquired using an A360 UV–Vis spectrophotometer (AOR Instruments, Shanghai, China) with an interval of 0.2 nm and medium scan speed in the range of 200 nm to 800 nm.

Scanning electron microscopy (SEM) images for the two layers, (i) PTB7 powder compressed into the culet and (ii) formed by evaporation of dichloromethane, were investigated using a Zeiss EVO 40 scanning electron microscope.

The PTB7 sample and the sample after evaporation of 1, 2-dichlororobenzene were characterized under ambient conditions by X-ray powder diffraction (XRD). A Bruker AXS D8 diffractometer equipped with a Johansson monochromator selecting the Cu Kα1 line was used (λ = 1.54060 Å). Silicon single-crystal plates were used as the sample cuvette to reduce the background.

The thermal behaviour was observed upon the application of a potential using a thermographic camera (VIGOcam v50, VIGO System S. A., Ożarów Mazowiecki, Poland) and a multichannel potentiostat–galvanostat (PGStat Autolab M101, Metrohm, Barendrecht, Nederland) as described in detail elsewhere.[60] The samples were prepared through the spin casting method with the PTB7 solution (10 mg mL^{-1} in chlorobenzene) on ITO-coated PET or the glass support (900 rpm, 30 s). Additionally, to improve the electric contact, a layer of silver paste was used to bind the electrode separated from the sample.

The mechanical properties (tensile strain) were investigated using an Instron 33R4469 (Instron, Norwood, MA, USA) testing machine with a load cell of 5 kN, and the results were registered using the Bluehill 3.0 software (Instron, Norwood, MA, USA). The PTB7 solution (10 mg mL^{-1} in chlorobenzene) was spun cast (900 rpm, 30 s) on a 5 × 5 cm^2 ITO-coated PET support. For mechanical tests, 5 × 1 cm^2 plates were used.

Conclusions

We have performed complex experiments aimed at determining the performance of PTB7 layers in flexible photovoltaic devices using both glass and PET substrates. The PTB7 polymer, an efficient donor material for photovoltaic devices, displays a bathochromic shift in the absorption edge and E_g energy gap narrowing under high pressure, both in solution and in the solid state. Different concentrations of PTB7 dissolved in chlorobenzene and *o*-chlorobenzene and solid layers prepared through different methods were investigated. The disordered arrangement of polymer agglomerates starts at concentrations above 1.81 × 10^{-7} M (2.28 × 10^{-2} mg mL^{-1}) and is more evident for the *o*-DCB solution due to the higher dipole moment of *o*-DCB molecules. The high pressure measurements for the films formed by evaporating the solutions in dichloromethane, chlorobenzene and *o*-dichlorobenzene, both without and with the addition of DIO, demonstrate that the redshift in the range of 740–880 nm is approximately 25 nm GPa^{-1}. Both spectroscopic studies in the UV-vis range provided evidence of PTB7 ordering and two-step aggregation. In solution, only the concentration-dependent disordering of the polymers was observed, whereas the pressure-induced aggregation appears more favourable for disordering macroscopic aggregates and polymeric side-chain aggregation (nanoaggregation), which more efficiently compensate for the external force. Both the PET- and glass-supported PTB7 layers have similar electrical conductivities and performances up to 6 V. However, for higher current, the PET-supported samples degrade at locations starting from point defects when the temperature reaches 140 °C. The mechanical performance of the flexible PET/ITO support is nearly identical for single- and double PTB7 layers in the elastic region up to 0.8% elongation. However, this performance shows significant differences in both the plastic deformation and breaking point values of 93.1 ± 7.9 MPa and 155.4 ± 7.9 MPa, respectively. This result demonstrates that the resistance to mechanical and electrical damage can be substantially improved by depositing additional layers. However, the number of layers does not affect the elastic region of the stress–strain behaviour.

Author contributions

Paulina Ratajczyk: investigation, visualization and writing (original draft); Andrzej Katrusiak: writing (original draft), supervision, writing (reviewing and editing), and conceptualization; Krzysztof Artur Bogdanowicz: investigation, visualization, analyses, and writing (original draft); Wojciech Przybyl: investigation; Piotr Krysiak: investigation and analyses; Anna Kwak: investigation; Agnieszka Iwan: writing (original draft), supervision, conceptualization, and writing (reviewing and editing).

Conflicts of interest

All authors have read and agreed to the published version of the manuscript.

Acknowledgements

The authors are grateful for financial support from the Polish National Centre of Research and Development (TECHMATSTRATEG1/347431/14/NCBR/2018) and from the Polish

Ministry of Education and Science within the Diamentowy Grant DI2019 0160 49. The authors would like to thank Ms B. Jewloszewicz for conducting the UV-vis experiment.

Notes and references

1 M. Riede, D. Spoltore and K. Leo, *Adv. Energy Mater.*, 2021, **11**, 2002653.
2 J. D. Roehling, D. Baran, J. Sit, T. Kassar, T. Ameri, T. Unruh, C. J. Brabec and A. J. Moulé, *Sci. Rep.*, 2016, **6**, 30915.
3 C. Zhong, V. K. Sangwan, C. Wang, H. Bergeron, M. C. Hersam and E. A. Weiss, *J. Phys. Chem. Lett.*, 2018, **9**, 2484–2491.
4 Z. Zhang, J. Miao, Z. Ding, B. Kan, B. Lin, X. Wan, W. Ma, Y. Chen, X. Long, C. Dou, J. Zhang, J. Liu and L. Wang, *Nat. Commun.*, 2019, **10**, 3271.
5 J. Miao, Y. Wang, J. Liu and L. Wang, *Chem. Soc. Rev.*, 2022, **51**, 153–187.
6 Y. Wang, W. Xu, J. Yi, C. Zuo, Y. Gong, Y. Liu, W. Y. Lai and W. Huang, *J. Mater. Chem. A*, 2018, **6**, 15977–15984.
7 L. Duan and A. Uddin, *Adv. Sci.*, 2020, **7**, 1903259.
8 Y. Wang, B. Wu, Z. Wu, Z. Lan, Y. Li, M. Zhang and F. Zhu, *J. Phys. Chem. Lett.*, 2017, **8**, 5264–5271.
9 C. Yang, Y. Sun, Q. Li, K. Liu, X. Xue, Y. Huang, K. Ren, L. Li, Y. Chen, Z. Wang, S. Qu and Z. Wang, *J. Phys. Chem. Lett.*, 2020, **11**, 927–934.
10 H. Chen, J. Qu, L. Liu, W. Chen and F. He, *J. Phys. Chem. Lett.*, 2019, **10**, 936–942.
11 C. K. Lyu, F. Zheng, B. H. Babu, M. S. Niu, L. Feng, J. L. Yang, W. Qin and X. T. Hao, *J. Phys. Chem. Lett.*, 2018, **9**, 6238–6248.
12 S. Karuthedath, J. Gorenflot, Y. Firdaus, N. Chaturvedi, C. S. P. De Castro, G. T. Harrison, J. I. Khan, A. Markina, A. H. Balawi, T. A. Dela Peña, W. Liu, R. Z. Liang, A. Sharma, S. H. K. Paleti, W. Zhang, Y. Lin, E. Alarousu, D. H. Anjum, P. M. Beaujuge, S. De Wolf, I. McCulloch, T. D. Anthopoulos, D. Baran, D. Andrienko and F. Laquai, *Nat. Mater.*, 2021, **20**, 378–384.
13 Y. Gong, J. Zhang, B. Du, M. Wang, W. Y. Lai and W. Huang, *ACS Appl. Electron. Mater.*, 2019, **1**, 854–861.
14 X. Li, H. Wang, H. Nakayama, Z. Wei, J. A. Schneider, K. Clark, W. Y. Lai, W. Huang, J. G. Labram, J. R. De Alaniz, M. L. Chabinyc, F. Wudl and Y. Zheng, *ACS Appl. Energy Mater.*, 2019, **2**, 3805–3814.
15 K. Fukuda, K. Yu and T. Someya, *Adv. Energy Mater.*, 2020, **10**, 2000765.
16 D. Koo, S. Jung, J. Seo, G. Jeong, Y. Choi, J. Lee, S. M. Lee, Y. Cho, M. Jeong, J. Lee, J. Oh, C. Yang and H. Park, *Joule*, 2020, **4**, 1021–1034.
17 Y. Sun, T. Liu, Y. Kan, K. Gao, B. Tang and Y. Li, *Small Sci.*, 2021, **1**, 2100001.
18 L. Lu and L. Yu, *Adv. Mater.*, 2014, **26**, 4413–4430.
19 X. Y. Liu, W. K. Chen, W. H. Fang and G. Cui, *J. Phys. Chem. Lett.*, 2019, **10**, 2949–2956.
20 G. Dennler, M. C. Scharber, T. Ameri, P. Denk, K. Forberich, C. Waldauf and C. J. Brabec, *Adv. Mater.*, 2008, **20**, 579–583.
21 H. Chen, R. Zhang, X. Chen, G. Zeng, L. Kobera, S. Abbrent, B. Zhang, W. Chen, G. Xu, J. Oh, S. H. Kang, S. Chen, C. Yang, J. Brus, J. Hou, F. Gao, Y. Li and Y. Li, *Nat. Energy*, 2021, **6**, 1045–1053.
22 T. Wu, Z. Qin, Y. Wang, Y. Wu, W. Chen, S. Zhang, M. Cai, S. Dai, J. Zhang, J. Liu, Z. Zhou, X. Liu, H. Segawa, H. Tan, Q. Tang, J. Fang, Y. Li, L. Ding, Z. Ning, Y. Qi, Y. Zhang and L. Han, *Nano-Micro Lett.*, 2021, **13**, 152.
23 H. Bin, J. Wang, J. Li, M. M. Wienk and R. A. J. Janssen, *Adv. Mater.*, 2021, **33**, 2008429.
24 D. Li, W. Y. Lai, Y. Z. Zhang and W. Huang, *Adv. Mater.*, 2018, **30**, 1704738.
25 T. Cheng, Y. Zhang, W. Y. Lai and W. Huang, *Adv. Mater.*, 2015, **27**, 3349–3376.
26 L. Duan, B. Hoex and A. Uddin, *Sol. RRL*, 2021, **5**, 2100041.
27 A. Iwan, W. Pellowski and K. A. Bogdanowicz, *Energies*, 2021, **14**, 6186.
28 L. Wang, S. Zhao, Z. Xu, J. Zhao, D. Huang and L. Zhao, *Materials*, 2016, **9**, 171.
29 Z. He, C. Zhong, S. Su, M. Xu, H. Wu and Y. Cao, *Nat. Photonics*, 2012, **6**, 591–595.
30 K. Lang, Q. Guo, Z. He, Y. Bai, J. Yao, M. Wakeel, M. S. Alhodaly, T. Hayat and Z. Tan, *J. Phys. Chem. Lett.*, 2020, **11**, 9596–9604.
31 I. P. Murray, S. J. Lou, L. J. Cote, S. Loser, C. J. Kadleck, T. Xu, J. M. Szarko, B. S. Rolczynski, J. E. Johns, J. Huang, L. Yu, L. X. Chen, T. J. Marks and M. C. Hersam, *J. Phys. Chem. Lett.*, 2011, **2**, 3006–3012.
32 D. Zhang, R. Hu, J. Cheng, Y. Chang, M. Huo, J. Yu, L. Li and J. P. Zhang, *Polymers*, 2018, **10**, 332.
33 S. Park, J. Jeong, G. Hyun, M. Kim, H. Lee and Y. Yi, *Sci. Rep.*, 2016, **6**, 35262.
34 Z. Jin, D. Gehrig, C. Dyer-Smith, E. J. Heilweil, F. Laquai, M. Bonn and D. Turchinovich, *J. Phys. Chem. Lett.*, 2014, **5**, 3662–3668.
35 N. Zarrabi, P. L. Burn, P. Meredith and P. E. Shaw, *J. Phys. Chem. Lett.*, 2016, **7**, 2640–2646.
36 V. Savikhin, L. K. Jagadamma, L. J. Purvis, I. Robertson, S. D. Oosterhout, C. J. Douglas, I. D. W. Samuel and M. F. Toney, *iScience*, 2018, **2**, 182–192.
37 J. Kettle, Z. Ding, M. Horie and G. C. Smith, *Org. Electron.*, 2016, **39**, 222–228.
38 U. N. V. Huynh, T. P. Basel, E. Ehrenfreund and Z. V. Vardeny, *J. Phys. Chem. Lett.*, 2018, **9**, 4544–4549.
39 M. Szafrański and A. Katrusiak, *J. Phys. Chem. Lett.*, 2016, **7**, 3458–3466.
40 A. Jaffe, Y. Lin and H. I. Karunadasa, *ACS Energy Lett.*, 2017, **2**, 1549–1555.
41 P. Postorino and L. Malavasi, *J. Phys. Chem. Lett.*, 2017, **8**, 2613–2622.
42 X. Lü, W. Yang, Q. Jia and H. Xu, *Chem. Sci.*, 2017, **8**, 6764–6776.
43 M. Szafrański and A. Katrusiak, *J. Phys. Chem. Lett.*, 2017, **8**, 2496–2506.

44 M. Coduri, T. A. Strobel, M. Szafrański, A. Katrusiak, A. Mahata, F. Cova, S. Bonomi, E. Mosconi, F. De Angelis and L. Malavasi, *J. Phys. Chem. Lett.*, 2019, **10**, 7398–7405.
45 G. Liu, L. Kong, W. Yang and H. Mao, *Mater. Today*, 2019, **27**, 91–106.
46 L. Zhang, Y. Fang, L. Sui, J. Yan, K. Wang, K. Yuan, W. L. Mao and B. Zou, *ACS Energy Lett.*, 2019, **4**, 2975–2982.
47 S. Jiang, Y. Fang, R. Li, H. Xiao, J. Crowley, C. Wang, T. J. White, W. A. Goddard, Z. Wang, T. Baikie and J. Fang, *Angew. Chem.*, 2016, **128**, 6650–6654.
48 F. Aguado, F. Rodríguez, R. Valiente, J. P. Itiè and M. Hanfland, *Phys. Rev. B: Condens. Matter Mater. Phys.*, 2012, **85**, 100101.
49 Y. Lee, D. B. Mitzi, P. W. Barnes and T. Vogt, *Phys. Rev. B: Condens. Matter Mater. Phys.*, 2003, **68**, 020103.
50 F. Capitani, C. Marini, S. Caramazza, P. Postorino, G. Garbarino, M. Hanfland, A. Pisanu, P. Quadrelli and L. Malavasi, *J. Appl. Phys.*, 2016, **119**, 185901.
51 G. Liu, L. Kong, J. Gong, W. Yang, H. Mao, Q. Hu, Z. Liu, R. D. Schaller, D. Zhang and T. Xu, *Adv. Funct. Mater.*, 2017, **27**, 1604208.
52 C. Zhu, X. Niu, Y. Fu, N. Li, C. Hu, Y. Chen, X. He, G. Na, P. Liu, H. Zai, Y. Ge, Y. Lu, X. Ke, Y. Bai, S. Yang, P. Chen, Y. Li, M. Sui, L. Zhang, H. Zhou and Q. Chen, *Nat. Commun.*, 2019, **10**, 815.
53 G. H. Ahn, M. Amani, H. Rasool, D. H. Lien, J. P. Mastandrea, J. W. Ager, M. Dubey, D. C. Chrzan, A. M. Minor and A. Javey, *Nat. Commun.*, 2017, **8**, 608.
54 Y. Liang, Z. Xu, J. Xia, S. T. Tsai, Y. Wu, G. Li, C. Ray and L. Yu, *Adv. Mater.*, 2010, **22**, 135–138.
55 D. Wang, Y. Yuan, Y. Mardiyati, C. Bubeck and K. Koynov, *Macromolecules*, 2013, **46**, 6217–6224.
56 G. J. Hedley, F. Steiner, J. Vogelsang and J. M. Lupton, *J. Phys. Chem. Lett.*, 2017, **8**, 3494–3499.
57 L. Merrill and W. A. Bassett, *Rev. Sci. Instrum.*, 1974, **45**, 290–294.
58 G. J. Piermarini, S. Block, J. D. Barnett and R. A. Forman, *J. Appl. Phys.*, 1975, **46**, 2774–2780.
59 H. K. Mao, J. Xu and P. M. Bell, *J. Geophys. Res.*, 1986, **91**, 4673.
60 A. Rózycka, K. A. Bogdanowicz, N. Górska, J. Rysz, M. Marzec, A. Iwan, R. Pich and A. Januszko, *Materials*, 2019, **12**, 1097.
61 M. Podsiadło, K. Dziubek and A. Katrusiak, *Acta Crystallogr., Sect. B: Struct. Sci.*, 2005, **61**, 595–600.
62 D. Kurzydłowski, T. Chumak and J. Rogoża, *Crystals*, 2020, **10**, 920.

10. Authorship declarations

Poznań, 15.10.2025

Paulina Ratajczyk
Adam Mickiewicz University
Uniwersytetu Poznańskiego 8,
61-614 Poznań, Poland

PhD candidat's declaration

I declare that I am a co-author of the publications:

- P. Ratajczyk, S. Sobczak, P. Woźny, A. Wcisło, T. Poręba, A. Katrusiak, *Unlocking the sensing potential of phenyl-substituted perylene diimides under extreme conditions*, J. Mater. Chem. C, 2023, 11, 11055-11065, DOI: 10.1039/D3TC01146A.
  My contributions to this paper include designing and performing the structural and UV-Vis absorption experiments, preparing the samples in the diamond anvil cell, analyzing the data, providing relevant literature, depositing the structural data in the CSD database, preparing the figures for the manuscript and supporting information, writing and editing the manuscript and its supporting information.

- P. Ratajczyk, S. Sobczak, M. Andrzejewski, F. Marin, M. Marchini, L. Maini, A. Katrusiak, *Pressure- and temperature-driven transitions and conformational conversions of n-hexyl substituted perylene diimide (PDI-C6) crystals*, J. Mater. Chem. C, 2025, 13, 13509-13518, DOI: 10.1039/d5tc00809c.
  My contributions to this paper include project conceptualization, performing the single-crystal X-ray diffraction experiments, preparing the sample in the diamond anvil cell, analyzing the experimental data, creating the figures for the manuscript and supporting information, depositing the structural data in the CSD database, writing and editing the manuscript and its supporting information.

- P. Ratajczyk, A. Katrusiak, K. A. Bogdanowicz, W. Przybył, P. Krysiak, A. Kwak, A. Iwan, *Mechanical strain, thermal and pressure effects on the absorption edge of an organic charge-transfer polymer for flexible photovoltaics and sensors*, Mater. Adv., 2022, 3, 2697-2705, DOI: 10.1039/D1MA01066B.

My contributions to this paper include project conceptualization, designing and performing the high-pressure UV-Vis absorption experiments, preparing samples for scanning electron microscopy and powder X-ray diffraction measurements, analyzing the experimental data, creating some figures, writing the manuscript section detailing the high-pressure results, editing the manuscript.

- P. Ratajczyk, S. Sobczak, M. Andrzejewski, P. Woźny, L. Maini, A. Katrusiak, *The odd-even alkyl chain effect on the structure and optoelectronic properties of alkyl-substituted perylene diimide (PDI) derivatives at highly strained environments*, 2025, DOI: 10.26434/chemrxiv-2025-2fjc9

  My contributions to this paper include project conceptualization, designing and performing the structural and UV-Vis absorption experiments, preparing the samples in the diamond anvil cell, analyzing the experimental data, conducting the literature review, creating the figures for the manuscript and supporting information, depositing the structural data in the CSD database, writing and editing the manuscript and its supporting information.

Paulina Ratajczyk
A. Katrusiak

Poznań, 15.10.2025

Prof. Andrzej Katrusiak
Adam Mickiewicz University
Uniwersytetu Poznańskiego 8,
61-614 Poznań, Poland

Supervisor's declaration

With reference to Paulina Ratajczyk's application for the Doctoral degree in Chemical Sciences at Adam Mickiewicz University in Poznań, I declare that I am a co-author of the following publications:

- P. Ratajczyk, S. Sobczak, P. Woźny, A. Wcisło, T. Poręba, A. Katrusiak, *Unlocking the sensing potential of phenyl-substituted perylene diimides under extreme conditions*, J. Mater. Chem. C, 2023, 11, 11055-11065, DOI: 10.1039/D3TC01146A.
- P. Ratajczyk, S. Sobczak, M. Andrzejewski, F. Marin, M. Marchini, L. Maini, A. Katrusiak, *Pressure- and temperature-driven transitions and conformational conversions of n-hexyl substituted perylene diimide (PDI-C6) crystals*, J. Mater. Chem. C, 2025, 13, 13509-13518, DOI: 10.1039/d5tc00809c.
- P. Ratajczyk, A. Katrusiak, K. A. Bogdanowicz, W. Przybył, P. Krysiak, A. Kwak, A. Iwan, *Mechanical strain, thermal and pressure effects on the absorption edge of an organic charge-transfer polymer for flexible photovoltaics and sensors*, Mater. Adv., 2022, 3, 2697-2705, DOI: 10.1039/D1MA01066B.
- P. Ratajczyk, S. Sobczak, M. Andrzejewski, P. Woźny, L. Maini, A. Katrusiak, *The odd-even alkyl chain effect on the structure and optoelectronic properties of alkyl-substituted perylene diimide (PDI) derivatives at highly strained environments*, 2025, DOI: 10.26434/chemrxiv-2025-2fjc9

My contributions to these papers included supervising the research and reviewing the manuscripts.

A Katrusiak

Poznań, 15.10.2025

Dr Szymon Sobczak
Adam Mickiewicz University
Uniwersytetu Poznańskiego 8,
61-614 Poznań, Poland

Co-author declaration

With reference to Paulina Ratajczyk's application for the Doctoral degree in Chemical Sciences at Adam Mickiewicz University in Poznań, I declare that I am a co-author of the following publications:

- P. Ratajczyk, S. Sobczak, P. Woźny, A. Wcisło, T. Poręba, A. Katrusiak, *Unlocking the sensing potential of phenyl-substituted perylene diimides under extreme conditions*, J. Mater. Chem. C, 2023, 11, 11055-11065, DOI: 10.1039/D3TC01146A.

  My contribution to this paper includes project conceptualization, analyzing high-pressure and variable-temperature single-crystal X-ray diffraction experiments, performing ab inito calculations, writing and editing the manuscript.

- P. Ratajczyk, S. Sobczak, M. Andrzejewski, F. Marin, M. Marchini, L. Maini, A. Katrusiak, *Pressure- and temperature-driven transitions and conformational conversions of n-hexyl substituted perylene diimide (PDI-C6) crystals*, J. Mater. Chem. C, 2025, 13, 13509-13518, DOI: 10.1039/d5tc00809c.

  My contributions to this paper include project conceptualization, experimental design, investigation and analysis of high-pressure and high-temperature single-crystal X-ray diffraction data, as well as writing and editing the manuscript.

- P. Ratajczyk, S. Sobczak, M. Andrzejewski, P. Woźny, L. Maini, A. Katrusiak, *The odd-even alkyl chain effect on the structure and optoelectronic properties of alkyl-substituted perylene diimide (PDI) derivatives at highly strained environments*, 2025, DOI: 10.26434/chemrxiv-2025-2fjc9.

  My contributions to this paper include project conceptualization, experimental design, investigation and analysis of high-pressure and high-temperature single-crystal X-ray diffraction data, as well as writing and editing the manuscript.

Szymon Sobczak

Poznań, 13.10.2025

Dr Przemysław Woźny
Adam Mickiewicz University
Uniwersytetu Poznańskiego 8,
61-614 Poznań, Poland

Co-author declaration

With reference to Paulina Ratajczyk's application for the Doctoral degree in Chemical Sciences at the Adam Mickiewicz University in Poznań, I declare that I am a co-author of the publications:

- P. Ratajczyk, S. Sobczak, P. Woźny, A. Wcisło, T. Poręba, A. Katrusiak, *Unlocking the sensing potential of phenyl-substituted perylene diimides under extreme conditions*, J. Mater. Chem. C, 2023, 11, 11055-11065, DOI: 10.1039/D3TC01146A.
- P. Ratajczyk, S. Sobczak, M. Andrzejewski, P. Woźny, L. Maini, A. Katrusiak, *The odd-even alkyl chain effect on the structure and optoelectronic properties of alkyl-substituted perylene diimide (PDI) derivatives at highly strained environments.*

My contributions to these papers include conducting and analyzing luminescence spectroscopy measurements, as well as writing and editing the manuscript.

Przemysław Woźny

P. Woźny

Poznań, 19.08.2025

Angelika Wcisło
Adam Mickiewicz University
Uniwersytetu Poznańskiego 8,
61-614 Poznań, Poland

Co-author declaration

With reference to Paulina Ratajczyk's application for the Doctoral degree in Chemical Sciences at the Adam Mickiewicz University in Poznań, I declare that I am a co-author of the publication:

- P. Ratajczyk, S. Sobczak, P. Woźny, A. Wcisło, T. Poręba, A. Katrusiak, *Unlocking the sensing potential of phenyl-substituted perylene diimides under extreme conditions*, J. Mater. Chem. C, 2023, 11, 11055-11065, DOI: 10.1039/D3TC01146A.

My contributions to this paper included assisting with the preparation of figures and tables.

Wcisło Angelika

Poznań, 24.08.2025

Dr Tomasz Poręba
Laboratory of Quantum Magnetism, Institute of Physics
École Polytechnique Fédérale de Lausanne
CH-1015 Lausanne, Switzerland

Co-author declaration

With reference to Paulina Ratajczyk's application for the Doctoral degree in Chemical Sciences at the Adam Mickiewicz University in Poznań, I declare that I am a co-author of the publication:

- P. Ratajczyk, S. Sobczak, P. Woźny, A. Wcisło, T. Poręba, A. Katrusiak, *Unlocking the sensing potential of phenyl-substituted perylene diimides under extreme conditions*, J. Mater. Chem. C, 2023, 11, 11055-11065, DOI: 10.1039/D3TC01146A.

My contributions to this paper include recrystallizing the PTCDI-Ph sample, collecting high-pressure X-ray diffraction data at the European Synchrotron Radiation Facility (ESRF), and assisting in the editing of the manuscript.

Tomasz Poręba

Schenefeld, 13.10.2025

Dr Michał Andrzejewski
European X-ray Free Electron Laser
Holzkoppel 4
22869 Schenefeld, Germany

Co-author declaration

With reference to Paulina Ratajczyk's application for the Doctoral degree in Chemical Sciences at Adam Mickiewicz University in Poznań, I declare that I am a co-author of the following publications:

- P. Ratajczyk, S. Sobczak, M. Andrzejewski, F. Marin, M. Marchini, L. Maini, A. Katrusiak, *Pressure- and temperature-driven transitions and conformational conversions of n-hexyl substituted perylene diimide (PDI-C6) crystals,* J. Mater. Chem. C, 2025, 13, 13509-13518, DOI: 10.1039/d5tc00809c.
- P. Ratajczyk, S. Sobczak, M. Andrzejewski, P. Woźny, L. Maini, A. Katrusiak, *The odd-even alkyl chain effect on the structure and optoelectronic properties of alkyl-substituted perylene diimide (PDI) derivatives at highly strained environments.*

My contributions to these papers include the investigation and analysis of high-pressure single-crystal X-ray diffraction data, theoretical studies, as well as manuscript writing and editing.

Michał Andrzejewski

Bologna, 11.09.2025

Dr Francesco Marin

Co-author declaration

With reference to Paulina Ratajczyk's application for the Doctoral degree in Chemical Sciences at the Adam Mickiewicz University in Poznań, I declare that I am a co-author of the publication:

- P. Ratajczyk, S. Sobczak, M. Andrzejewski, F. Marin, M. Marchini, L. Maini, A. Katrusiak, *Pressure- and temperature-driven transitions and conformational conversions of n-hexyl substituted perylene diimide (PDI-C6) crystals*, J. Mater. Chem. C, 2025, 13, 13509-13518 DOI: 10.1039/d5tc00809c.

My contributions to this paper included conducting high-pressure and high-temperature experiments and analyzing the resulting data.

Bologna, 30.06.2025

Dr Marianna Marchini
Department of Chemistry "G. Ciamician"
University of Bologna
via Selmi 2, 40126 Bologna, Italy

Co-author declaration

With reference to Paulina Ratajczyk's application for the Doctoral degree in Chemical Sciences at the Adam Mickiewicz University in Poznań, I declare that I am a co-author of the publication:

- P. Ratajczyk, S. Sobczak, M. Andrzejewski, F. Marin, M. Marchini, L. Maini, A. Katrusiak, *Pressure- and temperature-driven transitions and conformational conversions of n-hexyl substituted perylene diimide (PDI-C6) crystals,* J. Mater. Chem. C, 2025, DOI: 10.1039/d5tc00809c.

My contribution to this paper includes conducting high-temperature measurements and analyzing the resulting data.

Bologna, 26.06.2025

Prof. Lucia Maini
Department of Chemistry "G. Ciamician"
University of Bologna
via Selmi 2, 40126 Bologna, Italy

Co-author declaration

With reference to Paulina Ratajczyk's application for the Doctoral degree in Chemical Sciences at the Adam Mickiewicz University in Poznań, I declare that I am a co-author of the publication:

- P. Ratajczyk, S. Sobczak, M. Andrzejewski, F. Marin, M. Marchini, L. Maini, A. Katrusiak, *Pressure- and temperature-driven transitions and conformational conversions of n-hexyl substituted perylene diimide (PDI-C6) crystals,* J. Mater. Chem. C, 2025, DOI: 10.1039/d5tc00809c.

My contribution to this paper includes developing the initial idea, conducting the high-temperature data analysis, and participating in the writing and editing of the manuscript.

Digitally signed
by: LUCIA MAINI,
on: 1 luglio 2025

Bologna, 09.10.2025

Prof. Lucia Maini
Department of Chemistry "G. Ciamician"
University of Bologna
via Pietro Gobetti 85, 40129 Bologna, Italy

Co-author declaration

With reference to Paulina Ratajczyk's application for the Doctoral degree in Chemical Sciences at the Adam Mickiewicz University in Poznań, I declare that I am a co-author of the publication:

- P. Ratajczyk, S. Sobczak, M. Andrzejewski, P. Woźny, L. Maini, A. Katrusiak, *The odd-even alkyl chain effect on the structure and optoelectronic properties of alkyl-substituted perylene diimide (PDI) derivatives at highly strained environments.*

My contribution to this paper includes developing the initial idea, providing recrystallized compounds, and editing the manuscript.

Wrocław, 09.09.2025

Dr Krzysztof Artur Bogdanowicz
Military Institute of Engineer Technology,
Obornicka 136,
50-961 Wrocław, Poland

Co-author declaration

With reference to Paulina Ratajczyk's application for the Doctoral degree in Chemical Sciences at the Adam Mickiewicz University in Poznań, I declare that I am a co-author of the publication:

- P. Ratajczyk, A. Katrusiak, K. A. Bogdanowicz, W. Przybył, P. Krysiak, A. Kwak, A. Iwan, *Mechanical strain, thermal and pressure effects on the absorption edge of an organic charge-transfer polymer for flexible photovoltaics and sensors,* Mater. Adv., 2022, 3, 2697-2705, DOI: 10.1039/D1MA01066B.

My contributions to this paper include the investigation of thermal behaviour, data visualization and analysis, and manuscript writing.

K. Bogdanowicz

Wrocław, 10.09.2025

Dr Piotr Krysiak
Military Institute of Engineer Technology,
Obornicka 136,
50-961 Wrocław, Poland

Co-author declaration

With reference to Paulina Ratajczyk's application for the Doctoral degree in Chemical Sciences at the Adam Mickiewicz University in Poznań, I declare that I am a co-author of the publication:

- P. Ratajczyk, A. Katrusiak, K. A. Bogdanowicz, W. Przybył, P. Krysiak, A. Kwak, A. Iwan, *Mechanical strain, thermal and pressure effects on the absorption edge of an organic charge-transfer polymer for flexible photovoltaics and sensors,* Mater. Adv., 2022, 3, 2697-2705, DOI: 10.1039/D1MA01066B.

My contributions to this paper include the investigation of mechanical properties and their analysis.

Wrocław, 08.09.2025

Prof. Agnieszka Iwan
Military Institute of Engineer Technology,
Obornicka 136,
50-961 Wroclaw, Poland

Co-author declaration

With reference to Paulina Ratajczyk's application for the Doctoral degree in Chemical Sciences at the Adam Mickiewicz University in Poznań, I declare that I am a co-author of the publication:

- P. Ratajczyk, A. Katrusiak, K. A. Bogdanowicz, W. Przybył, P. Krysiak, A. Kwak, A. Iwan, *Mechanical strain, thermal and pressure effects on the absorption edge of an organic charge-transfer polymer for flexible photovoltaics and sensors,* Mater. Adv., 2022, 3, 2697-2705, DOI: 10.1039/D1MA01066B.

My contributions to this paper included project supervision, conceptualization, and manuscript writing and editing.

A. Iwan